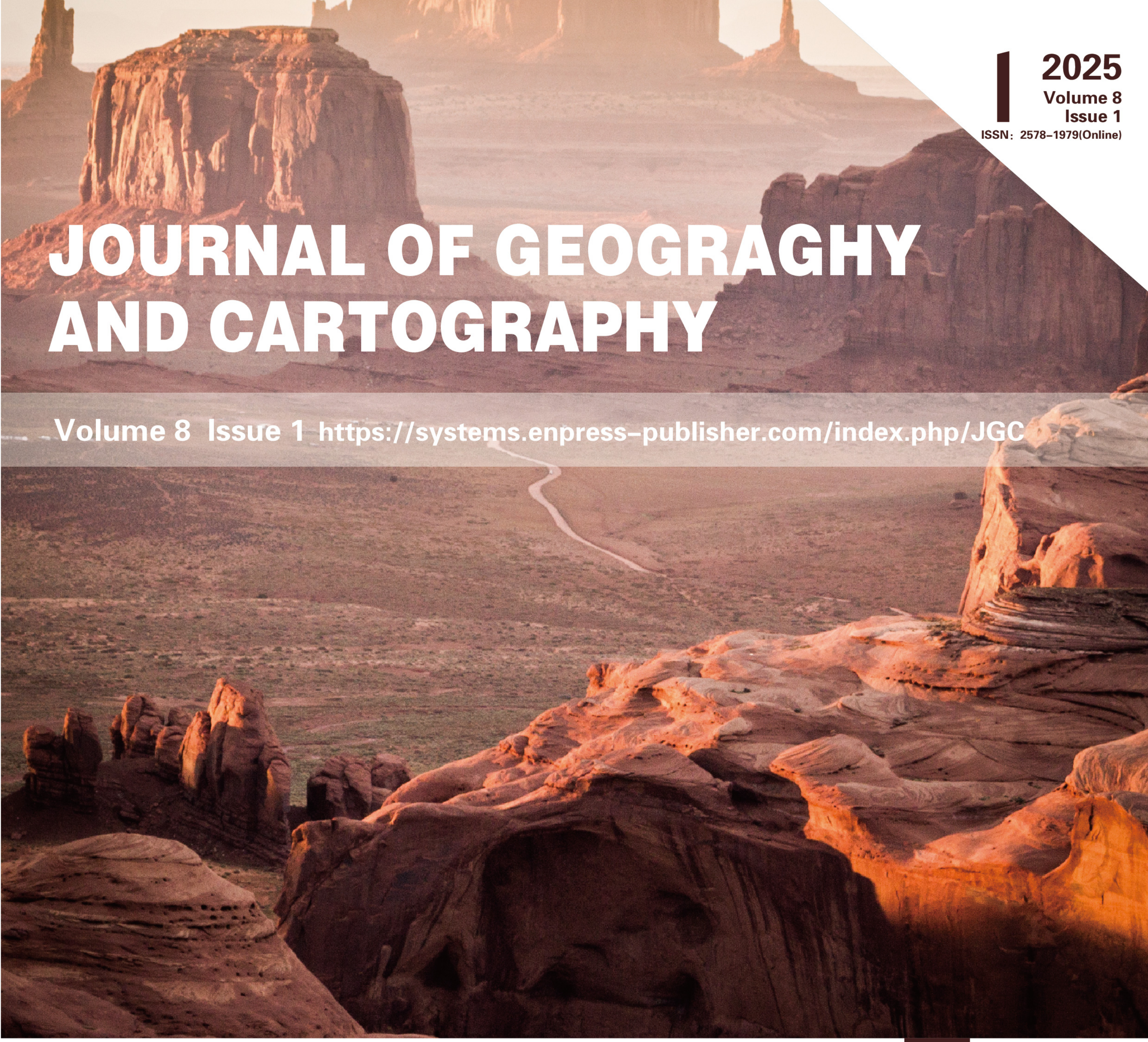

2025
Volume 8
Issue 1
ISSN: 2578-1979(Online)

JOURNAL OF GEOGRAGHY AND CARTOGRAPHY

Volume 8 Issue 1 https://systems.enpress-publisher.com/index.php/JGC

JGC

ISSN 2578-1979

EnPress Publisher

Carmine Apollaro
University of Calabria
Italy

Ahmed Mohammed El Kenawy
Mansoura University
Egypt

Ionut Cristi Nicu
Norsk Institutt for Kulturminneforskning
(NIKU) | Flinders University
Norway

Pravat Kumar Shit
Vidyasagar University
India

Volume 8 Issue 1 • 2025

Journal of Geography and Cartography

EnPress Publisher

2025 | Volume 8 | Issue 1

Journal of Geography and Cartography

https://systems.enpress-publisher.com/index.php/JGC

Contents

Articles

Journal of Geography and Cartography 2025, 8(1), 8785.
https://doi.org/10.24294/jgc8785

Article

Hydrological dynamics and road infrastructure resilience: A case study of river Nile state, Sudan

Hossam Aldeen Anwer*, Abubakr Hassan

Surveying Department, College of Engineering, Karary University, Omdurman 12304, Sudan
*** Corresponding author:** Hossam Aldeen Anwer, hossamanwe234@gmail.com

CITATION

Anwer HA, Hassan A. Hydrological dynamics and road infrastructure resilience: A case study of river Nile state, Sudan. Journal of Geography and Cartography. 2025; 8(1): 8785. https://doi.org/10.24294/jgc8785

ARTICLE INFO

Received: 17 November 2024
Accepted: 20 December 2024
Available online: 2 January 2025

Abstract: This study investigates the relationship between hydrological processes, watershed management, and road infrastructure resilience, focusing on the impact of flooding on roads intersecting with streams in River Nile State, Sudan. Situated between 16.5° N to 18.5° N latitude and 33° E to 34° E longitude, this region faces significant flooding challenges that threaten its ecological and economic stability. Using precise Digital Elevation Models (DEMs) and advanced hydrological modeling, the research aims to identify optimal flood mitigation solutions, such as overpass bridges. The study quantifies the total road length in the area at 3572.279 km, with stream orders distributed as follows: First Order at 2276.79 km (50.7%), Second Order at 521.48 km (11.6%), Third Order at 331.26 km (7.4%), and Fourth Order at 1359.92 km (30.3%). Approximately 27% (12 out of 45) of the identified road flooding points were situated within third- and fourth-order streams, mainly along the Atbara-Shendi Road and near Al-Abidiya and Merowe. Blockages varied in distance, with the longest at 256 m in Al-Abidiya, and included additional measurements of 88, 49, 112, 106, 66, 500, and 142 m. Some locations experienced partial flood damage despite having water culverts at 7 of these points, indicating possible design flaws or insufficient hydrological analysis during construction. The findings suggest that enhanced scrutiny, potentially using high-resolution DEMs, is essential for better vulnerability assessment and management. The study proposes tailored solutions to protect infrastructure, promoting sustainability and environmental stewardship.

Keywords: hydrology dynamics; road infrastructure resilience; river Nile state; stream order; watershed

1. Introduction

The complex interchange between stream order, watershed basins, and road infrastructure has become a focal point of study within the fields of hydrology and environmental planning. The concept of stream order, which plays a fundamental role in hydrology and geomorphology, was initially introduced by Horton in 1945 and subsequently refined by Strahler in 1957. It functions as a crucial tool for categorizing and examining river networks, providing valuable insights into their hierarchical structure and behavior. Horton's original work focused on organizing streams within watersheds, highlighting the process by which smaller streams merge to form larger ones [1,2]. Strahler expanded upon this by introducing a more organized method for assigning stream orders based on patterns of stream merging. According to Strahler's system, streams are assigned numerical orders according to their position within the hierarchy: small tributaries form first-order streams, and subsequent orders increase as streams merge, maintaining the highest order of the merging streams unless a higher-order stream is encountered [3]. This hierarchical framework allows researchers to investigate various aspects of river networks, such as drainage patterns, sediment transport, and ecological dynamics, across different spatial scales. Through this structured approach to understanding river systems, stream order classification enhances our comprehension of fluvial processes and their effects on landscapes and ecosystems. It's worth noting that streams can also act as barriers and channels for water, a characteristic that may increase flood risks under specific conditions [4,5], offers a tight approach to categorize streams within a watershed hierarchy. This classification system is helpful in elucidating the geomorphological and ecological processes within riverine systems [6]. Watershed basins, defined as areas where precipitation collects and flows toward a common outlet, are critical in managing water resources and maintaining ecological equilibrium [7]. The dynamics between watershed systems and road networks are intricate, as roadways can drastically modify the natural flow of water across landscapes, which may lead to inundation and deterioration of road infrastructure during flood incidents [8].

The design and configuration of roadways within a watershed are pivotal factors affecting hydrological phenomena, including surface runoff, sediment displacement, and stream connectivity [9]. Roads frequently serve dual roles as barriers and channels for water, a characteristic that can heighten flood risks under certain conditions [10]. The occurrence of roads being severed by floodwaters underscores the difficulties in sustaining infrastructure resilience and promoting environmental sustainability. Prior research has underscored the necessity of incorporating hydrological insights into road design and strategic planning to mitigate the detrimental effects of flooding [11,12]. Additionally, the influence of road networks on hydrological processes within both urban and rural settings demonstrates that without proper drainage and strategic placement, roads can profoundly interrupt natural watercourses, thereby increasing flood hazards and causing ecological disturbances [13].

In addressing these challenges, contemporary advances in watershed management practices have championed the implementation of sustainable and robust road design principles that account for the hydrological and ecological attributes of watersheds [14]. These approaches not only strive to diminish the hydrological impacts of roads but also aim to bolster the overall vitality of watershed ecosystems. This research paper endeavors to examine the intersection among stream order, watershed basin management, and road infrastructure, with a specific focus on the impacts of flooding on roads. By integrating insights from extensive research and numerous case studies over the past decade, this study will propose strategies to alleviate flood impacts on road infrastructure while promoting watershed health and resilience.

1.1. Hydrology analysis

Over the past ten years, advancements in technology and a deeper comprehension of watershed dynamics have substantially advanced hydrological modeling and analysis [15,16]. This paper presents a comprehensive review of the critical processes involved in hydrological analysis, encompassing precipitation interpolation, flow direction assessment, flow accumulation, stream order classification, and watershed delineation.

1.2. Precipitation filling

Precipitation interpolation serves as a fundamental preliminary phase in hydrological modeling, aimed at rectifying deficiencies in precipitation data critical for precise hydrological simulations. Contemporary methods for addressing these data gaps have transitioned to employing advanced statistical methods and machine learning algorithms, which deliver enhanced accuracy in predicting missing data points [17,18]. These techniques utilize patterns from historical data and spatial interpolation strategies to improve both the integrity and dependability of precipitation datasets.

1.3. Flow direction

The calculation of flow direction over a landscape is essential in hydrological modeling. Typically, this process utilizes Digital Elevation Models (DEMs), where specialized algorithms predict the probable paths of water flow downhill at each dataset point [19]. Sophisticated algorithms like D8, MFD (Multiple Flow Direction), and D8 [20,21]. have been introduced to yield more refined and precise predictions of flow trajectories by considering variations in slope and terrain features.

1.4. Flow accumulation

Subsequent to determining flow direction, flow accumulation methodologies are utilized to estimate the volume of water amassing across a landscape, a critical step for delineating stream channels and potential flood areas [22]. Contemporary approaches leverage high-resolution Digital Elevation Models (DEMs) and remote sensing data, facilitating a more accurate mapping and evaluation of hydrological characteristics [23].

1.5. Stream order

Stream order classification plays a pivotal role in comprehending the hierarchy of river networks and in watershed management endeavors. The widely utilized Strahler system assigns orders according to tributary structure [24]. Contemporary research frequently integrates traditional classification methods such as the Horton method and Strahler's system are foundational tools in the study of river networks and watershed management, with Geographic Information Systems (GIS) and remote sensing data to augment the precision and efficiency of stream network analyses [25].

1.6. Watershed delineation

Watershed delineation is essential for effective water resource management and environmental planning. This process entails identifying the geographic boundaries of a watershed by tracing water flow to a shared outlet. Recent advancements have leveraged automated tools integrated within Geographic Information System (GIS) platforms, alongside high-resolution topographic data, to achieve more accurate and efficient watershed delineation [26].

1.7. Basin

Basin analysis is fundamental for the sustainable management of water resources and environmental evaluations. This procedure entails delineating the physical boundaries of a drainage basin by tracking the convergence of water to a singular outflow point. Recent technological advancements have utilized automated tools within Geographic Information System (GIS) platforms, supplemented with high-resolution topographic data, to facilitate more accurate and efficient basin analysis [27].

1.8. Differences between watershed and basin

In hydrological terms, "watershed" and "basin" have different meanings based on their scale and application. A watershed refers to a smaller land area where all surface water converges at a single point, such as a stream, river, or lake, via a network of tributaries. It encompasses the region where precipitation collects and flows towards a common outlet [28,29]. On the other hand, a basin, also known as a drainage basin or river basin, covers a larger geographic area that includes multiple interconnected watersheds. The basin serves as the broader system through which all water drains into a major river, lake, or ocean, integrating the main river and its tributary network within a specified drainage region [30,31].

1.9. Study area

The research focuses on the River Nile State in Sudan, strategically located along the Nile as shown in **Figure 1**, the world's longest river, which progresses northward through the area before flowing into Egypt. The River Nile State in Sudan is physio graphically characterized by predominantly flat terrain with occasional modest elevations rarely exceeding a few hundred meters above sea level. The Nile River, a dominant geographical feature, flows through the region, shaping its landscape and influencing hydrological processes. The catchment area is defined by low-lying topography, making it prone to flooding during heavy rainfall, an arid to semi-arid climate that contributes to variability in water availability and runoff patterns, and the presence of alluvial plains formed by sediment deposition from the Nile and its tributaries. These features collectively influence the region's hydrology and its susceptibility to environmental and climatic challenges. Geographically, the River Nile State is positioned approximately between 16.5° N to 18.5° N latitude and 33° E to 34° E longitude, situated on a vital segment of the Nile River that is key to both its ecological and economic significance within the region.

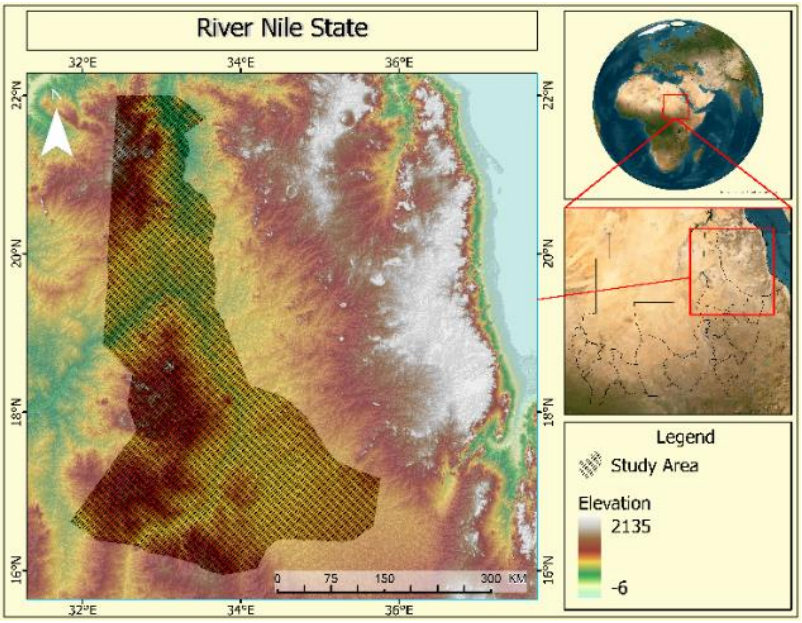

Figure 1. Study area location.

Nile River State in Sudan has experienced major floods in August 2022 and September 2023, driven by seasonal river flow changes and heavy rainfall. The low-lying landscape heightens flood vulnerability, causing disruptions to communities, infrastructure, and agriculture. The increasing severity and unpredictability of these events may be linked to climate change, underscoring the need for better flood forecasting, resilient infrastructure, and effective water management [32].

The aim of this study is to conduct a comprehensive analysis of the hydrology of River Nile State, focusing on the characteristics of streams, their classifications, and associated watersheds. Additionally, the study investigates the intersections between roads and streams to identify potential vulnerabilities that could lead to road disruptions, specifically referencing the significant flooding incidents on the Atbara-Shendi roads in 2022. This research will examine the hydrological dynamics and the resulting infrastructural damage observed at various road-stream intersections, providing insights to inform future mitigation strategies.

2. Methodology

To delineate stream orders, watersheds, and basins using ArcGIS Pro 3.0.2, the methodology began with preparing and refining Digital Elevation Models (DEMs) by clipping the DEM for the study area and projecting the DEM as shown in **Figure 2**. The Global Terrain Model (GTM) 2010 utilized in this study was sourced from the United States Geological Survey (USGS). It features a spatial resolution of 30 arcseconds (around 1 km) in both the East-West (X) and North-South (Y) dimensions. For vertical resolution (Z), the GTM achieves a finer resolution of 1 arcsecond (about 30 m). GTM-10, with a 10-meter spatial resolution, was selected over other freely available DEM data due to its global accessibility, ease of use, and suitability for medium-resolution geospatial analysis without complex processing. In contrast, Other DEM data Like Polsar, while providing more detailed 3D information, requires advanced processing and additional resources, making it less practical for this study.

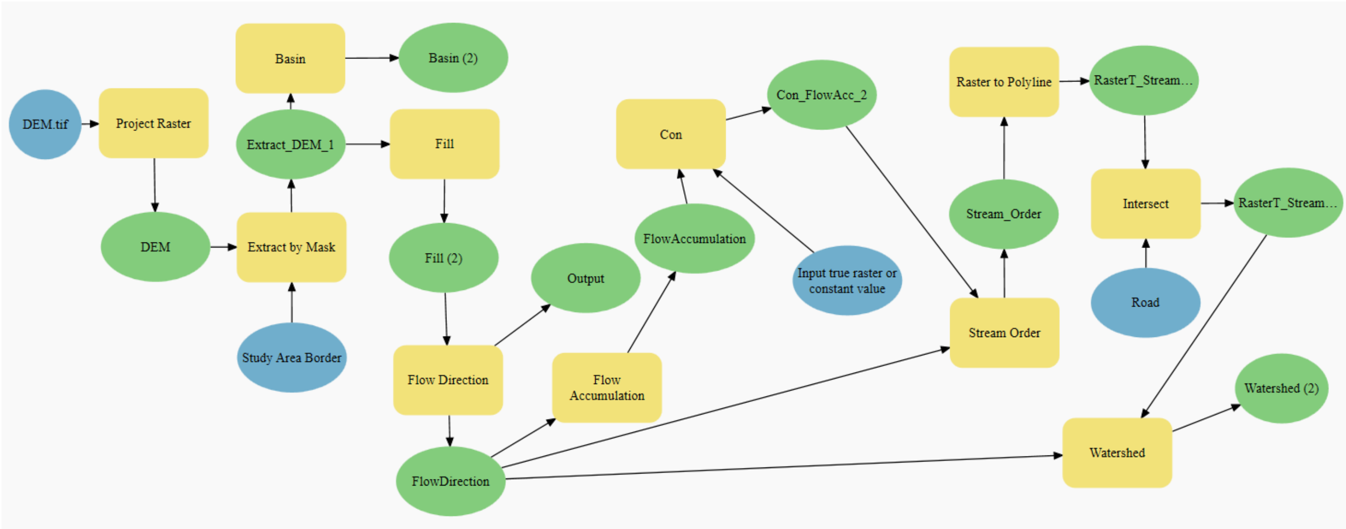

Figure 2. Hydrology analysis steps.

This level of detail in spatial granularity is essential for conducting precise terrain analysis and supporting diverse geographical and environmental research. The Hydrology toolset was then employed to calculate flow direction and accumulation, which supported the identification and segmentation of stream networks through a defined flow accumulation threshold. Stream segments were classified using the Strahler method via the Stream Order tool to elucidate the hierarchical structure of the network. Watershed delineation for each stream segment was conducted based on the flow direction raster using the Watershed tool, while larger drainage basins were identified using the Basin tool, which pinpoints all catchment areas converging to a unified outlet. This systematic approach in ArcGIS Pro 3.0.2 enabled a thorough and accurate hydrological analysis, critical for the effective management and planning of water resources and environmental considerations.

3. Results and analysis

In summary, our investigation has revealed the intricate relationship between hydrological dynamics, watershed management, and the resilience of road infrastructure, particularly focusing on flood impacts at intersections of roads and streams within the River Nile State, Sudan. Through rigorous analysis, we have discerned that intersections with second-order streams are particularly vulnerable to flood-induced disruptions in road infrastructure.

To prevent future disasters, we advocate for a proactive strategy utilizing high-precision Digital Elevation Models (DEMs) to accurately evaluate runoff dynamics at all 45 intersections of roads and streams. Employing advanced hydrological modeling techniques enables us to identify optimal solutions, such as the installation of overpass bridges or other infrastructure enhancements, to effectively mitigate flood risks.

Furthermore, our recommendation underscores the importance of comprehensive evaluation and strategic planning to ensure the long-term resilience of transportation networks in flood-prone regions. Integration of cutting-edge DEM data and advanced hydrological analysis allows for the development of tailored solutions that not only protect critical infrastructure but also promote sustainability and environmental stewardship.

Ultimately, our research advocates for the integration of scientific rigor and innovative engineering methodologies to tackle the multifaceted challenges posed by hydrological hazards. Through collaborative efforts and forward-thinking initiatives, we can foster resilient communities and infrastructure systems capable of navigating the complexities of our ever-evolving natural environment.

Situated in areas susceptible to seasonal flooding, the Nile River Road encounters heightened risk due to both localized and upstream precipitation patterns. The year 2022 witnessed exceptionally high rainfall during the monsoon season, which pushed river levels beyond normal limits, causing overflows at stream intersections. These hydrodynamic forces triggered erosion and partial destruction of the roadway infrastructure.

The vulnerability of the Nile River Road at its intersections with tributary streams arises from their specific geographical and hydrological configurations. An in-depth review of the flood incidents in 2022 revealed that 45 intersections were impacted: 30 intersections involved first-order streams, which are typically smaller, less complex stream channels that directly feed from the watershed. The interaction between these streams and the roadway often results in acute, localized damage due to sudden influxes of water and sediment.

13 intersections with second-order streams were documented. These are typically larger than first-order streams and can carry greater volumes of water and sediment, leading to more extensive erosive activities and structural damage to road infrastructures. Only two intersections with third-order streams were noted. Such streams represent a further increase in complexity and water flow, contributing to significant hydrodynamic pressures on road structures at their crossing points.

This detailed categorization of intersections by stream order highlights the scale and variety of the flood challenges faced, emphasizing the need for a differentiated approach in infrastructure planning and resilience building tailored to the hydrological characteristics of each stream type.

In this work, **Figure 3** is depicted to provide a Digital Elevation Model (DEM) of the selected study area. This model offers a three-dimensional portrayal of terrain elevations essential for delineating geographical and hydrological features that are crucial for flood modeling and assessing infrastructure vulnerabilities.

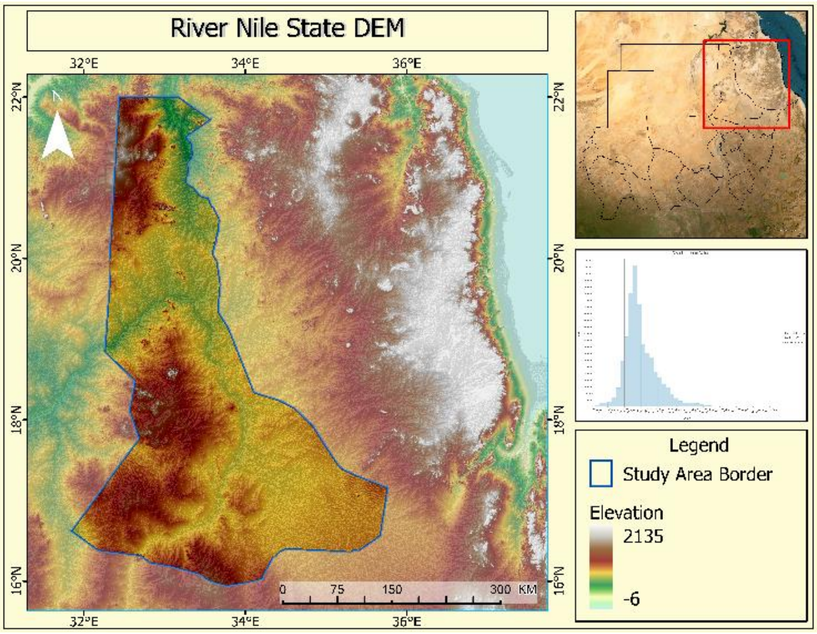

Figure 3. Study area DEM.

Figure 4 is dedicated to showcasing the stream order, derived from a hydrological analysis of the study area. This classification system illuminates the hierarchical structure and connectivity of stream networks, which is instrumental in evaluating their potential impacts on road networks during flood conditions.

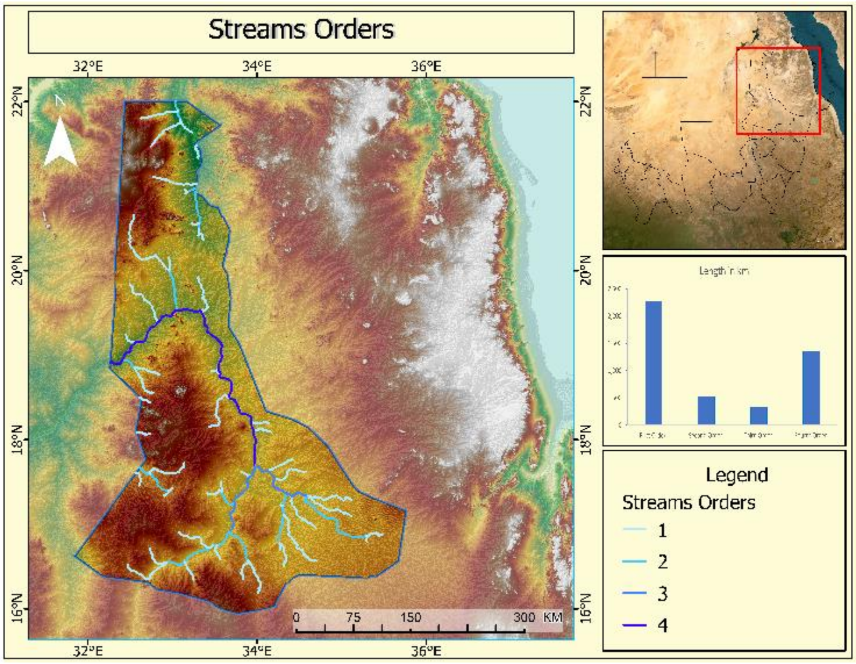

Figure 4. Stream orders over study area.

In **Figure 5**, the focus shifts to the layout of the road network within the study area. The visualization of this network is imperative for pinpointing critical infrastructure that may be susceptible to interruptions due to hydrological disturbances, thereby establishing a foundation for assessing infrastructural vulnerabilities. **Figure 6** reveals the intersections of roads with streams, a critical factor in assessing the potential flood risks to the road network. Such figure pinpoints the exact locations where the infrastructural elements are most at risk of failure during flooding, highlighting the intersection points as critical areas for flood risk management.

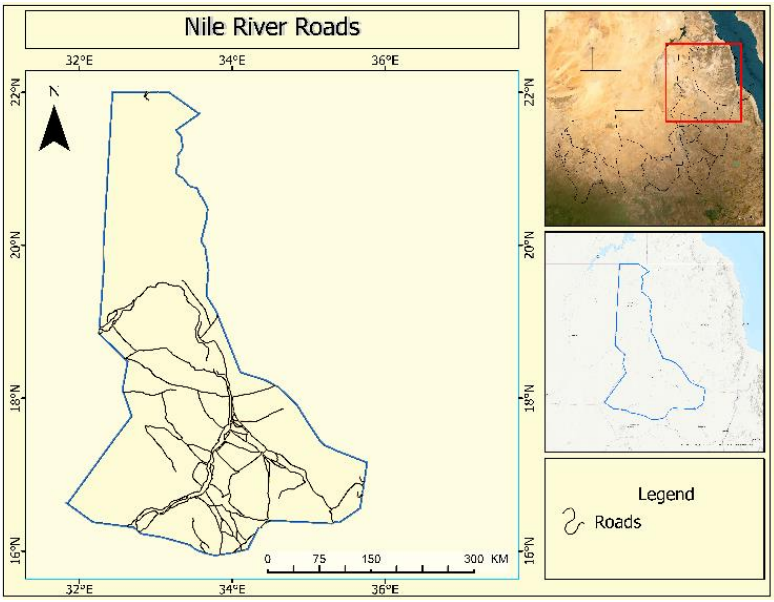

Figure 5. Study area roads.

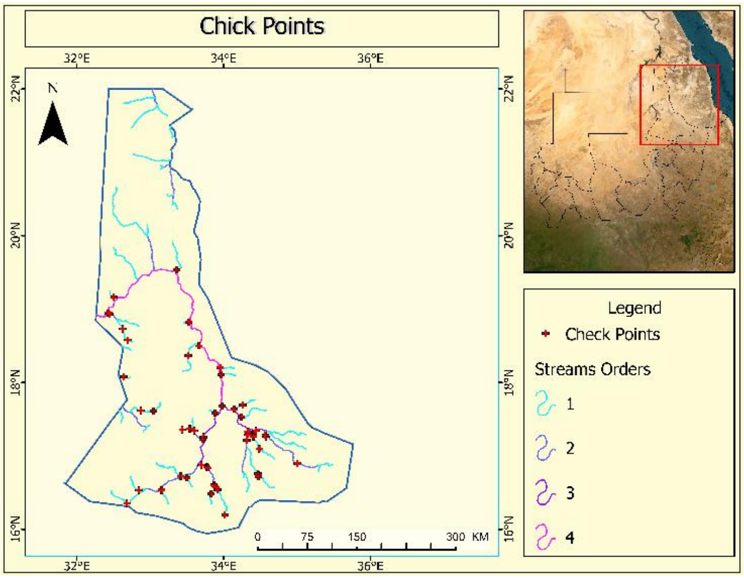

Figure 6. Intersect of roads with streams.

Lastly, **Figure 7** presents an intricate depiction of the road-stream intersections, complemented by the intersect values for stream orders. This granular view enhances the understanding of flood risks by correlating the frequency and severity of flood events with the stream orders at each intersection point. This level of detail is vital for formulating targeted strategies to mitigate risks and bolster infrastructure resilience against future hydrological threats.

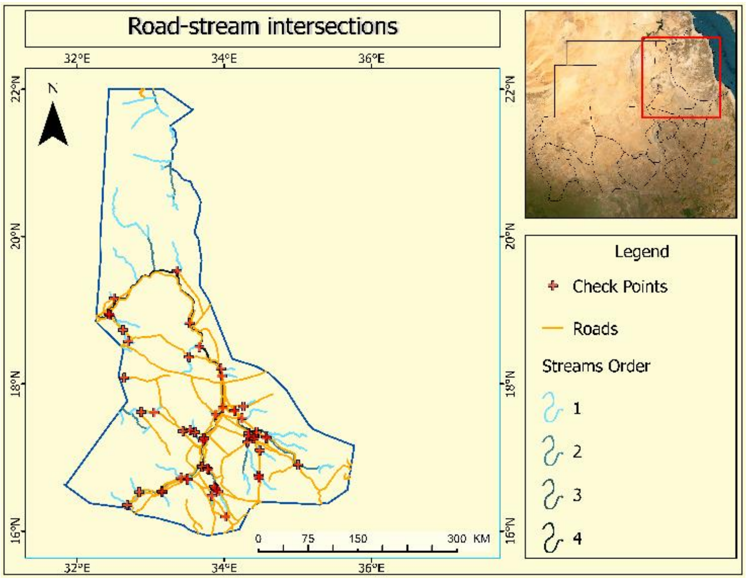

Figure 7. Depiction of the road-stream intersections.

3.1. First order streams

The total length of first order streams is approximately 2276.79 km. These streams represent the smallest in the hierarchy, yet they contribute significantly to the overall network. They make up about 50.7% of the total length of all streams as shown in **Figure 8**.

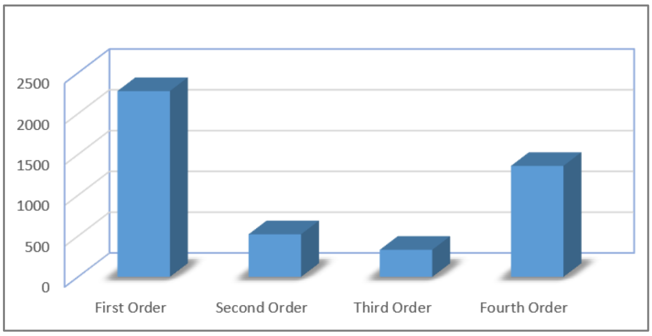

Figure 8. Streams orders length.

3.2. Second order streams

Second order streams have a combined length of around 521.48 km, representing the next level in the stream hierarchy. They account for about 11.6% of the total Streams length.

3.3. Third order streams

With a total length of approximately 331.26 km, third order streams play a vital role in the watershed system. They constitute around 7.4% of the total Streams length.

3.4. Fourth order streams

Fourth order streams, the largest in this dataset, have a combined length of about 1359.92 km. Despite being fewer in number, they contribute significantly to the overall stream network, making up approximately 30.3% of the total length as shown in **Table 1**.

Total Streams Length:

When considering all stream orders, the total length of the streams amounts to approximately 4489.45 km.

Table 1. Stream orders: Length and percentage distribution.

Stream orders	Length in KM	Percentage
First Order	2276.79	50.7%
Second Order	521.48	11.6%
Third Order	331.26	7.4%
Fourth Order	1359.92	30.3%

Streams of higher orders typically boast expanded drainage basins and augmented discharge capacities, thereby facilitating the conveyance of substantial water volumes during flood occurrences. Consequently, roads intersecting with such streams are subjected to heightened risks of inundation, erosion, and structural degradation due to the intensified hydrodynamic forces exerted by floodwaters.

Moreover, second and third order streams, distinguished by heightened flow velocities and channel intricacies, are predisposed to more pronounced sediment transportation and channel alterations during flood events. This heightened erosional propensity can exacerbate the impacts on adjacent road infrastructure, precipitating disruptions and potential safety hazards for vehicular traffic.

To summarize, roads intersecting with streams of higher order, particularly those classified as second and third order, are predisposed to experiencing flood-related hazards owing to their augmented discharge capacities and erosional tendencies. Comprehending these interrelations is imperative for guiding the formulation of efficacious mitigation measures and fortifying the resilience of transportation networks against flood events.

In the realm of transportation infrastructure management, the accurate determination and evaluation of road length serve as fundamental metrics underpinning effective planning and operational strategies. In our investigation, we have meticulously quantified the total road length to be 3572.279 km within the designated area under study.

Furthermore, the intricate interplay between road networks and natural watercourses cannot be overstated. Our analysis has revealed that these roads intersect with streams at 45 distinct points. It is imperative to acknowledge that such intersections not only denote critical junctures in the transportation network but also entail potential environmental and engineering challenges.

In response to past incidents wherein flooding compromised road integrity, leading to significant disruptions, our research endeavors to proactively mitigate future occurrences of such disasters. By meticulously identifying intersect points and discerning the sequential order of streams, our aim is to develop a comprehensive understanding of the spatial dynamics influencing flood risk.

To address these challenges, the implementation of specialized infrastructure solutions, such as underpasses or overpasses, emerges as a pivotal consideration. The design and deployment of these structures necessitate a nuanced approach, accounting for factors such as topographical constraints, traffic flow patterns, financial feasibility, and available space allocations.

By integrating advanced detection methodologies and leveraging spatial analytics, our research endeavors to offer actionable insights aimed at optimizing infrastructure resilience and safeguarding against potential calamities. Through the judicious application of data-driven decision-making, we aspire to foster sustainable and resilient transportation systems that effectively navigate the complex interplay between natural and built environments.

Based on the conducted analysis, it was found that approximately 12 out of 45 (27%) road intersect points were located within third- and fourth-order Streams. These points were primarily situated along the Atbara-Shendi Road, near Al-Abidiya, and in proximity to the Merowe Road. The blockage distances included Al-Abidiya at approximately 256 m (840 feet), and several locations along the Atbara-Shendi Road as shown in **Figures 9** and **10**, with measurements of 88 m (289 feet), 49 m (161 feet), 112 m (367 feet), 106 m (348 feet), 66 m (217 feet), 500 m (1,640 feet), and 142 m (466 feet).

(a)

(b)

(c)

(d)

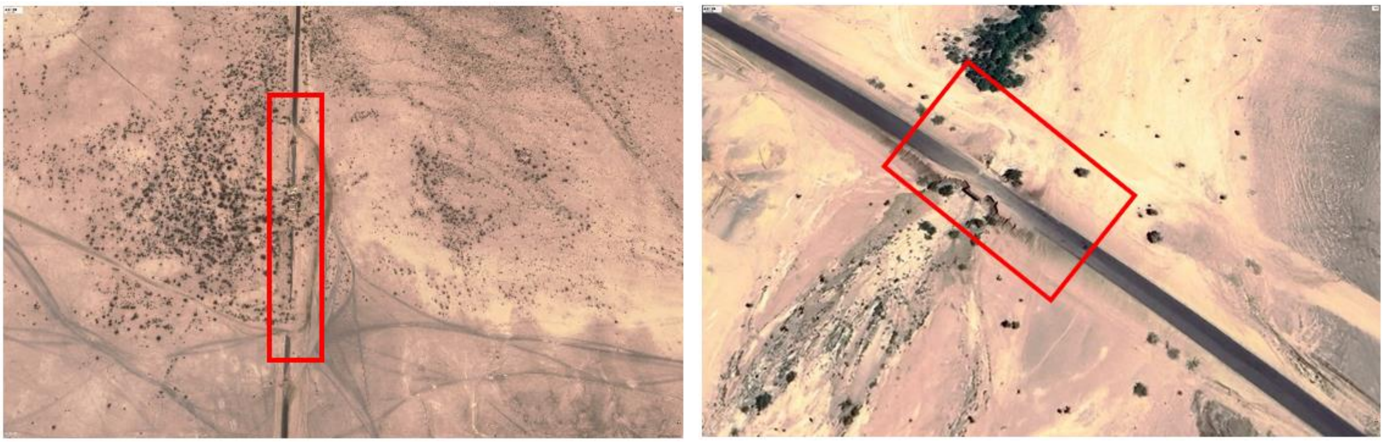

(e) **(f)**

Figure 9. Affected area. **(a)** Atbara-port Sudan road; **(b)** Atbara - port Sudan road; **(c)** Abu Hamad Road; **(d)** Al-Abidiya; **(e)** Atbara-Shendi Road; **(f)** Atbara-Shendi Road.

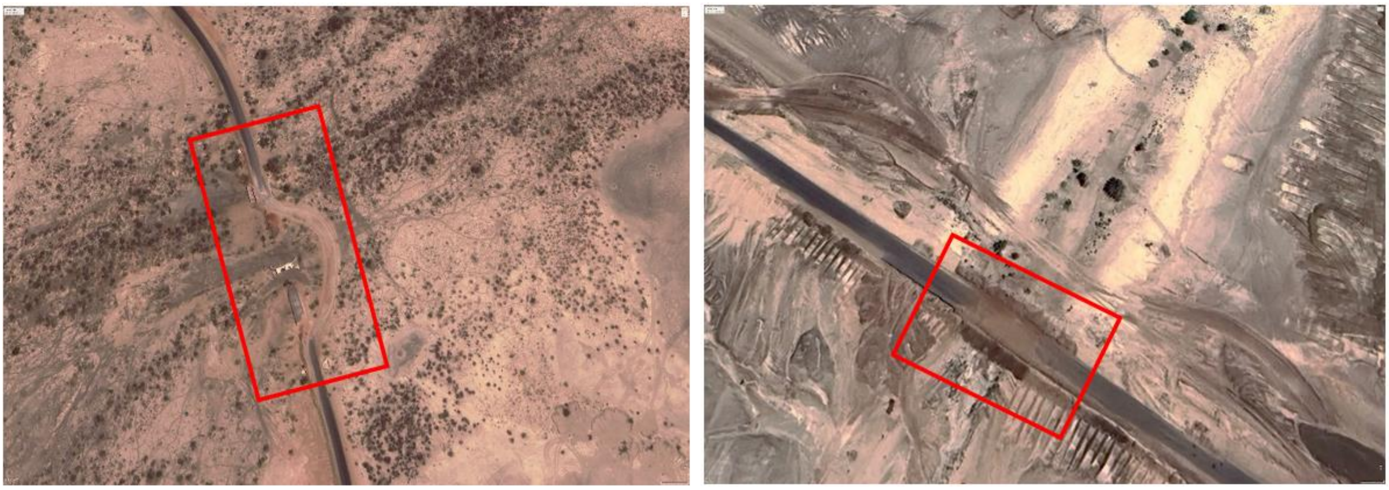

(a) **(b)**

(c) **(d)**

(e) **(f)**

Figure 10. Affected area. **(a)** Atbara-Shendi Road; **(b)** Atbara-Shendi Road; **(c)** Atbara-Shendi Road; **(d)** Atbara-Shendi Road; **(e)** Atbara-Shendi Road; **(f)** Atbara-Shendi Road.

In addition, some points experienced partial damage from flooding. Among the 13 locations with complete road intersect, 7 points were equipped with concrete water culverts. Additionally, near Abu Hamad, the flood cut approximately 1800 m, while along the Atbara-Port Sudan road, the affected sections measured about 106 m and 186 m.

In delving into watershed domains, the use of key statistical parameters reveals deep insights into the complex spatial patterns and changing dynamics of hydrological phenomena. These metrics, likened to celestial navigation stars, encapsulate the vastness and depth of watershed dimensions within the examined area. The mean area acts as a guiding light, representing the typical size of observed watersheds as shown in **Figure 11**, while the range from minimum to maximum values delineates the spectrum of spatial extents, marking the transition from small catchments to large drainage basins.

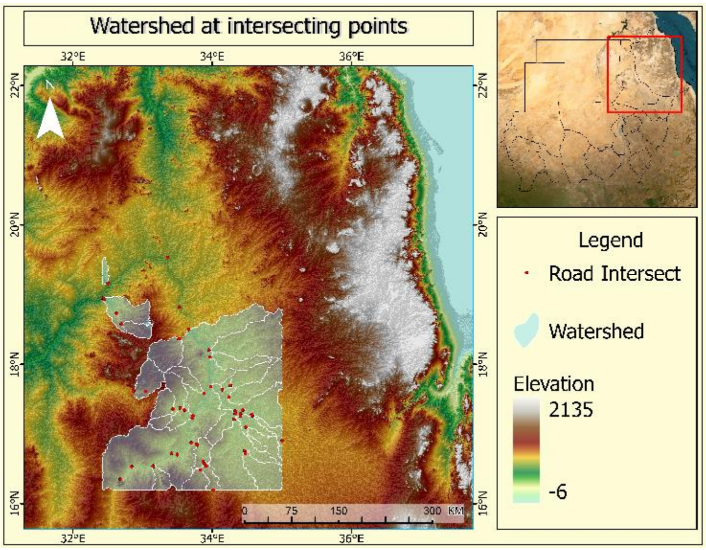

Figure 11. Watershed at intersecting points.

Beyond mere numbers, these ethereal statistical summaries become heralds of hydrological foresight, resonating through hydrological modeling to guide land use planners and water managers. By unveiling the intricate diversity of watersheds, these celestial metrics serve as navigational aids, directing efforts to enhance watershed resilience, mitigate hydrological risks, and preserve the integrity of water ecosystems.

Some watersheds, resulting from the intersection points of roads and streams, are too small to be displayed on the map.

From the dataset the following summary statistics are derived:

Mean area: 1331.7 square km;

Minimum area: 0.034961 square km;

Maximum area: 22,206 square km.

The research area consists of eight distinct hydrological basins, each exerting a unique influence on the hydrological processes under scrutiny. These basins vary considerably in size, ranging from a nominal area of 0.049946235 square km to the largest basin, which covers an extensive 107,852.9014 square km, as depicted in **Figure 12**.

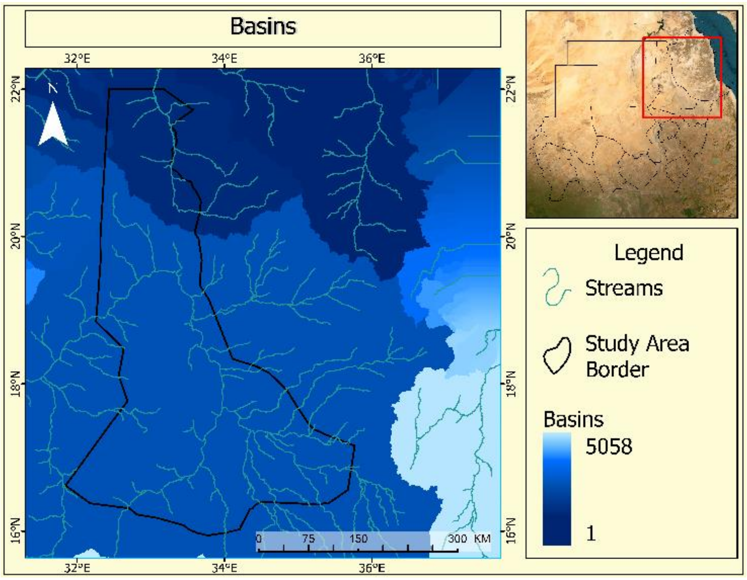

Figure 12. Basin map.

The location where the flood caused a road cut was found to have a watershed area of 214 square km. This indicates that any point where the road intersects with a watershed area of 214 square km or larger is at a higher risk of being affected by flooding. Therefore, it is essential to assess these points to prevent similar issues. A total of 26 such points were identified; however, not all of them are on the main road; some are on secondary or unpaved roads. Enhanced scrutiny, potentially using high-resolution digital elevation models (DEMs), is recommended for greater accuracy.

Comparative analyses with similar studies from various geographical contexts, such as those conducted in Louisiana, USA [33], Southeast Asia [34], and Jakarta, Indonesia [35], highlight the universal applicability of integrating hydrological data into infrastructure planning and design. For instance, the Louisiana study utilized high-resolution DEMs and GIS tools to evaluate flood risks on coastal road infrastructure, recommending elevated roadways and enhanced drainage systems as key mitigation strategies. Similarly, research in Southeast Asia, focusing on monsoon-induced floods in Thailand and Vietnam, underscored the significant role of DEMs and hydrological models in evaluating flood impacts and recommending optimal solutions, such as elevated roads and improved drainage systems. The study in Jakarta addressed urban flooding issues, emphasizing the necessity of sustainable urban drainage solutions and strategic planning to ensure the resilience of road infrastructure.

These comparative studies reinforce the necessity of employing elevated roadways, improved drainage systems, and sustainable urban drainage solutions as key strategies for enhancing infrastructure resilience. While specific solutions may vary depending on regional characteristics, the underlying principles of integrating hydrological data, enhancing drainage systems, and employing strategic planning are universally applicable.

Table 2. Comparative analysis of methodologies and DEM data used in hydrological studies.

Methodology Step	volcanic island [33]	Southeast Asia [34]	Rio de Janeiro [35]	This study
Watershed Delineation	Yes	Yes	Yes	Yes
Stream Network Extraction	Yes	Yes	Yes	Yes
Stream Order Classification	No	Yes	Yes	Yes
High-Resolution DEM Analysis	Yes	Yes	Yes	No
Identification of High-Risk Points	Yes	Yes	Yes	Yes
Vertical Resolution	1m	20 m	16 m	16m
Spatial Resolution	1m-10m	30 m	30 m	30 m

Our results, aligned with these similar studies, demonstrate that comprehensive evaluations and strategic planning, supported by high-precision DEMs and advanced hydrological modeling, are crucial for ensuring the long-term resilience of transportation networks in flood-prone areas.

The comparative analysis of studies from Louisiana, USA, Southeast Asia, Jakarta, Indonesia, and River Nile State, Sudan, underscores the universal importance of integrating hydrological data into infrastructure planning and design. All studies utilized Digital Elevation Models (DEMs) and hydrological models to assess flood risks and propose mitigation strategies. The Louisiana study and our study in River Nile State employed Medium-resolution DEMs (10 m–20 m) as shown in **Table 2** for detailed analysis, focusing on elevated roadways and enhanced drainage systems. Southeast Asia's research used medium to high-resolution DEMs (10 m–30 m) to address monsoon-induced floods with similar mitigation recommendations. Jakarta's study, with medium-resolution DEMs (10 m–30 m), emphasized sustainable urban drainage solutions for urban flooding. Despite regional differences, the consistent use of high-precision DEMs, advanced hydrological modeling, and strategic planning highlights the global applicability of these methodologies to enhance infrastructure resilience against floods.

4. Conclusion

Our investigation into the "Hydrological Dynamics and Road Infrastructure Resilience: A Case Study of River Nile State, Sudan," reveals the intricate relationship between hydrological patterns, watershed management, and the vulnerability of road infrastructure to flood events. The analysis identified 26 high-risk intersections where roads meet watersheds of 214 square km or larger, particularly near second-order streams, making these locations especially susceptible to flood-induced disruptions. Additionally, 27% of the analyzed road intersections that flooded (12 out of 45) were found within third- and fourth-order streams, particularly along the Atbara-Shendi Road, near Al-Abidiya, and the Merowe Road. The blockage distances in these areas varied significantly, including notable instances at Al-Abidiya (256 m), Atbara-Shendi Road (88, 49, 112, 106, 66, 500, and 142 m), Abu Hamad (1800 m), and the Atbara-Port Sudan road (106 and 186 m). Some locations also experienced partial damage, with seven of the 13 completely intersected points equipped with concrete culverts.

These findings emphasize the necessity of high-resolution Digital Elevation Models (DEMs) for more precise assessments and advanced hydrological modeling techniques to evaluate runoff dynamics effectively at all road-stream intersections. Incorporating these tools will enhance the identification of optimal mitigation strategies, such as the construction of overpass bridges, drainage improvements, and other infrastructure upgrades, to manage flood risks proactively.

The study underscores the critical importance of combining scientific rigor with innovative engineering methodologies to address the multifaceted challenges posed by hydrological hazards. Comprehensive evaluations and strategic planning are essential for ensuring the long-term resilience of transportation networks in flood-prone areas. Employing cutting-edge DEM data and advanced hydrological analysis facilitates the development of tailored solutions that protect critical infrastructure and promote sustainability and environmental stewardship.

Recommendation

1) Utilize High-Resolution DEMs for Improved Flood Risk Assessment: Implement high-resolution DEMs (5–10 m) to enhance the accuracy of identifying vulnerable road-stream intersections and assessing potential flood risks.
2) Upgrade Infrastructure at Identified High-Risk Locations: Focus on the 26 high-risk intersections and areas with significant blockage distances for infrastructure enhancements. Priority should be given to locations like Al-Abidiya, Atbara-Shendi Road, Abu Hamad, and Atbara-Port Sudan Road, where mitigation structures such as overpasses, culverts, and elevated road sections can reduce flood vulnerability.
3) Improve Drainage Systems: Upgrade existing drainage infrastructure to handle increased runoff volumes, particularly at points already equipped with culverts. Consider sustainable drainage solutions, such as bioswales and permeable pavements, to further manage stormwater and reduce flooding risks.
4) Implement Routine Monitoring and Maintenance Programs: Establish continuous monitoring and maintenance programs for critical road-stream intersections to ensure the infrastructure remains effective in mitigating flood risks.
5) Future Research Directions: Further studies should aim to refine hydrological modeling techniques, explore innovative infrastructure solutions like real-time flood monitoring systems, and adopt adaptive road design strategies to enhance

road resilience against hydrological hazards.

Author contributions: Conceptualization, HAA and AH; methodology, HAA; software, HAA; validation, HAA; formal analysis, HAA and AH; investigation, HAA; resources, HAA and AH; data curation, HAA; writing—original draft preparation, HAA; writing—review and editing, HAA; visualization, HAA; supervision, AH; project administration, HAA and AH. All authors have read and agreed to the published version of the manuscript.

Conflict of interest: The authors declare no conflict of interest.

References

1. Horton RE. Erosional development of streams and their drainage basins; hydrophysical approach to quantitative morphology. Geological Society of America Bulletin. 1945; 56(3): 275-370. doi: 10.1130/0016-7606(1945)56[275:EDOSAT]2.0.CO;2
2. Krishnan A, Ramasamy J. Morphometric assessment and prioritization of the South India Moyar river basin sub-watersheds using a geo-computational approach. Geology, Ecology, and Landscapes. 2022; 8(2): 129-139. doi: 10.1080/24749508.2022.2109819
3. Strahler AN. Quantitative analysis of watershed geomorphology. Transactions of the American Geophysical Union. 1957; 38(6): 913-920. doi: 10.1029/TR038i006p00913
4. D'Ambrosio JL, Williams LR, Witter JD, et al. Effects of geomorphology, habitat, and spatial location on fish assemblages in a watershed in Ohio, USA. Environmental Monitoring and Assessment. 2008; 148(1-4): 325-341. doi: 10.1007/s10661-008-0163-3
5. Johnson K, Jankowski KJ, Carey JC, et al. Climate, Hydrology, and Nutrients Control the Seasonality of Si Concentrations in Rivers. Journal of Geophysical Research: Biogeosciences. 2024; 129(9). doi: 10.1029/2024jg008141
6. Leopold LB, Wolman MG, Miller JP, et al. Fluvial processes in geomorphology. Courier Dover Publications; 2020.
7. Dingman SL. Physical hydrology. Waveland press; 2015.
8. Forman RTT, Alexander LE. Roads and their major ecological effects. Annual Review of Ecology and Systematics. 1998; 29(1): 207-231. doi: 10.1146/annurev.ecolsys.29.1.207
9. Montgomery DR. Road surface drainage, channel initiation, and slope instability. Water Resources Research. 1994; 30(6): 1925-1932. doi: 10.1029/94wr00538
10. Berges SA. Ecosystem services of riparian areas: stream bank stability and avian habitat [Master thesis]. Iowa State University; 2009.
11. Brun SE, and Band LE. Simulating runoff behavior in an urbanizing watershed. Computers, environment and urban systems. 2000; 24(1): 5-22. doi:10.1016/S0198-9715(99)00040-X
12. Wemple BC, Jones JA, Grant GE. Channel network extension by logging roads in two basins, western cascades, oregon1. JAWRA Journal of the American Water Resources Association. 1996; 32(6): 1195-1207. doi: 10.1111/j.1752-1688.1996.tb03490.x
13. Ellis JB. Managing Urban Runoff. Handbook of Catchment Management; 2009. pp. 155-182.
14. Parkinson J, Mark O. Urban stormwater management in developing countries. IWA publishing; 2005.
15. Ayalew AD, Wagner PD, Tigabu TB, et al. Hydrological responses to land use and land cover change and climate dynamics in the Rift Valley Lakes Basin, Ethiopia. Journal of Water and Climate Change. 2023; 14(8): 2788-2807. doi: 10.2166/wcc.2023.138
16. Fallon K, Wheelock SJ, Sadegh M, et al. Post-fire hydrologic analysis: a tale of two severities. Hydrological Sciences Journal. 2023; 69(1): 139-148. doi: 10.1080/02626667.2023.2284306
17. Sattari MT, Rezazadeh-Joudi A, Kusiak A. Assessment of different methods for estimation of missing data in precipitation studies. Hydrology Research. 2016; 48(4): 1032-1044. doi: 10.2166/nh.2016.364
18. Vaze J, Chiew FHS, Perraud JM, et al. Rainfall-Runoff Modelling Across Southeast Australia: Datasets, Models and Results. Australasian Journal of Water Resources. 2011; 14(2): 101-116. doi: 10.1080/13241583.2011.11465379

19. Guillet G, Bolch T. Probabilistic estimation of glacier surface elevation changes from DEM differentiation: a Bayesian method for outlier filtering, gap filling and uncertainty estimation with examples from High Mountain Asia; 2022.
20. Tarboton DG. A new method for the determination of flow directions and upslope areas in grid digital elevation models. Water Resources Research. 1997; 33(2): 309-319. doi: 10.1029/96wr03137
21. Folton N. Using spot flow measurements in a regionalized hydrological model to improve the low flow statistical estimations of rivers: The case of Réunion Island. Journal of Hydrology: Regional Studies. 2024; 52: 101730. doi: 10.1016/j.ejrh.2024.101730
22. Tarboton D. Terrain analysis using digital elevation models in hydrology. In: Proceedings of the 23rd ESRI international users conference; 2003; San Diego, California.
23. Gao H, Sabo JL, Chen X, et al. Landscape heterogeneity and hydrological processes: a review of landscape-based hydrological models. Landscape Ecology. 2018; 33(9): 1461-1480. doi: 10.1007/s10980-018-0690-4
24. Godsey SE, Kirchner JW. Dynamic, discontinuous stream networks: hydrologically driven variations in active drainage density, flowing channels and stream order. Hydrological Processes. 2014; 28(23): 5791-5803. doi: 10.1002/hyp.10310
25. Pradeep K. Rawat, P.C. Tiwari, and Charu C. Pant. Morphometric analysis of third order river basins using high resolution satellite imagery and GIS technology: special reference to natural hazard vulnerability assessment. E-Int Sci Res J. 2011; 3(2): 70-87.
26. Datta S, Karmakar S, Mezbahuddin S, et al. The limits of watershed delineation: implications of different DEMs, DEM resolutions, and area threshold values. Hydrology Research. 2022; 53(8): 1047-1062.
27. Gonzales-Inca C, Calle M, Croghan D, et al. Geospatial Artificial Intelligence (GeoAI) in the Integrated Hydrological and Fluvial Systems Modeling: Review of Current Applications and Trends. Water. 2022; 14(14): 2211. doi: 10.3390/w14142211
28. Mikaeili O, Shourian M. Assessment of the Analytic and Hydrologic Methods in Separation of Watershed Response to Climate and Land Use Changes. Water Resources Management. 2022; 37(6-7): 2575-2591. doi: 10.1007/s11269-022-03324-9
29. Abdissa AG, Chuko FW. Climate change and watershed hydrology: assessing variability in water balance components and groundwater flow patterns. Journal of Water and Climate Change. 2024; 15(9): 4389-4404. doi: 10.2166/wcc.2024.080
30. Erikson CM, Renshaw CE, Magilligan FJ. Spatial variation in drainage area—Runoff relationships and implications for bankfull geometry scaling. Geomorphology. 2024; 446: 108998. doi: 10.1016/j.geomorph.2023.108998
31. Chen H, Huang S, Xu Y, et al. Using Baseflow Ensembles for Hydrologic Hysteresis Characterization in Humid Basins of Southeastern China. Water Resources Research. 2024; 60(4). doi: 10.1029/2023wr036195
32. Osman HA, Elhag A, Hassan A. GIS Applications in Land Management: Enhancing Flood Risk Assessment and Village Replanning. Journal of Karary University for Engineering and Science. 2024; 3(2). doi: 10.54388/jkues.v3i2.259
33. Najafi MR, Zhang Y, Martyn N. A flood risk assessment framework for interdependent infrastructure systems in coastal environments. Sustainable Cities and Society. 2021; 64: 102516. doi: 10.1016/j.scs.2020.102516
34. Noi LVT, Cooper RT, Trang DTT, et al. Climate change risk assessment and adaptation for loss and damage of urban transportation infrastructure in Southeast Asia. APN Science Bulletin. 2021; 11(1). doi: 10.30852/sb.2021.1436
35. Bertilsson L, Wiklund K, de Moura Tebaldi I, et al. Urban flood resilience—A multi-criteria index to integrate flood resilience into urban planning. Journal of Hydrology. 2019; 573: 970-982. doi: 10.1016/j.jhydrol.2018.06.052

Journal of Geography and Cartography 2025, 8(1), 10129.
https://doi.org/10.24294/jgc10129

Article

Valencia's battle against floods: A cartographic review to assess water management strategies

Bárbara Polo-Martín[1,2]

[1] Universitat de Lleida (UdL), 25003 Lleida, Spain; barbarapolomartin@gmail.com
[2] CNRS (Centre National de la Recherche Scientifique), Nanterre Université, 92000 Nanterre, France

CITATION

Polo-Martín B. Valencia's battle against floods: A cartographic review to assess water management strategies. Journal of Geography and Cartography. 2025; 8(1): 10129. https://doi.org/10.24294/jgc10129

ARTICLE INFO

Received: 6 November 2024
Accepted: 18 December 2024
Available online: 3 January 2025

Abstract: The modification of the Turia River's course in the 1960s marked a pivotal transformation in Valencia's urban landscape, evolving from a flood protection measure into a hallmark of sustainable urban development. However, recent rainfalls and flooding events produced directly by the phenomenon known as DANA ((Isolated Depression at High Levels) in October 2024 have exposed vulnerabilities in the infrastructure, particularly in the rapidly urbanized southern areas, raising questions about the effectiveness of past solutions in the context of climate change and urban expansion. As a result of this fragility, more than 200 deaths have occurred, along with material losses in 87 municipalities, whose industrial infrastructure accounts for nearly one-third of the economic activity in the Province of Valencia, valued at 479.6 million euros. This paper presents, for the first time, a historical-document-based approach to evaluate the successes and shortcomings of Valencia's flood management strategies through policy and spatial planning analysis. Also, this paper remarks the ongoing challenges and potential strategies for enhancing Valencia's urban resilience, emphasizing the need for innovative water management systems, improved drainage infrastructure, and the renaturalization of flood-prone areas. The lessons learned from Valencia's experience in 1957 and 2024 can inform future urban planning efforts in similar contexts facing the dual pressures of environmental change and urbanization.

Keywords: historical cartography; Valencia; DANA; floods; water management

1. Introduction

Valencia's geographical and hydrological characteristics have made it historically vulnerable to flooding. It is a city shaped by its proximity to the Mediterranean Sea and its position within the fertile plains of the Turia River basin, playing a central role in shaping this risk. While these features have historically supported agriculture and urban growth, they also contribute to the city's heightened vulnerability to flooding. To that problem, the city's flat topography amplifies its flood risk. Low-lying and largely featureless, the terrain facilitates rapid water accumulation during intense rainfall, a hallmark of the region's Mediterranean climate. Seasonal storms often result in heavy downpours that overwhelm the city's natural and man-made drainage systems.

The intense rainfall and following flooding that affected Valencia on 29 October 2024 has reignited the debate around preventive measures for extreme weather events in the city, and also, in other areas of Spain prone to suffer heavy rainfalls. These recent episodes of torrential rain have highlighted both the strengths and limitations of the current protection and drainage systems, as well as the older plans designed for the riverbed and the city itself. The modification of the Turia River's course, carried out in the 1960s after the catastrophic flood of 1957—which caused over 80 deaths-, serves as a key reference for understanding how Valencia has historically managed flood risks and what additional measures may be needed to address climate change and increasingly intense floods.

The modification of the river was not only an ambitious engineering project but also an initiative that would reshape Valencia's urban, social, and cultural landscape. This article explores the historical context of the city´s growth, execution of the modification of the river, and effects of this historic intervention, as well as the legacy it has left in the lives of Valencians and the city's image.

The floods of 2024, caused by a series of *gota fría* phenomena similar to the 1957 events, have had similar consequences, but now in the area where the modifications were made. Valencia experienced a year's worth of rain in just eight hours, leading to severe flash floods that caused significant damage to any kind of infrastructures. The most affected areas included the Ribera Alta, Horta Sud, and municipalities such as Chiva and Utiel, where rivers and streams like the Magro River overflowed. Some regions recorded rainfall of up to 500 mm (20 inches) in a single day, highlighting the intensity of the storm. The consequences were more than 200 deaths, along with material losses in 87 municipalities, whose industrial infrastructure accounts for nearly one-third of the economic activity in the Province of Valencia, valued at 479.6 million euros [1].

As we present here, this is not new.but these episodes, have become increasingly frequent and severe in the Mediterranean, exacerbated by climate change. This event has demonstrated that the previous land management and planning were adequate at that moment but due to the expansion of the city, other solutions need to be implemented to prevent future events from resulting in the same consequences.

Flood risk management in urban areas has increasingly moved beyond traditional engineering solutions, focusing instead on urban resilience frameworks and blue-green infrastructure (BGI) to ensure sustainable development [2]. BGI refers to the integration of natural systems (green) and water management (blue) into urban spaces to sustainably manage stormwater while delivering multiple co-benefits. Valencia's response to the catastrophic 1957 flood offers valuable lessons and allows to evaluate new approaches to the problem. Urban resilience emphasizes a city's ability to anticipate, adapt, and recover from environmental shocks while promoting long-term sustainability and inclusivity. Valencia's Plan Sur—diverting the Turia River to prevent recurrent flooding—is an early example of resilience-focused planning. Yet, it primarily addressed immediate risks through large-scale engineering, missing opportunities to integrate more systemic adaptation approaches. To deepen the discussion and align with global trends, integrating concepts such as resilient cities and BGI could elevate Valencia's urban planning model as a benchmark for future climate-adaptive strategies.

2. The legal framework for water management in Spain

The urban design in many countries today is largely influenced by 19th and 20th-centuries efforts to address water management issues. During this period, the rapid growth of cities and the increasing demand for solving problems related to water, such as spread of diseases and effective waste removal led several nations to adopt new approaches to urban planning [3,4]. For instance, in the last third of the 19th century, England became a leader in sanitation infrastructure. During this time, strategies for managing water resources were re-evaluated, preventive measures against waterborne problems were implemented, and attention shifted from the environment to the well-being of the population [5]. In response, new urban by-laws were passed in many cities, addressing issues like sewage and drainage.

In most countries, however, water management reforms spread slowly. Spain, for example, remained behind in terms of economic, political, and social development by the late 19th century, prompting proposals to adopt the infrastructure improvements already present in other European countries [6–9]. Modernization efforts included significant sanitation upgrades, as Spanish urban areas faced severe challenges with water quality and waste management [10].

Madrid, for instance, struggled with severe water infrastructure deficiencies despite extensive public works on its sewer and drainage systems since 1856. The city still had over 3000 cesspits, while many neighborhoods lacked proper sewer traps to contain odors, and more than 4000 homes had no direct water supply [11] Likewise, between 1885 and 1893, Barcelona City Council undertook a sanitation initiative, constructing water tanks intended to circulate water through the sewer system to counteract the limited connections to residences [12]. In Seville, a dispute in 1901 between the League of Property Owners and the City Council nearly halted the expansion of drainage systems in the historic district [13].

Among Spain's cities with populations exceeding 100,000, only Zaragoza and Seville had relatively modern drainage systems, though water supply remained inadequate. In Madrid, Valencia, and Malaga, designated areas for water infrastructure were in disrepair, rendering them unusable and dangerous in case of heavy rainfalls; in Barcelona and Murcia, the facilities were also insufficient. The urgency of the water management crisis became apparent, as these infrastructure challenges contributed to high mortality rates and underscored Spain's need for immediate urban reform [14–16].

Since the 19th century, regulations have evolved to meet the specific needs of each era, addressing everything from epidemic prevention to protection against extreme weather events and earthquakes. This article outlines the key milestones in the development of Spain's legal framework for disaster management, showing how the country has moved from reactive approaches to a comprehensive, preventive system today.

In the 19th century, Spanish disaster laws focused primarily on responses to health emergencies, diseases, and large fires—serious problems in a Spain marked by urban growth and a lack of resources for crisis management. Within this context, laws were aimed at tackling cholera outbreaks that hit the country in 1833 and 1855, as well as other epidemics.

In 1855, the General Law of Public Welfare was passed, which included provisions for public health and began to introduce an assistance-based approach in crisis situations. Another notable regulation was the Health Law of 1885, which aimed to establish more coordinated responses to public health issues, laying the first foundations for health assistance during emergencies. Although "disaster management" was not explicitly mentioned at this stage, these early efforts were pioneering steps in state intervention during emergencies.

Natural catastrophes, particularly floods, began to receive legislative attention toward the end of the 19th century. In 1866, the first Water Law was enacted to regulate water resources and prevent urban overflow, a recurring problem due to Spain's climate and geography. This regulation was an initial step toward flood control, with provisions for the construction of canals and dikes.

At the beginning of the 20th century, Spain recognized the importance of building infrastructure to prevent natural disasters. The Public Works Act of 1907 gave the state a central role in the creation and management of disaster defense infrastructure, especially dikes, canals, and hydraulic works for flood control. The Water Law of 1926 reinforced this policy and created Hydrographic Confederations; regional entities responsible for managing river basins in an integrated effort to reduce flood risks. These confederations were essential for water management and risk reduction and continue to operate today.

After the Civil War, the country's infrastructure and population were devastated, prompting the government to establish more organized measures for emergency and disaster management. In 1941, following a severe flood in Santander, a Civil Protection Law was approved, officially establishing this institution for disaster management. This law became a benchmark for the organization of state response to emergencies. It was developed further in the 1950s and 1960s, expanding to cover both natural disasters like floods, earthquakes or fire and human-induced emergencies.

The Civil Protection Act of 1985 was a milestone in disaster management in Spain, representing the first comprehensive legislation that organized emergency response levels (state, regional, and local) in a coordinated manner. This law established the modern framework for Spanish Civil Protection, organizing emergency plans into territorial (by zone) and specific (by type of disaster, such as forest fires, earthquakes, or floods) categories. It also delegated responsibilities to the Autonomous Communities, enhancing response capacity in each region [17].

Spain's incorporation into the European Union brought new standards and regulations for disaster management. In 2002, the country joined the European Civil Protection Mechanism, which provides cooperation guidelines among member states for mutual assistance in case of disasters. This mechanism enables Spain to coordinate resources and teams with other countries, increasing the efficiency of response to large-scale emergencies.

In 2015, the National Civil Protection System Law (Law 17/2015) was approved, renewing and modernizing the Civil Protection framework with a focus on prevention, planning, and risk management. This regulation also strengthens the involvement of the Autonomous Communities and establishes measures for inter-administration collaboration, focusing on adaptation to climate-related risks [15].

Today, disaster management in Spain faces new challenges. Increasingly intense phenomena, such as heat waves, forest fires, and torrential rains—such as those experienced in Valencia in October 2024—partly due to climate change, require preventive and adaptive policies that integrate both the central government and the autonomous communities. Current Climate Adaptation Plans focus on mitigating the effects of these phenomena through a combination of infrastructure, education, and specific emergency protocols to reduce risks.

3. Previouys strategies adopted in Valencia: The reconfiguration of the river Turia after 1957

The Turia River has been a central element in the historical development of Valencia. Originating in the province of Teruel, the Turia flows for 280 km before reaching the Mediterranean Sea. For centuries, it provided water for agriculture and served as an important resource for trade and industry, though it was also characterized by its instability and tendency to overflow.

The Turia had already caused several significant floods before the catastrophic flood of 1957, including those in 1517 and 1776 [18]. These floods struck cyclically, devastating crops, buildings, and lives (**Figure 1**). Both floods clearly signaled the city's inability to manage such catastrophes due to its proximity to the river, especially as it continued to expand. This expansion is visible in 16th-century views (**Figure 2**) and the maps from the 17th (**Figure 3**), 18th (**Figure 4**), and 19th centuries (**Figure 5**), which depict the city's growth. In the 19th-century map, the historical center is highlighted with visible city walls—both the Muslim wall and the larger medieval wall ordered by Pedro the Ceremonious between 1356 and 1370. By this period, the center was already overcrowded, with buildings beginning to extend beyond the city walls.

By the late 19th century (**Figure 6**), thanks to more precise military mapping, it becomes clear that the city was gradually expanding into neighboring areas, both to the north (across the river) and to the south [17,19]. Finally, with the city's industrial development and the demolition of the walls, urban expansion became unstoppable from the early 20th century onwards (**Figure 7**).

Figure 1. View of the Puente del Mar in Valencia, ruined by the Turia River on 5 November 1776.
Source: [20].

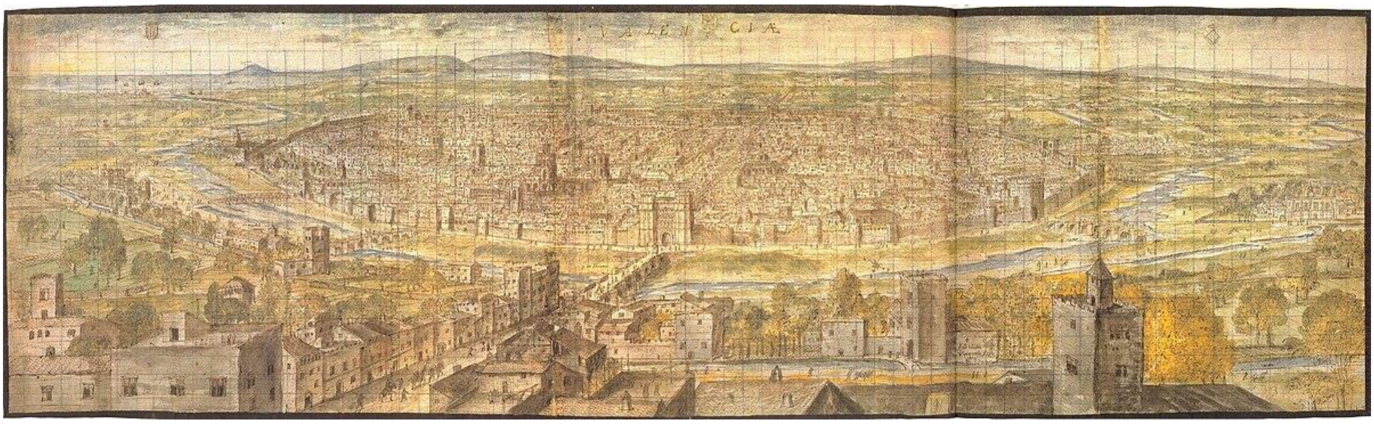

Figure 2. View of Valencia in 1563, made by Anton van der Wyngaerde.

Source: www.urbanity.es.

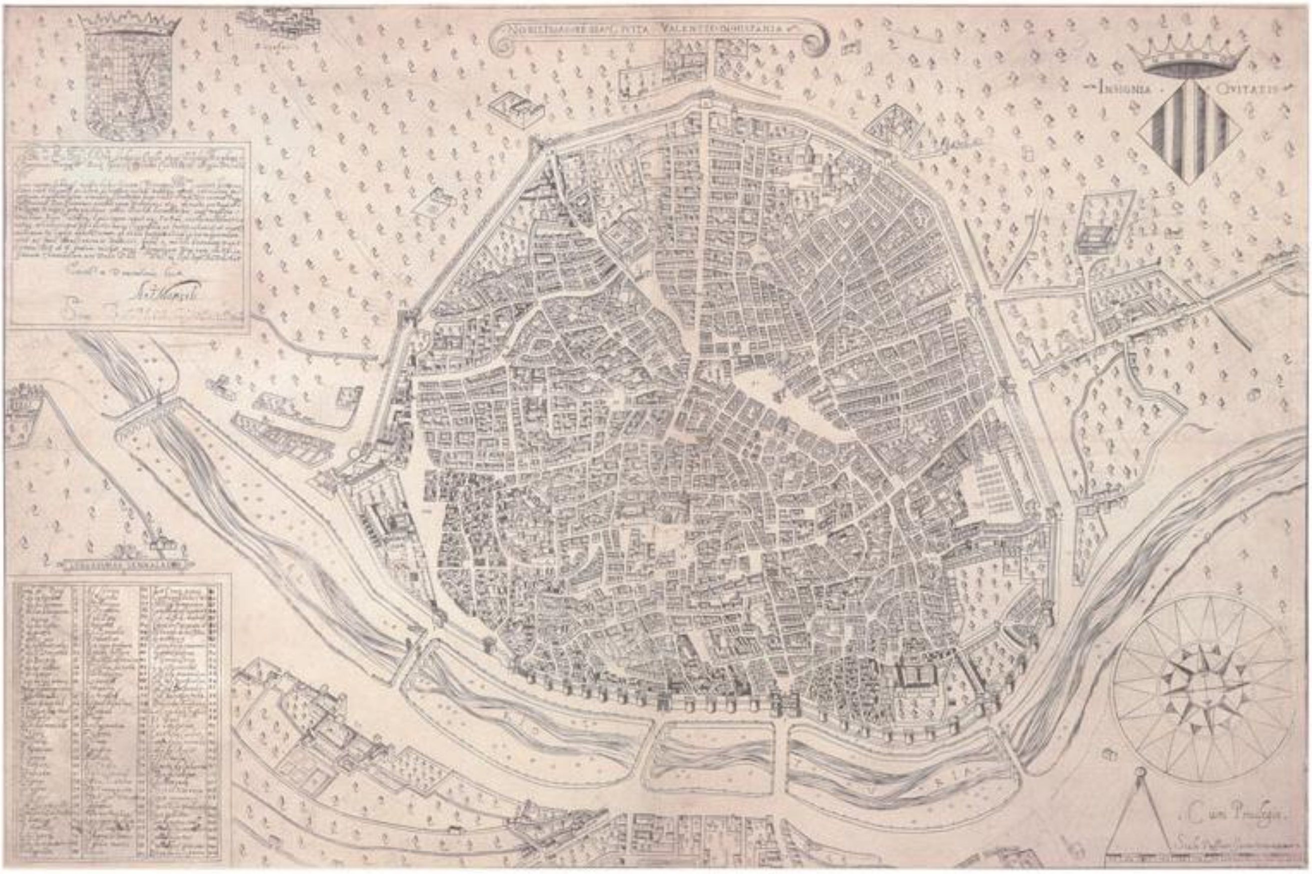

Figure 3. *Nobilis ac regia civitas Valentiae in Hispania*. The Noble and Royal City of Valencia in Spain Antonio Mancelli, 1608.

Source: Instituto Geográfico Nacional, 31-F-16.

Figure 4. *Valentia Edetanorum aliis Contestanorum, vulgo del Cid.* Valencia of the Edetani, also of the Contestani, commonly known as "of the Cid". Vicent Tosca i Mascó, 1704.

Source: Wikipedia.

Figure 5. Detail of Plan de Valence assiégée et prise le 9 janvier 1812 par l' Armeé Française d' Aragon aux ordres de S.E. Le Marechal Suchet. Plan of Valencia, besieged and captured on 9 January 1812, by the French Army of Aragon under the command of His Excellency Marshal Suchet.

Source: Instituto Geográfico Nacional, 47-K-1.

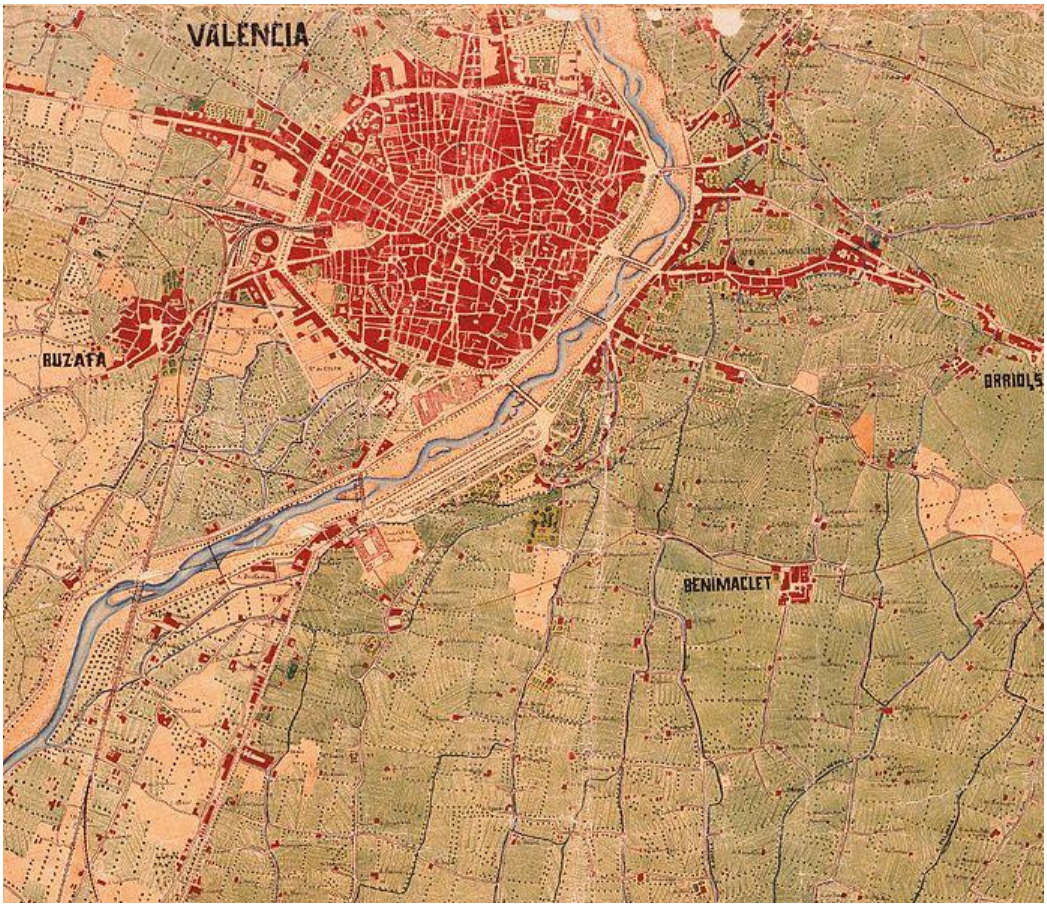

Figure 6. Detail of *Plano de Valencia y sus alrededores*. Map of Valencia and its surroundings. Francisco Ponce León, Jesús Tamarit, Pedro Bentabol. 1882–1883.

Source: Cuerpo de Estado Mayor del Ejército.

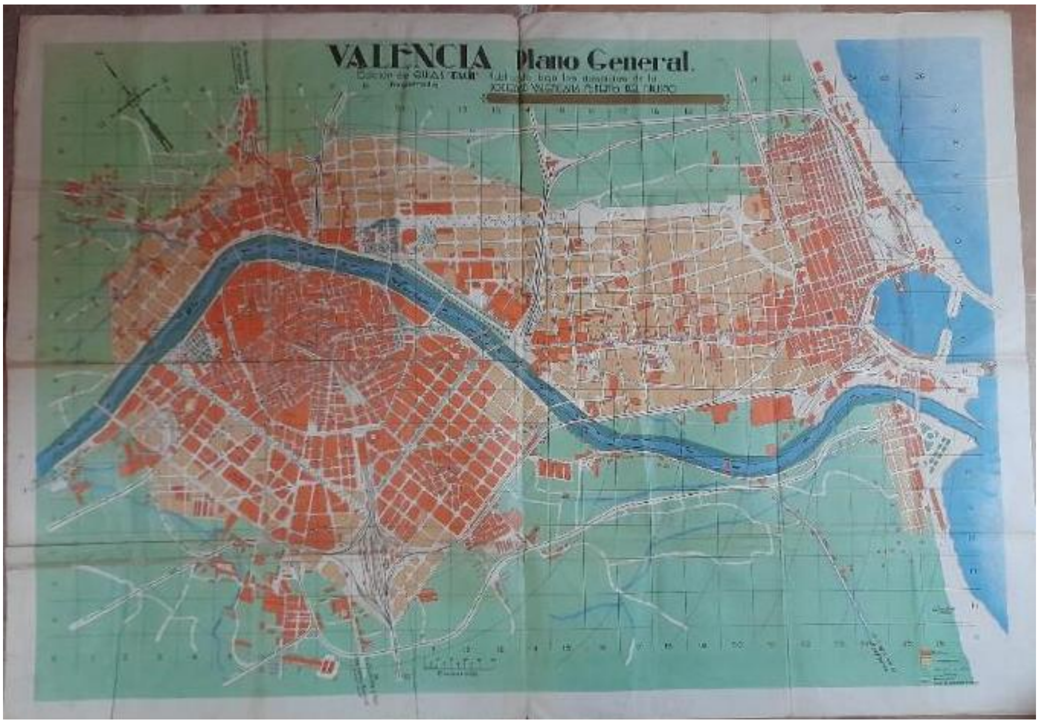

Figure 7. Valencia. Plano General. General Map.

Source: Sociedad Valenciana de Fomento del Turismo.

The 1957 flood marked a key point, far surpassing previous flood magnitudes and making it clear that the natural course of the Turia River was no longer sustainable for an expanding city like Valencia. On 14 October 1957, Valencia was hit by torrential rain resulting from an extreme meteorological phenomenon. Known as *gota fría*, this intense Mediterranean rain event caused an accumulation of up to 300 liters of water per square meter within hours. The Turia could not contain such a volume, and in just a few hours, the water breached the dikes and channels, inundating the city [21].

The resulting catastrophe devastated not only much of the historic center but also critical infrastructure, including hospitals, bridges, and transportation networks. Material damages were estimated at over one billion pesetas—like 6.010.121.000 millions uf Euros—a huge sum at the time. Local and national authorities realized that without decisive intervention, Valencia would remain exposed to future disasters.

The flood resulted in more than 80 deaths and extensive material losses, especially impacting the urban core. This event spurred the creation of the Plan Sur, an ambitious project aimed at diverting the Turia River southward, moving its course away from central Valencia. This approach followed similar patterns used by other Mediterranean cities [22–24].

The Plan Sur was a direct response to the 1957 tragedy. Valencia's mayor at the time, Tomás Trénor Azcárraga, Marqués del Turia, worked from late 1957 to find solutions to implement Valencia's adoption decree granted by Francisco Franco after the flood (issued by the Ministry of Housing on 23 December 1957), though it initially lacked funding [25].

This project became one of Spain's first major postwar urban infrastructure works, involving an investment and technical complexity unusual for the time. The execution of the Plan Sur required not only redesigning the river's course but also reorganizing road networks, irrigation systems, and connections between various neighborhoods in the city. Redirecting the Turia River altered the landscape and structure of the city, leaving a legacy in Valencia's urban, environmental, and cultural management that endures to this day. Conceived by the Spanish government in collaboration with local authorities and hydraulic engineering experts, the plan aimed to divert the Turia to protect the urban core of Valencia. A new channel was constructed south of the city's center, designed to manage large-scale flooding without impacting the population.

In 1958, García Ordóñez was appointed to oversee both Valencia's urban planning and the so-called Solución Sur, outlined in the Esquema Director, under the direction of Pedro Bidagor Lasarte, Director General of Urban Planning [26,27]. García Ordóñez, a prominent Spanish architect whose professional career focused on urban planning and infrastructure in the latter half of the 20th century, joined the Oficina Técnica de Gran Valencia alongside Valencian architects Mauro Lleó Serret (Chief Architect), Víctor Bueso Bellot, and Antonio Gómez Llopis [28]

In addition to these works, García Ordóñez was tasked by the Obra Sindical del Hogar y la Arquitectura to plan 614 social housing units near the Cabañal neighborhood. His approach reflected a strong commitment to modernizing Spanish cities during a period marked by urban reconstruction and expansion, especially after the Civil War and during Franco's dictatorship, when development and public works policies began to gain momentum toward national modernization. The Virgen del

Carmen housing group, designed as an autonomous neighborhood with typological innovations, exemplifies the highest level of volumetric composition and formal coherence among all the sets included in the "Flood Plan" [29–31]

A few weeks after García Ordóñez joined the Oficina Técnica, Mayor Trénor was dismissed, and Adolfo Rincón de Arellano replaced him. By order of the Directorate General of Urban Planning, the Administrative Corporation—whose Executive Committee was chaired by the mayor of Valencia—regained control to revise the Gran Valencia Plan. Within months, efforts to adapt the Plan intensified; it became essential to accurately position the new riverbed within Valencia's General Plan and make corrections associated with the river diversion.

The Plan Sur project, which redirected the Turia south of the city to mitigate flood risk, illustrates the scope and urban vision characteristic of the works García Ordóñez and his contemporaries promoted. Although he was not the primary author of this project, the Plan Sur aligns with García Ordóñez's ideas on urban intervention as a tool for solving complex problems and enhancing the safety and functionality of cities [29]. These ideas paralleled those emerging at the time around metropolitan development, following the example of cities like Madrid with its General Urban Planning Plan for the Madrid Metropolitan Area, dated 1961, published in 1962, and approved by a specific law on 2 December 1963 [32].

The infrastructure and urban redesign involved in the Plan Sur reflect the principles García Ordóñez valued in his projects, where the efficient organization of urban space and the integration of advanced technical solutions were paramount. This plan, which necessitated redesigning roads, irrigation networks, and neighborhood connections, also reflects a modern conception of the city as an interconnected system—a perspective fundamental to Ordóñez's urban planning vision. Also, the Southern Solution has contained the city's development towards that area (**Figure 8**).

Figure 8. Model of the 1988 General Plan of Valencia.

Source: Ajuntament de València, La Valencia de los noventa. Una ciudad con futuro. València, 1987.

The Plan Sur also demonstrated a forward-thinking approach, aimed at anticipating future challenges, such as potential flooding. This principle was essential to Ordóñez, who insisted on the need for infrastructures that would not only fulfill immediate functions but also meet future demands. Although completed in the 1970s, due to the delayed approval of the Adaptación del Plan General de Ordenación Urbana de Valencia y su Comarca a la Solución Sur (Adaptation of the General Urban Planning Plan of Valencia and its Surrounding Area to the Southern Solution) until 30 June 1966, the Plan Sur has been tested by recent rainfall events, like those of 2024. These tests highlight the ongoing relevance of the plan's original vision, which continues to protect the center of Valencia. However, they also emphasize the current challenges in urban planning—an area in which García Ordóñez would have advocated for adapting projects to urban and climatic changes to protect the now-developed areas that previously had low population density [33].

The Plan Sur was designed to safeguard the city from future floods by constructing a new riverbed that diverted the Turia's waters southward, away from populated areas. This measure has proven effective for decades, as the center of Valencia has not experienced severe flooding from the Turia since then. Nevertheless, the intense rains of 2024 have tested this infrastructure, underscoring persistent risks in areas adjacent to the diverted riverbed. The construction of the new Turia channel involved significant engineering feats, from digging large channels to constructing massive dikes and bridges. A 12-kilomkmeter-long, 175-meter-wide canal was excavated to channel the river's waters without affecting the urban core.

One of the primary challenges was ensuring that the new channel could withstand floods equal to or greater than the one in 1957. For this purpose, the project incorporated expansion zones as well as channels and gates capable of regulating water flow. The work was completed in the 1970s, becoming a symbol of Valencia's resilience through innovation and collective effort [34].

This project allowed Valencia to divert the river during heavy rains without risking overflow in the most densely populated areas. This transformation not only mitigated flood risks but also contributed to the city's aesthetic and recreational spaces. The project was essential for reducing the exposure of urban areas to floodwaters while also offering opportunities for recreational spaces and tourism, thus benefiting both urban livability and economic activity.

Regarding the capacity of the new channel, it has a length of 12,692 m and a width of 200 m. The diversion would begin between the towns of Manises and Quart de Poblet, following a straight line past Xirivella and curving with a radius of approximately 2000 m in a west-east direction near Castellar, where it would slightly turn southward. This adjustment allowed for the expansion of the port, with the river eventually flowing into the sea between Pinedo and El Saler. The drainage capacity was designed to handle 5000 m^3/s, exceeding the "maximum" flood wave recorded during the October 1957 flood by 35% (**Figure 9**)

However, recent urbanization in the southern areas of the channel has altered flood impacts. The heavy rains of 2024 have shown that, while Valencia's city center remains protected, the southern region is still vulnerable, affecting neighborhoods and municipalities that have grown in these areas.

Figure 9. Aerial image showing the exact location where the river was diverted following the implementation of the Plan Sur.

Source: Newspaper Valencia Hui: [35].

4. The results of the new configuration

One of the most important and unique aspects of this intervention was the abandonment of the Turia's former riverbed. After the river's diversion, the old channel was emptied, sparking numerous ideas for repurposing this space. The government's initial proposal was to construct an urban highway connecting northern and southern Valencia. However, residents and environmental groups opposed this, arguing that the old channel could become a green space for the enjoyment of Valencians.

After a lengthy process of debate and negotiation, the creation of an urban park in the former riverbed was approved. This decision represented a victory for the public and marked a shift in the approach to managing urban spaces, resulting in what is now known as the Turia Gardens. The design of the Turia Gardens began to take shape in the 1980s. Today, this park spans over 110 hectares, being one of the largest urban parks in Spain and a model of urban revitalization and environmental management. Highlights include the Gulliver Park, the City of Arts and Sciences, and the Palau de la Música, each a testament to Valencia's cultural and architectural richness(**Figure 10**).

Figure 10. Aerial photo of Valencia in the mid 70 s.

Source: [36].

Economically, the park has boosted tourism and stimulated sectors such as hospitality, commerce, and services. The City of Arts and Sciences, situated within the gardens, attracts visitors from around the world, generating revenue and employment for city residents. This park has significantly enhanced the quality of life in Valencia, improving the city's image and providing a space for recreation, sports, and culture. (**Figure 11**).

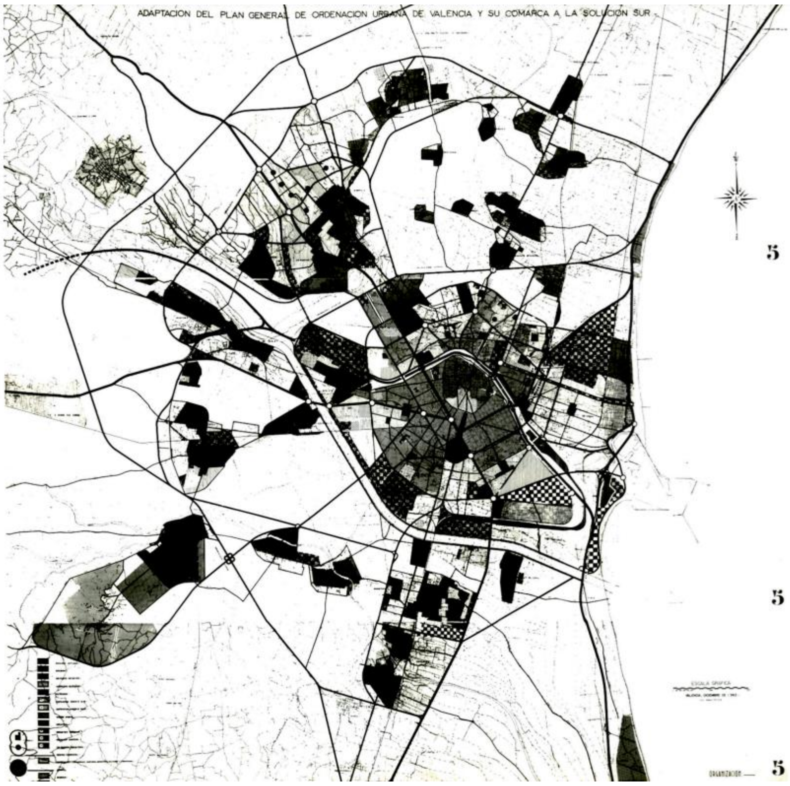

Figure 11. Adaptation of the General Urban Development Plan of Valencia and its Region to the South Solution. Photographic reproduction of Plan 5. Organization (Green Areas). December 1963.

Source: Archivo de Planeamiento del Ayuntamiento de Valencia.

On a social level, the park has become a gathering place for Valencians, who use it for sports, cultural, and recreational activities. The accessibility and connectivity offered by the former riverbed have enhanced mobility and integration between neighborhoods, fostering greater social cohesion.

Today, the old Turia riverbed is a model of urban planning that prioritizes sustainability and quality of life. The Turia Gardens are considered an example of how a city can transform an abandoned infrastructure into an ecologically and socially beneficial space [37]. Additionally, the park contributes to urban temperature regulation and air quality, helping to mitigate the heat island effect in Valencia. Once a source of risk for the city, the Turia River has become the green heart of Valencia, with its success inspiring similar projects in other Spanish and European cities. However, the recent 2024 floods have exposed that the previous plan was useful at that moment but maybe not any more. Floods have affected former flood-prone areas south of the city, like Pinedo and El Saler, which saw urban expansion and infrastructure improvement after the transformation of the Turia. Also, new residential and industrial zones were established, particularly along the newly created flood-free zones. The cartographic comparison between 1956 and 2023 showcases these dramatic changes, emphasizing the shift from a flood-prone river basin to a more controlled and urbanized landscape (**Figures 12** and **13**). Also, because of the huge growth of population in this area—75 municipalities with a resident population of 1.8 million people [38,39], road and rail infrastructure systems were improved, including bridges over the new riverbed and strengthened connections between southern municipalities like Quart de Poblet, Xirivella, and central Valencia.

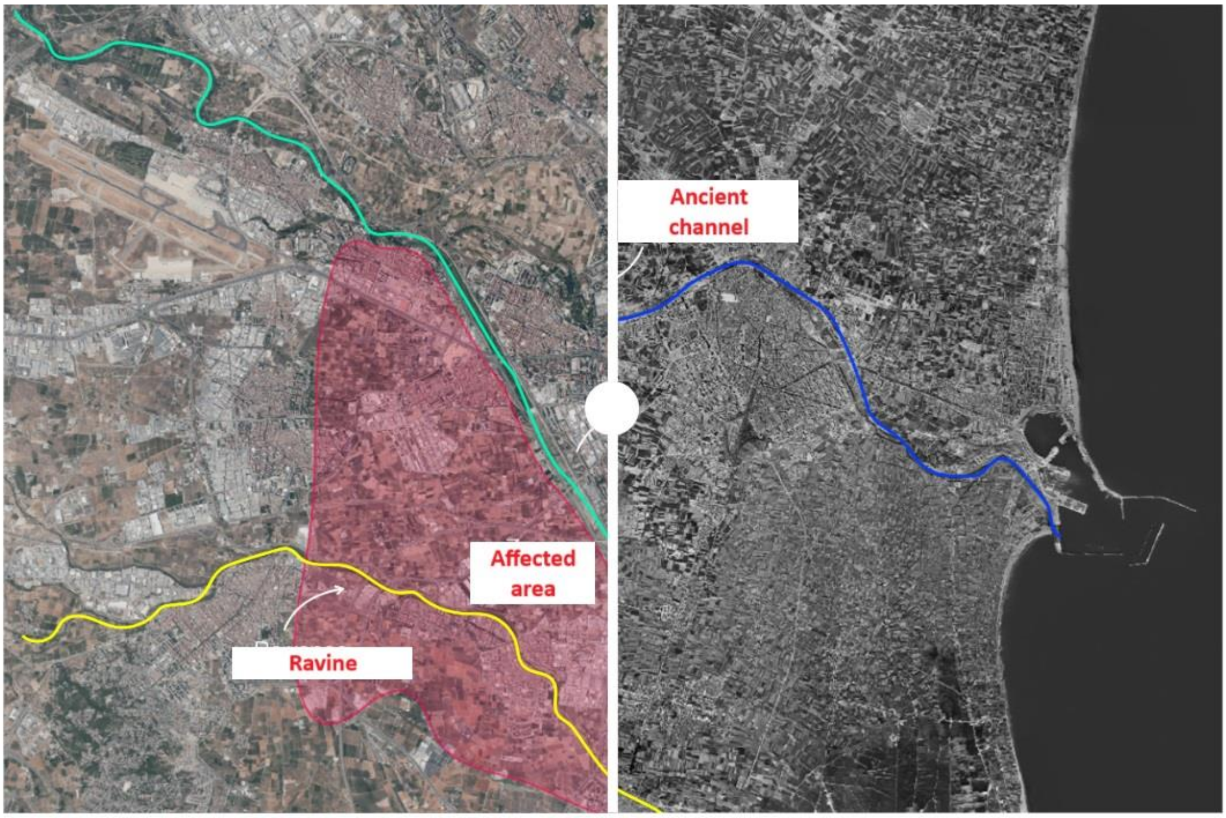

Figure 12. 1956 Photograph, 2023 Photograph.
Source: Cartographic Viewer of Valencia.

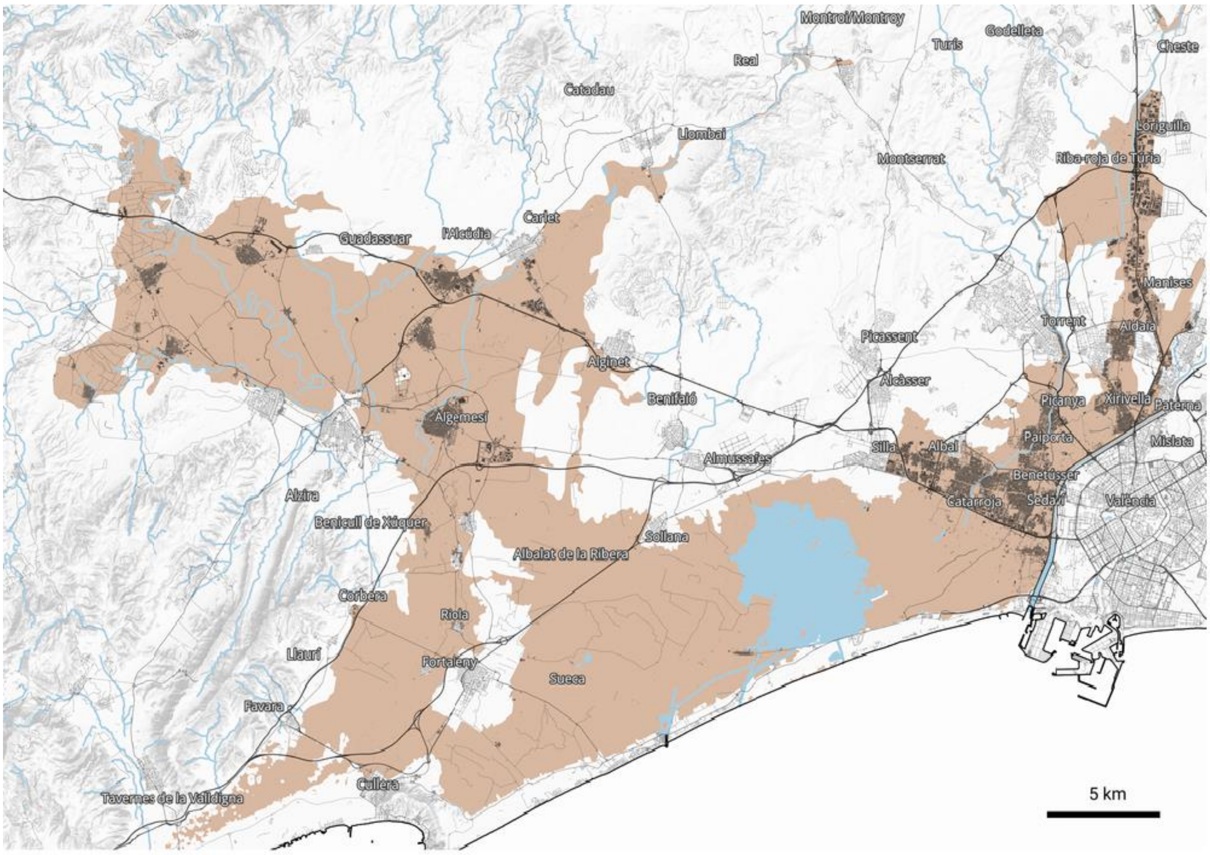

Figure 13. In orange, flooded areas.
Source: Universitat de València, Copernicus EMS, IGN.

5. Reflections about the problem and future directions

Due to all these elements, experts consider whether the old reconfiguration is still useful, in other words, if the park's current use might be adapted to better retain and manage rainwater during the increasingly frequent intense rains in the Mediterranean, driven by climate change or if the changes implemented at that time are enough or which strategies can be implemented regarding the blue-green infrastructure (BGI). Valencia's Turia Gardens, repurposing the old riverbed as a green corridor, embodies the potential of BGI. However, expanding BGI's scope could bolster Valencia's flood resilience and urban sustainability

Since the 1957 flood, Valencia's urban planning incorporated advanced flood management infrastructure such as retention basins, levees, and improved drainage systems. The city's stormwater management system has been enhanced to handle larger volumes of water, with a focus on sustainable urban drainage systems (SUDS). These systems aim to not only divert water but also promote natural water infiltration, reducing urban heat island effects and improving ecological health. However, it seems that some improvements are necessary. Regarding other European cities with similar historical problems—such as Amsterdam, Venice, Paris, London or Copenhagen -, Valencia has a lot of possibilities to enhance the problem to prevent future flooding situations [40].

Amsterdam is often seen as a global leader in flood management [41–43]. Due to its location below sea level, the city has implemented extensive water management strategies for centuries. Amsterdam's approach focuses on integrated flood risk management, using a combination of dikes, storm surge barriers, and flood retention areas. Notably, the city's Room for the River program is a standout strategy, where water is allowed to flow into specially designated floodplains during extreme weather events, reducing the pressure on urban infrastructure. This contrasts with Valencia's river diversion strategy but shares a common focus on land use adaptation and water retention.

Venice, another city vulnerable to flooding due to its low-lying position, has faced growing challenges with sea level rise and increased flooding. The city is implementing the MOSE project, a series of movable barriers designed to protect the Venetian Lagoon from high tides [44]. While this strategy is more focused on protecting the city from tidal surges, it shares similarities with Valencia's flood barrier strategies, such as protecting vital urban areas from inundation [45,46]. However, Venice's challenges are different from those in Valencia, which faces flood risks from inland rivers rather than sea surges. Both cities, however, demonstrate a strong focus on technological innovation in flood risk mitigation.

Paris has employed a more natural approach in managing flood risks, particularly through urban green spaces and floodplain restoration. After the catastrophic floods of 1910, Paris implemented a comprehensive flood management plan that includes levees, locks, and water retention basins [47–50]. The city has increasingly focused on green infrastructure, such as permeable surfaces, which help manage runoff and reduce flood risks [51]. This approach contrasts with Valencia's heavy reliance on engineering solutions like the Plan Sur but reflects a growing European trend towards sustainable and nature-based solutions in flood management.

London's flood management strategy involves the Thames Barrier, which protects the city from tidal surges. The city's flood risk management is integrated into the Thames Estuary 2100 Plan, which takes into account future climate change predictions [52,53]. London also uses a combination of levees, flood defenses, and land use planning to manage river flooding. Similar to Valencia, London has recognized the need for multifaceted solutions, combining hard engineering solutions with better urban planning, though London's focus is more on tide and surge protection compared to Valencia's emphasis on river flooding [54].

Inspired by other cities like Copenhagen [55,56], Valencia could design floodable parks or wetlands that temporarily store stormwater, preventing urban inundation while supporting biodiversity. Also, encouraging green roofs, rain gardens, and permeable pavements across urban developments would enhance water infiltration and reduce runoff, mitigating the impact of extreme precipitation events

The recent events have shown that even with sophisticated flood management strategies, challenges remain. Municipalities along the southern area of Valencia, particularly in areas like Albufera and L'Horta Sud, were still heavily impacted by floods. This highlights the need for continuous updates to flood risk assessments and the further adaptation of urban spaces to a changing climate. It is essential to continuously improve resilience strategies, ensuring that newer urban developments incorporate flood-prone area considerations.

Learning from Amsterdam and Paris, Valencia could enhance its approach by expanding nature-based solutions, such as creating more permeable surfaces and expanding green spaces to manage runoff more effectively. Or, as seen in London, flood management is increasingly focused on long-term climate change scenarios. Valencia could benefit from incorporating more adaptive measures to handle the anticipated impacts of climate change, particularly sea level rise and changing precipitation patterns.

Also, there is a significant focus on public engagement and education about flood risks and prevention. Valencia could enhance public awareness of flood risks and encourage community involvement in flood preparedness.

6. Conclusions

The modification of the Turia River's course in the 1960s marked a turning point in Valencia's history. What began as a protective measure against flooding transformed into one of the most significant and positive urban transformations in the city. Today, the Gardens of Turia, which run through the city, symbolize not only Valencia's resilience in the face of adversity but also its ability to reinvent and adapt itself, seeking a balance between urbanization and sustainability.

This project, which arose in response to a tragedy, has become an example of how cities can be redesigned to protect their inhabitants and improve their quality of life. The transformation of the Turia River has left an indelible mark on Valencia's identity and continues to serve as a model of urban planning for other cities around the world.

However, with the floods that occurred in 2024, Valencia's infrastructure, designed decades ago, is being put to the test, especially in areas where urban growth has been more rapid, such as the south. This area is the most affected during heavy rains, as the diversion of the Turia River in the Sur Plan shifted the flood risk from the center to the south. Although the new course is designed to withstand large floods, it is not equipped to efficiently drain in the nearby urbanized areas. Urbanization has reduced the natural spaces that absorb water, making these areas prone to flooding in the event of heavy rainfall.

In 2024, the rapid runoff from urbanized areas exacerbated the flooding, particularly in locations where the infrastructure is insufficient to handle such volumes. This situation has sparked debates about the need to redesign these infrastructures and add new containment measures.

While the Sur Plan has effectively protected the center of Valencia, the 2024 floods have highlighted the limitations of its effectiveness in the context of climate change and accelerated urbanization. The drainage infrastructure and water containment systems need to adapt to current conditions to reduce the risk in the southern area and in regions close to the new river course.

The river diversion model, which was innovative in the 1960s, should be complemented with more modern solutions, such as water capture and retention systems in the old course, to prevent excess water from flowing into urban areas. The modification of the Turia River in the 1960s was an innovative solution that protected central Valencia from future flooding, but the recent events of 2024 have shown that it is necessary to update infrastructures and water management strategies in the city. Valencia finds itself at a crucial moment to apply a forward-looking vision that combines the effectiveness of the Sur Plan with innovations that reduce flooding risks throughout the territory, including the southern area. The recent floods of 2024 should be seen as a wake-up call to invest in resilient urbanism that prioritizes both the safety of the population and environmental sustainability. In the face of the growing threats posed by climate change, Valencia could implement a series of additional measures, such as retention infrastructures in the old course, drainage and absorption systems in the southern area, that implies improving the sewage and drainage systems in the neighborhoods and municipalities of southern Valencia or the renaturalization of floodable areas.

Valencia's flood management history is a testament to the potential of large-scale engineering solutions. However, as climate challenges intensify, adopting resilient city frameworks and blue-green infrastructure strategies can provide a more comprehensive, sustainable approach. Cities like Paris, Copenhagen, Venice or London offer valuable lessons, underscoring the importance of integrating water management with urban development. Valencia stands at a crossroads to evolve its legacy into a model of 21st-century flood resilience, demonstrating how to balance protection, sustainability, and urban vibrancy.

Conflicts of interest: The author declares no conflict of interest.

References

1. de Valencia C. Report on damage to industry in the 87 municipalities affected by the DANA (Spanish). Cámara Valencia; 2024.
2. Joshi PK, Rao KS, Bhadouria R, et al. Blue-Green Infrastructure for Sustainable Urban Settlements. Springer; 2024.
3. Hamlin C. The Sanitarian Becomes an Authority, 1859. In: Proceedings of the International Conference on the History of Public Health and Prevention; 9 June–15 September 199; Sundsvall, Sweden.
4. Hamlin C. Predisposing causes and public health in early nineteenth century medical thought. Soc. Hist. Med. 1992; 5: 43–70. doi:10.1093/shm/5.1.43.
5. Rodríguez Ocaña E. Public health in Spain in the European context, 1890–1925 (Spanish). Revista de Sanidad e Higiene Pública. 1994; 68(0): 11–27.
6. Arnould J. New hygiene features (French). Libr. J.B. Baillière et Fils; 1902. pp. 1.003.
7. Sussman GD. Enlightened Health Reform, Professional Medicine and Traditional Society: The Cantonal Physicians of the Bas-Rhin, 1810–1870. Bull. Hist. Med. 1977; 51: 565–584.
8. Pogliano C. L'utopia igienista (1870–1920). In: Della Peruta F (editor). Storia d'Italia. Annali 7. Malattia e Medicina. Einaudi editori; 1984. pp. 589–631.
9. Hildreth ML. Doctors, Bureaucrats and Public Health in France, 1888–1902. Garland publishing Inc.; 1987.
10. de Sanidad RC. Fundamental issues of Public Hygiene in Spain. E (Spanish). Teodoro; 1901.
11. Hauser P. Madrid bajo el punto de vista medico-social (Spanish). In: Madrid ES (editor). del Moral y C. Editora nacional; 1902.
12. Capel H, Tatjer M. Reforma social, serveis assistencials i higienisme a la Barcelona de final del segle XIX (1876–1900). In: Roca Rosell A (editor). Cent anys de Salut Pública a Barcelona. Ajuntament de Barcelona; 1991. pp. 31–73.
13. Pulido Fernandez A. Public health in Spain and social ministry of the medical classes (Spanish). Est. Tip. Enrique Teodoro; 1902.
14. Hauser P. Medical geography of the Iberian Peninsula (Spanish). Eduardo Arias; 1913. pp. 235–236.
15. Polo Martín B. Floods and insalubrity as the trigger for city restructuring in Spain: the case of Burgos. UPLanD-Journal of Urban Planning, Landscape & Environmental Design. 2018; 3(2): 5–14.
16. Olcina J, Sauri D, Hernández M, et al. Flood policy in Spain: a review for the period 1983–2013. Disaster Prevention and Management. 2016; 25(1): 41–58.

17. Faus Prieto A. The cities of Valencia in the face of the floods of the Turia in 1776 (Spanish). Cuadernos de Geografía. 1999; 65–66: 122–123.
18. Martínez Magallanes LA. Los planos urbanos del Cuerpo de Estado Mayor del Ejército, 1865–1900. Scripta Nova; 2017.
19. Polo Martín B. History of urban cartography in Burgos: 19th-20th centuries. Unpublished doctoral thesis. Directors: Francesc Nadal Piqué and José Luis Urteaga González (Spanish). Universitat de Barcelona; 2020.
20. Cavanilles AJ. Observations on the natural history, geography, agriculture, population and fruits of the Kingdom of Valencia. [Volume I]. Madrid: Royal Printing Office; 1795 (Spanish). Biblioteca Digital de Floridablanca; 1795.
21. Sánchez-García C, Schulte L. Historical floods in the southeastern Iberian Peninsula since the 16th century: Trends and regional analysis of extreme flood events. Global and Planetary Change. 2023; 231: 104317.
22. Giménez-Font P. Historical cartography and alteration of river courses in Mediterranean Spain (Spanish). In: Alberola A, Olcina J (editors). Natural disaster, daily life and popular religiosity in modern and contemporary Spain. Universidad de Alicante; 2009.
23. Polo Martín B. A History of the Cartography of Burgos in the Nineteenth and Twentieth Centuries. Imago Mundi. 2018; 70(2): 253–254.
24. Pérez Puche F. The flood reached this point (Spanish). Ayuntamiento de Valencia; 1997.
25. Selva Royo JR. Fernando Martínez García-Ordóñez. Trayectoria profesional. In: ViA Arquitectura. Premios 2005–2006. Colegio Oficial de Arquitectos de la Comunidad Valenciana; 2007.
26. García Heredia A. Beginning and end of the metropolitan area of Valencia. From autarchy to democracy (Spanish). In: Historia de la ciudad V. Tradición y progreso. ÍCARO (Colegio Territorial de Arquitectos de Valencia); 2008.
27. Peñín Ibáñez A. Valencia 1874-1959. City, architecture and architects (Spanish). Escuela Técnica Superior de Arquitectura de Valencia; 1978.
28. García-Ordóñez FM. A regional plan: new Valencia (Spanish). Nuestro Tiempo. 1958; 45.
29. García-Ordóñez FM. Urban renewal in Valencia (Spanish). Boletín Informativo y cultural del Ateneo Mercantil; 1959.
30. Larrodera López E, García Ordoñez FM. General Plans with application to the General Plan of Valencia (Spanish). In: Sesión de estudio para el 1er Congreso Nacional de Urbanismo ‘La Gestión Urbanística’. Barcelona; 1959. Ministerio de la Vivienda, Secretaría General Técnica; 1962.
31. Selva Royo JR. 29+1. Metropolitan urban planning of Greater Valencia (1947–1986) (Spanish). Tesis doctoral sin publicar; 2014.
32. Fernando de T. Urban planning in contemporary Spain. 1900–1980 (Spanish). Alianza; 1982.
33. Selva Royo JS. Background and formation of the General Plan of Valencia of 1966 (Spanish). Cuadernos de Investigación Urbanística. 2014.
34. Carmona González P, Olmos Llórens J. River and city: The case of Valencia (Spanish). Revista del Colegio de Ingenieros de Caminos, Canales y Puertos; 1994; volume 28.
35. Rivera Nebot A. Flood in Valencia, October 1957 (Spanish). Maradentro; 2024.
36. Ajuntament de València. Valencia in the nineties. A city with a future (Spanish). València; 1987.
37. Llopis Alonso A. The Turia Garden: other times, other projects, other images. In: Historia de la ciudad VI. Proyecto y complejidad. ÍCARO (Colegio Territorial de Arquitectos de Valencia); 2010.
38. Plaza V. The Dana causes damage in at least 65 Valencian municipalities, with 31.8% of the population (Spanish). Available online: https://valenciaplaza.com/dana-causa-danos-65-municipios-valencianos (accessed on 2 November 2024).
39. Delgado A. The map of the scope of the DANA in Valencia already affects 130,000 homes (Spanish). Datadista; 2024.
40. Dordi T, Henstra D, Thistlethwaite J. Flood risk management and governance: A bibliometric review of the literature. Journal of Flood Risk Management. 2022; 15(2): e12797.
41. Van Leusseni W. Flood management in the Netherlands: how risks are addressed (Spanish). Revista Catalana de Seguretat Pública. 2008; 89.
42. Lebesque S. Along Amsterdam’s waterfront: Exploring the architecture of Amsterdam’s Southern Ij Bank. Valiz; 2006
43. De Mulder FJ, De Pater B, Fortuijn D. The Netherlands and the Dutch. Springer; 2019.
44. Available online: https://www.mosevenezia.eu/mose/?lang=en (accessed on 2 November 2024).
45. Settis, S. Is it too late to save Venice? Apollo; 2019.
46. Tagliapietr D, Sigovini M, Keppel E, et al. Bioerosion effects of sea-level rise on the Doge’s Palace water doors in Venice (Italy). Facies. 2019; 65(34): 1–16

47. Cour des Comptes. Insufficient Flood Risk Prevention in Île-de-France (France). Available online: https://www.ccomptes.fr/fr/publications/la-preventioninsuffisante-du-risque-dinondation-en-ile-de-france (accessed on 3 November 2024).
48. DRIEAT. Flood Risk Management Plan: Seine-Normandy Basin (France). Available online: https://www.drieat.ile-de-france.developpementdurable.gouv.fr/IMG/pdf/fr_frh_frmp_no1_pgri.pdf (accessed on 3 November 2024).
49. Ville de Paris. Local Urban Planning (France). Available online: http://pluenligne.paris.fr/plu/sites-plu/site_statique_54/pages/page_1156.html (accessed on 3 November 2024).
50. Ville de Paris. Paris in the Face of Climate Change. Available online: https://cdn.paris.fr/paris/2021/11/16/088fcde428650ff1e3d9680f155a54a7.pdf (accessed on 3 November 2024).
51. Corrêa CJP, Tonello KC, Nnadi E. Urban Gardens and Soil Compaction: A Land Use Alternative for Runoff Decrease. Environmental Processes: An International Journal. 2021; 8(3): 1213–1230.
52. Jenkins K, Surminski S, Hall J, Crick F. Surface water flood risk and management strategies for London: An Agent-Based Model approach. E3S Web of Conferences. 2016; 7: 22003.
53. Sayers PB, Horritt M, Penning-Rowsell E, McKenzie A. Climate Change Risk Assessment 2017: Projections of future flood risk in the UK. Research undertaken by Sayers and Partners on behalf of the Committee on Climate Change. Committee on Climate Change; 2015.
54. Allison R, Haasnoot M, Reeder T, Green M. Literature review on an adaptive approach to flood and coastal risk management. Environment Agency, Horizon House, Deanery Road; 2021.
55. UWR. Large basins under the road network: How Frederiksberg will protect itself against cloudbursts in the future. Available online: https://uwrsystem.dk/en/large-basins-under-the-road-network/ (accessed on 5 November 2024).
56. Jørgensen ME, Kidmose J, van der Keur P, et al. Urban River Restoration, a Scenario for Copenhagen. Greening Water Risks. 2023; 347–365.

Journal of Geography and Cartography 2025, 8(1), 9752.
https://doi.org/10.24294/jgc9752

Article

Adapting hydrological regionalization techniques to reconstruct rainfall fields in Haiti

Clertine Guerrier[1], Alfonso Gutierrez-Lopez[2,*]

[1] Water Research Center, International Flood Initiative Representative in Haiti (IFI-Haiti), Intergovernmental Hydrological Programme (IHP), Autonomous University of Queretaro, Queretaro 76010, Mexico
[2] Water Research Center, International Flood Initiative, Latin-American and the Caribbean Region (IFI-LAC), Intergovernmental Hydrological Programme (IHP), Autonomous University of Queretaro, Queretaro 76010, Mexico
*** Corresponding author:** Alfonso Gutierrez-Lopez, alfonso.gutierrez@uaq.mx

CITATION

Guerrier C, Gutierrez-Lopez A. Adapting hydrological regionalization techniques to reconstruct rainfall fields in Haiti. Journal of Geography and Cartography. 2025; 8(1): 9752. https://doi.org/10.24294/jgc9752

ARTICLE INFO

Received: 21 October 2024
Accepted: 25 December 2024
Available online: 3 January 2025

Abstract: The hydroclimatological monitoring network in Haiti was inadequate before 2010 due to a lack of meteorological stations and inconsistent data recording. In the aftermath of the January 2010 earthquake, the monitoring network was reconstructed. In light of the prevailing circumstances and the mounting necessity for hydroclimatological data for water resource management at the national level, it is of paramount importance to leverage and optimize the limited available data to the greatest extent possible. The objective of this research is to develop regional equations that facilitate the transfer of climatic data from climatological stations to locations with limited or absent data. Physiographic and climatological characteristics are used to construct the hydrologic information transfer equations for sites with limited or no data. The validity of the regionalization techniques was assessed using cross-validation. The results enable estimation of hydrological events through the specific patterns of behavior of each region of the country, identified in cartography of homogeneous zones.

Keywords: hydrological regionalization; homogeneous regions; information transfer; hydrological regime; Haiti

1. Introduction

A report by the World Health Organization (WHO) and the United Nations Children's Fund [1] revealed that approximately 2.2 billion individuals globally lack access to safe drinking water. This figure represents one in three individuals worldwide who are unable to access the vital liquid. In Haiti, only 12% of households have access to safe drinking water at their place of residence. This problem is particularly impactful for those residing in rural areas.

According to the World Bank, in 2020, only 43% of Haiti's rural population had access to an essential supply of drinking water, a statistic that represented a decline from 48% in 2015 and 50% in 1990. As evidenced by various studies, these river basins are distributed across approximately 30 river basins, which can be divided into six major river basins: the North-West, North, North-Central, South-Central, South-East and South-West basins. These regions encompass an area of 27,750 km^2 [2].

The country receives an average annual precipitation of 1500–2000 mm, of which only 10% infiltrates into the ground to replenish the aquifers. Consequently, a significant proportion of rainwater is transformed into runoff, which carries sediments and harmful products [3]. One of the most significant challenges in water management in Latin America and the Caribbean is the dearth of a comprehensive network of climatological and hydrometric stations [4].

In Haiti, as is the case in the most countries in Latin America and the Caribbean, there is a scarcity of climatological monitoring networks, which are subject to numerous limitations. It is also noteworthy that Haiti is vulnerable to natural disasters, underscoring the need for a robust and reliable monitoring network to facilitate accurate forecasting. The country has been grappling with a plethora of challenges pertaining to water management for over three decades. These include deficiencies in water planning, floods, droughts, and the absence of a robust water supply system, urban drainage issues, and inadequate hydraulic engineering designs. Despite the passage of two decades, the fundamental problems remain unresolved. In some instances, residents are compelled to consume river water that has been contaminated. Furthermore, several urban centres in the country are vulnerable to flooding, with incidents occurring even when minimal precipitation is recorded.

The transfer of hydrological data to locations without a meteorological station can be accomplished through the utilization of regional equations. Regional equations are constructed on the basis of the assumption of by region homogeneity. The objective of this study is to present the steps of hydrological regionalization, adapted for Haiti, where climatological records are severely limited or non-existent.

1.1. Up-to-date bibliography

The current literature includes a number of publications on hydrologic regionalization techniques. A substantial number of contributions are published on a regular basis in almost all engineering-related topics, with a particular focus on those related to water resources. A typical example is the utilization of regional models to estimate surface runoff in ungauged basins, which has recently been combined with machine learning [5,6] and satellite observations [7]. To be specific, regionalization techniques are employed in the majority of Latin American and Caribbean countries to facilitate an understanding of the behaviour of homogeneous regions. For instance, Brazil utilises hydrological regionalization for the management of water resources, given the vast extent of its territory [8]. Furthermore, the estimation of extreme events in ungauged basins is extremely reliable when conducted within the context of an effective hydrological regionalization [9].

2. Materials and methods

The quality of the data is dependent on a number of factors, including the process of information collection, the size of the records and the representation of the information on the site. This presents two significant challenges for the hydrologist. The first issue represents the lack of suitable tools to assess the suitability of the data to be used. This requires the definition of precise concepts and their subsequent monitoring. The second issue attends the need to design projects in areas where climatological data or hydrometric records are limited or non-existent. There is consensus among studies on the use of hydrological regionalization as a tool for hydrological transfer [5,6,10–12]. Likewise, Gutierrez-Lopez and Aparicio [4] put forth a series of steps that must be undertaken for a proper hydrological regionalization.

2.1. Haiti's water resources

The issue of water scarcity represents a significant challenge for a considerable proportion of the Haitian population, particularly those residing in remote areas remote from the capital city. This situation concerns particularly with regard to the provision of drinking water. The most recent statistics indicate that the national drinking water coverage rate is 64%, with 77% in urban areas and only 48% in rural areas. In terms of poverty, the distribution of drinking water is highly precarious throughout Haiti. A review of the data reveals that only 26 municipalities out of 133 (19.5%) receive access to piped water services that can be considered satisfactory. In particular, three departments stand out: The highest rates of access to drinking water are found in Artibonite, Centre and Grande Anse [13]. A considerable proportion of the Haitian population has severely restricted access to drinking water, despite the country's vast potential for renewable water resources, currently distributed in an uneven manner. As evidenced by empirical research, these entities are dispersed across approximately 30 watersheds, which are themselves divided into six principal river basins as previously noted [2]. The country receives an average annual precipitation of 40 billion cubic meters, of which only 10% infiltrates into the ground to recharge the aquifers. The rainy season is defined as lasting 9.8 months, commencing on 24 February and concluding on 19 December. The interval between consecutive periods of rainfall represents 31 days, during which precipitation of at least 13 millimeters is required to qualify as a valid instance. The month with the highest precipitation levels in Haiti is May, with an average rainfall of 54 millimeters. The period of the year during which precipitation is absent lasts for 2.2 months, from 19 December to 24 February. The month with the lowest precipitation levels in Haiti is January, with an annual mean of 11 millimeters of rainfall.

2.2. Variables selection

The availability of hydro-climatological data in Haiti is limited. The country's meteorological network has been severely constrained for several decades, rendering the retrieval of information a challenging endeavour. As previously mentioned, the objective is to utilize the limited data that is available. The data presented in this study are derived from a number of meteorological stations distributed across the Haitian landscape. **Figure 1** illustrates the geographical distribution of meteorological stations that have been operational in Haiti. Stations marked with a red circle are characterized by a limited availability of data and are currently inactive. However, following the 2010 earthquake, some stations have continued in their operation, despite the numerous challenges that persist in Haiti. Consequently, only stations with reliable data were selected for inclusion in the study. **Table 1** presents a description of the physiographic and climatological characteristics of each station included in the study.

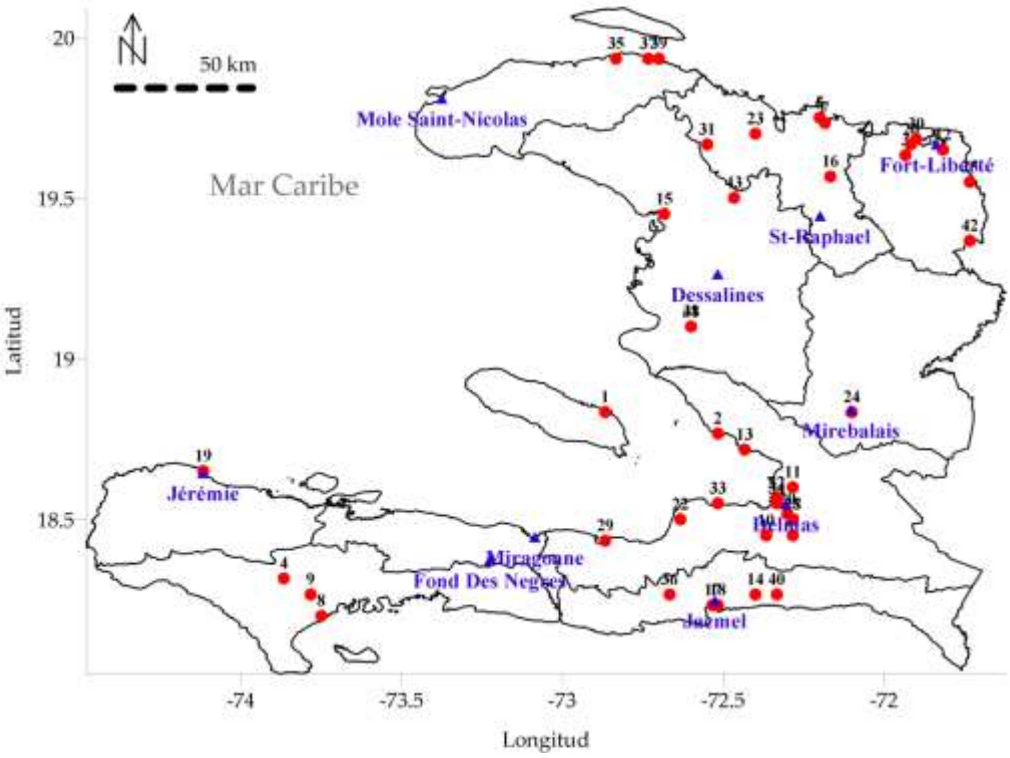

Figure 1. Location of weather stations in Haiti. Stations in operation (blue triangle). Stations out of operation (red circle).

Table 1. Characteristics used in the regionalization model for Haiti.

Variable	Symbology
Latitude	Lat
Longitude	Long
Altitude of the station (m)	Alt
Distance to ocean (m)	DistOc
Maximum annual precipitation height (mm)	HpMax
Minimum annual precipitation height (without taking zeros) (mm)	HpMin
Kurtosis of the maximum annual precipitation height, in mm	HpKurt
100-year precipitation height of the Gumbel Distribution (mm)	Gumb100
Scaling parameter of the Gumbel Distribution	Gumb-u
Scaling parameter of the Poisson/Exponential Distribution	Fuit-lamb

2.3. Independence of time series

The recommended methodology for conducting this analysis entails verifying the consistency of the variables to be utilized [14–16]. It is typically advised that, prior to undertaking any further analysis, tests of independence be conducted on historical data samples [17]. Moreover, a regression analysis or an analysis of variance is strongly advised to establish the relationship between variables (regional equations) [18]. It is recommended that an analysis of the covariance function be conducted, followed by a test of independence through the use of a correlogram. In the context of a time series comprising the maximum annual precipitation values (X_t), the time lag (k) is defined as the time lag in years of each record. In this context (N)

represents the total number of years of the data set, while ($\bar{X}$) denotes the mean value of the records. In accordance with this concept, the correlograms $r(k)$ of the AR(p) models serve as estimators of the variance (C_o) and autocovariance (C_k) (Equation (1)). This can be expressed in terms of the lag autocovariance function $k(C_k)$ as follows. Values close to zero in the correlogram indicate independence, homogeneity and consistency of the series.

$$r(k) = \frac{C_k}{C_0} = \frac{\frac{1}{N-k}\sum_{t=1}^{N}(X_t - \bar{X})(X_{t+k} - \bar{X})}{\frac{1}{N}\sum_{t=0}(X_0 - \bar{X})(X_0 - \bar{X})} \quad (1)$$

2.4. Cartography of hydrologically homogeneous regions

The considerable heterogeneity of regions represents a significant challenge when attempting to regionalize watersheds. The delineation of hydrologically homogeneous regions represents the most challenging aspect of the hydrological regionalization process [19]. The disaggregation of a region into similar subregions serves to reduce the errors generated when transferring hydrological storm data from one basin to another [20]. The techniques employed to ascertain the most appropriate homogeneous regions include residual analysis [21,22], time series statistics analysis [23] and multivariate techniques. It is essential to identify the significant variables or characteristics of the region to be studied prior to implementing any procedure [24,25]. The Surfer and Statistica software were employed for the purposes of cartography and multivariate analysis, respectively.

2.5. Construction of regional equations

The most frequently employed methodology for establishing regional relationships is multiple correlation analysis. It is conventional practice to correlate the events to be predicted, for example maximum flows or rainfall, with the physiographic characteristics of the basin. A typical practice is to make use of the results of frequency analysis, relating the parameters of the fitting distribution to the physiographic, climatic or environmental characteristics of the region [26–28].

3. Results

3.1. Multivariate analysis

The selection of variables was based on EOF analysis, as this multivariate method obtains the valuable capacity to determine the spatial dimensionality of the data, thereby allowing the dimensional space of the population to be reduced. The application of EOF to the characteristics matrix yielded the result that the first two principal components together explain 76.82% of the total variability. The first component explains 58.41%, while the second explains 18.41%. The variables were selected on the basis of their position, as indicated by their normalized correlation value, within the quadrants of the correlation circle, with the axes corresponding to the first two principal components (see **Figure 2**). On the other hand, the parameters related to all design events are grouped in the same zone. This means that the probability distribution used for design events is not very significant for regionalization purposes. It can be postulated that the variables which are proximate to each other in the multivariate space will tend to demonstrate similar behaviour. It is further postulated that variables with a greater projection on the axis of the first principal component are of more considerable importance. Furthermore, variables located in opposite quadrants generally exhibit inverse relationships. Likewise, it can be seen how the parameters related to the probability distribution of Fuites and Gamma have similar behaviors. That is, Fuit-lamb and Gam-lamb are placed in the same place, which makes sense considering the distributions have the same origin as extreme distributions and the parameters are similar.

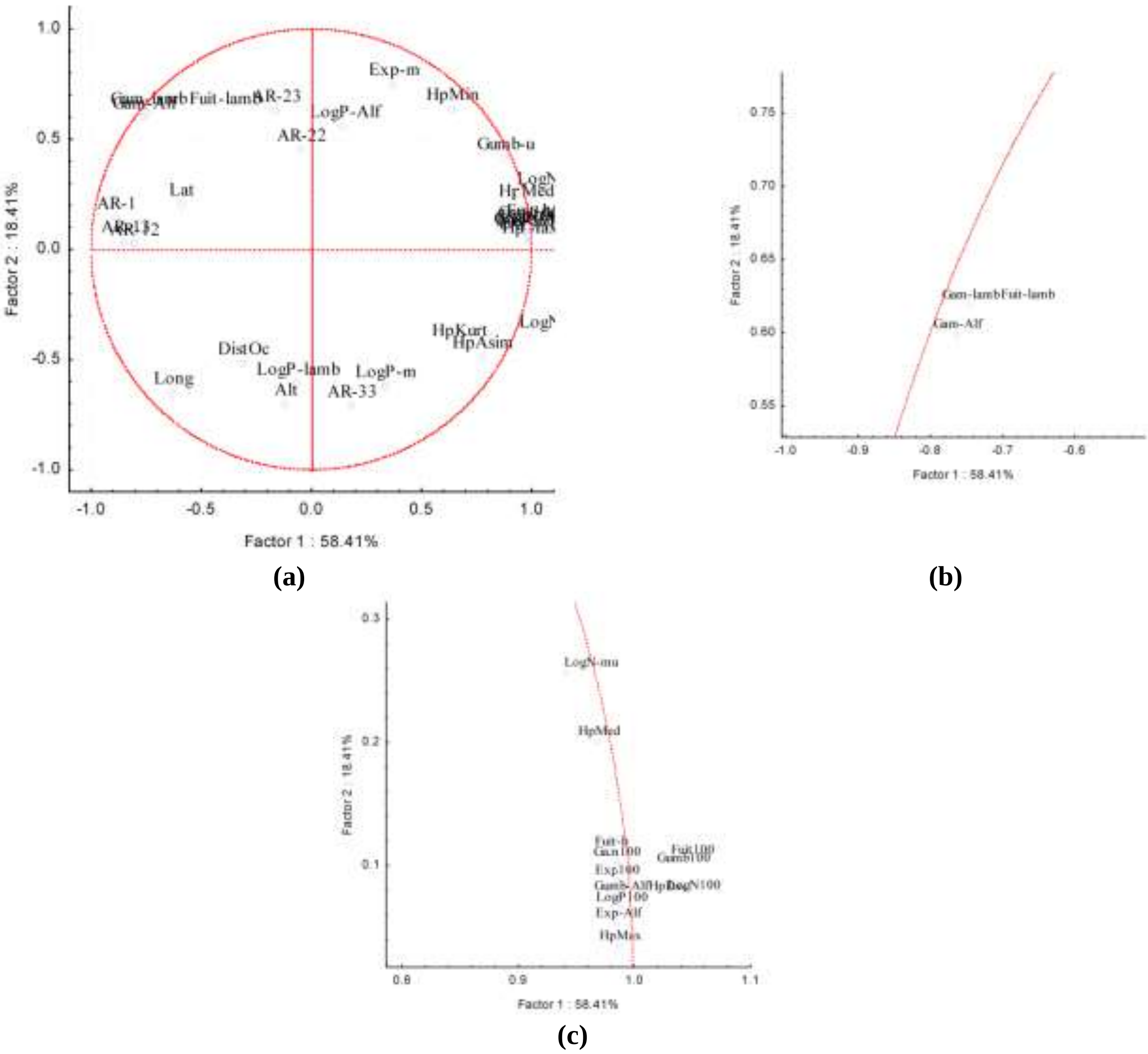

Figure 2. Correlation circle with EOF results for components 1–2 of all characteristics used in the study. Total representation 76.82%.

3.2. Independence of time series

As previously stated, the autocovariance function and the correlogram permit the verification of the independence of the time series. **Figures 3** and **4** illustrate the evolution of the correlogram over time for the same data series, in this case, for the annual maximum precipitation recorded at the Fort-Liberté station. From an examination of both figures, it can be concluded that the AR (1) model represent not an appropriate choice for this sample of Fort-Liberté data, given that the correlogram displays variability near the confidence limits. This phenomenon occurs at lag times for k = 3, k = 5, k = 7 and k = 9. Nevertheless, an AR (2) model, as illustrated in **Figures 3** and **4**, reveals that only lag time k = 1 exhibits a minor discrepancy, while the remaining series is consistent in its independence across all time lags.

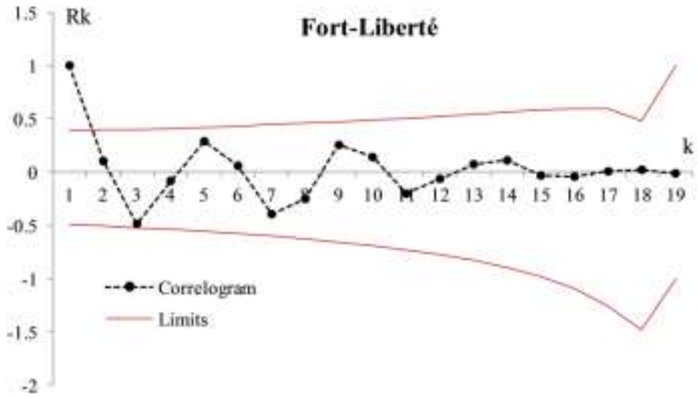

Figure 3. Correlogram for station Fort-Liberté AR (1) series of annual maximum rainfall.

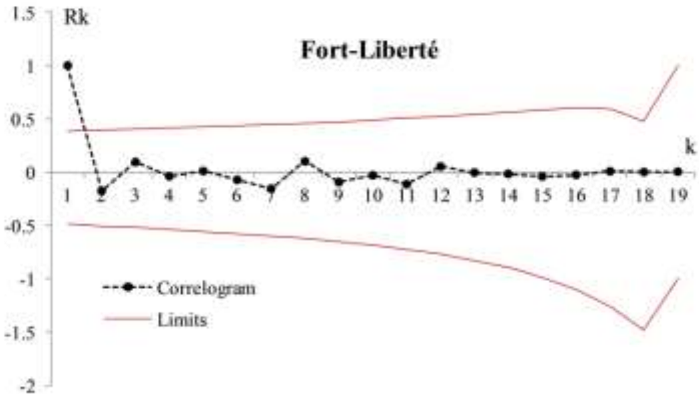

Figure 4. Correlogram for station Fort-Liberté AR (2) series of annual maximum rainfall.

3.3. Hydrologically homogeneous regions

The delineation of homogeneous regions was conducted through the utilization of EOF analysis. As illustrated in **Figure 5**, three regions were delineated within the country. The first region is located in the northern part of the country and is defined by the meteorological data from the stations Mole Saint-Nicolas and Dessalines. These regions exemplify the humid conditions characteristic of the Caribbean Sea. The second region is constituted by the stations of Jeremie, Fond Des Negres and Miragone. Situated in the southern region of the country, this area is distinguished by its elevated susceptibility to extreme meteorological events, including hurricanes. The remaining stations constitute the third hydrologically homogeneous region, which represents the dry condition of the country. The results of the configuration of the hydrologically homogeneous regions, created by the hierarchical clustering technique (dendograms) and the EOF analysis, respectively, are presented in **Figures 6** and **7**.

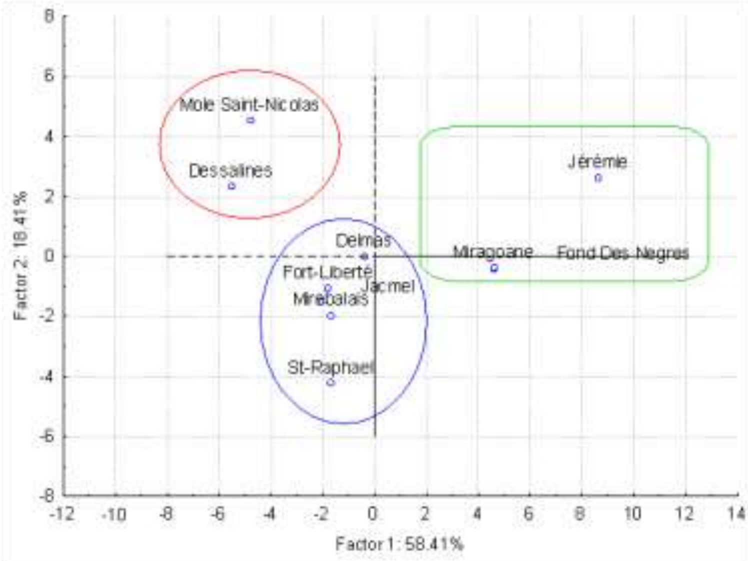

Figure 5. Results of EOF for homogeneity of regions.

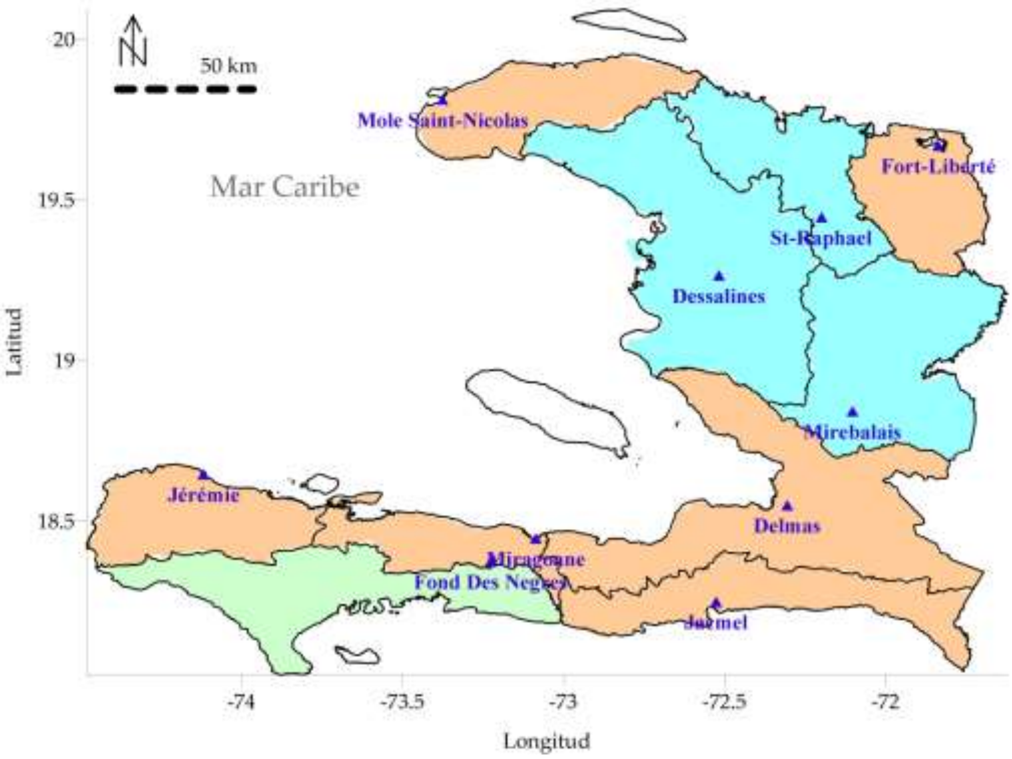

Figure 6. Results of the dendrogram analysis for homogeneity of regions.

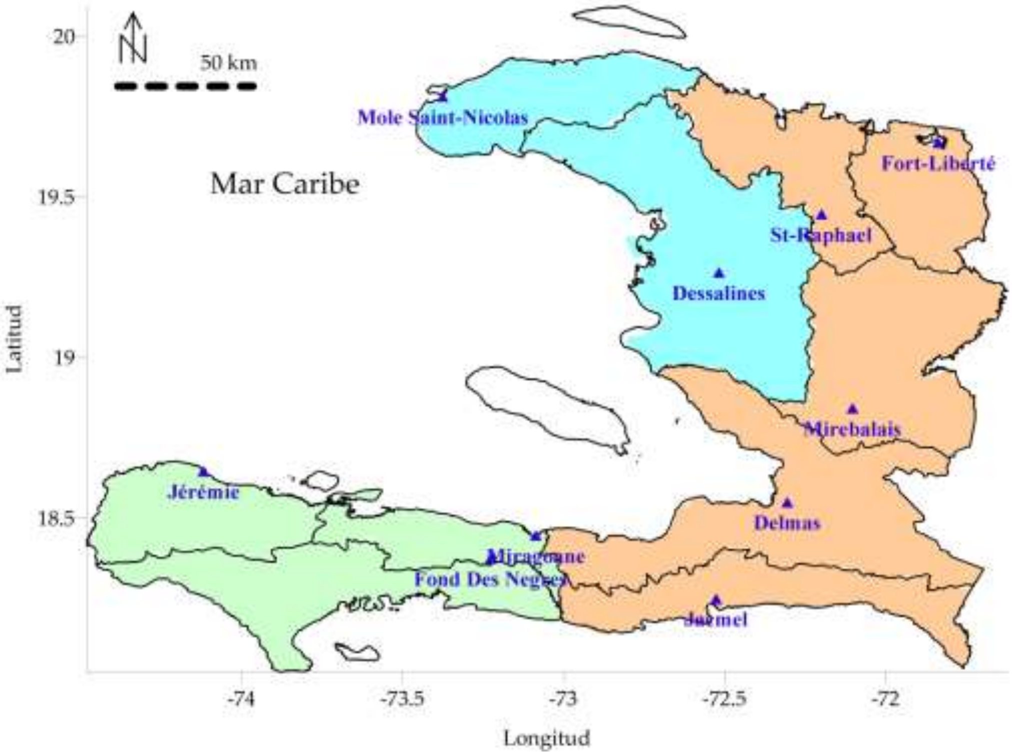

Figure 7. Results of EOF for homogeneity of regions.

4. Discussion

As previously stated, the construction of regional equations is achieved through the application of multiple correlations. In this instance, our focus is on the equations used to forecast the maximum 24-hour rainfall. Initially, all significant variables that have already been analyzed are employed (Equation (2)). It is crucial to exclude the data from the Delmas station, as this allows us to utilize genuine data to compare the values obtained with the regional equations (**Table 2**). The equation for the entire region, used to forecast the maximum 24-hour rainfall, is:

$$\begin{aligned}\mathrm{HpMax} = {} & (6.647208129 * \mathrm{Lat}) + (2.540808455 * \mathrm{Long}) - (0.019672487 * \mathrm{Alt}) - \cdots \\ & - (4.8897344 * \mathrm{HpMin}) + (3.724475655 * \mathrm{HpKurt}) + (5.903582493 * \mathrm{Gumbu}) \\ & + (0.643863993 * \mathrm{Gumb100}) + (0.535285418 * \mathrm{Fuitlamb})\end{aligned} \tag{2}$$

The same procedure is used to construct the regional equations for the other homogeneous regions. The equation (Equation (3)) for the region in orange (region A) (**Figure 7**), for the forecast of the maximum 24-hour rainfall is:

$$\begin{aligned}\mathrm{HpMax} = {} & -(0.00714296 * \mathrm{Alt}) + (2.95093\mathrm{E}^{05} * \mathrm{DistOc}) + (2.028189568 * \mathrm{HpKurt}) \\ & + (0.778523875 * \mathrm{Gumb100})\end{aligned} \tag{3}$$

The equation (Equation (4)) for the green region (region B) (**Figure 7**), for the forecast of the maximum 24-hour rainfall is:

$$\mathrm{HpMax} = (0.664288316 * \mathrm{Alt}) - (4.472\mathrm{E}^{-06} * \mathrm{DistOc}) + (0.670126744 * \mathrm{Gumb100}) \tag{4}$$

The equation (Equation (5)) for the blue region (region C) (**Figure 7**), for the forecast of the maximum 24-hour precipitation height is:

$$\mathrm{HpMax} = -(0.466551856 * \mathrm{Long}) + (4.483\mathrm{E}^{-05} * \mathrm{DistOc}) \quad (5)$$

The results facilitate the acquisition of events at sites with scarce or no data. In the conventional approach, a multiple correlation is employed to establish relationships between totally the variables and the event to be estimated (Equation (2)). Nevertheless, the methodology detailed herein enables the verification that the utilisation of all variables from the whole stations produces high-quality estimated values [13]. However, given the unique circumstances of Haiti, this research develops the following steps in light of that country's specific context: (i) Identify the variables that describe the phenomenon to be estimated [4]; (ii) verify the independence of the time series [7]; (iii) cartography of the hydrologically homogeneous regions [9]; (iv) construction of regional equations for hydrological information transfer; and (v) Verification of the applicability of the regional equations [11].

Table 2. Overview of the values estimated with the regional equations for the Delmas station. Maximum 24-hour rainfall (mm) and error*.

Real rainfall height (mm)	Equation (2) Regional Complete	Equation (3) Region A	Equation (4) Region B	Equation (5) Region C
69.89	59.53	70.83	131.31	34.93
	10.36*	0.94*	61.42*	34.95*

5. Limitations

The rigorous methodology implements several techniques (EOF, clustering, cross-validation) to ensure robust results. However, the quality is relatively limited by the scarcity and inconsistency of historical data in Haiti, which may limit precision. No statistics can measure the performance of hydrological regionalization. The only way to do this is to cross-validate, i.e. to remove a site's records from the beginning of the procedure and then verify with the regional equations the precision of the estimation of events at that site (possibly with a quadratic error). The main limitation is obviously the availability of and access to data. However, a complete execution of each of the steps mentioned here, with little data (<20 years), can provide absolutely reliable estimates in sites without records. A fundamental aspect is some researchers confuse regionalization with calculations that are carried out on a routine basis, such as [4]:

- Hydrologic regionalization is not: calculating and drawing iso-lines of some hydrologic variable; this is called cartography.
- Hydrologic regionalization is not: using different physiographic characteristics of a region; this is called spatial ponderation.
- Hydrologic regionalization is not: using probability distributions in several stations of a region; this is called multiple frequency analyses.
- Hydrological regionalization is not: using some method such as Inverse of distance, Kriging, Splines, etc.; this is called spatial interpolation.
- Hydrological regionalization is not: estimating envelope curve function of hydrological events; this is called analysis of extremes.

6. Conclusion

The creation of regional equations based on the delineation of homogeneous regions permitted the estimation of precipitation values at the Delmas station. The data obtained at the Delmas station were excluded from the regional analysis. Nevertheless, cross-validation demonstrated that if the complete regional equation had been employed, the resulting error would have been 10.36 mm. However, if the regional equation for the Delmas area had been utilized, the error would have been reduced to a mere 0.94 mm. The regional equations facilitate the reconstruction of rainfall fields and estimation of events at sites without historical records in Haiti. In the absence of a dense network of climatological stations in Haiti, the regional equations, derived from the cartography of hydrologically homogeneous basins, represent a valuable initial tool that can be enhanced with the incorporation of additional physiographic characteristics.

Hydrological regionalization has been identified as an exceedingly effective tool for the reconstruction of precipitation fields, like that of historical maximum rain in Haiti. The results obtained from this reconstruction allow for the estimation of rainfall values, which can then be used in the calculation of water balances. This initial regionalization of Haiti represents a significant advancement in the fact-finding field. Marking the beginning of a research sequence aimed at improving the availability of records and reliable historical series for the management of water resources; in a country confronted with such challenging social and political circumstances. Subsequent research will centre on constructing hydrological transfer equations, with the adjustment parameters of the probability distributions being a key priority. This approach will facilitate the estimation of not only a point value, but also a probability distribution at the analysis site.

Author contributions: Conceptualization, CG and AGL; methodology, CG and AGL; validation, AGL; formal analysis, CG and AGL; investigation, AGL; resources, CG; data curation, CG; writing-original draft preparation, CG; writing-review and editing, AGL. All authors have read and agreed to the published version of the manuscript.

Acknowledgments: For the support of the Consejo Nacional de Humanidades, Ciencias y Tecnologías (Conahcyt) by means of the postgraduate scholarship.

Conflict of interest: The authors declare no conflict of interest.

References

1. UNICEF & OMS. Progress on household drinking water, sanitation and hygiene 2000-2020: Five years into the SDGs. UNICEF & OMS; 2021.
2. Gonel J. Studying the potential of surface water in Haiti to address drinking water shortages (French). Available online: https://espace.inrs.ca/id/eprint/428/# (accessed on 2 June 2024).
3. FAO. Aligned National Action Program to Combat Desertification (French). FAO; 2015.
4. Gutiérrez-López A, Aparicio J. Las seis reglas de la regionalización en hidrología. Aqua-LAC. 2020; 12(1): 81-89. doi: 10.29104/phi-aqualac/2020-v12-1-07
5. Hlaing PT, Humphries UW, Waqas M. Hydrological model parameter regionalization: Runoff estimation using machine learning techniques in the Tha Chin River Basin, Thailand. MethodsX. 2024; 13: 102792. doi: 10.1016/j.mex.2024.102792

6. Dasgupta R, Das S, Banerjee G, et al. Revisit hydrological modeling in ungauged catchments comparing regionalization, satellite observations, and machine learning approaches. HydroResearch. 2024; 7: 15-31. doi: 10.1016/j.hydres.2023.11.001
7. Araujo ACS de, Frizzone JA, Camargo AP de, et al. Discharge sensitivity of collapsible drip tapes to water temperature. Revista Brasileira de Engenharia Agrícola e Ambiental. 2021; 25(1): 3-9. doi: 10.1590/1807-1929/agriambi.v25n1p3-9
8. Ye K, Liang Z, Chen H, et al. Regionalization Strategy Guided Long Short-Term Memory Model for Improving Flood Forecasting. Hydrological Processes. 2024; 38(10). doi: 10.1002/hyp.15296
9. Neelam TJ, Steinschneider S, Woodward DE, et al. Improved Regionalization of the CN Method for Extreme Events at Ungauged Sites across the US. Journal of Hydrologic Engineering. 2024; 29(6). doi: 10.1061/jhyeff.heeng-6180
10. Goovaerts P. Geostatistical approaches for incorporating elevation into the spatial interpolation of rainfall. Journal of Hydrology. 2000; 228(1-2): 113-129. doi: 10.1016/S0022-1694(00)00144-X
11. Guo Y, Zhang Y, Zhang L, et al. Regionalization of hydrological modeling for predicting streamflow in ungauged catchments: A comprehensive review. WIREs Water. 2020; 8(1). doi: 10.1002/wat2.1487
12. Finck LF, Leite IR, Almeida AK, et al. A streamflow regionalization method using hydrological data and geoprocessing tools—a Brazilian midwest analysis. Journal of South American Earth Sciences. 2024; 133: 104695. doi: 10.1016/j.jsames.2023.104695
13. Hazin LS. Working together for more efficient management of drinking water and sanitation services in Haiti (French). Publication des Nations Unies; 2005.
14. Ebisemiju FS. An objective criterion for the selection of representative basins. Water Resources Research. 1979; 15(1): 148-158. doi: 10.1029/wr015i001p00148
15. Nathan RJ, McMahon TA. Identification of homogeneous regions for the purposes of regionalisation. Journal of Hydrology. 1990; 121(1-4): 217-238. doi: 10.1016/0022-1694(90)90233-N
16. Caratti JF, Nesser JA, Lee Maynard C. Watershed classification using canonical correspondence analysis and clustering techniques: a cautionary note1. JAWRA Journal of the American Water Resources Association. 2004; 40(5): 1257-1268. doi: 10.1111/j.1752-1688.2004.tb01584.x
17. Kanishka G, Eldho TI. Streamflow estimation in ungauged basins using watershed classification and regionalization techniques. Journal of Earth System Science. 2020; 129(1). doi: 10.1007/s12040-020-01451-8
18. Hu C, Xia J, She D, et al. Parameter Regionalization With Donor Catchment Clustering Improves Urban Flood Modeling in Ungauged Urban Catchments. Water Resources Research. 2024; 60(7). doi: 10.1029/2023wr035071
19. Smithers JC, Schulze RE. A methodology for the estimation of short duration design storms in South Africa using a regional approach based on L-moments. Journal of Hydrology. 2001; 241(1-2): 42-52. doi: 10.1016/S0022-1694(00)00374-7
20. Leviandier T, Lavabre J, Arnaud P. Rainfall contrast enhancing clustering processes and flood analysis. Journal of Hydrology. 2000; 240(1-2): 62-79. doi: 10.1016/S0022-1694(00)00315-2
21. Bhaskar NR, O'Connor CA. Comparison of Method of Residuals and Cluster Analysis for Flood Regionalization. Journal of Water Resources Planning and Management. 1989; 115(6): 793-808. doi: 10.1061/(ASCE)0733-9496(1989)115:6(793)
22. Hall MJ, Minns AW, Ashrafuzzaman AKM. The application of data mining techniques for the regionalisation of hydrological variables. Hydrology and Earth System Sciences. 2002; 6(4): 685-694. doi: 10.5194/hess-6-685-2002
23. Kachroo RK, Mkhandi SH, Parida BP. Flood frequency analysis of southern Africa: I. Delineation of homogeneous regions. Hydrological Sciences Journal. 2000; 45(3): 437-447. doi: 10.1080/02626660009492340
24. Berger KP, Entekhabi D. Basin hydrologic response relations to distributed physiographic descriptors and climate. Journal of Hydrol. 2001; 247(3-4): 169-182. doi: 10.1016/S0022-1694(01)00383-3
25. Burn DH, Elnur MAH. Detection of hydrologic trends and variability. Journal of Hydrology. 2002; 255(1): 107-122. doi: 10.1016/S0022-1694(01)00514-5
26. Wiltshire SE. Identification of homogeneous regions for flood frequency analysis. Journal of Hydrol. 1986; 84(3-4): 287-302. doi: 10.1016/0022-1694(86)90128-9
27. Burn DH. Catchment similarity for regional flood frequency analysis using seasonality measures. Journal of Hydrol. 1997; 202(1-4): 212-230. doi: 10.1016/S0022-1694(97)00068-1
28. Castellarin A, Burn DH, Brath A. 2001. Assessing the effectiveness of hydrological similarity measures for flood frequency analysis. Journal of Hydrol. 2001; 241(3-4): 270-285. doi: 10.1016/S0022-1694(00)00383-8

EnPress Publisher

Journal of Geography and Cartography 2025, 8(1), 10602.
https://doi.org/10.24294/jgc10602

Article

Application of the SWAT model for water budgeting and water resource planning in Oued Cherraa basin (northeastern Morocco)

Mohammed Laaboudi*, **Abdelhamid Mezrhab, Zahar Elkheir Alioua, Ali Achebour, Mohammed Sahil, Wadii Snaibi, Said Elyagoubi**

Geographic Information Technologies and Space Management (ETIGGE), Communication, Education, Digital Usage and Creativity Lab, Faculty of Letters and Human Sciences, Mohamed First University, Oujda 60000, Morocco

*** Corresponding author:** Mohammed Laaboudi, mohammed.laaboudi@ump.ac.ma

CITATION

Laaboudi M, Mezrhab A, Alioua ZE, et al. Application of the SWAT model for water budgeting and water resource planning in Oued Cherraa basin (northeastern Morocco). Journal of Geography and Cartography. 2025; 8(1): 10602. https://doi.org/10.24294/jgc10602

ARTICLE INFO

Received: 28 November 2024
Accepted: 27 December 2024
Available online: 8 January 2025

Abstract: This study focuses on the use of the Soil and Water Assessment Tool (SWAT) model for water budgeting and resource planning in Oued Cherraa basin. The combination of hydrological models such as SWAT with reliable meteorological data makes it possible to simulate water availability and manage water resources. In this study, the SWAT model was employed to estimate hydrological parameters in the Oued Cherra basin, utilizing meteorological data (2012–2020) sourced from the Moulouya Hydraulic Basin Agency (ABHM). The hydrology of the basin is therefore represented by point data from the Tazarhine hydrological station for the 2009–2020 period. In order to optimize the accuracy of a specific model, namely SWAT-CUP, a calibration and validation process was carried out on the aforementioned model using observed flow data. The SUFI-2 algorithm was utilized in this process, with the aim of enhancing its precision. The performance of the model was then evaluated using statistical parameters, with particular attention being given to Nash-Sutcliffe efficiency (NSE) and coefficient of determination (R^2). The NSE values for the study were 0.58 for calibration and 0.60 for validation, while the corresponding R^2 values were 0.66 and 0.63. The study examined 16 hydrological parameters for Oued Cherra, determining that evapotranspiration accounted for 89% of the annual rainfall, while surface runoff constituted only 6%. It also showed that groundwater recharge was pretty much negligible. This emphasized how important it is to manage water resources effectively. The calibrated SWAT model replicated flow patterns pretty well, which gave us some valuable insights into the water balance and availability. The study's primary conclusions were that surface water is limited and that shallow aquifers are a really important source of water storage, especially for irrigation during droughts.

Keywords: SWAT model; water budgeting; Oued Cherraa watershed; evapotranspiration; groundwater recharge; sustainable water management

1. Introduction

Although it is not a luxury, water is essential to all living things. The survival of all living things depends heavily on it. Additionally, both require comparatively large amounts of water to function well; therefore, understanding the water demand is particularly crucial [1]. The amount of food available, economic prosperity, human and animal habitats, local and international ties, and population displacement are all impacted by water availability. The relationship between groundwater-dependent irrigation system water supply and availability has recently been discussed in a number of ways [2]. Particularly in arid, semiarid, and water-scarce regions [3], the rapid economic development, population growth, and global climate change are all placing a great deal of strain on the water resources [4,5]. Land use, the predominant cropping pattern, the sites of water applications, and the time of water usage all have an impact on the regional and season-wise distribution of water throughout the basins [6]. The prospective demand for water resources is influenced by the restricted supply in many arid and semi-arid locations. The estimation, comprehension, and sustainable management of water metrics are essential in the 21st century. According to Dovie and Kasei [2], climate change has an impact on the majority of water resource projects. Thus, scholars are focusing on water budgeting by quantifying water resources all around the world. The water by considering various water users, including public, industrial, agricultural, and residential uses [7,8]. When used with correct data sets, hydrologic models such as SWAT [9], MODFLOW [10,11] MIKE [12], and HEC-RAS prove to be highly effective.

In order to calculate the amount of water in the study basin, these GIS-based agro-hydrological models needed the following data as inputs: agricultural information, infrastructure and technology data, socioeconomic data, and meteorological data. One sector's cropping pattern and water use have an impact on another sector's water consumption and outputs; for example, irrigation in river basins reduces water discharge downstream of the river. However, despite the fact that climate change and excessive demand from such small-scale methods will support the sustainable growth of water resources for various water users [13]. To better comprehend and model the changes in water use brought on by anthropogenic activities [14], developed heuristic rainfall-runoff models. The computer capacity of those models enables users to better understand and predict the features of water resources through numerical simulations and testing of various management scenarios [13]. These numerical models, which integrate a number of empirical equations and scientific principles, allow users to assess the hydrological interactions in river basins [15]. Using hydrologic models is the most accurate and useful method for forecasting water availability and distribution in the study basin under different operating and demand scenarios. The semi-distributed, process-based, agro-hydrological SWAT model is used to depict both processes that generate runoff and how they affect the hydrology of the research area. To determine the long-term impact of an environmental change on the hydrologic response of a basin, authors have attempted to connect water availability and consumption using these models [15,16].

The primary novelty of this study is the application of the Soil and Water Assessment Tool (SWAT) to Oued Cherraa basin in north-eastern Morocco. This basin, renowned for its natural attractions, including the celebrated Camel and Pigeon Caves, has not previously been studied using this model. This study represents a pioneering application of the SWAT model to the region, offering a novel perspective on the hydrological system. Oued Cherraa basin faces intricate challenges related to water management, agriculture, and tourism. A distinguishing feature of this study is its capacity to adapt the SWAT model to a region characterized by limited and unreliable data availability. Our study decisively overcomes the challenge posed by scarce data. We demonstrate that the SWAT model's efficacy is unparalleled, even in regions with incomplete data. This model is invaluable for areas worldwide that face similar limitations.

The SWAT model is the best choice for our study because it has many advantages. SWAT is very good at modeling hydrological processes in complicated and varied watersheds like Oued Cherraa basin. It can simulate water flow, water quality, soil erosion and the impact of farming, which are all important for managing water sustainably in this area. Furthermore, the model's capacity to accommodate diverse climate scenarios and identify optimal management strategies is of paramount importance in the context of anticipating the repercussions of climate change on water resources.

The present study is distinguished by its practical application, offering critical insights into the management of water resources in the region, with particular reference to agriculture, drinking water supplies for Berkane, and tourism. The research provides a plan for making important decisions, including building dams, using better irrigation techniques, and other ways to make the most of water. This shows how important it is to manage water in a way that doesn't use up too much, especially in a place where there is a lot of pressure on water resources.

It also adds to our understanding of how climate change affects water availability and why it's important to have plans to deal with it. The study provides important information for people who make decisions about water management in Oued Cherraa and other places with similar water and climate issues. This research is very important because it uses new ways of collecting data and can be used in places where there is not much data about water management.

2. Materials and methodology

2.1. Study area

Oued Cherraa watershed is located in the northeastern region of Morocco, spanning a range of longitudes between 2°15'25" and 2°27'24" W and latitudes between 34°46'51" and 34°57'30" N. It encompasses an area of 267.29 km^2 (see **Figure 1**). The area is comprised of three deep, narrow valleys situated in the Beni-Snassene region, located upstream from the town of Berkane [17]. Oued Cherraa river flows in a straight line for approximately 12 km, with its primary tributary, the Oued Beni-Ouklane, joining before the river ultimately merges with the Moulouya River. Approximately 4 km downstream from Berkane, the river contributes to the recharge of the local water table, which then flows into the Moulouya River. The region's topography is characterized by a diverse range of mountain ranges, exhibiting considerable elevation differences. The ranges in question rise from 800 m (Jbel Aghil, located downstream) to 1532 m (Jbel Foughal, at the basin's easternmost point). The majority of the area lies between 700 and 1000 m above sea level, with steep slopes ranging from 20% to 80%. These slopes often feature vertical cliffs that overhang the rivers.

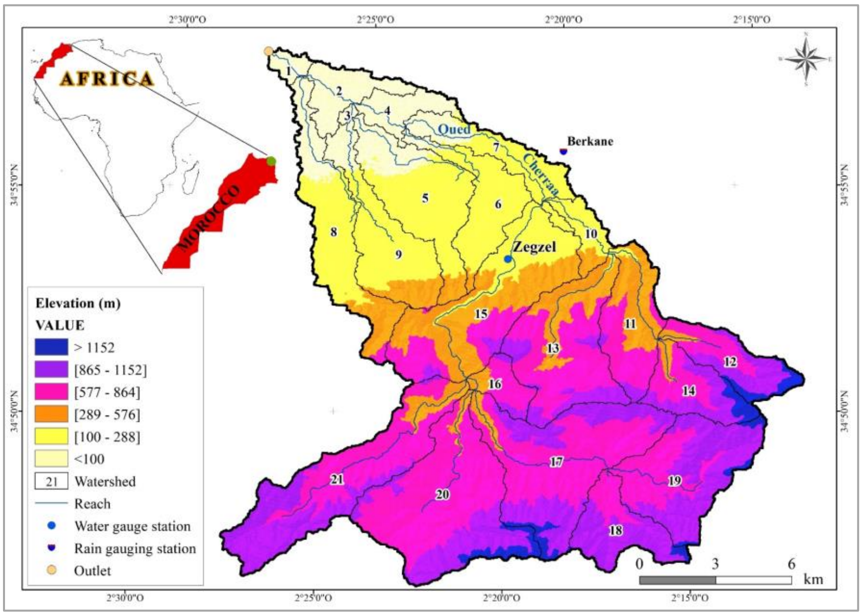

Figure 1. Site of the study area.

Geologically, the Beni Snassen region forms part of a SW-ENE-oriented Jurassic limestone massif, closely associated with the Atlas domain [18]. The highest peaks dominate the Triffa plain and the lower Moulouya valley to the north. The region is marked by deep gorges, such as the Zegzel gorges. The region's geological structure is primarily composed of Jurassic limestone and dolomite, which are underlain by impermeable substrata, typically Hercynian basement rocks such as schists and granites. The region's limestone is fissured and full of underground water. This water table is important for the local area.

Agriculture is a key economic activity in the region, particularly in the Trifa plain, where citrus farming is a dominant feature. Berkane province, located at the heart of the region, accounts for over 86% of the total area dedicated to citrus cultivation. Although citrus crops occupy only 3% of the region's agricultural land (SAU), which is 0.3% of Morocco's total agricultural land, this sector is of immense strategic importance to both the local and national economy. The province produces more than 88% of the region's citrus output, contributing 15% of Morocco's national citrus production. The cultivation of citrus fruits, particularly species such as oranges, lemons, and mandarins, plays a pivotal role in the region's export economy. In addition to enhancing local food security, this sector plays a pivotal role in bolstering the region's economic vitality. It's really important to be able to access groundwater from Oued Cherraa basin's aquifer system if we want to keep growing citrus fruits in this semi-arid region. So, having good irrigation systems that use these groundwater resources is really important for the success and sustainability of this agricultural industry.

2.2. Input data

The accuracy of the input data significantly improves the operational, realistic, and effective SWAT model when sub-basin-scale hydrological simulations are conducted using the ArcSWAT interface (GIS interface for the SWAT model). Oued

Cherraa watershed was the specific focus of this study. To meet certain input requirements, soil and land-use maps were superimposed on top of five slope categories (0%–5%, 5%–10%, 10%–15%, 15%–20%, and >20%) [19]. 21 sub-catchments, totaling 696 hydrological response units (HRUs), were created (**Figure 2A**). Depending on the objectives of the study, the number of HRUs may vary. In this case, we used a method that balanced a number of factors, such as computation time, spatial resolution, available data, model complexity, and calibration.

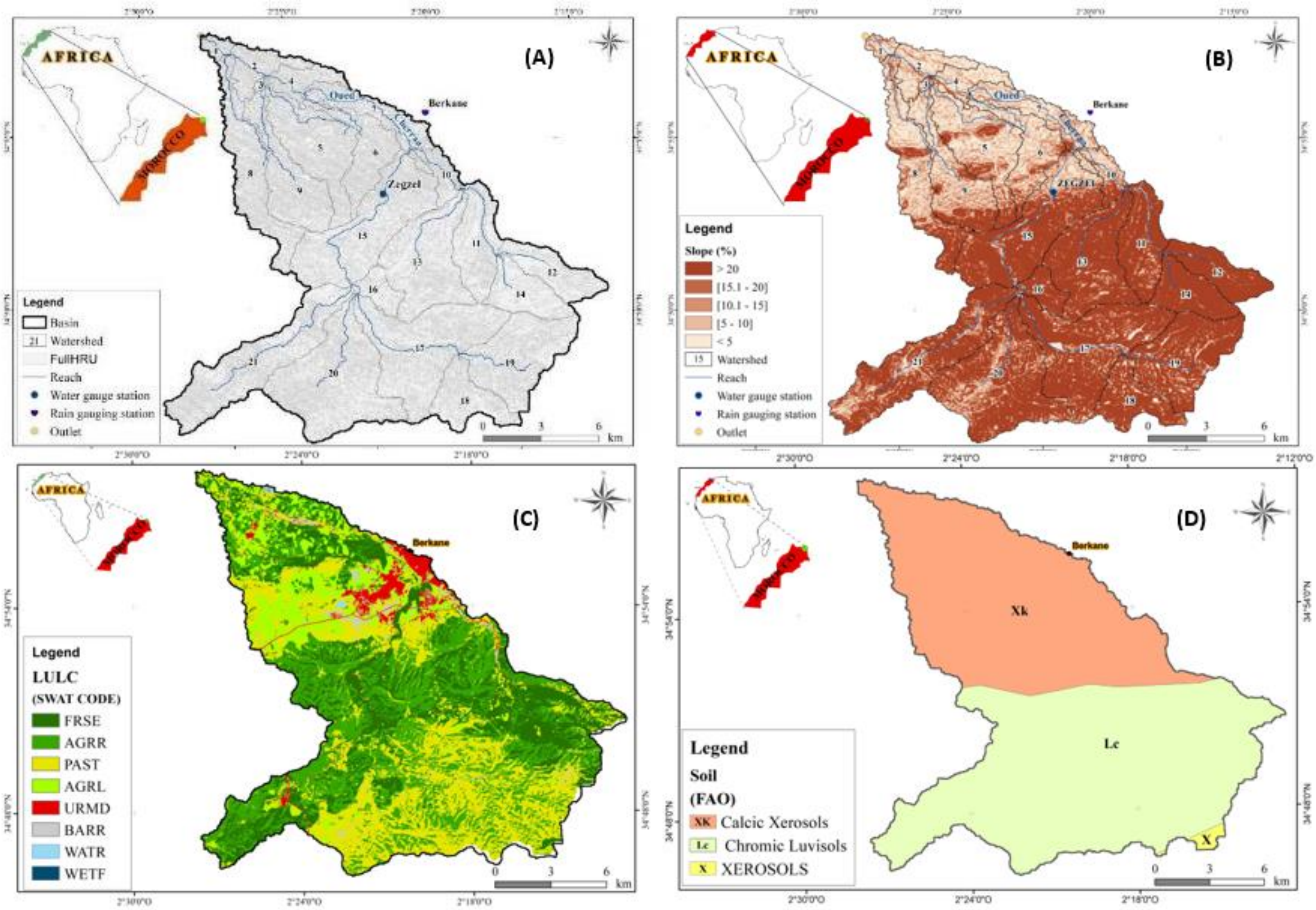

Figure 2. Input data for the SWAT: **(A)** watershed delimitation; **(B)** slope; **(C)** land cover; **(D)** Soil map.

2.2.1. Digital terrain model (DEM)

To define Oued Cherraa watershed and its drainage system, we used the digital terrain model (DEM) from the Shuttle Radar Topography Mission (SRTM). Areas between 60° North and 56° South are included in these data [20], which were first processed to a spatial resolution of 30 m. SRTM data from the United States Geological Survey (USGS) is available on the Earth Explorer website (accessed 29 January 2023). Oued Cherraa's altimetry, as determined by SRTM, is shown in **Figure 2A**, while the slope is shown in **Figure 2B**.

2.2.2. Land use

Land use and land cover maps (LULC) are important tools for determining various hydrological processes, such as surface erosion, evapotranspiration, and runoff, within a watershed. These maps provide a thorough illustration of how land was distributed and used during a specific time period. The LULC maps were meticulously created for the sake of this study using a Sentinel-2 satellite image, which was obtained on 18 June 2021, and had an impressive resolution of 10 m. High-resolution satellite images can be downloaded for free from the Copernicus Open Access Hub, which is managed by the European Space Agency (ESA) [19]. It is important to highlight the efforts made during the development process in order to ensure the accuracy and reliability of the maps. Suitable for the classification and detection of several land use categories, such as vegetation, water, bare soil, and urban areas, the satellite image bands used in this study are band 2 (blue—490 nm), band 3 (green—560 nm), and band 4 (red—665 nm). Satellite photos were processed and LULC maps were created using the ENVI 5.3 software. The software program ENVI 5.3, which is well-known for processing remote sensing data, was used to classify satellite photos and create the final land use map. Using the generic land use code and the terminology from the SWAT database, **Figure 2C** displays the LULC classes. This classification identified seven different land use types in the study area: forests (20.9%), orchards (34.4%), bare soil (1.7%), water bodies (0.1%), cropland (9.0%), built-up areas (3.0%), and grassland (30.8%). In addition to providing useful information on land use trends within the basin, this thorough classification provides an overview of the hydrological dynamics and behavior of the watershed.

2.2.3. Soil

It is vital to note that soil maps are challenging to find, particularly in underdeveloped nations [21]. To create a soil map, two sources of data were combined: 250 m resolution data from ISRIC’s SoilGrids and data from the United Nations Food and Agriculture Organization (FAO). It should be noted that only physical and chemical features are covered by the data that is currently available. The raster that was supplied into SWAT has an attribute table pinned to it with the data arranged in it. To represent the true breadth, all of the data that was downloaded from ISRIC’s SoilGrids has been updated. Different soil classifications with differing percentages of occupancy are found within the watershed [19]. These consist of Xersolos, Chromic Luvisols, and Calcic Xerosols; the first two classes are the most common (**Figure 2D**).

2.2.4. Climate data

The meteorological data utilized in this study was gathered at the Berkane meteorological station, which is managed by the Hydraulic Basin Agency of Moulouya (ABHM). The eight-year data collection period, which runs from 2012 to 2020, includes observations of rainfall and other meteorological parameters. Due to the lack of reliable meteorological data in semi-arid regions, it was essential to guarantee the accuracy and completeness of the time series. In accordance with the 1990 recommendations of Sharpley and Williams, the study filled in the data gaps using the ArcSWAT model and the WXGEN weather generator. This method produces thorough climate data that incorporates variables including sun radiation, wind speed, temperature, and relative humidity [22]. The goal of the study was to increase the quality and consistency of the meteorological data used in order to increase the reliability of the ArcSWAT model’s output.

2.2.5. Hydrological data

Using daily flow observations collected from the Tazarhine (on Oued Zegzel) station over a four-year period, from 2012 to 2016, the hydrological model was verified and calibrated. Since initial conditions are so important in ensuring simulation accuracy, model initialization was finished for the first two years of the study, or 2012–2013. Carefully calibrating the model and modifying parameters to achieve the highest possible agreement with the received data took place in 2014 and 2015. As a result of certain gaps in the available data for this time frame, the validation process focused on only one year of data, from 1 January to August 2016.

This strategic approach aimed to assess the SWAT model's ability to reliably and precisely reproduce observed flow, which is essential for guaranteeing the precision and dependability of the model's hydrological forecasts.

2.3. Methodology adopted

The semi-distributed SWAT model, created by the US Agriculture Research department [15,23,24], was employed in this study. The SWAT is a semi-distributed, GIS-based physical model that forecasts hydrological parameters and models the rainfall-runoff process [25]. The SWAT model can operate for a long time and is quite efficient. The model processes GIS-based data, such as digital elevation, the study area's land use and land cover (LULC), climate data, and soil data, to produce simulated outcomes in terms of water availability, loss of water, pesticide and nutrition transfer, etc. The following is the fundamental idea that underpins the SWAT model (Equation (1)) [15,23].

$$Wt = SW0 + \sum_{i=1}^{t}(Rday - Qsurf - Wseep - Ea - Qgw) \tag{1}$$

Based on the initial soil water content (SW0) on day (i), the amount of precipitation (Rday) on day (i) in mm H2O, the amount of surface runoff (Qsurf) on day (i), and the amount of water entering the vadose zone from the soil profile (Wseep) on day (i), the following formula provides the final soil water content (SWt) in millimeters of water (mm H2O). In addition, Ea denotes the amount of evapotranspiration on day (i) and Qgw denotes the return flow quantity (in milliliters of H2O) on day (i). Time is represented in days by the variable t [15,23]. Following this calculation, the model simulates the conveyance phase processes, which include the dispersion of chemicals, water, sediment, and nutrients down the channels and out of the watershed.

2.3.1. Configuring the SWAT model framework

We used SWAT 2012 with ArcGIS 10.4 for our modeling. First, we identified 21 sub-basins by delineating watershed boundaries and the drainage network using the digital terrain model (DEM). Hydrological response units (HRUs) were then created on the basis of soil type, land use and land cover (LULC) and slope (**Figure 2C**). In order to guarantee the precision and dependability of the data, the ArcSWAT extension was employed to categorize the watershed into sub-watersheds, slopes and drainage areas utilizing DEM data. Subsequently, the watershed was partitioned into homogeneous sections (HRU) in accordance with land use, soil and slope data. Input data for each sub-basin included soil type, weather conditions, land use and management practices, taking into account the impacts of physical processes on hydrology, river flow, runoff, sediment, nutrient and pesticide loading. Finally, meteorological data were verified and calibrated using the methods described in **Figure 3**.

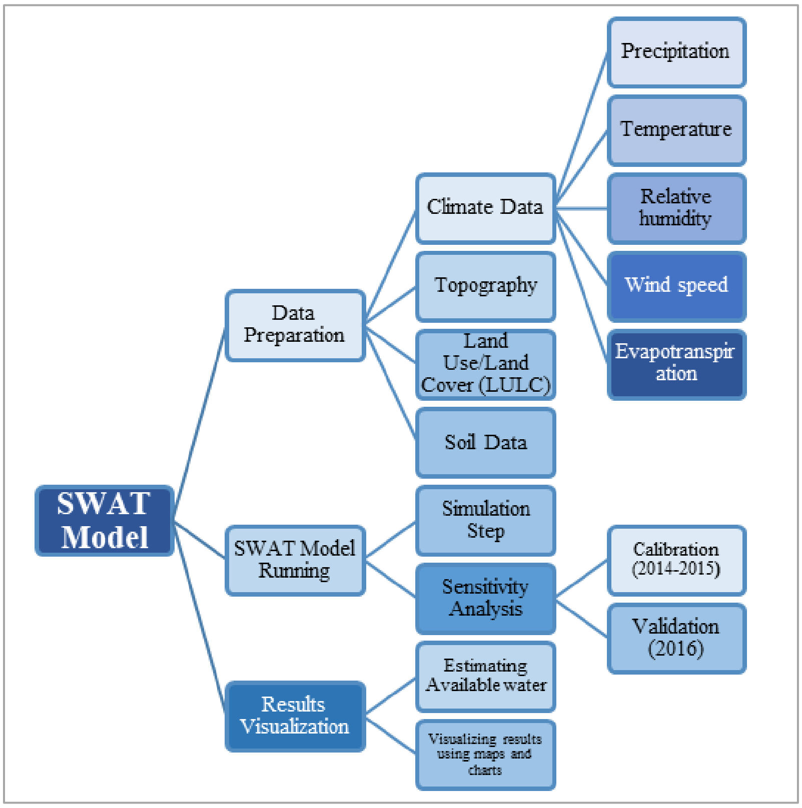

Figure 3. Working methodology.

2.3.2. Model calibration

Model calibration entails the adjustment of parameters until the model output aligns with the observed data [26]. In his publication [27], Beven outlines the calibration procedure for hydrological models as follows:

$$Q(x,t) = M(\theta, x, t) + \varepsilon(x,t) \tag{2}$$

$M(\theta,x,t)$ represents the estimated streamflow based on parameters θ and $\varepsilon(x,t)$ is the error during the time interval. $Q(x,t)$ is the flow at point x and time t. The model parameters are fine-tuned through both manual and automatic methods, with SWAT-CUP used for automatic calibration via the SUFI-2 algorithm. The model was calibrated for the years 2014–2015, with results compared to observed river flows during the same period.

2.3.3. Model validation

Validation serves to guarantee the precision of the model by means of a comparison between forecasts and field observations, without any alteration to the input parameters. In order to assess the model's performance, the validation process employed flow data from 2016, which had not been included in the calibration phase.

2.3.4. Model performance evaluation

The SWAT-SUFI 2 version of the model uses several objective functions to assess performance, such as the Nash-Sutcliffe Efficiency (NSE) and the Coefficient of Determination (R^2). The NSE compares the variance in observed data with the variance in the model's predictions [28]:

$$\text{NSE} = 1 - \left[\frac{\sum_{i=1}^{n}(Y_i^{obs} - Y_i^{sim})^2}{\sum_{i=1}^{n}(Y_i^{obs} - Y_i^{mean})^2}\right] \tag{3}$$

where Y^{mean} is the mean of observed data, Y^{obs} and Y^{sim} are the observed and simulated values, respectively.

The R^2 value represents the proportion of the observed data variance that can be explained by the model. As stated by Santhi [29], an R^2 value exceeding 0.5 is deemed acceptable. Equation (4):

$$R^2 = \frac{\left[\sum_{i=1}^{j}(Oi - \bar{O})(Pi - \bar{P})\right]^2}{\sum_{i=1}^{j}(Oi - \bar{O})^2 \sum_{i=1}^{j}(Pi - \bar{P})^2} \tag{4}$$

where Oi and Pi are the observed and predicted values, and $\bar{O}$ and $\bar{P}$ are their respective means.

Following calibration, the model's performance was validated using independent data from 2016. The calibration and validation of daily flow were evaluated using statistical metrics outlined by Moriasi [30], as illustrated in **Table 1**.

Table 1. A statistical evaluation of the SWAT model [30].

Model performance	PBIAS	NS	RSR
Excellent	PBIAS < ±10	0.75 < NS ≤ 1.00	0.00 ≤ RSR ≤ 0.50
Good	±10 ≤ PBIAS < ±15	0.65 < NS ≤ 0.75	0.50 ≤ RSR ≤ 0.60
Acceptable	±15 ≤ PBIAS < ±25	0.50 < NS ≤ 0.65	0.60 ≤ RSR ≤ 0.70
Insufficient	PBIAS ≥ ±25	NS ≤ 0.50	RSR ≤ 0.70

3. Results and discussions

3.1. Assessment of sensitivity

During the sensitivity analysis for model calibration, several parameters were identified as highly sensitive. These include the deep aquifer percolation fraction (RCHRG DP), the curve number (CN2), the base flow alpha factor (ALPHA_BF), the groundwater evaporation coefficient (GW_REVAP), the storage time constant for normal flow (MSK CO1) and the compensation factors for soil evaporation (ESCO) and plant uptake (EPCO). These parameters have a significant influence on flow dynamics. **Table 2** shows the fitted values for these sensitive parameters.

While curve number (CN2) is generally the most sensitive flow parameter in most Moroccan basins, in Oued Cherraa basin it is the RCHRG DP parameter that is the most sensitive. This difference highlights the unique hydrological characteristics of Oued Cherraa basin compared with other Moroccan basins.

Table 2. Parameter overview.

Parameter name	Full name and units	Parameter Range	Sensitivity Rank	Optimized Value
1: V_ALPHA_BF	Baseflow recession constant (days)	0.05–0.65	4	0.0013
2: r_CN2.mgt	Runoff curve number	−0.15–0.48	3	−0.4
3: v_SHALLST.gw	Initial depth of water in the shallow aquifer (mm)	500–10000	13	6870.8
4: v_EPCO.hru	Plant uptake compensation factor	0.29–0.82	6	0.53
5: v_FFCB.bsn	Initial soil water storage expressed as a fraction of field capacity water content	0.12–0.69	10	0.06
6: v_CH_K2.rte	Effective hydraulic conductivity in main channel alluvium	2.14–185.82	11	96.66
7: v_CH_N2.rte	Manning's "n" value for the main channel	0.25–0.76	12	0.92
8: v_MSK_CO1.bsn	Calibration coefficient used to control impact of the storage time constant for normal flow	1.33–8.15	2	3.39
9: v_ESCO.bsn	Soil evaporation compensation factor	0.11–0.94	9	0.57
10: v_REVAPMN.gw	Threshold depth of water in the shallow aquifer for "revap" to occur (mm)	122–3670	8	1937.84
11: v_SURLAG.bsn	Surface runoff lag time	0.98–21.77	7	8.91
12: v_GW_REVAP.gw	Groundwater "revap" coefficient	0.014–0.30	5	0.25
13: v_RCHRG_DP.gw	Deep aquifer percolation fraction	0.01–0.51	1	0.019

3.2. Calibration and validation

After identifying the most sensitive parameters, we refined their values through multiple calibration cycles in order to align the simulated flow with the observed data. Model calibration and validation were carried out using flow data collected from the gauging station near the outlet of Oued Cherraa basin. Compliance with the exacting calibration and validation standards established by SWAT-CUP necessitated the meticulous daily recording of measurements. The data has been thoroughly investigated to ensure effective calibration and validation of the SWAT model. A comparison of the calibrated and observed flow patterns is shown in **Figure 4**, which illustrates a high degree of agreement.

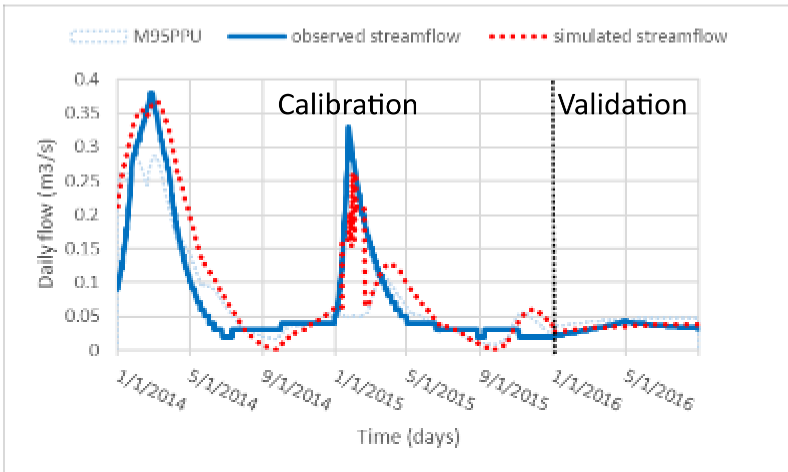

Figure 4. Hydrographs for assessing model calibration and validation.

Table 3 summarizes the additional performance. It should be noted that the Nash-Sutcliffe efficiency (NSE) values were very consistent, with NSE = 0.58 for calibration and 0.60 for validation. Furthermore, the correlation between observed and simulated flows remained consistent, with $R^2 = 0.66$ for calibration and $R^2 = 0.63$ for validation, as shown in **Figure 5**. These results demonstrate that the model performs adequately and provides a reliable simulation of flow dynamics in Oued Cherraa basin.

Table 3. Statistical summary for evaluating model performance.

Statistical parameter	Calibration	Validation
Nash-Sutcliffe (NSE)	0.58	0.60
Coefficient of determination (R^2)	0.66	0.63

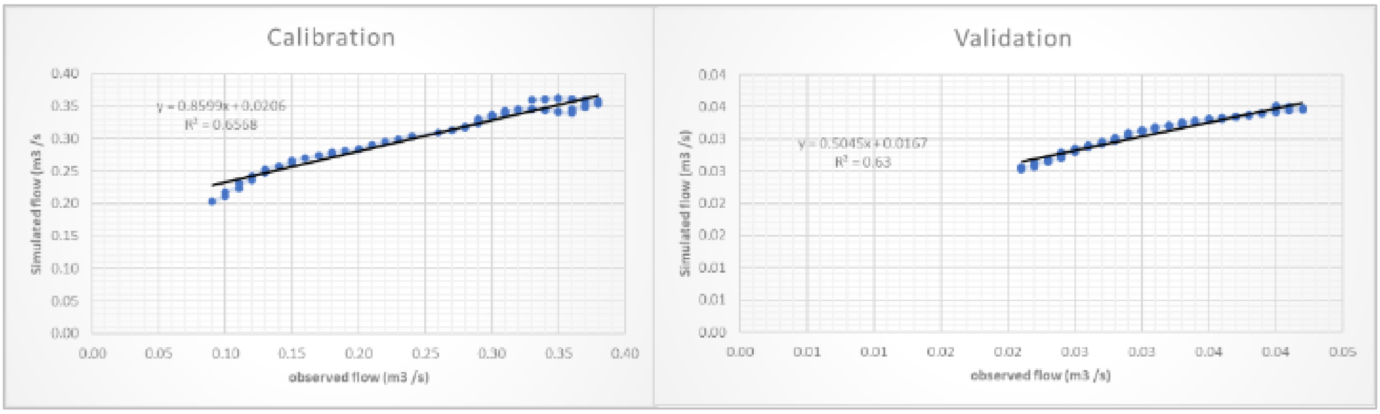

Figure 5. Scatter diagrams of the calibrated and validated models.

The feasibility and effectiveness of the model were demonstrated by its successful application in Oued Cherraa catchment. After examination, the model provided accurate results that corresponded well to the objectives of the study. Although the SWAT model generally underestimates flows, particularly during summer low-flow periods, the results remain acceptable, as confirmed by data from the Tazarhine station (on the Oued Zegzel).

3.3. Water budget

In order to conduct an accurate hydrological analysis of Oued Cherraa catchment, it was essential to develop models that had been calibrated and validated to the greatest extent possible. The calibration process enabled the parameters and input data to be refined in a manner that was consistent with real-world observations, thereby enhancing the overall performance of the model. Subsequently, the models underwent a validation process utilizing independent datasets to ascertain their precision and dependability in anticipating diverse scenarios. Model performance was modified through a comparison of the model outcomes with the observed data, identifying and rectifying discrepancies.

The components of the water balance, outlined in **Table 4**, facilitated a more comprehensive understanding of the hydrological dynamics within the catchment, encompassing runoff, evapotranspiration, precipitation and groundwater recharge. The calibration and validation phases generated coherent outcomes, thereby confirming the reliability of the models in simulating hydrological processes.

Table 4. Assessment of hydrological parameters.

Hydrological Components	Calibration Average (mm)	%	Validation Average (mm)	%
Precipitation	267.2	100	267.2	100
Surface flow	1.30	0.48	1.56	0.58
Lateral flow	15.45	5.78	12.8	4.79
Return flow	0.2	0.07	0.01	0.003
Recharging deep aquifers	0.89	0.33	0.76	0.28
Shallow aquifer storage	14.6	5.46	12.2	4.55
Evapotranspiration	234.66	87.88	239.92	89.79

These consistent results have served to reinforce the ability of the models to accurately represent the hydrological processes occurring within the catchment area, a fact that had previously been demonstrated by research [31]. This research emphasized the significance of calibrated and validated models for the assurance of reliable hydrological assessments. The average amount of rain that falls in Oued Cherraa catchment area is 267 mm (see **Figure 6A**). About 89% of this, or 239 mm, is lost through evaporation and transpiration. This shows just how important this is for the water balance. **Figure 6B** shows that there's more evaporation and plant transpiration in farmland than in forests. This is probably because of the weather, like temperature and humidity, as shown in **Figure 6**. As you can see in **Figure 6C**, runoff accounts for just 6% (15 mm) of annual rainfall. Surface runoff and base runoff are relatively minor compared to evapotranspiration. The study also showed that shallow aquifers get a higher proportion of rainfall (12.2 mm, 4.55%) than deep aquifers (0.76 mm, 0.28%). **Figure 6D** illustrates that groundwater levels in irrigated areas exhibit a decrease of less than 60 mm, whereas mountainous regions demonstrate an increase of over 80 mm. This phenomenon is shaped by irrigation practices and the distinctive characteristics of the soil. These findings highlight the necessity for close monitoring of groundwater levels to ensure the sustainable management of water resources and the prevention of over-exploitation of aquifers.

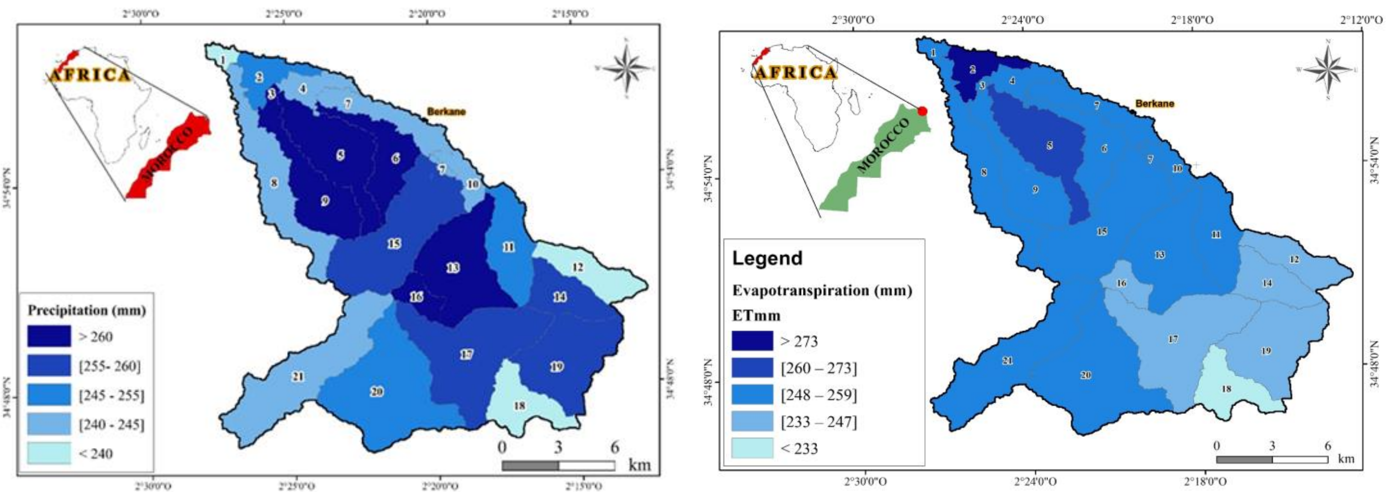

(A) **(B)**

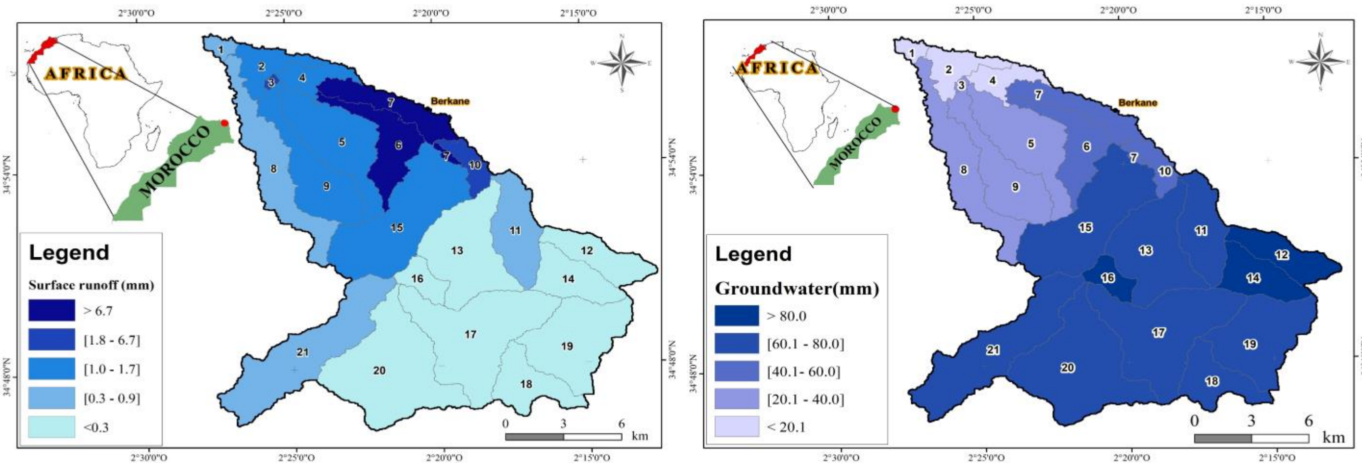

(C) **(D)**

Figure 6. Spatial variation of water balance components: **(A)** Precipitation; **(B)** Evapotranspiration; **(C)** Surface runoff; **(D)** Water table.

3.4. Available water

The study shows that around 89% of the water in Oued Cherraa catchment is lost through evaporation and transpiration. The rest is shared between the percolation reservoir (made up of the shallow aquifer, deep aquifer and unsaturated zone) and the runoff components (surface runoff, lateral runoff and return flow). Surface runoff accounts for only 5% of total runoff (see **Table 4**). The rainy season peaks in January, February, March, April, November and December, causing soil saturation and potential flooding, particularly in sub-catchment 7 (**Figure 6C**). Reservoirs rely heavily on runoff for water storage during the dry season, and during periods of low rainfall farmers often rely on stored soil moisture for irrigation, which can adversely affect late crops. Infiltration data indicates that 5.61% of annual rainfall (**Figure 7**) contributes to the percolation reservoir, with minimal loss in the form of return flow. The recharge rate of the deep aquifer is approximately 0.3%, while the shallow aquifer retains the majority of the water.

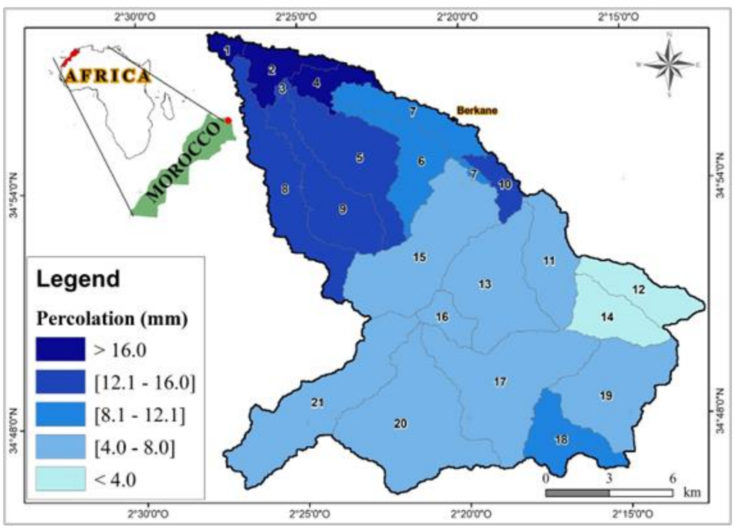

Figure 7. Distribution of infiltration within the Oued Cherraa watershed.

The watershed can store enough water in shallow aquifers to support irrigation during the dry season. Looking at the seasonal changes in the hydrological components (**Figure 8**), we can see that evapotranspiration goes up during dry periods and that there's a moderate water reserve in the catchment. This means there's potential for soil water storage in deep aquifers.

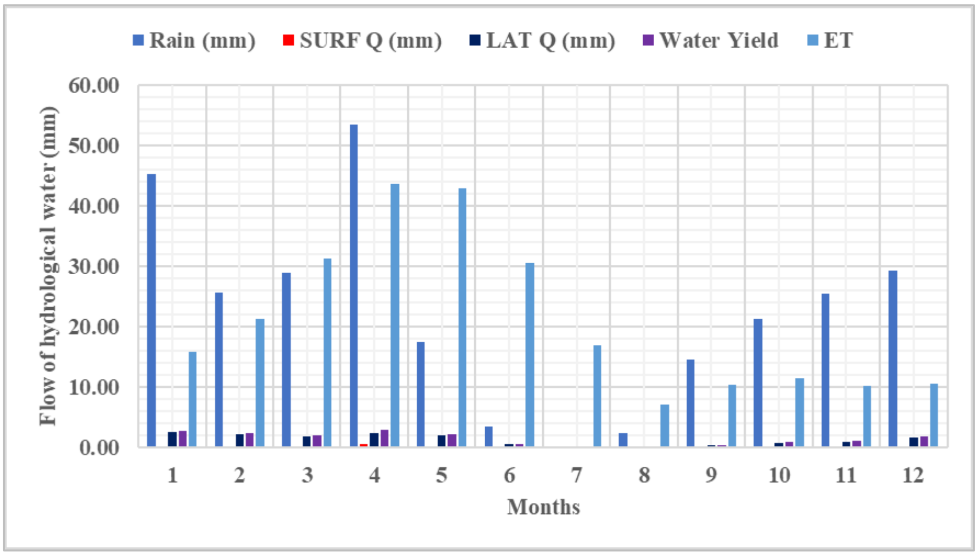

Figure 8. Seasonal fluctuations in the hydrological components of the Oued Cherraa catchment (SURF Q denotes surface runoff, WYLD represents water yield, ET refers to evapotranspiration, and rain signifies mean annual precipitation).

3.5. Discussion

The SWAT (Soil and Water Assessment Tool) model has proven to be an invaluable resource in Morocco, facilitating the assessment of the water balance and supporting the sustainable management of water resources. Prior research has demonstrated that evapotranspiration represents a significant component of the water balance in numerous Moroccan catchments. The estimated evapotranspiration rate for the R'dom catchment is approximately 72%, as reported by Alitane et al. [32]. By contrast, the M'dez catchment exhibits a higher evapotranspiration rate of 79.9%, as documented by Boufala et al. [33]. The results for Oued Cherraa catchment are in line with the aforementioned conclusions. It should be noted that the majority of precipitation is lost through evaporation and transpiration, representing approximately 89% of the total. It is essential to consider this factor when calculating regional water balances. It is essential that we prioritize the reduction of these losses in our water management strategies, particularly in arid and semi-arid zones.

Surface runoff in Morocco's watersheds has been shown to vary; for example, in the R'dom watershed, it accounts for 12.04% of the water balance [32], while in the M'dez watershed, it amounts to 13.83 mm [33]. Our study revealed that surface runoff in Oued Cherraa basin accounted for only 6% of annual rainfall, which is less than what we observed in other regions. This difference could be due to the different types of land, topography and soil that influence the amount of runoff generated. The limited runoff in our results suggests that the catchment relies more on groundwater recharge and evapotranspiration for its water budget, which has a big impact on how we manage water resources, especially during dry periods.

Groundwater recharge, an essential aspect of hydrological studies, was found to contribute minimally to the water balance in other Moroccan basins, such as 4.14% in R'dom [32] and 8% in the Ouergha basin [34]. The way in which we utilize the land and the impact of climate change on water movement are of great consequence. In the Oued Fez basin, there has been a notable increase in the amount of land dedicated to urban expansion and irrigation, which has resulted in a 55% surge in surface runoff and a 7.4% uptick in evapotranspiration [35]. While our study didn't look at the impact of land use changes, the results for Oued Cherraa catchment seem to indicate that the region might have similar issues. With all this variability in evapotranspiration and reduced runoff, it's clear we need integrated water management strategies to account for land use and climate conditions. These will help us to manage water stress and make sure we have enough water in the long term.

In summary, the comparison of our results with previous studies highlights both consistencies and unique features of Oued Cherraa catchment. Evapotranspiration plays a big part in the water balance, as we've seen in other parts of Morocco [32,33]. However, our study shows that surface runoff and groundwater recharge play a smaller role than we expected. This shows how important it is to have management strategies tailored to the particular hydrological features of the catchment area [13,34]. What's more, while our study didn't focus on land use and climate change, the data suggest we should consider these factors when planning water supplies in the region [35].

4. Conclusion

This study highlights the value of a comprehensive and context-specific approach to hydrological modelling and water resource management in Oued Cherraa catchment. A comprehensive sensitivity analysis allowed us to identify key parameters that significantly influence the simulation of flow dynamics. In particular, the deep aquifer percolation fraction (RCHRG DP) was demonstrated to be a crucial factor for this basin. This parameter represents the portion of water that percolates from the surface to the deep aquifer, significantly influencing the basin's groundwater recharge rates. It is clear that variations in the RCHRG DP directly affect the replenishment of deep groundwater reserves. These are essential for maintaining baseflow during dry periods. We must therefore accurately estimate them to understand subsurface water movement and ensure the reliability of hydrological models in predicting water availability over time. The calibration and validation phases showed that the SWAT model is an accurate tool for replicating observed hydrological patterns, with satisfactory performance metrics, including Nash-Sutcliffe efficiencies of 0.58 and 0.60 for calibration and validation, respectively.

The results show that evapotranspiration is the main factor, accounting for 89% of annual rainfall. This is in line with what we've seen in other Moroccan basins. By comparison, there's not much surface runoff or groundwater recharge, which is in line with the unique hydrological characteristics of Oued Cherraa basin. This points to the significance of tailored water management strategies that prioritize sustainable practices, especially considering the area's reliance on groundwater storage, which supports irrigation during dry periods.

The study also demonstrates the critical need for ongoing monitoring and strategic water management in light of potential challenges posed by land use changes and climate variability. Although this research didn't look at these factors directly, the insights gained show that we need to manage water more holistically, taking into account how land use, climate and hydrological responses affect each other. This is going to be really important for making sure there's enough water and that resources are used sustainably in arid and semi-arid areas like Oued Cherraa.

Author contributions: Conceptualization, investigation, methodology, software, validation, formal analysis, resources and writing-original draft preparation, ML, AM and ZEA; writing-review and editing, ML, AA, WS, MS and SE; supervision, AM. All authors have read and agreed to the published version of the manuscript.

Conflict of interest: The authors declare no conflict of interest.

References

1. Singh A. Conjunctive use of water resources for sustainable irrigated agriculture. Journal of Hydrology. 2014; 519: 1688-1697. doi: 10.1016/j.jhydrol.2014.09.049
2. Dovie DBK, Kasei RA. Hydro-climatic stress, shallow groundwater wells and coping in Ghana's White Volta basin. Science of The Total Environment. 2018; 636: 1268-1278. doi: 10.1016/j.scitotenv.2018.04.416
3. Prabhanjan A, Rao EP, Eldho TI. Application of SWAT Model and Geospatial Techniques for Sediment-Yield Modeling in Ungauged Watersheds. Journal of Hydrologic Engineering. 2015.
4. Samimi M, Mirchi A, Moriasi D, et al. Modeling arid/semi-arid irrigated agricultural watersheds with SWAT: Applications, challenges, and solution strategies. Journal of Hydrology. 2020; 590: 125418. doi: 10.1016/j.jhydrol.2020.125418
5. Ross A. Speeding the transition towards integrated groundwater and surface water management in Australia. Journal of Hydrology. 2018; 567: e1-e10. doi: 10.1016/j.jhydrol.2017.01.037
6. Du E, Tian Y, Cai X, et al. Evaluating Distributed Policies for Conjunctive Surface Water-Groundwater Management in Large River Basins: Water Uses Versus Hydrological Impacts. Water Resources Research. 2022; 58(1). doi: 10.1029/2021wr031352
7. Ridoutt BG, Eady SJ, Sellahewa J, et al. Water footprinting at the product brand level: case study and future challenges. Journal of Cleaner Production. 2009; 17(13): 1228-1235. doi: 10.1016/j.jclepro.2009.03.002
8. Vairavamoorthy K, Gorantiwar SD, Pathirana A. Managing urban water supplies in developing countries—Climate change and water scarcity scenarios. Physics and Chemistry of the Earth, Parts A/B/C. 2008; 33(5): 330-339. doi: 10.1016/j.pce.2008.02.008
9. Sabale R, Venkatesh B, Jose M. Sustainable water resource management through conjunctive use of groundwater and surface water: a review. Innovative Infrastructure Solutions. 2022; 8(1). doi: 10.1007/s41062-022-00992-9
10. Abdalla OAE. Groundwater modeling in semiarid Central Sudan: adequacy and long-term abstraction. Arabian Journal of Geosciences. 2009; 2(4): 321-335. doi: 10.1007/s12517-009-0042-4
11. Baalousha HM. Development of a groundwater flow model for the highly parameterized Qatar aquifers. Modeling Earth Systems and Environment. 2016; 2(2). doi: 10.1007/s40808-016-0124-8
12. Kaleris V, Langousis A. Comparison of two rainfall–runoff models: effects of conceptualization on water budget components. Hydrological Sciences Journal. 2016; 62(5): 729-748. doi: 10.1080/02626667.2016.1250899
13. Sabale RS, Bobade SS, Venkatesh B, et al. Application of Arc-SWAT Model for Water Budgeting and Water Resource Planning at the Yeralwadi Catchment of Khatav, India. Nature Environment and Pollution Technology; 2024.
14. Oki T, Agata Y, Kanae S, et al. Global assessment of current water resources using total runoff integrating pathways. Hydrological Sciences Journal. 2001; 46(6): 983-995. doi: 10.1080/02626660109492890

15. Neitsch SL, Arnold J, Kiniry J, et al. Soil & Water Assessment Tool Theoretical Documentation Version 2009. Texas Water Resour; 2009.
16. Liu L, Cui Y, Luo Y. Integrated Modeling of Conjunctive Water Use in a Canal-Well Irrigation District in the Lower Yellow River Basin, China. Journal of Irrigation and Drainage Engineering. 2013.
17. Carlier P. Triffa Plain: Water Resources of Morocco: 1. Domains of the Rif and Eastern Morocco, Notes&Mém (French). Serv. Géol; 1971.
18. Laouina, A. Le Maroc nord-oriental: reliefs, modelés et dynamique du calcaire. [Master's thesis]. Univ. Paris I, Paris; 1990.
19. Laaboudi M, Mezrhab A, Alioua ZE, et al. Analyzing Water Availability Via the SWAT Hydrological Model in Oued Cherraa Basin (Northeastern Morocco). Water Conservation Science and Engineering. 2024; 9(2). doi: 10.1007/s41101-024-00290-8
20. Farr TG, Rosen PA, Caro E, et al. The Shuttle Radar Topography Mission. Reviews of Geophysics. 2007; 45(2). doi: 10.1029/2005rg000183
21. Rafik A, Ait Brahim Y, Amazirh A, et al. Groundwater level forecasting in a data-scarce region through remote sensing data downscaling, hydrological modeling, and machine learning: A case study from Morocco. Journal of Hydrology: Regional Studies. 2023; 50: 101569. doi: 10.1016/j.ejrh.2023.101569
22. Sharpley AN, Williams JR. EPIC, erosion/productivity impact calculator. Tech. Bull; 1990.
23. Arnold JG, Srinivasan R, Muttiah RS, et al. Large Area Hydrologic Modeling and Assessment Part I: Model Development1. Jawra Journal of the American Water Resources Association. 1998; 34(1): 73-89. doi: 10.1111/j.1752-1688.1998.tb05961.x
24. Kim NW, Chung IM, Won YS, et al. Development and application of the integrated SWAT–MODFLOW model. Journal of Hydrology. 2008; 356(1-2): 1-16. doi: 10.1016/j.jhydrol.2008.02.024
25. Eini MR, Massari C, Piniewski M. Satellite-based soil moisture enhances the reliability of agro-hydrological modeling in large transboundary river basins. Science of The Total Environment. 2023; 873: 162396. doi: 10.1016/j.scitotenv.2023.162396
26. Gupta HV, Sorooshian S, Yapo PO. Status of Automatic Calibration for Hydrologic Models: Comparison with Multilevel Expert Calibration. Journal of Hydrologic Engineering. 1999.
27. Beven K. A manifesto for the equifinality thesis. Journal of Hydrology. 2006; 320(1-2): 18-36. doi: 10.1016/j.jhydrol.2005.07.007
28. Nash JE, Sutcliffe JV. River flow forecasting through conceptual models part I—A discussion of principles. Journal of Hydrology. 1970.
29. Santhi C, Arnold JG, Williams JR, et al. Validation of The Swat Model On A Large Rwer Basin With Point And Nonpoint Sources1. Jawra Journal of the American Water Resources Association. 2001; 37(5): 1169-1188. doi: 10.1111/j.1752-1688.2001.tb03630.x
30. Moriasi DN, Arnold JG, Van Liew MW, et al. Model Evaluation Guidelines for Systematic Quantification of Accuracy in Watershed Simulations. Transactions of the ASABE. 2007; 50(3): 885-900. doi: 10.13031/2013.23153
31. Obuobie E. Estimation of groundwater recharge in the context of future climate change in the White Volta River Basin, West Africa. Available online: https://bonndoc.ulb.uni-bonn.de/xmlui/handle/20.500.11811/3712 (accessed on 7 November 2024).
32. Alitane A, Essahlaoui A, Van Griensven A, et al. Towards a Decision-Making Approach of Sustainable Water Resources Management Based on Hydrological Modeling: A Case Study in Central Morocco. Sustainability. 2022; 14(17): 10848. doi: 10.3390/su141710848
33. Boufala M, El Hmaidi A, Essahlaoui A, et al. Assessment of the best management practices under a semi-arid basin using SWAT model (case of M'dez watershed, Morocco). Modeling Earth Systems and Environment. 2021; 8(1): 713-731. doi: 10.1007/s40808-021-01123-6
34. Lamia E, Soufiane T, Souad H, et al. Semi-Distributed Modeling of a Large Scale Hydrological System Using SWAT Model. In: Proceedings of the 2020 IEEE 2nd International Conference on Electronics, Control, Optimization and Computer Science (ICECOCS); 2020.
35. EL Garouani A, Nabunya V. Analysis of Climate Trend and Effect of Land Cover Change on Streamflow in Oued Fez Basin, Morocco. SSRN; 2023.

Journal of Geography and Cartography 2025, 8(1), 10320.
https://doi.org/10.24294/jgc10320

Article

Geoelectric, geomagnetic and vertical gradient investigation on Knossos area, Crete Island for detection of archaeological settlements

Panos Stephanopoulos*, **Stavros Papamarinopoulos**

Laboratory of Geophysics, Sector of Applied Geology & Geophysics, Department of Geology, School of Natural Sciences, University of Patras, 26504 Patras, Greece

*** Corresponding author:** Panos Stephanopoulos, stefanop@upatras.gr

CITATION

Stephanopoulos P, Papamarinopoulos S. Geoelectric, geomagnetic and vertical gradient investigation on Knossos area, Crete Island for detection of archaeological settlements. Journal of Geography and Cartography. 2025; 8(1): 10320. https://doi.org/10.24294/jgc10320

ARTICLE INFO

Received: 13 November 2024
Accepted: 24 December 2024
Available online: 9 January 2025

Abstract: A Detailed geophysical investigation was conducted on Knossos territory of Crete Island. Main scope was the detection of underground archaeological settlements. Geophysical prospecting applied by an experienced geophysical team. According to area dimensions in relation to geological and structural conditions, the team designed specific geophysical techniques, by adopted non-catastrophic methods. Three different types of geophysical techniques performed gradually. Geophysical investigation consisted of the application of geoelectric mapping and geomagnetic prospecting. Electric mapping focusses on recording soil resistance distribution. Geomagnetic survey was performed by using two different types of magnetometers. Firstly, recorded distribution of geomagnetic intensity and secondly alteration of vertical gradient. Measured stations laid along the south-north axis with intervals equal to one meter. Both magnetometers were adjusted on a quiet magnetic station. Values were stored in files readable by geophysical interpretation software in XYZ format. Oasis Montaj was adopted for interpretation of measured physical properties distribution. Interpretation results were illustrated as color scale maps. Further processing applied on magnetic measurements. Results are confirmed by overlaying results from three different techniques. Geoelectric mapping contributed to detection of a few archaeological targets. Most of them were recorded by geomagnetic technique. Total intensity aimed to report the existence of magnetized bodies. Vertical gradient detected subsurface targets with clearly geometrical characteristics.

Keywords: geophysical investigation; geomagnetic intensity; soil resistance; vertical gradient

1. Introduction

Knossos territory belongs in the subarea of Crete Island. Located in Central South Crete, specifically south of Heraklion town (**Figure 1**). In ancient times Knossos had been involved in the Minoan empire. It was acting as the main capital wherein located Minoan palace. During 1991 the University of Cambridge requested contribution in geophysical investigation on Knossos area. Request accepted by Lab of Geophysics, University of Patras and a specialized team begun journey for Crete Island. The geophysical team examined territory specifications and applied electric and magnetic non-destructive techniques [1–11]. Electric prospecting focuses on soil resistance distribution. As electrometer was chosen the Geoscan RM4. Main scope was alteration of soil resistance on specific depth by adopting twin-probe technique. Alternatively magnetic prospecting applied by two different types of magnetometers proton and fluxgate. Two of the same kind proton magnetometers are utilized for total intensity recording. One was acting as base by measuring drift values every ten seconds. The second unit record geomagnetic field value along the south-north axis. The vertical gradient of magnetic field is recorded by using fluxgate magnetometer such as

Geoscan FM36. Bothof magnetometers were adjusted on a magnetic quiet point. Also, fluxgate microcomputer was updated with geophysical grid dimensions. The survey was performed by measuring discreet points stations on profiles along the south-north axis. Discreet data stations and profiles were measured at one meter interval. By adopted Oasis Montaj executive geophysical software, distribution of measured physical properties was presented as color maps with represented color scale bar.

Figure 1. Map of Crete.

Geological and structural setting

Crete geology consisted of Neogene and Upper Miocene structures. Specifically, there were two geological formations named Finikia and Ag. Varvara. The first formation consisted of white homogenous marls, clays structure with gray color and brown thin-bedded intercalations. Base of formation consisted in general from unsorted agglomerate with influence by white homogeneous marls, limestones and marls, greenish clays and prenoegene rocks. Finikia formation overlays incompatible on Ag. Varvara formation.

The Second formation consisted mostly of bioclastic and reef limestones, which locally could be conglomerate or agglomerate. Laterally seemed to be passed into alternating foliated homogenous calcium marls or even limestones. Occasionally were found with local unconformity with underlying formation [12,13]. In **Figure 2** illustrated geological map of Crete, indicating Knossos area.

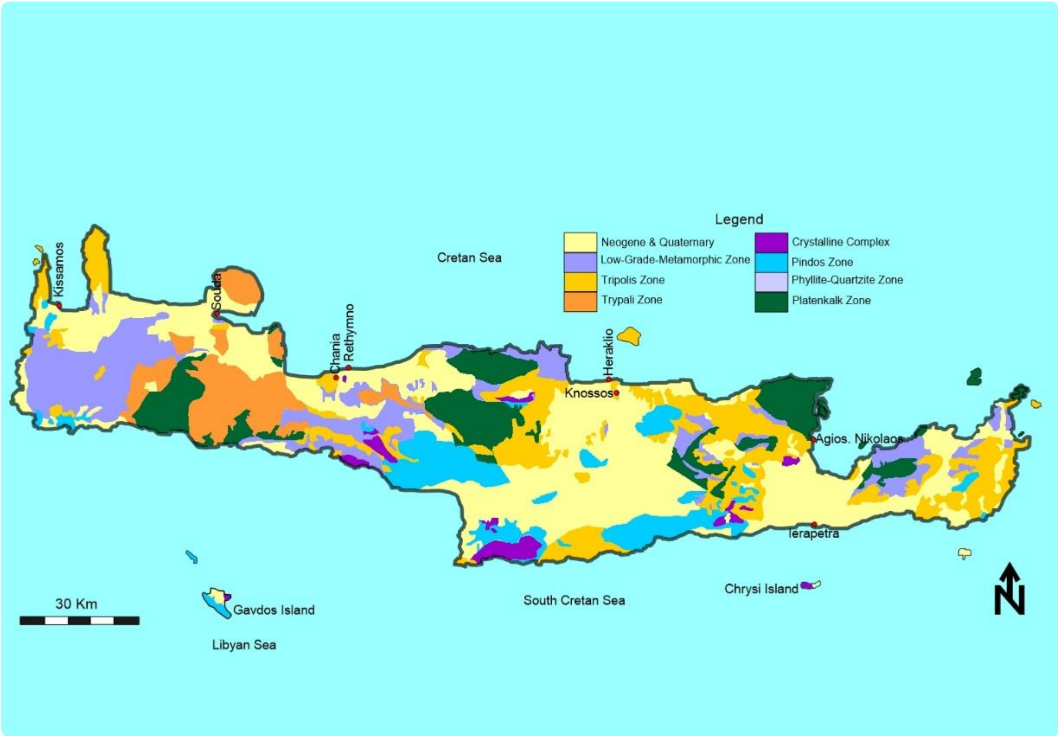

Figure 2. Geological map of Crete.

2. The used geophysical techniques and their limits

Knossos field topography characterized as level ground with very few points of discriminations. As main scope of the project was the detection of possible underground archaeological settlements in a depth equal to 1.5 to 2 meters. According to that, geophysical survey was adjusted and performed in a non-destructive way. As main techniques were chosen electric and magnetic prospecting in relation to existing geological formations. Survey field had been divorced in square geophysical grids with acme equal to 20 meters (**Figure 3**) [14–18]. Borders of grids were represented by adopting red wooden marks (no magnetic material). Each of them had been addressed by using unique name consisted by name of area, type of measurements, year. By adopting an electrometer as Geoscan RM4 (**Figure 4**), distribution of soil resistance recorded on specific depth along horizontal layer. During measurements two pairs of electrodes were involved. One of them was acting as base, while the other pair measured discreet points stations along the south-north axis with interval equal to one meter. Both electrode's pairs consisted of a potential and current electrode. The electrode pair distance was set equal to 0.75 meters. The unmovable pair was located away from mobile at a distance at least equal to fifteen times internal distance (pair distance). The above technique was known as twin-probe (**Figure 5**), ideal for mapping purposes [19,20], devoid by topographical alterations. Each measured point of soil resistance was stored on data logger or alternative on paper grid schedule. Before the main survey, location of electrodes was tested in case of artifact noise. By adopted shifted mode, electrodes were acting as mobile and base. Two different values of soil resistance were recorded. The difference between the two mentioned values should be equal to one ohm. In that case measurements accepted; alternatively highest difference values were rejected. In case of rejection another base point was examined through the same procedure. The penetration depth of twin-probe arrangement was equal to three times the pair distance. Magnetic prospecting utilized by proton [21] and differential magnetometers. That technique corresponded to a very rapid method [8,22–25] which could be disturbed by susceptibility variations [3,10,26–28] from subsurface archaeological targets, according to sensor sensitivity. Two such kind of instruments (proton magnetometers) type Elsec 820 (**Figure 6**), were involved during geomagnetic investigation. One of them was located outside the main line of geophysical grids on a quiet magnetic point, acting as base station [29–32]. During magnetic survey, the base recorded drift intensity by interval of ten seconds. The second unit recorded magnetic intensity variations inside grids profiles along the south-north axis with one meter interval. Before the main survey procedure, proton magnetometers were adjusted to a quiet magnetic point [33,34]. The quiet magnetic point was checked by measuring discreet values of magnetic intensity by rotating proton magnetometer sensor with interval of 90 degrees. If the difference of values were less or equal than 1 nT, then that point was baptized as quite magnetic. Accordingly, the geophysical team was tested for artifact magnetic noise. Profiles on geophysical grids were utilized by using non-magnetic material, such as calibrated rope [29] per one meter. Two of them were laying at the south and north acme of geophysical grid, while third was perpendicular to previous. Both proton magnetometers were adjusted about internal time, value of magnetic field, memory erase [29,32]. Differential magnetometer (Geoscan FM36) (**Figure 7**) was adjusted on same quiet magnetic point along north, south, west, and east axis. Before the main survey procedure, fluxgate magnetometer was updated in relation to geophysical grids dimensions. Measurements were stored into instrument memory. After successful accomplish of field geophysical investigation, measurements were directed to pc through rs232 cable for further processing. Magnetic sources could be recorded up to a depth equal to three-five times the sensor height above surface ground [35].

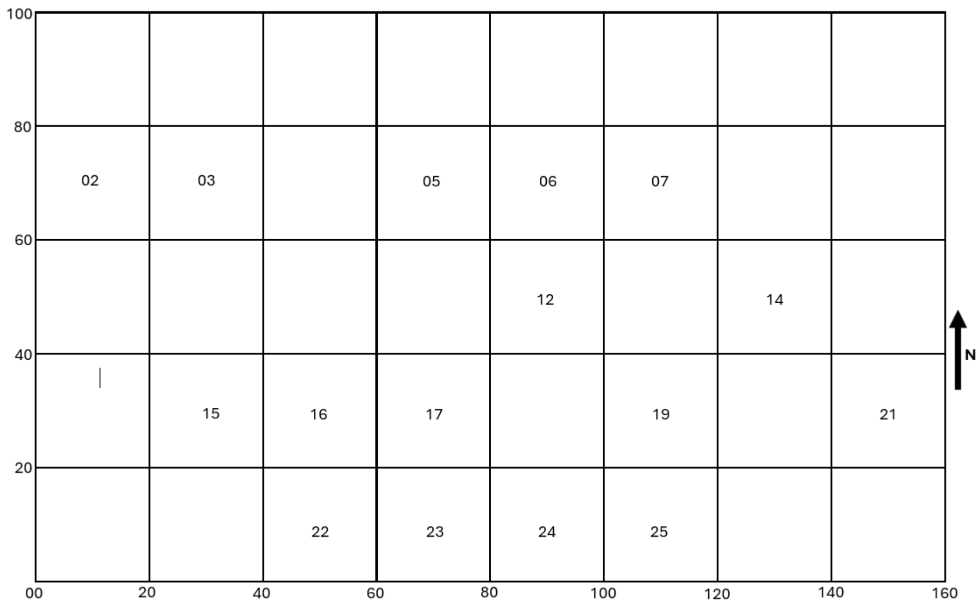

Figure 3. Location of geophysical grids.

Figure 4. Electrometer Geoscan RM4, with electrodes, base cable and frame.

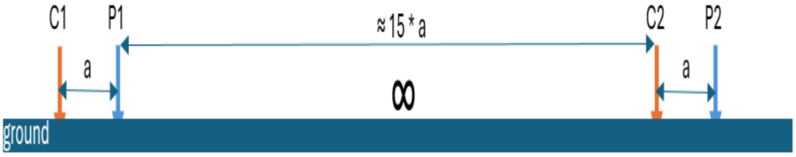

Figure 5. Twin-probe technique.

Figure 6. Proton magnetometer type Elsec 820.

Figure 7. Differential magnetometer Geoscan FM36.

3. Processing of measured values

Distribution of physical property was recorded by adopted specific instruments along vertical or horizontal layer with no-destructive way, where real observation was unavailable. The survey focusses on differences between subsurface structures and surrounding environmental soil [9,16,26,27,36]. Electric mapping measurements were transferred to a pc through special software in relation to rs232 cable. Otherwise, values were typed on surfer worksheets with direction same as during their collection on field. Data were examined for the existence of possible bad points which could be represented as valleys or hills, matter which could easily produce shadow phenomenon. Next, data were dimensioned according to area length. Dimensions were produced through special software [35] or alternatively by using specific surfer subroutines. Values were stored into specific file with unique code name and readable format (XYZ) by interpreted geophysical software.

Magnetic data transferred into pc files through specific software, through rs232 cable. Data from base station (proton magnetometer) and mobile magnetometer stored into specific ascii format file. Geomagnetic data were corrected from daily geomagnetic drift by subtracting mobile values file from responsive base file according recording time [18,36,37]. Before correction procedure, base station measurements were examined comprehensively in case of existing noisy points. In that case noise data were removed or substituted by average of previous and next values. In corrected measurements, basic value of geomagnetic intensity is added. Fluxgate measurements were processed by using the same way as total intensity without drift correction procedure. Accomplishing transfer, values were modified in readable XYZ format file by using specific software. Vertical gradient could provide horizontal position and shape information of subsurface targets [38]. Recorded measurements from three techniques combined by using statistical analysis and reduced to a level by calculating common average value [18].

Final data from both geophysical surveys were fed in specific database of Oasis Montaj software [26,31,32,39] for further interpretation. As result color maps illustrated distribution of physical properties such soil resistance, geomagnetic intensity, and vertical gradient. During color map development measurements interpolated by adopted Akima equation [40] with interval equal to ¼ of initial step during field procedure.

Advanced geophysical interpretation applied on magnetic measurements (Total & Differential). First, performed calculation of Z derivative on total intensity measurements [26,32,39,41]. Secondly, total intensity values redacted to North Magnetic Pole and Equator [7,32,39]. Noisy values were eliminated by performing downward and upward continuation [32]. Amount of apparent magnetic susceptibility calculated on specific depths [26]. As last procedure enforcement three-dimensional Euler Deconvolution [26,42,43]. More details about advanced geophysical interpretation will be reported in the discussion paragraph.

4. Obtained results

Geoelectric mapping with twin-probe array divided the field area into subdomains consisting of low and high interesting structures. Some of them were illustrated with hot colors (orange until red), which represented structures as bad current conductors. These were presented with partially clear geometric characteristics.

Low soil resistance values indices structures existence in greater depth according to prospect of twin-probe array. Reduction of grids to mean average value through statistical analysis in relation with level coordinates, had as result the combination of measured geophysical grids. Geomagnetic technique seemed to be more effective in alterations of measured total intensity alterations along to a horizontal layer. That procedure applied with interval equal to one meter along the south-north axis. After necessity corrections, processing with oasis montaj software located enough geophysical anomalies, which covered most lengthening of total intensity map. Values represented by cold and hot colors. Cold values were indicated sources with low magnetic susceptibility or alternatively sources in greater depth, according to sensor sensitivity. Hot values represented the existence of magnetic source with high susceptibility contrast between structure and surrounding soil [44]. Total intensity distribution reported clear geometric characteristics. Fluxgate application confirmed the existence of magnetic sources with geometric characteristics. Application of mathematical filter on magnetic values through oasis montaj software, reported details which were not founded on normal total intensity map.

5. Discussion of results

Geomagnetic intensity distributed with floating values between 45,108 to 45,799 nT (**Figure 8**). The total intensity map is covered almost by the existence of measurements with clear geometric characteristics in most cases. Indication of lower values (cold colors) represented sources in greater depths or material of low magnetic response. For detailed results total intensity measurements interpreted through special mathematical algorithm for calculation of Z derivative [40] which could easily enhance the shallowest magnetic sources from collected data (**Figure 8**). The calculated Z gradient seemed to be divorced in smaller geophysical anomalies. After derivative procedure there was growth of magnetic dipoles and well-defined geometric characteristics (**Figure 8**). Calculation of X and Y derivatives (**Figure 8**) didn’t plus new details relative to existing magnetic anomalies. Reduction (north magnetic pole, Equator) reported alteration of magnetic dipoles, expansion of geophysical anomalies and confirmation of geophysical anomalies existence respectively (**Figure 8**). Reduction to the north magnetic pole and equator gave the opportunity for illustration of more detailed information. Implementation of shaded relief at total intensity and calculated vertical gradient reported new information in relation to initial map (geometrical characteristics). For eliminating noise total intensity measurements are interpreted by performing upward and downward continuation [40]. **Figure 9** presented results from upward continuation between zero (0) to fifty (50) meters. Upward processing consisted of a clean filter without any artifact result. It was used to remove or minimize effects of shallow sources and noise in geophysical grids, with unrecognized geometrical characteristics. Geophysical anomalies seemed to have expanded. According to color scale bar total intensity was floating between 45,374 to 45,443 nT.

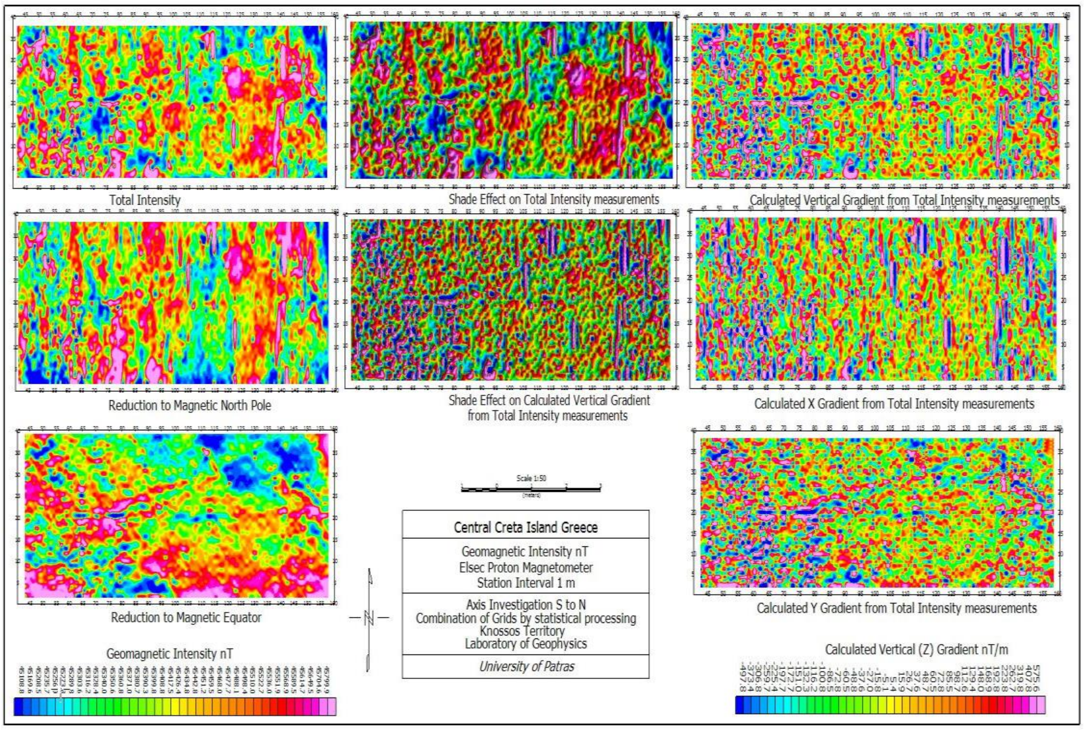

Figure 8. Distribution of total intensity & calculated vertical gradient (normal & shaded relief), reduction to north magnetic pole & equator, calculated verting gradient along X & Y axis.

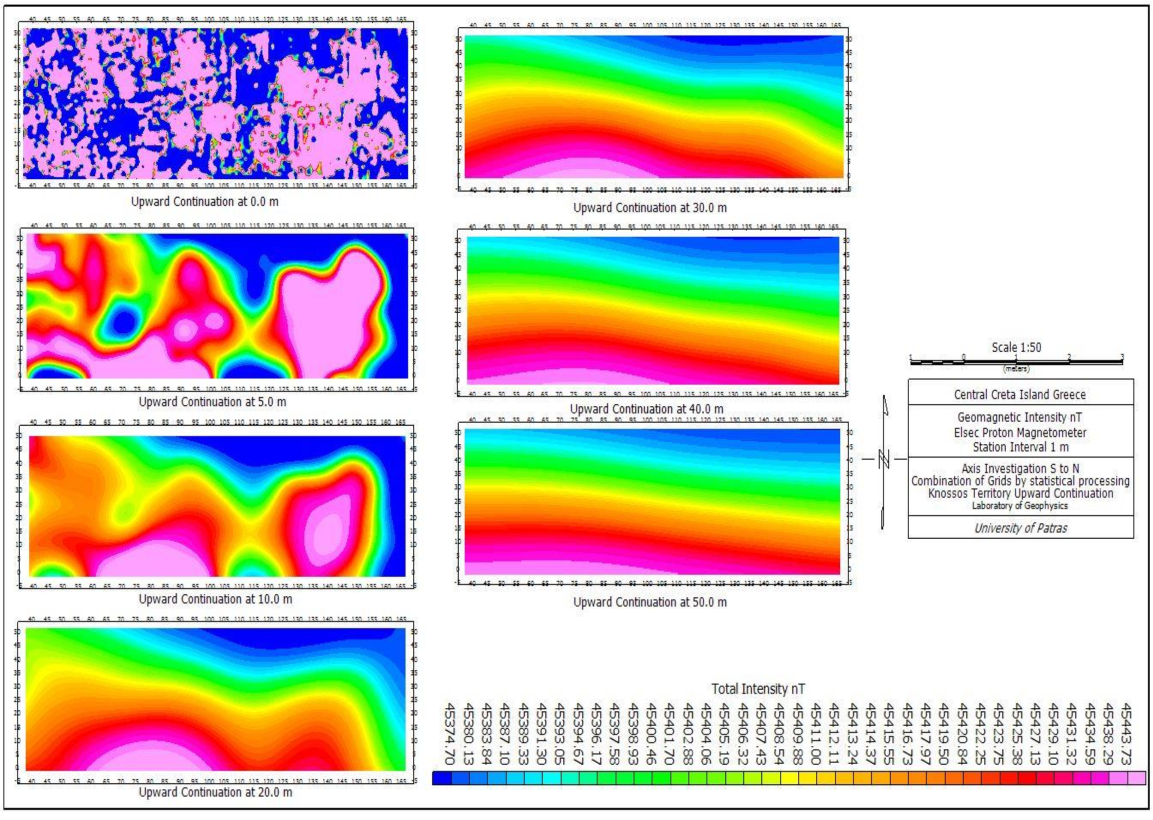

Figure 9. Application of upward continuation on total intensity measurements.

Existence of geometrical characteristics observed on downward continuation (**Figure 10**) after thirty meters depth. Such an application is used to enhance the responses from sources at depth by effectively bringing the plane of measurement closer to the sources. According to the existing color scale bar, total intensity values were distributed between 4.04335e^{21} to 4.04339e^{21} nT. As next step of interpretation is calculation of apparent magnetic susceptibility by using floating depth values [40]. In **Figure 11** illustrated results from distribution of apparent susceptibility. Interpretation of measurements accomplished by combining total magnetic field, reduction to the magnetic pole, inclination, declination and susceptibility depth. A stronger apparent susceptibility was given at depth of 10 m (**Figure 11**). At two first depths (0,5) meters there were low apparent susceptibility targets. Highest values observed after ten meters depth and specific between 20- and 50-meters depth. Increasing apparent susceptibility indicating existence of possible magnetized structure. Euler deconvolution [40] algorithm performed as last total intensity data interpretation procedure (**Figure 12**). According to that equation, magnetic field is related with its gradient components to the location of the source of a geophysical anomaly. Homogeneity Degree expressed as “structural index”. At each solution a prespecified square window in relation to the number of grid cells used during calculations. The window is in the center of each solution. Inversing distance from the center of window becomes one solution in Euler equation. Window dimensions are floating to include many solutions, but not large enough to include adjacent anomalies. The algorithm of Euler deconvolution applied gradually by using floating values of structural index between zero to three with interval equal to one. In **Figure 12** represented results in map schedule from that processing, which accomplished with small deviation error. Solutions presented by tighten cycles. Small diameters corresponded to low depth magnetic sources while, highest diameter represented deepest magnetic sources. By careful observation in **Figure 12** was obvious existence of distinct geometric characteristics at SI equal to 0, 1, 2 and 3. That matter ensured that existing magnetic underground targets corresponding to human remains, while geological evidence was absent.

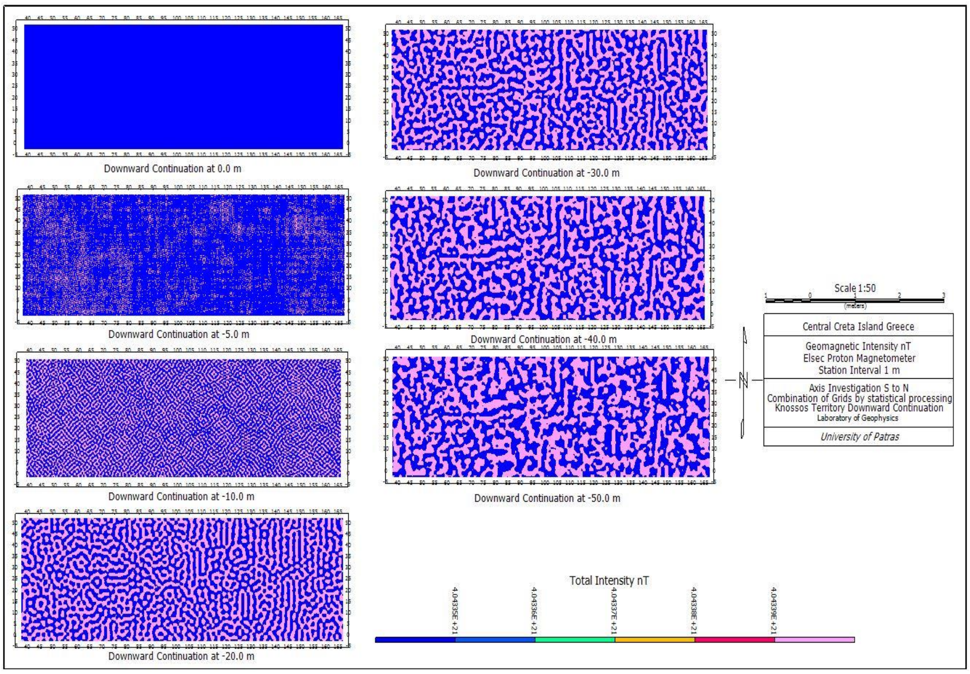

Figure 10. Appearance of downward continuation on total Intensity measurements.

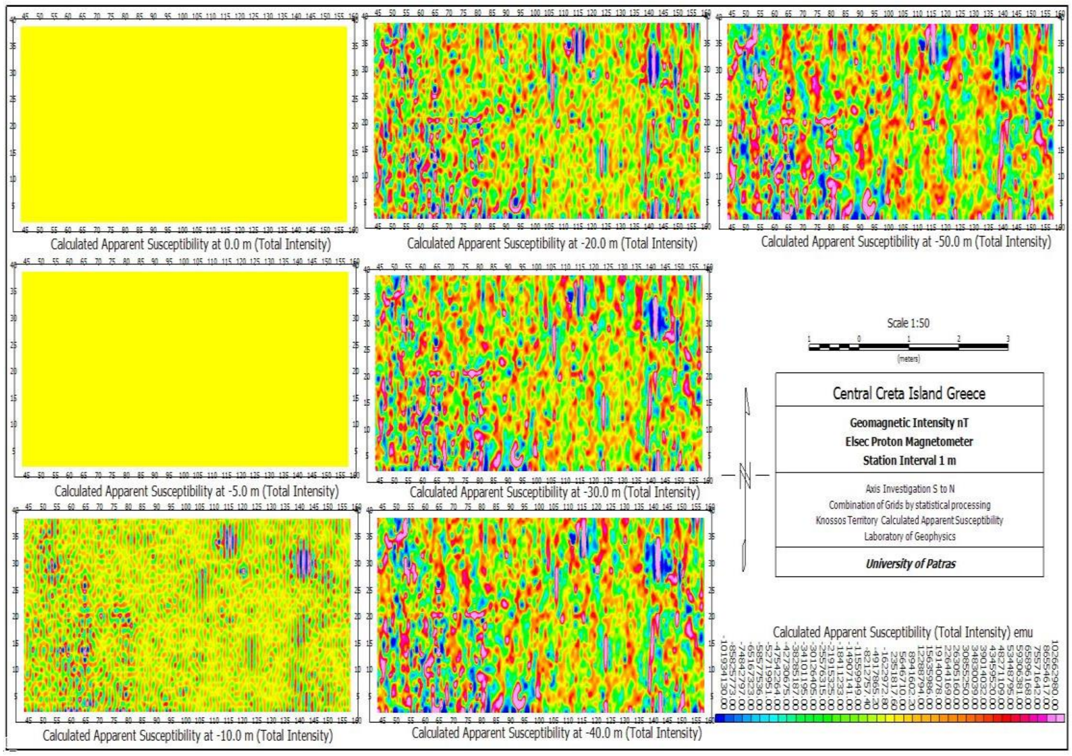

Figure 11. Distribution of apparent susceptibility on total intensity data.

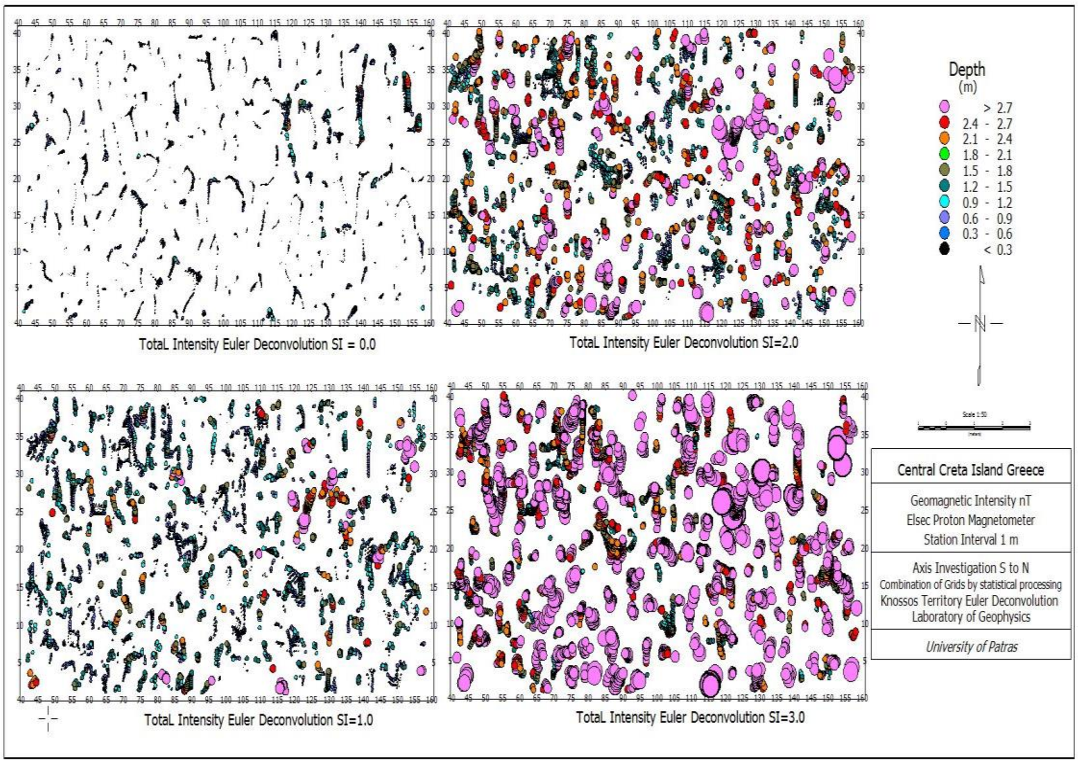

Figure 12. 3D Euler deconvolution on total intensity data.

Measured vertical gradient is illustrated in **Figure 13** with floating values between 44,987 to 45,012 nT/m. A huge number of magnetic dipoles located on vertical gradient allocation. Most of them are distributed on the west side of the map. In the center detected clearly geometrical characteristics which seemed like members of an existing wall. That conclusion can be confirmed by shaded relief interpretation. By applied reduction to north magnetic pole (**Figure 13**) magnetic dipoles and geometric elements were detected more emphasized. Also, some magnetic dipoles were detected on the east side of that map, matter which was absent on initial presentation. Reduction to magnetic equator (**Figure 13**) just confirmed existence of magnetic dipoles on west side, with unrecognized geometrical elements. By applying the gradient calculation along X and Y axis, magnetic dipoles were reported on the east side of gradient map. (**Figure 13**). Existing geometrical characteristics were present with low clarity. Application of reduction to north magnetic pole and equator illustrated existence of many magnetic dipoles with low clarity. In **Figure 14** are presented results from upward continuation. Magnetic anomalies on vertical gradient were clearly detected at one meter continuation. Gradually expansion of vertical gradient was observed from fifth to fifty meters. That matter had as consequence the elimination of vertical gradient geophysical anomalies. Apparent susceptibility interpretation was given in **Figure 15** with floating values. That process performed gradually. Calculation of apparent susceptibility obtained at 5, 10, 20, 30, 40 and 50 m depth. The appearance of magnetic sources was present at 5 meters depth. After 5 meters depth the existence of that parameter increased gradually. Between 30 to 50 meters apparent susceptibility seemed to be with highest values. Between thirty-to-fifty-meter depth, geometrical elements were located like straight walls with evidence of corners. As last technique on vertical gradient data is applied Euler deconvolution (**Figure 16**). Main difference focuses on height value of magnetic sensor from ground surface. In the case of total intensity sensor height was equal to 0.3 m. In the case of vertical gradient, that parameter was increased to 0.5 m. In **Figure 16** presented results are presented from Euler deconvolution equation. Interpretation applied gradually with structural index from zero to three with one interval. Results from that procedure consisted of low deviation error. Magnetic sources were represented by cycles, with floating diameters (same as total processing). Cycles classification was characterized as tight. Observers could easily recognize existing geometrical elements after careful remark more than total intensity. The depth of magnetic sources is related to the increment of structural index value. In **Figure 17** reported soil resistance allocation. Geoelectric mapping technique performed on discreet geophysical grids, which were combined by using statistical analysis and reduction to specific level by using common average value. Soil resistance allocation illustrated by floating values between 27 to 48 ohms. High values extended in the greatest area of map. Alternatively low values located in specific subareas of given map in **Figure 17**. High level values corresponded to soil with low conductivity, represented material as bad current contactor. In opposite direction low values (cold color), corresponded to material with high conductivity, with other words good current contactor. Also, such indices could be mentioned existence of material in greater depth. Geometrical characteristics were clearly detected at most of the highest values of soil resistance. Application of shade relief confirmed the existence of geometrical characteristics, which seemed as linear geophysical anomalies. By applying analytic signal with Fast Fourier Transform soil resistance illustrated clear geometric structure at north side of soil resistance map. Also, at east side confirmed the existence of increased levels of that physical property. In **Figure 18** illustrated a specific interpretation of geophysical grids. By adopted special subroutine of oasis montaj software, developed an overlay of three different maps. Measurements from each technique interpolated by using interval equal to ¼ of station and profile distance during field procedure. As next step firstly reported distribution of vertical gradient. On that overlayed alteration of total intensity and last soil resistance. By careful remark a researcher could easily recognize the existence of geometrical characteristics which indicated linear geophysical anomalies. Also, in the center of the overlayed map becomes clear existence of geophysical anomaly with square structure.

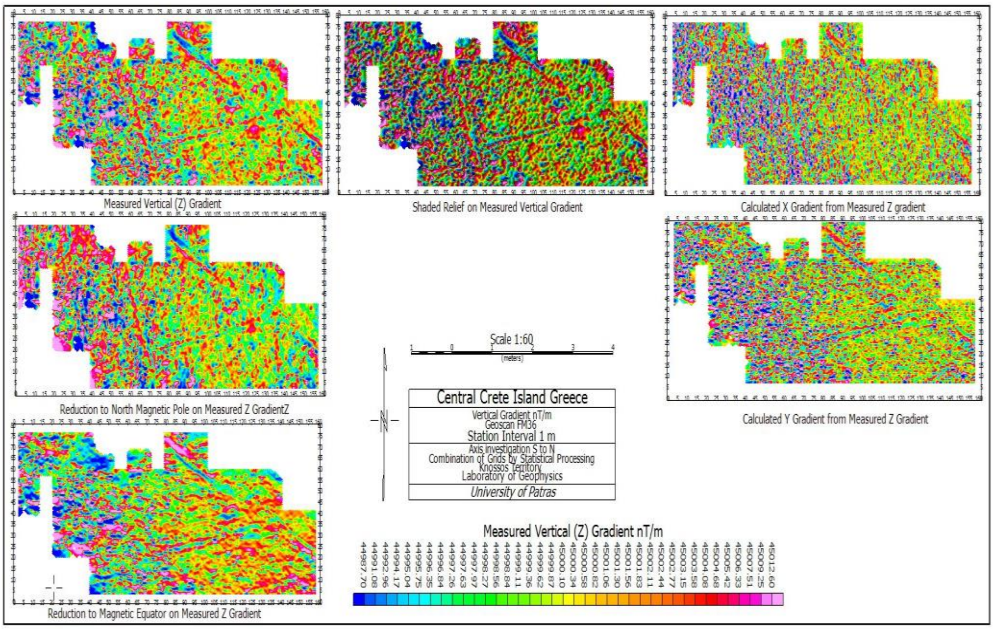

Figure 13. Distribution of measured vertical gradient (normal & shaded relief), reduction to north magnetic pole & equator, calculated verting gradient along X & Y axis.

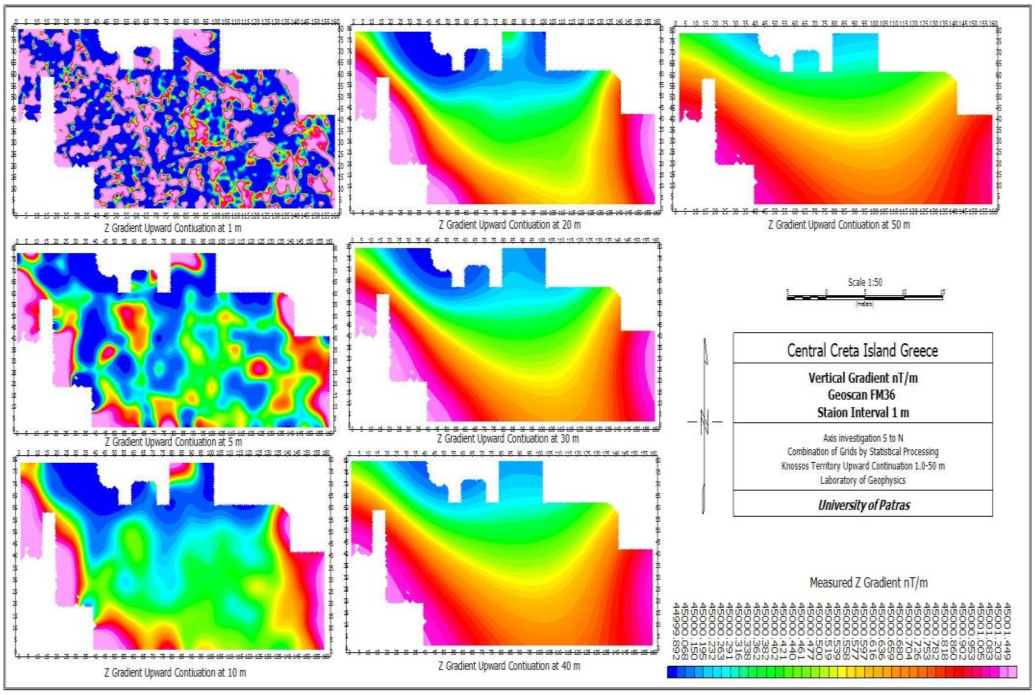

Figure 14. Application of upward continuation filter on measured vertical gradient data.

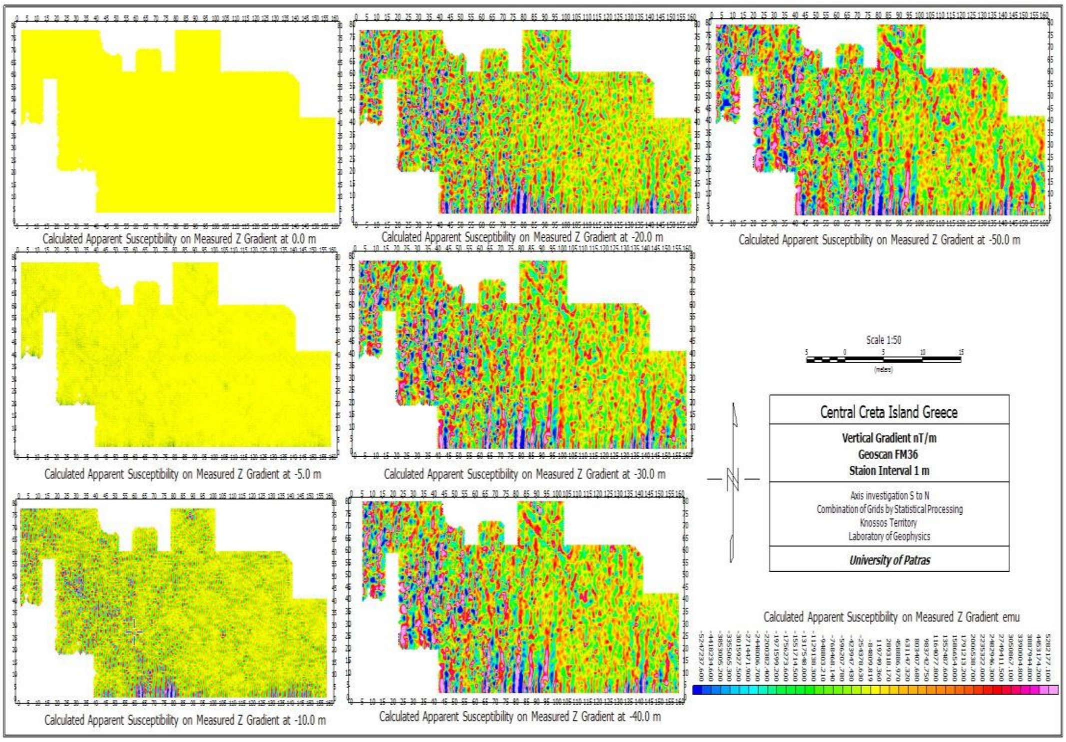

Figure 15. Distribution of apparent susceptibility on measured vertical gradient data.

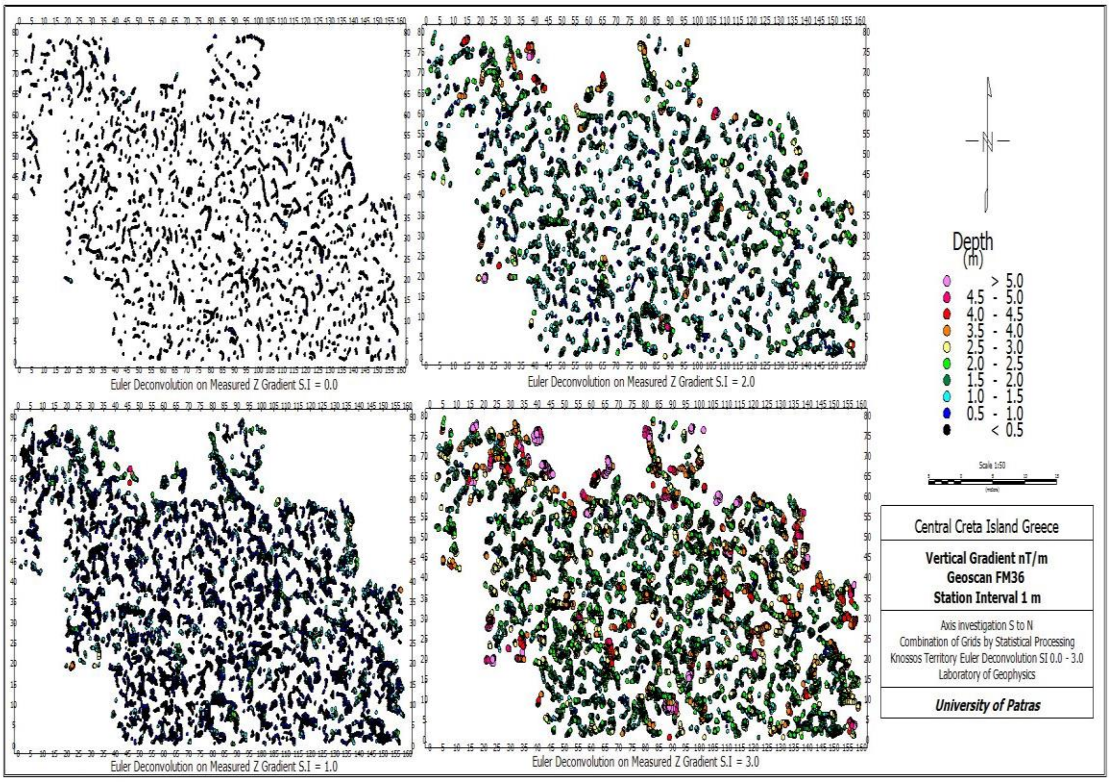

Figure 16. 3D Euler deconvolution on measured vertical gradient data.

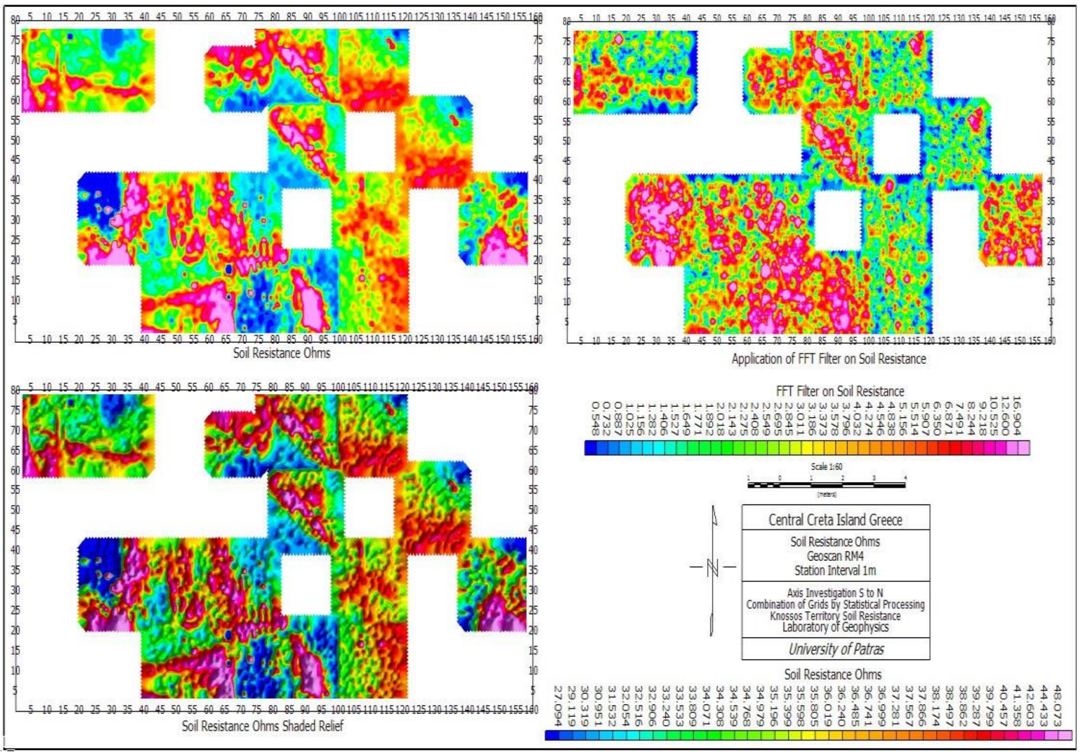

Figure 17. Soil resistance allocation on Knossos area (normal & shaded relief), application of FFT mathematical filter.

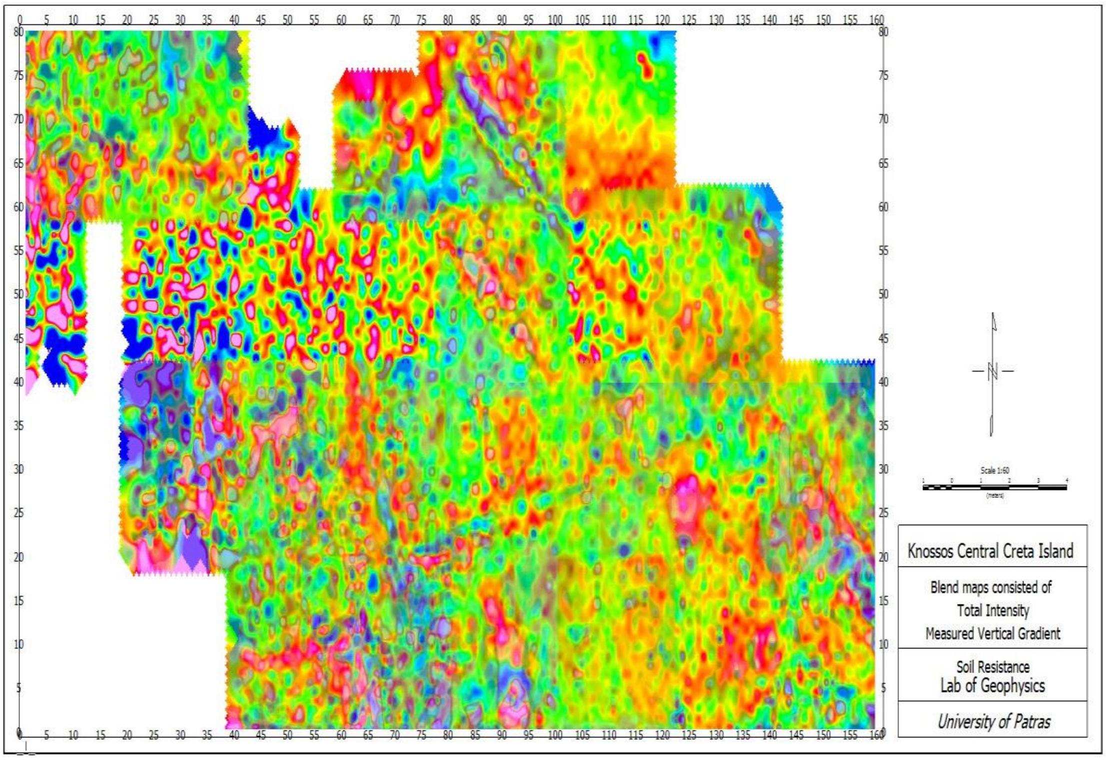

Figure 18. Blend map consisted of total intensity, measured vertical gradient and soil resistance.

6. Conclusion

Non-destructed geophysical techniques applied on Knossos territory for detection of archaeological settlements. Geophysical prospecting was performed by utilized two different families of geophysical investigation. The survey area divided into several geophysical grids, focuses on recording of physical property distribution. Each of them had an acme equal to twenty meters. Combination of electric mapping with total intensity and vertical gradient applied gradually on each geophysical grid. Electric mapping recorded soil resistance allocation at depths of 1.5 to 2 m. The second technique focuses on total intensity recording until a depth 3 to five times the sensor height above ground surface. Third geophysical method applied vertical gradient, a technique with low noise [10,45]. The three above techniques were performed on separated data points along the south-north axis, located in parallel profiles with one meter interval. Measurements were interpreted through Oasis Montaj geophysical software. Recording of total intensity reported existence of magnetized structures. Some of them were reported to have hot colors meaning high susceptibility magnitude. In some areas of total intensity map there was evidence of low clarity geometrical characteristics. There was a great number of existing magnetic dipoles, which reported with combination of low and high values of total intensity. In the center of the total map there was evidence of linear geophysical anomalies. Application of shaded relief on total intensity measurements confirmed the existence of geometrical characteristics. Also, application of redaction to magnetic north pole and equator reported much more details of total intensity which were upsent on initial map. Upward and downward continuation cleared existing noise and illustrated existing evidence of human action at greater depths. Calculated apparent susceptibility certificate the existence of magnetic dipoles and confirmed in evidence of magnetized bodies. Euler deconvolution on total intensity values confirmed the existence of geometrical structures. Vertical gradient confirmed detection of geometrical characteristics from total intensity application. By using shaded relief filter on vertical gradient values, geometrical structures located better. The combination of reduction to north magnetic pole and equator just confirmed existence of human activity. Upward continuation illustrated high clarity linear geophysical anomalies at deeper levels. Calculation of apparent susceptibility on vertical gradient reported huge number of magnetic dipoles, which was detected by apparent susceptibility on total intensity values. Euler deconvolution on vertical gradient has as result the detection of geometrical structures, which was confirmed from total intensity Euler equation. Application of soil resistance divided area of survey in subareas of low and high interest. In some areas there was the existence of geometrical formations. That matter was confirmed by the application of shaded relief on soil resistance measurements. Also, by interpreted soil resistance values through analytical signal (Fast Fourier Transform), evidence of geometrical formations certificated. Overlay of maps from three different techniques confirmed the existence of geometrical characteristics which disentangle from existence of geological formation.

Author contributions: Conceptualization, PS and SP; methodology, PS and SP; software, PS; validation, PS and SP; formal analysis, PS; investigation, PS; resources, PS; data curation, PS; writing—original draft preparation, PS; writing—review and editing, PS and SP; visualization, PS; supervision, PS and SP; project administration, PS and SP; funding acquisition, SP. All authors have read and agreed to the published version of the manuscript.

Acknowledgments: The authors would like to thank Kollin Sell from University of Cambridge for absolute collaboration during geophysical prospecting on Knossos territory. Many thanks to the general secretary of research and development and NATO SfS program for equipment and total support. Also, many thanks to underground students from University of Patras for surveying supporting during field procedure.

Conflict of interest: The authors declare no conflict of interest.

References

1. Alashloo SYM, Saad R, Nawawi MNM, et al. Using Integrated Geophysical Techniques to Prospect an Unexcavated Archaeological Site at Sungai Batu, Kedah, Malaysia. Journal of Applied Sciences. 2011; 11(19): 3389-3396. doi: 10.3923/jas.2011.3389.3396
2. Arciniega-Ceballos A, Hernandez-Quintero E, Cabral-Cano E, et al. Shallow geophysical survey at the archaeological site of San Miguel Tocuila, Basin of Mexico. Journal of Archaeological Science. 2009; 36(6): 1199-1205. doi: 10.1016/j.jas.2009.01.025
3. Cardarelli E, Fischanger F, Piro S. Integrated geophysical survey to detect buried structures for archaeological prospecting. A case-history at Sabine Necropolis (Rome, Italy). Near Surface Geophysics. 2007; 6(1): 15-20. doi: 10.3997/1873-0604.2007027
4. Di Fiore B, Chianese D. Electric and magnetic tomographic approach for the geophysical investigation of an unexplored area in the archaeological site of Pompeii (Southern Italy). Journal of Archaeological Science. 2008; 35(1): 14-25. doi: 10.1016/j.jas.2007.02.020
5. Křivánek R. Application of geophysical methods for monitoring of surface and subsurface changes of origin archaeological terrains &ndahs; case studies of sites in the Czech Republic. The International Archives of the Photogrammetry, Remote Sensing and Spatial Information Sciences. 2015; XL-5/W7: 257-262. doi: 10.5194/isprsarchives-xl-5-w7-257-2015
6. Křivánek R, Tirpák J. Geophysical Survey and Changes in the Use of the Cultural Landscape. Interdisciplinaria Archaeologica Natural Sciences in Archaeology. 2023; XIV(1): 9-29. doi: 10.24916/iansa.2023.1.1
7. Martorana R, Capizzi P, Pisciotta A, et al. An Overview of Geophysical Techniques and Their Potential Suitability for Archaeological Studies. Heritage. 2023; 6(3): 2886-2927. doi: 10.3390/heritage6030154
8. Mateiciucová I, Milo P, Tencer T, et al. Geophysical survey at archaeological sites in northeastern Syria. ArchéoSciences. 2009; 33 (suppl.): 111-113. doi: 10.4000/archeosciences.1385
9. Milo P, Vágner M, Tencer T, et al. Application of Geophysical Methods in Archaeological Survey of Early Medieval Fortifications. Remote Sensing. 2022; 14(10): 2471. doi: 10.3390/rs14102471
10. Note N, Saey T, Gheyle W, et al. Evaluation of fluxgate magnetometry and electromagnetic induction surveys for subsurface characterization of archaeological features in World War 1 battlefields. Geoarchaeology. 2018; 34(2): 136-148. doi: 10.1002/gea.21700
11. Vagnon F, Comina C, Canepa MC, et al. Experiences and preliminary results of geophysical methods on historical statues. IOP Conference Series: Earth and Environmental Science. 2023; 1124(1): 012132. doi: 10.1088/1755-1315/1124/1/012132
12. Heraklion Sheet. Geological Map of Greece. Institute of Geology and Mineral Exploration, IGME; 1996.
13. Martha SO, Dörr W, Gerdes A, et al. The tectonometamorphic and magmatic evolution of the Uppermost Unit in central Crete (Melambes area): constraints on a Late Cretaceous magmatic arc in the Internal Hellenides (Greece). Gondwana Research. 2017; 48: 50-71. doi: 10.1016/j.gr.2017.04.004
14. Butler DK, Llopis JL, Briuer FL. Geophysical and Archaeological Investigations for Location of a Historic Cemetery, Fort Stewart, Georgia. Defense Technical Information Center; 1993. doi: 10.21236/ada267096
15. Papamarinopoulos P, Stefanopoulos P, Papaioannou M. Geopysical investigations in search of ancient Helike and the protection of the archaeological site versus the rapid building expansion. In: Proceedings of the international Symposium on Engineering Geology and the Environment Organized by the Greek National Group Of IAEG/Athens/Greece/23-27; June 1997.

16. Rizzo E, Dubbini R, Capozzoli L, et al. Preliminary geophysical investigation in the archaeological site of Bocca delle Menate (Comacchio, FE). Journal of Physics: Conference Series. 2022; 2204(1): 012107. doi: 10.1088/1742-6596/2204/1/012107
17. Saleh S, Saleh A, El Emam AE, et al. Detection of Archaeological Ruins Using Integrated Geophysical Surveys at the Pyramid of Senusret II, Lahun, Fayoum, Egypt. Pure and Applied Geophysics. 2022; 179(5): 1981-1993. doi: 10.1007/s00024-022-03010-2
18. Savvaidis A, Tsokas G, Tsourlos P, et al. A geophysical survey in the archaeological site of Archontiko, Yannitsa. Bulletin of the Geological Society of Greece. 2001; 34(4): 1379. doi: 10.12681/bgsg.17231
19. Branko M, Jana H, Dimc F. Comparison of different geophysical techniques in relation to archaeological data for settlement reconstruction - the case study of Nauportus. Slovenia; 2007.
20. Ogden J, Keay S, Earl G, et al. Geophysical Prospection at Portus: An Evaluation of an Integrated Approach to the Interpretation of Subsurface Archaeological Features, Computer Applications to Archaeology. Physical Sciences; 2009.
21. Jirků J, Belov T, Bárta J, et al. Geophysically – archaeological survey at the Hradčany square in Prague. EGRSE – Exploration Geophysics, Remote Sensing and Environment. 2018; (XXV/2): 20-26. doi: 10.26345/egrse-020-18-203
22. Bianco C, De Giorgi L, Giannotta MT, et al. The Messapic Site of Muro Leccese: New Results from Integrated Geophysical and Archaeological Surveys. Remote Sensing. 2019; 11(12): 1478. doi: 10.3390/rs11121478
23. Eppelbaum Lev. System of Potential Geophysical Field Application in Archaeological Prospection. In: Switzerland AG, D'Amico S, Venuti V (editors). Handbook of Cultural Heritage Analysis. Springer Nature; 2022.
24. Lowe KM, Fogel AS, Sneddon A. Archaeological geophysical survey of a Prehistoric Bronze Age site in Cyprus (Alambra Mouttes)—applications and limitations. Archaeological and Anthropological Sciences. 2017; 10(8): 1971-1989. doi: 10.1007/s12520-017-0508-3
25. Tonkov N. Complex magnetic and resistivity geophysical survey at the national archaeological reserve "Kabyle". Bulgarian Academy of Sciences; 2017
26. Abudeif AM, Abdel Aal GZ, Ramadan HS, et al. Geophysical Prospecting of the Coptic Monastery of Apa Moses Using GPR and Magnetic Techniques: A Case Study, Abydos, Sohag, Egypt. Sustainability. 2023; 15(14): 11119. doi: 10.3390/su151411119
27. Eppelbauir Lev V. Applicability of geophysical methods for localization of archaeological targets: An introduction. Geoinformatics. 2000; 11(1): 25-34. doi: 10.6010/geoinformatics1990.11.1_25
28. Grassi S, Morreale G, Lanteri R, et al. Integration of Geophysical Survey Data for the Identification of New Archaeological Remains in the Subsoil of the Akrai Greek Site (Sicily, Italy). Heritage. 2023; 6(2): 979-992. doi: 10.3390/heritage6020055
29. Bevan B. A Geophysical Survey at the West House, Richmond National Battlefield. Technical Report; 2002
30. Bevan B. Design of Geophysical Surveys. Technical Report; 2004.
31. Hannian S, Hijab B, Laftah A. Geophysical Investigation of Babylon archeological City, Iraq. Diyala Journal For Pure Science. 2021; 17(3): 1-24. doi: 10.24237/djps.17.03.533c
32. Olorunfemi MO, Ogunfolakan BA, Oni AG. Geophysical and Archaeological Survey in Igbo Oritaa (Iwo), Southwest Nigeria. African Archaeological Review. 2019; 36:535-552. doi: 10.1007/s10437-019-09357-7
33. Eppelbaum LV, Itkis SE, Khesin BE. Detailed magnetic survey unmasks prehistoric archaeological sites in israel. In: Proceedings of the 19th EEGS Symposium on the Application of Geophysics to Engineering and Environmental Problems; April 2006.
34. Scheiblecker M, Mühl S, Faßbinder J. Geophysical survey of single phase archaeological sites: New Global Perspectives on Archaeological Prospection. ResearchGate; 2019.
35. Panos S. Contribution of geophysics in solution of archaeological and environmental problems [PhD thesis]. University of Patras, Greece; 2002.
36. Rizzo E, Dubbini R, Clementi J, et al. Geomagnetic and FDEM Methods in the Roman Archaeological Site of Bocca Delle Menate (Comacchio, Italy). Heritage. 2023; 6(2): 1698-1712. doi: 10.3390/heritage6020090
37. Bárta J, Belov T, Frolík J, et al. Applications of Geophysical Surveys for Archaeological Studies in Urban and Rural Areas in Czech Republic and Armenia. Geosciences. 2020; 10(9): 356. doi: 10.3390/geosciences10090356
38. Shi Z, Tian G, Hobbs RW, et al. Magnetic gradient and ground penetrating radar prospecting of buried earthen archaeological remains at the Qocho City site in Turpan, China. Near Surface Geophysics. 2015; 13(5): 477-485. doi: 10.3997/1873-0604.2015033

39. Augie AI, Salako KA, Rafiu AA, et al. Geophysical Magnetic Data Analyses of the Geological Structures with Mineralization Potentials Over the Southern Part of Kebbi, NW Nigeria. Mining Science. 2022; 29. doi: 10.37190/msc222911
40. Oasis Montaj. Mapping and processing system. Oasis Montaj; 2008.
41. Filzwieser R, Olesen LH, Neubauer W, et al. Large-scale geophysical archaeological prospection pilot study at Viking Age and medieval sites in west Jutland, Denmark. Archaeological Prospection. 2017; 24(4): 373-393. doi: 10.1002/arp.1576
42. Papamarinopoulos StP, Papaioannou MG, Stefanopoulos P, et al. The Geophysical Discovery of a Second World War Battlefield in Central Crete During Construction Activities by a Building Company. Environmental & Engineering Geophysical Society; 1995.
43. Ahmed SB, El Qassas RAY, El Salam HFA. Mapping the possible buried archaeological targets using magnetic and ground penetrating radar data, Fayoum, Egypt. The Egyptian Journal of Remote Sensing and Space Science. 2020; 23(3): 321-332. doi: 10.1016/j.ejrs.2019.07.005
44. Lichtenberger A, Meyer C, Schreiber T, et al. Magnetic Prospection in the Eastern Lower City of Artashat-Artaxata in the Ararat Plain of Armenia. Electrum. 2022; 29: 109-125. doi: 10.4467/20800909el.22.008.15778
45. Fedi M, Florio G, Garofalo B, et al. Integrated geophysical survey to recognize ancient Picentias buried walls, in the Archaeological Park of Pontecagnano Faiano (Southern Italy). Annals of Geophysics. 2009; 51(5-6). doi: 10.4401/ag-3017

Journal of Geography and Cartography 2025, 8(1), 8816.
https://doi.org/10.24294/jgc8816

Article

Ophiolite Association in the Rhodope Massif as indicator of the paleogeographical setting

Evgenia Kozhoukharova

Geological Institute of Bulgarian Academy of Science, 1113 Sofia, Bulgaria; ekozhoukharova@abv.bg

CITATION

Kozhoukharova E. Ophiolite Association in the Rhodope Massif as indicator of the paleogeographical setting. Journal of Geography and Cartography. 2025; 8(1): 8816. https://doi.org/10.24294/jgc8816

ARTICLE INFO

Received: 22 November 2024
Accepted: 27 December 2024
Available online: 16 January 2025

Abstract: All ophiolite associations mark epochs of active tectonic movements, which lead to significant petrological processes and modification of the relief of the Earth's crust. Here we present a geological-petrographical characterization of one ophiolitic associations composed of: a) serpentinites; b) amphibolites-metamorphosed volcanic rocks and tuffs; c) metagabbros and metagabbrodiabases, placed among the Proterozoic metamorphic complex in the Rhodope Massif of Bulgaria on the Balkan Peninsula, South-Eastern Europe. The goal is to clarify the paleogeographical and geological setting during its creation. The methods of lithostratigraphic profiling and correlations on the database of geological field mapping were used, supplemented by microscopic, geochemical and isotopic studies of numerous rock samples. The summarized results confirm a certain stratigraphic level of the Ophiolite Association among the metamorphic complex and a complicated and protracted heterogenetic development, which is typical for the ophiolite associations created in eras of closing oceans, opposite movement of tectonic plates, subduction-obduction environment with appearance of autochthonous Neoproterozoic magmatism. Obducted fragments of serpentinites mark an old erosional continental surface, subsequently covered by transgressively deposited pelitic-carbonate sediments. The general conclusion of our study confirms the concept that the metamorphic complex of the Rhodope Massif represents a unified stratigraphic system consisting of two petrographic groups of different ages, with which we oppose the idea of a trust construction, launched by a group of geologists.

Keywords: ophiolites; serpentinites; obduction; magmatism; Neoproterozoic; Rhodope Massif; Bulgaria

1. Introguction

The article offers a systematization and analysis of geological data for an Ophiolite Association from the Rhodope Massif, Bulgaria, South-Eastern Europe. The goal is to achieve new knowledge about the paleogeographic situation and dynamic processes during a period of the Neoproterozoic—700–550 Ma. The Ophiolite Association was chosen as the basis of the study because the creation and development of such formations mark epochs of active tectonic and petrological processes.

Interest in ophiolitic associations called "green rocks" began as early as the 18th and 19th centuries, but the first generalization was the so-called "Steinmann trinity", where three main rock types are distinguished: serpentinites, volcanics and gabbro/diabases [1]. The evolution of the ophiolite concept passed through conflicting views until it reached the Penrose Conference Definition in 1972, presenting ophiolites as a pseudostratigraphic sequence [2]. Coleman's [3] original obduction model was a successful solution for the implantation of serpentinite fragments on continental margins. Other researchers develop the concept in petrological and tectonic aspects [4,5].

The Ophiolites are distinctive and highly informative rock associations regarding in terms of plate tectonics. Then the relief of the ocean floor and the continental surface changes, new portions of igneous rocks appear, which renew the rock composition the old metamorphic terrains of Earth's crust. They considered to have been formed in different tectonic setting, marking epochs of oceanic closure and countermovement of the plates in which a suprasubduction setting is created upon their collision.

The Rhodope Ophiolite Association is a good example that reveals many moments of such development. The knowledge we have of this rock association has been acquired after many years of field and laboratory research on the spatial distribution and geological place in the structures of the Rhodope Massif. This allows us to determine with a fairly high degree of certainty its stratigraphic position in the metamorphic complex and the main petrographic, mineralogical and geochemical characteristics.

2. Materials and methods

In the Rhodope Massif is widespread a Neoproterozoic continental ophiolite association, composed of metamorphosed basic volcanites, metagabro and serpentinites, located among the metamorphic complex of the Rhodope Mountains. The serpentinites have been known since the beginning of the last century. The conditional geological mapping at a scale of 1:25,000 of the Rhodope Massif was carried out according to the lithostratigraphic method in 1948–1962 years, supplemented with stratigraphic correlations between different areas of the Rhodope Massif and thematic field research. The study was accompanied by laboratory microscopic observations and geochemical sampling. The results were summarized in a Geological Map of Bulgaria on a scale of 1:100,000, with descriptive Notes attached to it provided a complete picture of the distribution and the main petrographic characteristics of the serpentinites and amphibolites as well relationships between stratigraphic units and serpentinite bodies. Systematic geochemical study began with the works of Zhelyazkova-Panayotova [6] on the serpentinite from the Eastern Rhodopes.

The complex field and petrographic studies on the geological and stratigraphic position of ophiolites and their metamorphic changes led to the concept of a uniform heterogeneous Ophiolite Association undergoing regional metamorphism [7–11]. The finding of eclogites in metamorphic rocks posed the problem of high pressure metamorphism in Rhodope Massif [12–15]. A curious problem is the genesis of gabbronorites with a corona-structure [16–18]. Geochemical studies have revealed valuable mineralization of platinum and native gold in the serpentinites as well as provided material for interpretation on the geodynamic area of ophiolite creation [19–23]. The finding of microdiamonds included in garnet, sharpen attention to regional problems of construction and metamorphism in the Rhodope Massif [24–26]. One important achievement in knowledge of ophiolites was the determination of the absolute age of metabasites and serpentinites [27–30]. The determination of the Archaean age of the serpentinites is of key importance for the initial moments of the development of the ophiolites [31].

3. Geological setting

The Rhodope Massif is situated in the central part of the Balkan Peninsula—Southeast Europe on the territory of South Bulgaria and North Greece. The metamorphic basement of the Rhodope Massif is built of high-grade Precambrian metamorphic rocks divided into two complexes, named: Prarhodopian and Rhodopian Supergroups of different age and petrographic composition [32,33].

An updated version of lithostratigraphic division, based on additional field research, petrographic correlations and analyzes of the lithostratigraphic units affirm the existence of two complexes of different lithology and age: Prarhodopian and Rhodopian Groups (**Figure 1**) [34].

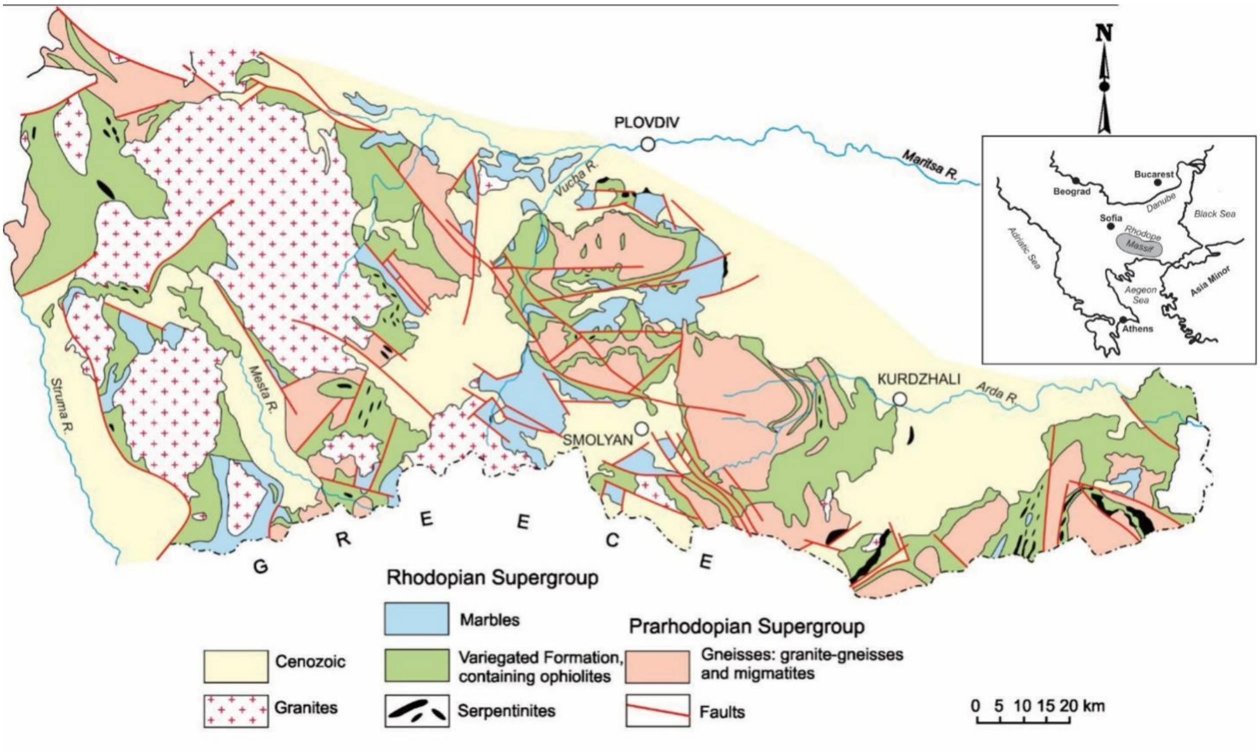

Figure 1. Geological map of the metamorphic complex of the Rhodope Massif.

The lower Prarhodopian Group (PRG) shows features of an ancient infracrustal continental complex, which may have been a fragment from some supercontinent. It consists of biotite and leptite gneisses with the packets of migmatic and granite-gneisses represented into three lithostratigraphic units up to top: Boykovo Formation, Bachkovo Formation and Punovo Formation. The absence of marbles is a specific feature of this group. The PRG builds up the core of anticlines and dome structures.

The upper Rhodopian Group (RG) is a well stratified supracrustal variegated complex that has been transgressively deposited on the Prarhodopian one. It is represented by metamorphosed volcanogenic-sedimentary rocks: amphibolites, eclogites, garnet-lherzolites, schists, quartzites, marbles, serpentinites, grouped in three parts, up to top: Lukovitsa Variegated Formation, Dobrostan Marble Formation and Belashtitsa Calc-silicate Formation. The Ophiolite Association is represented in the Lukovitsa Variegated Formation, where its rocks alternate with metamorphosed pelitic-carbonate sediments.

The Prarhodopian and Rhodopian Groups were subjected to folding at least twice. In the general structural plan, the diapiric raised domes and linear positive fold structures are clearly outlined by layers of the Rhodopian group. The spaces between them are occupied by deeply sunk subvertical, inclined or lying synclines, filled by the rocks of the Variegated Formation with ophiolites and marbles. Regardless of the folding deformations the ophiolites preserve their position in the crystalline complex and serve as basic stratigraphic marker. Sutures and deep tectonic zones, marked by ophiolites or discordant serpentinite wedges, are not found anywhere in the Rhodope Massif. The ideas of some authors presenting the Rhodopian Massif as Alpine nappe complex remained unproved by geological facts [35,36]. Later the author’s views evolved with the recognition of “crustal-scale duplex terranes with different lithologies, deformation and metamorphic histories” [37].

4. The Ophiolite Association

4.1. Spread and stratigraphic position of the Ophiolite Association

The Ophiolite Association occupies a clearly defined stratigraphic position in the lower levels of the Variegated Lukovitsa Formation of the Rhodopian Group [34]. The association has an uneven area in the Rhodope Massif (**Figure 2**). It is more widespread in the Eastern Rhodopes. The largest serpentinite massifs as elongated bodies, lenses or megabudins in size from meters to 10–13 km in lentgth are located in the Eastern Rhodopes: Bela Reka dom-anticline, Avren syncline and Drandovo horst. The Ophiolite Association has awide and characteristic development in the Western Rhodopes—Gotse Delchev district. It covered large areas with orthoamphibolites among which bodies of metagabbro and serpentinites are revealed. In the Central Rhodopes and Pirin Mountains the serpentinites have a limited presence. A series of irregular serpentinite bodies are located also on the northern edge of the Rhodopes. Isolated small lenticular bodies are often found among the rocks of the Variegated Formations, in association with amphibolites and schists.

The serpentinite bodies are placed concordantly between the lower layers of the Lukovitsa Variegated Formation often directly on the gneiss sole of the Prarhodopian Group. Thus, the serpentinites mark the erosion level on the gneiss PRG complex and become a stratigraphic bench mark. They are covered or included by amphibolites and, less frequently, by schists and marbles. Discordant serpentinite wedges crossing metamorphic layers are not observed anywhere.

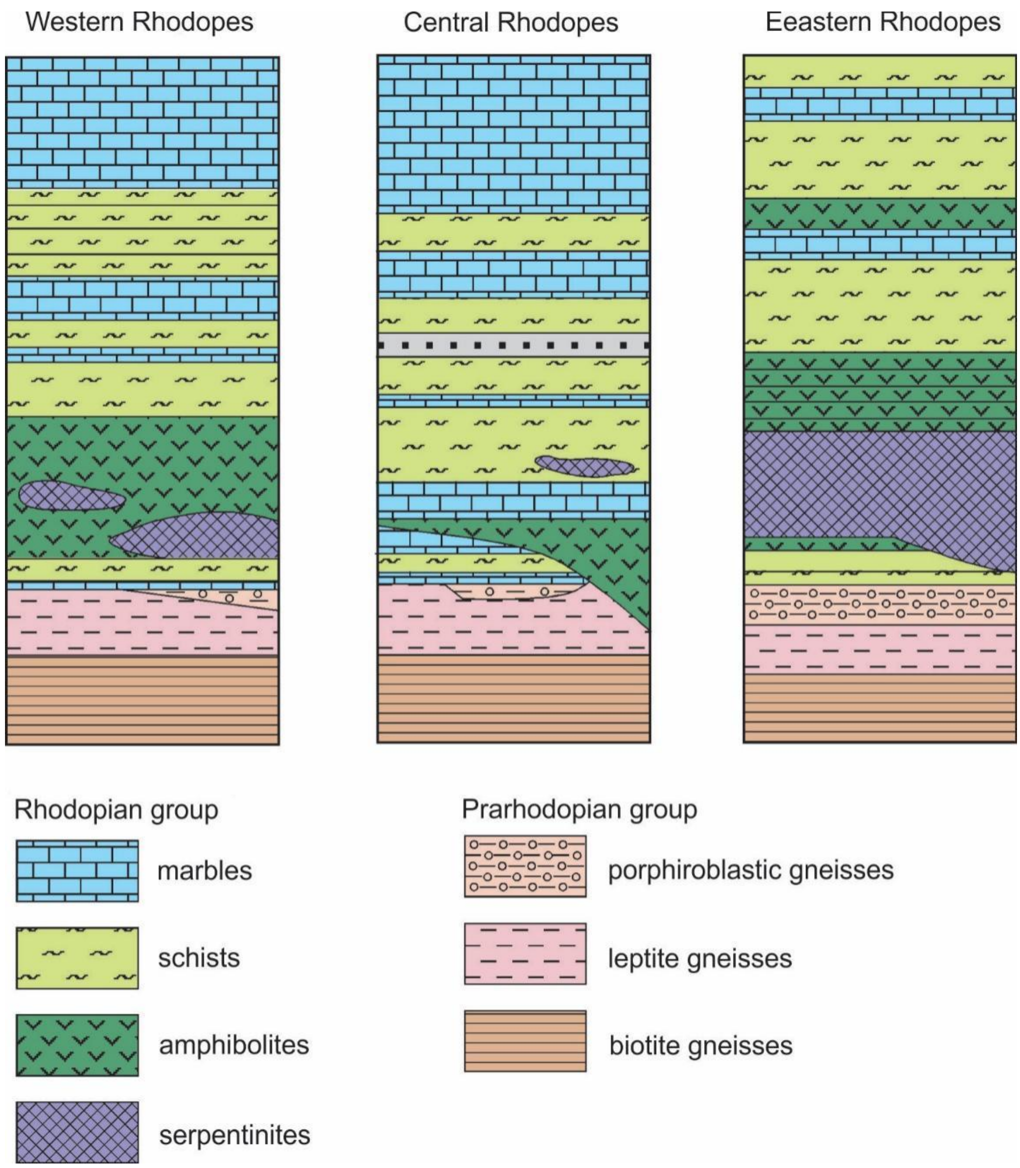

Figure 2. Stratigraphic columns of the Lukovitsa Formation in the Western, Central and Eastern Rhodopes.

4.2. Composition of the Ophiolite Association

The Ophiolite Association consists of: a) serpentinites; b) amphibolites (metamorphosed low potassium-high magnesium tholeiites and their tuffs); c) subintrusive bodies and dykes of metagabbros and metagabbrodiabases.

4.2.1. Serpentinites

The serpentinites are composed of lysardite, chrysotile and antigorite, rare relics of olivine (forsterite type), pyroxene and chromite. Lizardite is preserved inside large bodies. It fills the cells of the lattice microstructure characteristic of serpentinites, where together with chrysotile it forms a semi-isotropic, cryptocrystalline, vaguely fibrous mass, which often shows sectoral darkening. The cells are outlined by multi-layered chrysotile "cords", where the mineral builds cylindrical-fibrous individuals located perpendicular to the cell boundaries. Powdered to fine-grained magnetite, arranged in rows among the chrysotile, emphasizes the mesh structure. Larger chrysotile crystals fill cracks in serpentinite. Antigorite develops mainly on the peripheral parts of the bodies and in fault zones. The small thin bodies are composed entirely by fine scaly antigorite which orientation coincides with the general stratification and schistosity of the host rocks, evidence of its synmetamorphic crystallization.

The serpentinites from the Golyamo Kamenyne group—Eastern Rhodopes correspond to dunites and harzburgites, with the subordinate participation of lerzolites, pyroxenites, rhodingites and gondites developed mainly on the periphery of some bodies [6]. The rocks are ore-bearing. Relics of primary minerals-magnochromite in dunite zones, and chrompicotite in harzburgite zones are preserved. Sulfide copper-nickel and platinum mineralizations have also been found by Zhelyazkova-Panayotova [38], 1989. Chromites form nests and small bodies. They are classified into four groups: a) partially altered chromite; b) porous chromite; c) homogeneous chromite; d) zonal chromite.

Chromite deposits, forming about 200 bodies have been found also in the Dobromir serpentinite as well as mineralizations of native copper, gold, pyrhotite, nickel sulfides and elements from the platinum group [39]. Dobromirtsi serpentinites are enriched in Os, Ir and especially Ru and depleted in Pt and Pd [40]. During serpentinization and regional metamorphism, mobilization of some components occurs: enrichment of iron in the peripheral areas of the grains of chromium spinel [41], redistribution and recrystallization of native gold together with magnetite and tremolite. The chromites in chemistry are systematized in two groups: a) enriched with Os, Ir, Ru and b) enriched in platinoids, latter a third group with limited chromicity and increased magnesium has been distinguished [39-40]. The chemistry of primary magmatic chromite changes under the influence of metamorphic fluids. It is believed that the ultrabasic magma is fractionated by island arc toleite in archaic times—3000 Ma which underlined the continental crust, assimilated and later reworked.

Cr-Ni magnetite agregates present at the contacts of ultrabasic bodies with marbles, in the Central Rhodopes, Ardino region [42].

A number of ores have been also identified in the serpentinires from Western Rhodopes, Satovcha district as: magnetite, chromite, pentlandite, laurite, sulfarsenides and others the platinum group Os, Jr, Ru, Rh, Pt, Pd, as well as Au [43].

The chemical composition of serpentinites in their current form after Bazylev et al. [44], corresponds to dunites and peridotites with a magnesian coefficient M/F = 6 to 9. As in serpentinization the magnesian ratio increases the probability of extensive dunite involvement decreases. During serpentinization, silicate minerals such as olivine and pyroxene are highly altered, some of the calcium and iron content is extracted from the water, and the magnesian ratio increases. So, it must be assumed that the dunites were the smaller part of the serpentinite protolith where peridotites predominated.

The oldest ages according to U-Pb dating of zircons from the chromitites of the Dobromirtsi serpentinite massif indicate Paleoproterozoic era 2257 ± 80 Ma and 1952 ± 82 Ma, which is the age of the oceanic plate in the ancient ocean, from which the serpentinite fragments have been torn off [31].

The complex of petrographic, mineralogical, geochemical and isotopic data clearly indicates that the serpentinites are hydrated derivatives of peridotites from an old Archaean-Paleoproterozoic oceanic mantle plate.

4.2.2. Amphibolites

The amphibolites are widely distributed as layers of different thickness (0.5-15-20 m), alternating with amphibole-schists, amphibole-biotite or muscovite-biotite schists, gneisso-schists, carbonate schists and marbles. They are composed of amphibole (tschermakite-hastingsite) and plagioclase (andesine to bytownite) and with volatile and variable amounts of quartz, biotite, garnet, epidote, pyroxene, titanite, rutile, magnetite, ilmenite. Most of the amphibolites have clear foliation, but there are often those with a more massive texture. The rocks are fine, medium or coarse-grained, with a granoblastic structure. In terms of chemical composition, amphibolites correspond most often to high-magnesium toleites and less often to picrites.

In terms of chemistry, amphibolites correspond to gabbro group and according to basic toleic volcanics. Amphibolites from the Lukovitsa Formation, according to their content of trace and RRF elements, show a certain affinity for island-arc basic volcanics from the continental margins [45].

Amphibolites which are not affected by migmatization generally correspond to low-potassium toleite basalts, locally enriched in titanium (TiO 2%–4%) and iron (FeO 14%–18%), and to a lesser extent to basaltic and peridotite comatites. Variations in the main components are relatively limited. Zakariadze et al. [46] divided the amphibolites from the Eastern Rhodopes into three groups in the TiO vs. MgO. Examining the distribution of RRE the authors conclude that the high titanium amphibolites refer to the basalts of the mid-ocean ridges, while the low titanium ones are compared with those of the island arcs. According to petrochemical coefficients authors identified three groups of compositions: oceanic rift tholeiites, intraplate basalts and island arc tholeiites. Amphibolites from the Lukovitsa Formation, according to their content of trace and RRF elements, show a certain affinity for island-arc basic volcanics from the continental margins [45]. The amphibolites in Western Rhodopes correspond to toleite and high-magnesium toleiite basalts, with increased content of Fe, Ti, Al. Individual thin layers composed of actinolite schists, with high concentrations of magnesium, chromium and nickel, bring them closer to comatiites. The geochemical characteristics of individual samples of amphibolites from the vicinity of the villages Satovcha, Pletena, Oreshe and Kochan show affinity for island arc toleite and calcium-alkaline basalts and andesites [47].

Contemporary data of Bonev et al. [22] for the rare and trace elements in amphibolites indicate increased contents of Zr, Nb, Y, Ni, Cr interpreted as indicating a high degree of fractionation from a primitive mantle magma. According to the authors, the high-titanium group of metabasites has an affinity to the toleite magmas of the Mid-Ocean Ridges and partly of the Inland Ocean Plates while the low-titanium ones approach the island arc toleites.

Such a division by petrochemical calculations is difficult to find in accordance with the geological setting. The content of trace and RRE elements varies depending on the variations of the main components. There is a direct dependence in the contents of Fe and V, as well as between Mg and Cr, Ni, Co. The migmatization of amphibolites also increases the contents of Si, Al, alk, Ti, Sr and decreases that of Mg, Fe, Cr, Ni, Co.

The comparative analysis on the chemical character of the metamorphosed basic magmatites—amphibolites and gabbro shows their common belonging mainly to the group of basalts and a smaller part of them to the picrite basalts respectively to the normal and magnesium toleites. The great diversity of the chemical composition of the amphibolites, however, cannot be considered fully adequate to the primary composition of the magma, which does not give us the right to draw precise conclusions about the geodynamic zone of their creation. In our opinion, the great geochemical diversity in the amphibolites, where both basic and ultrabasic composition signatures are combined, is more reminiscent of contamination than of fractional magmatic processes. This circumstance supports an idea of suprasubduction rather than an island arc setting.

4.2.3. Metagabbros

The metagabbros form isolated small bodies associated with the amphibolites. Rare dykes of massive amphibolites cross biotite and leptite gneisses of the Prarhodopian Groupe in Eastern, Central and Western Rhodopes. They are thin from 10–20 cm to 1 m, straight or deformed. Dykes of massive amphibolites cross also serpentinites. At the contacts between them the serpentinites become dehydrated and veins of elongated prisms of chrysotile appear. This is thought to be a reaction between the hot magma dyke and the serpentine.

A subintrusive body (300 × 700 m) crosses with intrusive contacts the leptite gneisses of the Bachkovo Formation in the Northern Rhodope anticline—Central Rhodopes and includes xenoliths from the gneisses [9]. It is related to the horizon of epidote amphibolites from the Lukovitsa Formation. The body is built of metagabbro-diabases with massive texture, relict gabbroophitic microstructure and mineral composition: tschermakite amphibole, garnet, andesine, epidote, zoisite, quartz, ilmenite and rutile. The chemical composition corresponds to high-aluminum diabases and gabbro. The body is evidence of the autochthony of the basic magmatism. The higher magnesium character of the metagabbro with respect to amphibolites is illustrated in all petrochemical diagrams. On the diagram in the parameters SiO_2 vs. (Na_2O + K_2O) gabbro falls in the low alkaline part of the basalt and picrobasalts.

The lack of certainty in the petrochemical definitions of the type of magma and the geodynamic zone of formation, again shows the complex relationship between the genesis of ophiolites and the numerous factors influencing,

The absolute age of the metamorphous basic protolith is determined by U-Pb dating on zircon as Neoproterozoic—610 Ma in eclogites from Central Rhogopes; 678–572 Ma—metagabbro Bubino and 566 Ma—metagabbro Bela Reka [27–30]. These dates coincide with the time of ocean closure preceding the amalgamation of the Gondwana supercontinent.

5. Formation of the Ophiolite Association

The overall geological, petrological and geochemical characteristics of the Rhodope Ophiolite Association testify to a complex and long-lasting process of formation. We attempt to trace the development of of the association based on several points of reference:

a) serpentinites are hydrated derivatives of Archaean-Paleoproterozoic mantle peridotites. According to Deschamps et al. [48] a high degree of serpentinization—85%–95% in lizardite and chrysotile is only possible in the ocean basins, where on an ultrabasic ocean plate a layer of clay-like serpentinites up to several kilometers thick is developed;

b) the constant stratigraphic level of serpentinite bodies on a gneiss base on an eroded continental surface indicates tectonic processes of plate movement, the presence of a subduction zone and the transfer of serpentinite fragments on the continent by the mechanism of obduction;

c) Neoproterozoic basic volcanic rocks cover the serpentinite fragments, alternating with the metasediments of the Lukovitsa Variegatet Formation,

We propose a possible scenario for the formation of the Ophiolite Association, which unites in a logical scheme all known geological and theoretical arguments (**Figure 3**):

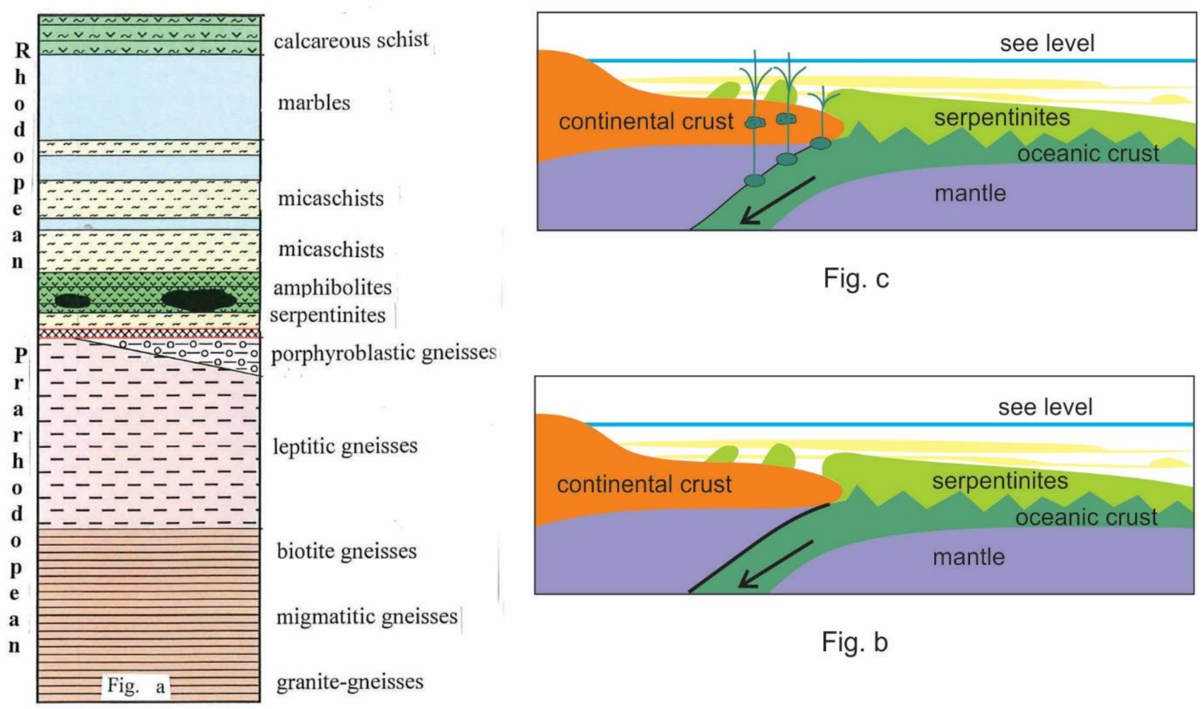

Figure 3. Simplified drawing of suprasubducting zone. **(a)** stratigraphic column of the metamorphic complex of the Rhodope Massif. Serpentinite bodies mark an erosional surface and the boundary between the Prarhodope and Rhodope groups. **(b)** subduction of the oceanic plate under the continental one and obduction of serpentinite fragments; **(c)** formation of melt and autochthonous magmatism.

During the Neoproterozoic, a situation of basin closure was created, which caused counter movement and collision between oceanic and continental plates. A microcontinent, the prototype of the Rhodope Massif, built from the gneisses of the Prarhodope Group, collides with an Archean-Paleoproterozoic oceanic mantle plate that is covered by clay-like soft serpentinites. A suprasubduction zone was developed at their convergent boundaries. The serpentinite fragments were scraped off from the serpentinite cover of the oceanic plate by the principle of the grater and obduced on the erosion plane of gneiss continental crust (**Figure 3**). As a result of the strong friction on the contact surface between the huge continental and oceanic plates and the resulting high temperature and pressure at certain depths, foci of molten gneiss and ophiolite rocks appeared. The melt penetrated into the gneisses through channels. Along the way it builds subintrusive bodies and dykes and covered the serpentinites as lavas and tuffs, together with pelitic-carbonate sediments. The location of the large serpentinite massifs is a known indication of proximity to the coastline of the microcontinent where the serpentinite fragments were obducted [49].

The formation of the Rhodope Ophiolite Association had taken place in three stages: a) static—serpentinization of the oceanic ultrabasic plate; b) dynamic—ocean closure, plate tectonic movement and obduction of serpentinite fragments, scraped from the hydrated coat of the sliding ultrabasic plate; c) constructive—autochthonous subintrusive magmatism and volcanism including and covering serpentinite bodies. This determines the heterogeneous nature of formation of the Ophiolite Association—a combination of rock members appearing in different places, times and geological setting.

6. Metamorphism of the ophiolites

Three main types of changes are distinguished on the metamorphic complexes in the Rhodope Massif: a) regional metamorphism; b) local high pressure metamorphism (HPM); c) metasomatism. They differ in their spatial, temporal and thermodynamic features and develop in distinctly diverse geological settings.

6.1. Regional metamorphism

Regional metamorphism as a broad spatial and comprehensive recrystallization where geothermal gradient and lithostatic (confining) pressure control the TP conditions of crystallization. All ophiolite rocks underwent a regional metamorphism of amphibolite facies: basic volcanic rocks were recrystallized into amphibolites, subintrusive ones—into metagabbros or metadiabases. The large serpentinite bodies were only peripherally metamorphosed in antigorite, talc-chlorite and chlorite-actinolite-tremolite schists, while in the inner parts they retained the lizardite-chrysotile aggregate in mesh cells. Anthophyllite mineralizations are localized mainly in cracks inside the serpentinites and less frequently in their contacts, forming anthophyllite-asbestos cores that were once exploited. In the veins, anthophyllite is associated with talc, tremolite, magnesite, and in rare cases with dolomite. The background regional metamorphism of the rocks is in amphibolite facies: T = 480 °C–560 °C, P = 0.5–0.7 GPa. The preservation of lizardite-chrysotile indicate that the temperature of the general regional metamorphism never exceeded 600 °C. Otherwise, all serpentinites would have become pyroxenites. The latter, being in the relatively dry continental crust, would never be serpentinized again.

6.2. High pressure metamorphism (HPM)

High pressure metamorphism (HPM) posses completely opposite characteristics. They appear locally only within the range of shear zones of friction, formed as a consequence of seismotectonic events. While the regional metamorphism is a prolonged state of certain conditions, the HPM is a short living event. Earthquake events cause movement and friction between rock blocks and bedrock layers. The temperature and pressure rapidly rise to high values, causing recrystallization or melting of the zone's wall rocks. The main factor in this metamorphism is friction, which is why we call it *geotribometamorphism*. In petrology HPM is also known as eclogitization—sensu lato which affects different rock varieties, manifested in new mineral parageneses depending of the chemical composition of the host rock. Typical eclogites, consisting of garnet, omphacie and rutile occur on a basic substrate among amphibolites, while garnet-lherzolites of pyrope, enstatite, olivine, spinel, augite, diopside are formed on serpentinites [50]. Calcifieres are found among marbles as thin (0.5–3 mm) layers, composed of fine-grained: garnet, scapolite, diopside, zoisite, spinel, calcite, dolomite, phlogopite, plagioclase, titanite, quartz. HPM in metapellites are represented by kyanite and phengite schists in some cases with microdiamond-bearing garnet [25,26].

6.2.1. Eclogites

Eclogites are typical representatives of high-baric metamorphic rocks, the genesis of which is still a subject of discussion. Eclogite bodies are found in all metamorphic terrains of South Bulgaria—the Rhodopes, Verila Mt., Sredna Gora Mt. and Ograzhden Mt. [10,12–15,51–55]. Everywhere eclogites are included in formations, analogous in rock composition to the Lukovitsa Variegated Formation. The eclogites associate with the amphibolites and form among them concordant thin layers and lenses up to 10–20 cm as well as rarely compact layers with a thickness of 1–1.5 m. The eclogites often appear on the contact with mica-poor leptite and aplitoid gneisses in geological setting indicating an old friction zone. Eclogites are encountered also in cracks of 2–5 cm, intersecting gabbronorites, which is the most convincing evidence for their formation in friction zones [55]. The crystallization temperatures are most often within the range of 580 ℃–680 ℃ at pressures of 1–1.6 to more seldom 2 GPa. Temperature of 800 ℃–1100 ℃ and pressure of 2–4 GPa are recorded for the coesite and microdiamond containing eclogites [25,54]. All eclogites are affected by alterations [56]. The omphazite is replaced by symplectites of quartz, albite and diopside, garnet—by amphibole, which ultimately leads to complete replacement of eclogites by amphibolites. A characteristic eclogite deposit is known near the village of Kazak, Ivaylovgrad region, Eastern Rhodopes [10,57,58]. There, the eclogites show a layered structure due to the alternation of about 10 cm thin layers of coarse-grained and fine-grained garnet varieties deformed in small folds. All features of the eclogites indicate that they are not exotic bodies, but are an integral part of the Lukovitsa Variegated Formation formed in situ along mobile zones on lithological contacts and shear zones of friction.

6.2.2. Banded eclogizited serpentinites

A rare case of rhythmic banded eclogitization is observed on a serpentinite body south of Avren village, Krumovgrad district—Eastern Rhodopes [50]. The body is a part of the Lukovitsa Variegated Formation which is related with the Kimi complex in North Greece where microdiamonds in garnet are found [24]. The body's peripheral parts (30–40 m) are affected by eclogitization. Bands of garnet lherzolites (1–20 mm), which are parallel to the contact, alternate with strips of unchanged serpentinite. The lherzolite bands close to the contact are more frequent and consist of pyrope-garnet diopside, enstatite, olivine and spinel, crystallized under conditions of *T* = 560 °C–820 °C, *P* = 8–15 kbar. Towards the interior of the serpentinite body the bands become rarer, do not contain garnet and gradually disappear. Obviously eclogitization is associated with the contact between the serpentinites and host gneisses, which has been most probably a previous paleoseismotectonic zone.

6.2.3. Calcifires

Calcifiers are observed in many places among marbles as thin (0.5–3 mm) layers, composed of fine-grained: garnet, scapolite, diopside, olivine, spinel, calcite, dolomite, phlogopite, plagioclase, titanite, quartz. The calculated crystallization conditions are: *T* = 745 °C–770 °C, *P* = 0.5–1 GPa [58].

6.2.4. Kyanite and fengite schists

Kyanite and fengite schists are found also in zones of interlaminar sliding. Microdiamond-containing garnet porphyroblasts in gneiss schists of the Variegated Formation are encountered in the Chepelare region of the Central Rhodopes; *T* = 700 °C–800 °C, *P* = 3.5–4.6 GPa [25,26].

High-thermobaric rocks are also an important indicator of the setting when they occur in friction zones. Since friction zones are seismic zones, this means that HPM rocks document paleoseismic events and the age of the eclogites fixes the age of the seismic events in our earth's past.

6.3. Metasomatism

Metasomatism is a process of bulk chemical change in which deep derivatives from anathectic and granitoid magmas, as pegmatite-aplite veins, penetrate the regional metamorphic rocks, enriching them with Si, Al, K, Na. Metasomatic pegmatite-aplite pulses have occurred repeatedly during Proterozoic and Phanerozoic times of granitic magmatism, respectively. Ophiolites are strongly affected by metasomatism due to the contrasting chemistry between them and pegmatite-aplites resulting in hybrid rocks such as metasomatic gabbroides [56] and gabbro-norites with a corona-structure are created [18,59]. The genesis of the gabbro-norites with corona-structure is still a matter of debate. In our opinion, the most plausible version is the metasomatic one. It is likely that small serpentinite bodies, included in the amphibolite layer, reacted with the quartz-feldspar mineral composition of the surrounding migmatization environment. However, the metasomatic version is supported by findings of serpentinite inclusions in pegmatite veins in Ograzhden metamorphic rocks that show the same corona structure during recrystallization [59].

7. Discusion

The Rhodope Ophiolite Association is a highly informative formation in the Rhodope Massif. It is presented in a lot of instructive outcrops that allow us to consider and resolve some controversial questions regarding stratigraphy, tectonics, high thermobaric tribometamorphism and metasomatic hybridization.

One of the most hotly debated issues is the construction of the metamorphic complex in the Rhodope Massif and the place of ophiolites in it. To the established concept introduced in 1963 by Vergilov et al. [32], which presents the metamorphic complex as a single unified stratigraphic system, Bürg et al. [35–37] opposes a new version considering the metamorphic complex as a system of discordant plates "pile of thrust", based on observed somewhere mylonitized gneisses and microstructures that showed shear of sence deformation. The factual database of the two concepts is unmatched in weight and importance. The stratigraphic concept is substantiated by a huge database of geological mapping of the entire massif at a scale of 1:25,000, shown in numerous geological maps, stratigraphic profiles and correlation analyses of different parts of the terrain, which unequivocally confirm a normal stratigraphic sequence, underwent a general plastic deformation resulting in folded structures [32]. The opponents have so far not presented graphic material where the thrust plates in

question, being actual physical entities, must be delineated with clear boundaries and areal coverage. Then such material could be accepted as evidence for existence of the mentioned thrusts. In recent years, the rhetoric about the thrusts has evolved and there is already talk of undefined allochthons, shown on tectonic sketches of various shapes [60–62] In fact, the authors continue Bürg's idea about the tectonic structure of the Rhodope Massif. However, the arguments advanced by them do not correspond to the established geological facts about the relationships between the lithological units, which unequivocally show a lithostratigraphic sequence and normal rather than tectonic contacts.

The stable stratigraphic position of the Ophiolite Association also confirms the concept of a single stratigraphic sequence of the metamorphic complex and refutes the ideas of thrusting [35–37]. The Ophiolites have a definite and permanent stratigraphic position in the metamorphic complex and do not delineate suture zones anywhere. Also, meso- and microdeformations in the metamorphic rocks, marked as shear in cense criteria, cannot be accepted as evidence of Alpine nappe complex, because similar deformation microstructures can also appear in every fold structures.

The well preserved and uniform for the whole massif stratigraphic sequence and the dominating fold structure disprove the existence of thrust structures and suture zones in the outcropped part of the metamorphic basement on Bulgarian territory.

The statement that eclogites and ophiolites "are found in various units of crustal-scale duplex structure" and at the same time "these rocks delineate a suture zone" between two units as Burg [37] considers is factually unconfirmed and contradictory. The Ophiolites have a definite and permanent stratigraphic position in the metamorphic complex and do not delineate suture zones anywhere. Eclogites themselves form in friction seismic zones at high temperatures and pressures. In Rhodope Mountain, they mark old paleoseismic zones, among the amphibolites of the Ophiolite Association Lukovitsa Formation Ophiolite Association of the Rhodope Group and therefore they can by no means be accepted as markers of tectonic boundaries of thrust plate. We also believe that the Paleoproterozoic age definitions of the Dobromirtsi serpentinites can be applied to all serpentinites, due to their constant stratigraphic and geological position. This disproves the notion of their different age of implantation in the Rhodope metamorphic complex [63].

Determining the geochemical nature of ophiolites as well as the geodynamic zone of their formation directly from chemical analyzes is, in our opinion, an incorrect approach that carries the risk of errors. Very often highly hydrated ophiolites are not called by their current rock name "serpentinites", but the indefinite "ultramafites", "ultrabazites" or even simply "dunites" and "peridotites", calculated by the ratio of the components. It ignores the well-known fact that serpentinization extracts calcium and iron, which greatly increases the magnesianity and directs the interpretation to dunites. However, replacing the name of serpentinite, which is a magnesian clay formed in a water basin, with the name of an igneous rock - dunite or peridotite, radically changes the interpretation of the composition, genesis and development of an ophiolite association.

Analogous mistakes are made when interpreting the primary nature of amphibolites and metagabbras. When it comes to a continental Ophiolite Association created in a suprasubduction setting, such as the Rhodope ophiolites considered here, the composition of the autochthonous magmatism is to varying degrees contaminated. In the frictional surface of the subduction zone, both the ultrabasic rocks of the subducting oceanic mantle plate and the continental gneisses melt. Therefore, middle basic rocks sometimes bear geochemical signatures of a mantle signature. Very often, researchers overrely on geochemical data and, recalculating them using various formulas, coefficients and diagrams without comparing them to the specific geological situation, arrive at contradictory and unrealistic genetic interpretations.

An eloquent example of a geochemical study of three small metagabbro bodies in the Eastern Rhodopes is presented by Haydoutov et al. [21]. Petrochemical work is filled with a great diligence. Numerous recalculations of chemical analyzes and diagrams by different methods were made, as many ratios as possible between the components were deduced and compared with examples from recent basic volcanics from various distant regions of the planet, however, in the complete absence of consideration of the geological position and stratigraphic location of the studied samples. In the end, the authors came to the controversial conclusion that the rocks are boninites and island arc tholeiites, which together with metasediments form an ensimatic island arc. But at the same time the ultramafic rocks (as they call the serpentinites) were serpentinised in a supra-subduction zone (???) and may have had a genetic connection to the aforementioned ensimatic island arc. The mentioned article is an example of perfectly conducted geochemical calculations, which, however, without a solid geological base and terminological accuracy lose their interpretative value.

8. Conclusion

- The Rhodope Ophiolite Association is a continental heterogeneous serpentinite-basite supra-subduction rock formation. It is part of the Precambrian metamorphic complex of the Rhodope Massif on the Balkan Peninsula, Southeastern Europe. The association occupies the lower stratigraphic levels of the Lukovitsa Formation of the Rhodope Group of the metamorphic complex;
- The Ophiolite Association unites allochthonous serpentinites and autochthonous basic magmatic rocks, which are formed in different places, time and geological setting over a long period of time. The beginning of its creation takes place in a deep-sea ocean environment where a Paleoproterozoic mantle ultrabasic plate is subjected to prolonged serpentinization;

- Serpentinite fragments were obducted on the erosional surface of an old continent. This event marks an epoch of tectonic activity of ocean closure, countermovement and collision of continental and oceanic plates and formation of a subduction zone along the convergent boundaries of the two plates;
- Friction in the subduction zone produced autochthonous basic subintrusive and volcanic magmatism during the Neoproterozoic (700–550 Ma) concurrent with transgression and deposition of pelitic-carbonate sediments. The uneven distribution of the large serpentinite bodies gives an indication of their distance from the shoreline;
- The well-preserved stratigraphic sequence mainly the fold tectonic structure and the absence of regional thrusts, testifies that the subsequent development of the metamorphic terrain was relatively tectonically calm with a probable softer relief. Widespread regional amphibolite facies metamorphism, with no apparent zonation, also supports the view of a relatively more relaxed tectonic regime;
- It is assumed that deep slides in the roots of the Rhodope Massif provoked the formation of magmatic centers and granodiorite batholiths. Their derivatives such as pegmatite-aplite veins penetrate the higher levels and metasomatize the rocks. The metasomatic changes are clearly visible in the ophiolites, due to the contrasting chemical composition between them and the pegmatite-aplite granite derivatives;
- The metamorphic complex during the Precambrian and Phanerozoic was repeatedly cut by seismic zones of strong friction between rock blocks and layers marked by high-thermobaric rocks: eclogites, garnet lherzolites, calcifiers, kyanite and fengite schists;
- The Rhodope Massif was included in the Caledonian-Hercynian and Alpine mobile belts, but it has relatively well preserved its primary lithostratigraphic sequence, which is an indication of its consolidation. Only during the Paleogene did significant disintegrations occur and it was divided into three parts: Western, Central and Eastern Rhodopes.

Conflict of interest: The author declares no conflict of interest.

References

1. Steinmann, G. The ophiolitic zones in the Mediterranean chain mountains. In: Proceedings of the 14th international geological congress in Madrid; 2003. pp. 638–667.
2. Anonymous. Penrose Field Conferenceon ophiolites. Geotimes. 1972; 17: 24–25.
3. Coleman RG. Ophiolites. Springer; 1977. p. 229.
4. Miyashiro A. Classification, Characteristics, and Origin of Ophiolites. The Journal of Geology. 1975; 83(2): 249–281. doi: 10.1086/628085
5. Dilek Y, Furnes H. Ophiolite genesis and global tectonics: Geochemical and tectonic fingerprinting of ancient oceanic lithosphere. Geological Society of America Bulletin. 2011; 123(3–4): 387–411. doi: 10.1130/b30446.1
6. Zhelyazkova-Panayotova M. Golyamokamenyane ultrabasic group and their chromite bearing (Bulgarian) Sofia University Annual. Biol. Geol. Geograph. Fac. 1960; 53(2): 59–142.
7. Kozhoukharova E, Kozhoukharov D. Studies on the rocks and the construction plan of the North Rhodope anticline in the Assenovgrad area (German). Bull. Geol. Inst. Bulgarian Acad. of Sci. 1962; 11: 125–162.

8. Boyanov I, Mavrudchiev B, Vaptsarov I. On the structural-formational features of a part of the Eastern Rhodopes (Bulgarian). Bull. of Geol. Inst. Bulgarian Acad. of Sci. 1963; 12: 125–178.
9. Kozhoukharova E. Precambrian metamorphozed basic volcanites from the Central Rhodope mountains (Russian). Bull. of Geol. Inst. Bulgarian Acad. of Sci., ser. Geochem., Mineral and Petrol. 1972; 21: 147–165.
10. Kozhoukharova E. Origin and structural position of the serpentinized ultrabasic rocks from the Precambrian Ophiolite Association in the Rhodope Massif. I Geologic position and composition of the ophiolite association. Geologica Balcanica. 1984; 14 (4): 9–36.
11. Kozhoukharova E. Origin and structural position of the serpentinized ultrabasic rocks from the Precambrian Ophiolite Association in the Rhodope Massif. III. Development stages and age of the ophiolite association. Geologica Balcanica. 1985; 15(5): 53–89.
12. Kozhoukharova E. Eclogites in the Precambrian from the Eastern Rhodope block. Comptes Rendus of Acad. Bulg. Sci. 1980; 33(3): 375–378.
13. Dimitrova E, Belmustakova H. Relics of eclogites in the crystalline complex of Ihtiman Sredna Gora Mountains (Russian). Geologica Balcanica. 1982; 12(1): 115–120.
14. Kolcheva K. Zhelyazkova-Panayotova M, Dobretsov NP. Fragments of an ancient Ophiolite Association in the region of Ardino town (Central Rhodope, Bulgaria) (Russian). Comptes Rendus of Acad. Bulg. Sci. 1984; 37(2): 187–190.
15. Liati A. Amphibolitized eclogites in the Rhodope Crystalline Complex, near Xanthi (N. Greece). N. Jb. Miner. H. 1988; 1: 1–8.
16. Toprakchieva V. Petrochemical characterization of the basic intrusions around the villages of Ahryan and Deliasanovtsi, Smolyan District (Bulgarian). Annual of General Depart. of Geology. 1964; 14: 81–93.
17. Kozhoukharov D. Precambrian metamorphosed ultrabasic and basic magmatites in the Central Rhodopes (Bulgarian). Rev. Bul. geol. soc. 1966; 2(1): 51–62.
18. Pristavova S. Metamorphozed basic magmatites from Eastern marginal parts of Madan-Davidkovo structure (Bulgarian). Rev. Bulg. Geol. soc. 1996; 57(1): 9–20.
19. Zhelyazkova-Panayotova M, Tsintsov Z, et al. Hydrothermal gold mineralization in ultrabasite near the village of Dobromirtsi, Kardzhali region (Bulgarian). Sofia University Annual, geol.-geogr. fac. 2000; 1: 173–186
20. Tarkian M, Naidenova E, Zhelyaskova-Panayotova M. Platinum-group minerals in chromitites from the Eastern Rhodope ultramafic complex, Bulgaria. Mineralogy and Petrology. 1991; 44(1–2): 73–87. doi: 10.1007/bf01167101
21. Haydoutov I, Kolcheva K, Daieva LA, et al. Evidence of boninitic type magmatism in the Variegated Firmation from the East Rhodope. Geochem., Mineral. and Petrol. 2003; 40: 55–71.
22. Bonev N, Dilek Y, Hanchar J, et al. Nd-Sr-Pb isotopic composition and mantle sources of Triassic rift units in the Serbo-Macedonian and the western Rhodope Massifs (Bulgaria-Greece). Geol. Mag. 2012; 149(1). doi: 10.1917/S0016756811000938
23. Froitzheim N, Jahn-Ave S, Frei D, et al. Age and composition of meta-ophiolite from the Rhodope Middle Allochthon (Satovcha, Bulgaria): a test for the maximum-allochthony hypothesis of Helenides. Tectonics. 2014; 33(8): 1477–1500. doi: 0.1002/2014TC003526
24. Mposkos ED, Kostopoulos DK. Diamond, former coesite and supersilicic garnet in metasedimentary rocks from the Greek Rhodope: a new ultrahighpresure metamorphic province established. Earth Planet. Sci. Lett. 2001; 192: 497–506. doi: 10.1016/S0012-821X(01)00478-2
25. Collings D, Savov I, Maneiro K, et al. Late Cretaceous UHP metamorphism recorded in kyanite–garnet schists from the Central Rhodope Mountains, Bulgaria. Lithos. 2016; 246–247: 165–181. doi: 10.1016/j.lithos.2016.01.002
26. Petrík I, Janák M, Froitzheim N, et al. Triassic to Early Jurassic (c. 200 Ma) UHP metamorphism in the Central Rhodopes: evidence from U–Pb–Th dating of monazite in diamond-bearing gneiss from Chepelare (Bulgaria). Journal of Metamorphic Geology. 2016; 34(3): 265–291. doi: 10.1111/jmg.12181
27. Arkadakskiy SV, Bohm C, Heaman L, et al. Remnants of Neoproterozoic oceanic crust in the Central Rhodope metamorphic complex, Bulgaria. Geol. Soc. Am., Vancouver Annual Meeting. 2003.
28. Carrigan C, Mukasa S, Haydoutov I, et al. Ion microprobe U-Pb zircon ages of pre-Alpine rocks in the Balkan, Sredna Gora, and Rhodope terrains of Bulgaria: Constraints on Neoproterozoic and Variscan tectonic evolution. Journal of Czech Geol. Soc. 2003; 48(1–2).

29. Quadt A, Peycheva I, Sarov S, et al. Late Cretaceous subduction and magmatism in the Rhodopes: geochronological and isotope-geochemical evidence. In: Proceedings of Bulg. Geol, Soc., Nat. Conf. "Geosciences, 2010"; Sofia, Bulgaria. pp. 13–14.
30. Filipov P, Ichev M, Bonev N, et al. LA-ICP-MS U-Pb zircon age of amphibolite protoliths associated with the metaophiolites near the villages of Dobromirtsi and Bubino, East Rhodopes, Bulgaria. In: Proceedings of International Congress of CBGA; 7–11 September 2022; Plovdiv, Bulgaria. p. 275.
31. González-Jiménez JM, Locmelis M, Belousova E, et al. Genesis and tectonic implications of podiform chromitites in the metamorphosed ultramafic massif of Dobromirtsi (Bulgaria). Gondwana Research. 2015; 27(2): 555–574. doi: 10.1016/j.gr.2013.09.020
32. Vergilov V, Kozhoukharov D, Boyanov I, et al. Notes on the Pre-Paleozoic metamorphic complexes in the Rhodope Massif (Bulgarian). Bull. of the Geol. Inst. Bulg. Acad. of Sci. 1963; 12:187–211.
33. Kozhoukharov D. Precambrian in the Rhodope Massif. Lithostratigraphy. In: Zoubek V (editor). Precambrian in Younger Fold Belts. J. Wiley & Sons, Chichester; 1988. pp. 726–746.
34. Kozhoukharova E. Reconstruction of the primary stratigraphy and correlation of the Precambrian metamorphic complexes in the Rhodope Massif. Geologica Balcanica. 2008; 37(1–2): 19–31. doi: 10.52321/geolbalc.37.1-2.19
35. Burg JP, Ivanov Z, Ricou LE, et al. Implication of shear-sense criteria for the tectonic evolution of the Central Rhodope Massif, Southern Bulgaria. Geology. 1990; 18: 451–454. doi: 10.1130/0091-7613(1990)0182.3.CO;2
36. Burg J, Ricou L, Ivano Z, et al. Syn-metamorphic nappe complex in the Rhodope Massif. Structure and kinematics. Terra Nova. 1996; 8(1): 6–15. doi: 10.1111/j.1365-3121.1996.tb00720.x
37. Burg JP. Rhodope: From Mesozoic convergence to Cenozoic extension. Review of petro-structural data in the geochronological frame. Journal of the Virtual Explorer. 2012; 42. doi: 10.3809/jvirtex.2011.00270
38. Zhelyazkova-Panayotova M. Igneous deposits. Serpentinized ultrabasics. In: Trashliev S (editor). Non-metallic minerals in Bulgaria, II. Endogenous industrial minerals and rocks. DI & quot. Technique & quot; 1989. pp. 7–41.
39. Zhelyazkova-Panayotova M, Economou-Eliopoulos M. Platinium group elements (PGE) and gold concentration in oxide and sulfide mineralization from ultramafic rocks of Bulgaria. Annual Univer. Sofia, geol. -geograph. fac. 1994; 86(1): 196–218.
40. Kerestedjian T, Gervilla F, Gonzalez-Jiménez JM, et al. New data on chromitites from Dobromirtsi, Eastern Rhodopes. In: Proceedings of Nat. Conf. "Geosciences"; Sofia, Bulgaria. pp. 255–258.
41. Stanisheva G. Mineralogy and chemistry of the chromite ores near Dobromirtsi, Kardzhali region (Bulgarian). Rev. Bulg. geol. soc. 1962; 23(2): 149–169.
42. Zhelyazkova-Panayotova M, Kolcheva K. Chromium-nickel-magnetite ore formation. In: Endogenous Ore Formation. Nauka; 1985. pp. 150–158.
43. Naydenova E, Zhelyazkova-Panayotova M, Kudryavtseva G, et al. First finds of laurite and irarsite in Bulgaria (Russian). Comptes Rendus. 1984; 37(2): 183–186.
44. Bazilev BA, Zakariadze GS, Zhelyskova-Panayotova M, et al. Petrology of ultrabasites from the Ophiolite Association of crystalline basement of the Rhodope Massif. Petrology. 1999; 7(2): 191–212.
45. Kozhoukharova E., Daieva L. Petrochemical characteristics of Precambrian amphibolites from the northern parts of the Central Rhodopes. Geologica Balcanica. 1990; 20(4): 19–35. doi: 10.52321/geolbalc.20.4.19
46. Zakariadze GS, Adamia Sh, Kolcheva K. Geochemistry of metabasite series of pre- Alpine ophiolites of the eastern Mediterranean Transcaucasia and Rhodope Massif. Petrology. 1993; 1(1): 50–87.
47. Marinova A, Stankova M. Subduction related mafic rocks from the Sidironero-Mesta unit, Western Rhodopes-geochemistry and preliminare isotope data. In: Proceedings of Geoscieces 2012; Sofia, Bulgaria. pp. 57–58
48. Deschamps F, Godard M, Guillot S, et al. Geochemistry of subduction zone serpentinites: A review. Lithos. 2013; 178: 96–127. doi: 10.1016/j.lithos.2013.05.019
49. Kozhoukharova E. Obducted serpentinites in the Rhodope Massif and their stratigraphic, paleotectonic and metamorphic significance. Rev. Bulg. Geol. Soc. 2019; 80(3): 72–74.
50. Kozhoukharova E. Eclogitized layered serpentinites in the East Rhodope block. Comptes. Rendus. Acad. Bulg. Sci. 1996; 49(6): 69–71.
51. Kozhoukharova E, Ichev M, Pristavova S. Eclogites in the Precambrian of Verila Mountain. Comptes. Rendus Acad. bulg. Sci. 1993; 46(11): 69–72.

52. Machev P, Borisova B, Hecht L. Metaeclogites from the Sredna Gora terrain-petrological features and P-T path of evolution. In: Proceedings of the Geosciences 2006; Sofia, Bulgaria. pp. 185–188.
53. Gaggero L, Buzzi L, Haydoutov I, et al. Eclogite relics in the Variscan orogenic belt of Bulgaria (SE Europe). International Journal of Earth Sciences. 2008; 98(8): 1853–1877. doi: 10.1007/s00531-008-0352-x
54. Zidarov N, Nenova P, Dimov, V. Coesite in kyanite eclogite of Ograzden Mt., SW Bulgaria. Comptes. Rendus Acad. Bulg. Sci. 1995; 48(11–12): 59–62.
55. Nenova P, Zidarov N. Eclogites from Maleshevska Mountain, S.W. Bulgaria. In: Proceedings of the 80th Anniversary of Geology, Sofia University St. Kliment Ohridski; Sofia, Bulgaria. pp. 109–114.
56. Kozhoukharova E. Metasomatic gabbroids—markers in the tectono-metamorphic evolution of the Eastern Rhodopes. Geologica Balcanica. 1999; 29(1–2): 89–109. doi: 10.52321/geolbalc.29.1-2.89
57. Miladinova I, Froitzheim N, Nagel TJ, et al. Late Cretaceous eclogite in the Eastern Rhodopes (Bulgaria): evidence for sibduction under the Sredna Gora magmatic arc. International Journal of Earth Sciences. 2018. doi: 10.1007/s 00531-018-1589-7
58. Georgieva M, Cherneva Z, Hekimova S, et al. Petrology of marbles from the Arda tectonic unit, Central Rhodope, Bulgaria. In: Proceedings of Geosciences 2009; Sofia, Bulgaria. pp. 43–44.
59. Kozhoukharova E, Kozhoukharov D. Pseudomagmatic texture in ophiolites from Rhodope Massif. Geologica Balcanica. 2002; 32(2–4): 27–31. doi: 10.52321/geolbalc.32.2-4.27
60. Jahn-Awe S, Pleuger J, Frei D, et al. Time constraints for low-angle shear zones in the Central Rhodopes (Bulgaria) and their significance for the exhumation of high-pressure rocks. International Journal of Earth Sciences. 2012; 101(7): 1971–2004. doi: 10.1007/s00531-012-0764-5
61. Froitzheim N. Structure and evolution of the Rhodopes. In: Proceedings of Internat. Congress of the CBGA; 7–11 September 2022; Plovdiv, Bulgaria. p. 30.
62. Bonev N, Ovtcharova-Schaltegger M, Moritz R, et al. Peri-Gondwanan Ordovician crustal fragments in the high-grade basement of the Eastern Rhodope Massif, Bulgaria: evidence from U-Pb LA-ICP-MS zircon geochronology and geochemistry. Geodinamica Acta. 2013; 26(3–4): 207–229. doi: 10.1080/09853111.2013.858942
63. Bonev N, Filipov P, Dotseva Z. U-Pb zircon age constraints on a metaophiolite peridotite body from the high-grade metamorphic basement of the eastern Rhodope Massif, Bulgaria. In: Proceedings of Internat. Congres of the CBGA; 7–11 September 2022; Plovdiv, Bulgaria. p. 273.

Journal of Geography and Cartography 2025, 8(1), 10230.
https://doi.org/10.24294/jgc10230

Article

Spatial analysis and classification of land use patterns in Lucknow district, UP, India using GIS and random forest approach

Munizzah Salim[1,*], Shubham Bhattacharjee[1], Neerav Sharma[2], Kavita Sharma[3], Rahul Dev Garg[1]

[1] Department of Civil Engineering, IIT Roorkee, Roorkee 247667, India
[2] Purdue University, IN 47907, United States
[3] Pt. Ravishankar Shukla University, Raipur 492010, India
*** Corresponding author:** Munizzah Salim, munizzah_s@ce.iitr.ac.in

CITATION

Salim M, Bhattacharjee S, Sharma N et al. Spatial analysis and classification of land use patterns in Lucknow district, UP, India using GIS and random forest approach. Journal of Geography and Cartography. 2025; 8(1): 10230. https://doi.org/10.24294/jgc10230

ARTICLE INFO

Received: 19 November 2024
Accepted: 23 December 2024
Available online: 16 January 2025

Abstract: Mapping land use and land cover (LULC) is essential for comprehending changes in the environment and promoting sustainable planning. To achieve accurate and effective LULC mapping, this work investigates the integration of Geographic Information Systems (GIS) with Machine Learning (ML) methodology. Different types of land covers in the Lucknow district were classified using the Random Forest (RF) algorithm and Landsat satellite images. Since the research area consists of a variety of landforms, there are issues with classification accuracy. These challenges are met by combining supplementary data into the GIS framework and adjusting algorithm parameters like selection of cloud free images and homogeneous training samples. The result demonstrates a net increase of 484.59 km^2 in built-up areas. A net decrement of 75.44 km^2 was observed in forest areas. A drastic net decrease of 674.52 km^2 was observed for wetlands. Most of the wastelands have been converted into urban areas and agricultural land based on their suitability with settlements or crops. The classifications achieved an overall accuracy near 90%. This strategy provides a reliable way to track changes in land cover, supporting resource management, urban planning, and environmental preservation. The results highlight how sophisticated computational methods can enhance the accuracy of LULC evaluations.

Keywords: LULC; GIS; ML; spatial analysis; urban planning

1. Introduction

Mapping land use and cover (LULC) is essential to sustainable development, urban planning, and environmental management. Understanding the effects of human activity and natural processes on the environment requires knowledge of the geographical distribution and changes in land use and cover, which is provided by this information [1]. Traditionally, satellite and aerial photo interpretation was done by hand, which took a lot of time and was prone to human mistakes while doing LULC mapping [2]. However, the accuracy, effectiveness, and automation of LULC mapping have been greatly improved by developments in GIS and ML [3].

The integration of various datasets, including topographic maps, socioeconomic data, and remote sensing imagery, is made possible by GIS, which is essential for organizing, interpreting, and visualizing spatial data [4]. Automated pattern recognition and classification in LULC mapping have been possible because of the combination of ML and GIS [5]. The complexity and variability of LULC data have been successfully handled by machine learning, in particular, supervised learning algorithms like Random Forest [6–8], Support Vector Machines [9–12], and Neural Networks [13,14], which provide high classification accuracy (> 85%) even in heterogeneous landscapes [15,16].

The study of high-resolution satellite images, such as data from Landsat, Sentinel, and SPOT, IKONOS satellites, demonstrates the synergy between GIS and machine learning in particular [17–19]. These datasets offer comprehensive data on land cover, but to fully realize their potential, their complexity necessitates the use of sophisticated analytical methods. When combined with GIS, machine learning techniques with its automation, scalability, generalization and adaptiveness allow for important patterns to be extracted from high-dimensional data, resulting in LULC maps that are more precise and comprehensive [20].

Recent research has shown how well GIS and machine learning work together for LULC mapping in a variety of contexts. For instance, Myint et al. [21] mapped Phoenix, Arizona's urban land cover with great precision using object-based image analysis within a GIS framework. Similarly, Akar and Gungor [22] demonstrated the value of machine learning in managing complex landscapes by classifying land cover in Turkey using Support Vector Machines in a GIS setting. Maxwell et al. [23] showed the algorithm's resilience in handling varied land cover types in a different study where they mapped the forest cover in the Brazilian Amazon using Random Forests in conjunction with GIS.

Notwithstanding these developments, there are still difficulties in using machine learning and GIS for LULC mapping. The quality of the input data (data clarity, high resolution, good temporal extent) and the choice of suitable ML methods have an impact on the accuracy of LULC maps [24]. Furthermore, complex data fusion techniques are needed to maximize the information retrieved from each source when merging multi-source data into GIS, such as topographic, radar, and optical imaging [25]. More research is required to obtain more scalability, efficiency and further improve the potential of LULC mapping using GIS and machine learning.

With an emphasis on approaches, case examples, and difficulties, this study examines the state of LULC mapping using GIS and the Random Forest model now. Recent breakthroughs in remote sensing technologies, particularly with satellite imagery and Geographic Information Systems (GIS), have revolutionized the ability to monitor and analyze LULC changes at global, regional, and local scales. These innovations have enabled more precise mapping of land cover types, identification of land use patterns, and detection of environmental changes such as deforestation and urban expansion [26].

2. Study area

Lucknow Metropolis (**Figure 1**) lies between the coordinates of 26˚30′ N to 27˚10′ N latitudes and 80˚30′ E to 81˚13′ E longitudes. It is the capital city of India's most populous state Uttar Pradesh. Lucknow is situated in the middle of the Gangetic Plain and spreads on the banks of the river Gomati, a left-bank tributary of river Ganga. The height of Lucknow city above mean sea level is 123 m. The total land area of Lucknow city is 310 Sq. km. Lucknow has an extensive network of roads and railways and has grown all around in a radius of 25 km. Half of the rainfall occurs from June to October when the city gets an average rainfall of 896.2 mm (35.28 in) from the southwest monsoon winds, and occasionally frontal rainfall from the northeast monsoon will occur in January. Lucknow district is a densely populated district of Uttar Pradesh that witnessed remarkable expansion, growth, and development activities such as significant building construction, construction of highways, etc. Such a rapid increase in land consumption and modifications on land use and land cover changes need to be addressed through spatiotemporal dynamics of various LULC classes.

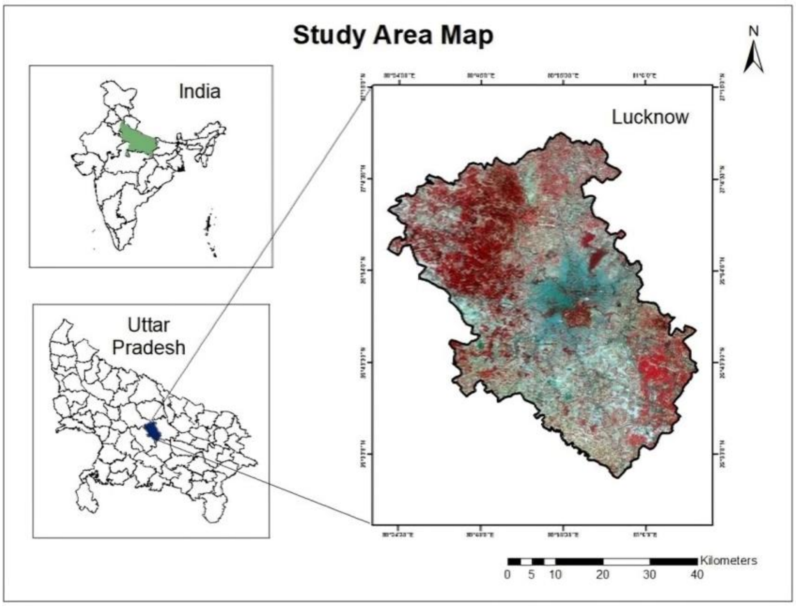

Figure 1. Location map showing the study area.

3. Data used and methodology opted

Cloud-free Landsat series (**Figure 2**) of datasets (resolution ~ 30 m) for the years 2004 (TM sensor) and 2024 (OLI sensor) have been deployed for the present study. Image classification was performed on the Google Earth Engine (GEE) platform. ArcMap was used for data visualization and preparation of maps.

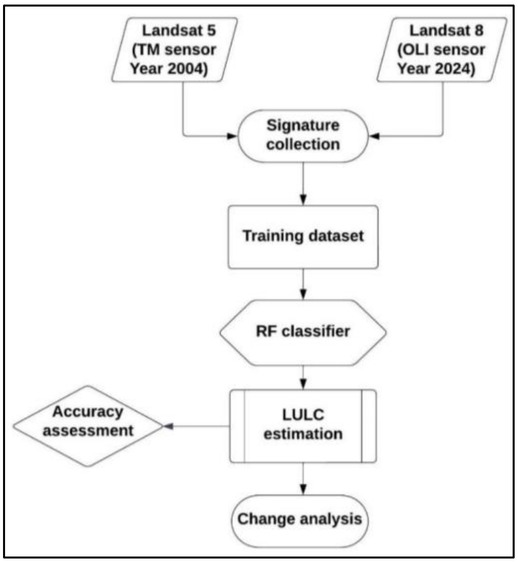

Figure 2. Methodological flowchart for the present study.

The study area boundary and respective cloud free and Top of Atmosphere (TOA) corrected satellite images were imported into the GEE console. Designated image bands (NIR-Red-Green) were assigned to the R-G-B color code for obtaining the fine-scale False color composite (FCC). Signatures corresponding to different land cover classes viz. built-up areas, forests, agriculture, water bodies, and wasteland were collected carefully to prepare the training samples for further use. Training samples on the pure pixels distributed throughout the imagery were selected to maintain class homogeneity. To obtain a singleton set of classes, the different identifiers of the class samples were merged into one. The signatures were then trained respectively for classifying the distinct classes through the satellite imagery.

An ML-based Random forest (RF) classifier was used to classify the imagery into different classes mentioned above based on the collected training samples. Being a bagging algorithm, RF depicts low prediction error for better accuracy. RF classifier works with multiple decision trees (DT). It reduces the variance of the individual DT through random selection. The prediction of a target variable (classes) was made with the usability of the maximum vote provided by each decision tree for every image pixel. To depict the correctness of the classification results, an accuracy assessment through confusion matrix carrying users and producers accuracy was made using Google Earth images. Areas for different classes were computed and transitions in the LULC classes were obtained between the years 2004 and 2024.

4. Results and discussions

The training samples collected were based on the land distribution of the study area, and visual comparison of the natural and false color composite images. There is a considerable amount of change between LULC classes for the years 2004 and 2024. Spatiotemporal changes are depicted in **Figure 3** and **Table 1**.

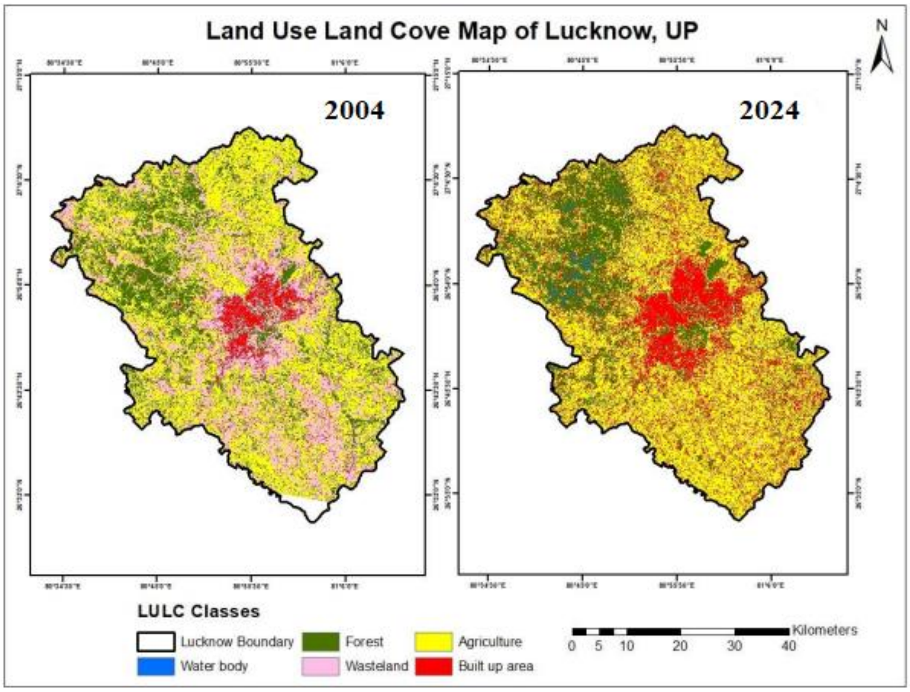

Figure 3. Spatiotemporal LULC dynamics in lucknow.

Table 1. Area changes in different LULC classes.

Classes	Area in 2004 (in km^2)	Area in 2024 (in km^2)
Built up area	157.48	642.07
Forest	611.16	535.72
Agriculture	1035.67	1313.60
Water bodies	23.58	22.02
Wasteland	698.84	24.32

Built-up area (**Figure 4**) increases from 157.48 km^2 to 642.07 km^2 (net increase ~ 484.59 km^2). This is because of rapid urbanization i.e. transmission of rural to urban in Lucknow. Many wastelands were transformed into settlements. Transforming wastelands into state and municipal ownership partially addresses the issue of limited space for high-rise buildings in urban areas, particularly through infill development. The growth was prominently seen over the eastward and southward sides of Lucknow. Growth around the Central Business district is also visible.

Figure 4. Google earth snapshot showing built-up areas of lucknow.

Forest cover (**Figure 5**) decreases from 611.16 km^2 to 535.72 km^2 (net decrease ~ 75.44 km^2). This is because many forested areas are converted into agricultural areas as well and deforestation is becoming a leading problem in the country [27]. So many forests were deforested and converted into built-up areas for settlement zones as well. Clearing forests results in the destruction of habitats for numerous plant and animal species, many of which are at risk of extinction. Additionally, deforestation disrupts the carbon cycle, as trees are essential in absorbing carbon dioxide, a key greenhouse gas. In the absence of trees, carbon is released into the atmosphere, further driving climate change. For instance the forested patch near Barkhurdarpur was degraded significantly throughout the study period.

Figure 5. Google earth snapshot showing forested areas of lucknow.

Agricultural area (**Figure 6**) increases from 1035.67 km^2 to 1313.60 km^2 (net increase ~ 277.93 km^2). This is because many forested areas were converted into agricultural areas as well as many fallow lands have been converted into cropped and matured cropped areas. Many wastelands based on their land suitability for agriculture have also been converted into agricultural areas. In the Misripur area forested patch was converted into agricultural area.

Figure 6. Google earth snapshot showing agricultural areas of lucknow.

The water body is not much affected throughout these 20 years. Forests and settlements cover most of the periphery areas of rivers and water bodies. Gomati River (**Figure 7**) crosses Lucknow. There are some other water bodies in Lucknow such as Kathauta Jheel.

Figure 7. Google earth snapshot showing the gomati river crossing lucknow.

Wasteland shows a major variation in Lucknow as they decrease from 698.84 km^2 to 24.32 km^2 (net decrease ~ 674.52 km^2). Most of the wastelands have been converted into urban areas (**Figure 8**) and agricultural land based on their suitability with settlements or crops. In 2004 generally, wastelands surrounded urban areas whereas in the year 2024, most of them have been converted into built-up areas.

Figure 8. Google earth snapshot showing wasteland converting to built-up areas.

Accuracy assessment was performed for the classified images for both years and confusion matrices were generated using the classified and reference points (collected from high-resolution Google Earth imagery). The confusion matrices with several training samples generated for both years depict classification accuracies of 89 % for the year 2004 (**Table 2**) and 90 % for the year 2024 (**Table 3**).

Table 2. Confusion matrix for the year 2004 (G.T signifies ground truth).

Classes	Ref 1	Ref 2	Ref 3	Ref 4	Ref 5	G.T
Built-up	80	0	0	3	0	80
Forest	0	45	0	7	0	54
Agriculture	0	6	32	0	0	38
Waterbody	0	0	4	51	0	53
Wasteland	9	0	0	2	51	65
Total	89	51	36	63	51	290

Table 3. Confusion matrix for the year 2024.

Classes	Ref 1	Ref 2	Ref 3	Ref 4	Ref 5	G.T
Built-up	72	3	0	0	0	71
Forest	0	60	6	2	0	69
Agriculture	0	6	38	0	0	44
Waterbody	3	0	1	56	0	60
Wasteland	6	9	0	0	61	78
Total	81	78	44	58	61	322

To reduce deforestation, effective strategies include fostering reforestation efforts, enforcing stricter land-use regulations, and advocating for sustainable forestry practices. Managing urban sprawl requires the implementation of smart growth initiatives, encouraging denser development, and enhancing public transportation systems to minimize the need for widespread urban expansion. In the realm of sustainable agriculture, promoting agroecology, diversifying crops, and adopting organic farming practices can help maintain soil health and biodiversity while decreasing reliance on harmful chemicals. By combining these approaches, we can achieve a more harmonious balance between environmental preservation and urban development [28].

The Random Forest classifier is a highly effective and commonly used machine learning algorithm, but it does have certain limitations. One significant issue is its potential to become computationally demanding and slow, especially with large datasets or when a high number of trees are included in the forest. Furthermore, due to the complexity, interpreting Random Forest models can be difficult. There is also a risk of overfitting if the model is not properly tuned, particularly when the number of trees or the depth of the trees is excessively large. These issues can be addressed through hybrid ML models and improved algorithms [29,30] which will fulfil the large computation time gap and the problems of overfitting.

5. Conclusions

This study aimed to identify and analyze general trends in LULC Changes that have taken place in Lucknow district over 20 years using Landsat satellite imagery and ML-based image classification in the GEE platform. The key findings of this study revealed that the major LULC classes of Lucknow district identified include agriculture, forest, wasteland, built-up areas, and water. Significant building construction and deforestation were major drives of LULC dynamics in the Lucknow district over the study period from 2004 to 2024. This study showed a continuous decrease in wasteland areas in the district. Consequently, the urban built-up area and the agriculture area increased. Some future insights could be the integration of IoT for smart technology based embedded infrastructure, waste management etc and urban growth prediction modelling for decision and policymaking. Some other recommendations could be the relationship between urban growth and urban heat islands etc. Such study is required to support environmental policy; physical planning purposes, sustainable land use, and land development.

Author contributions: Conceptualization, MS, SB, and NS; methodology, MS, SB and NS; software, MS and SB; validation, MS and SB; formal analysis, MS, SB and NS; investigation, MS and NS; resources, SB; data curation, MS, SB and NS; writing—original draft preparation, MS, SB and NS; writing—review and editing, MS, SB, NS, KS and RDG; visualization, MS; supervision, KS and RDG; project administration, KS and RDG. All authors have read and agreed to the published version of the manuscript.

Conflict of interest: The authors declare no conflict of interest.

References

1. Lambin EF, Turner BL, Geist HJ, et al. The causes of land-use and land-cover change: Moving beyond the myths. Global Environmental Change. 2001; 11(4): 261–269.
2. Foody GM. Status of land cover classification accuracy assessment. Remote Sensing of Environment. 2002; 80(1): 185–201.
3. Maxwell AE, Warner TA, Fang F. Implementation of machine-learning classification in remote sensing: an applied review. International Journal of Remote Sensing. 2018; 39(9): 2784–2817. doi: 10.1080/01431161.2018.1433343

4. Longley PA, Goodchild MF, Maguire DJ, et al. Geographical Information Systems: Principles, Techniques, Applications, and Management. Wiley; 2005.
5. Mountrakis G, Im J, Ogole C. Support vector machines in remote sensing: A review. ISPRS Journal of Photogrammetry and Remote Sensing. 2011; 66(3): 247–259. doi: 10.1016/j.isprsjprs.2010.11.001
6. Breiman L. Random forests. Machine Learning. 2001; 45(1): 5–32.
7. Svoboda J, Štych P, Laštovička J, et al. Random Forest Classification of Land Use, Land-Use Change and Forestry (LULUCF) Using Sentinel-2 Data—A Case Study of Czechia. Remote Sensing. 2022; 14(5): 1189. doi: 10.3390/rs14051189
8. Tikuye BG, Rusnak M, Manjunatha BR, et al. Land Use and Land Cover Change Detection Using the Random Forest Approach: The Case of The Upper Blue Nile River Basin, Ethiopia. Global Challenges. 2023; 7(10). doi: 10.1002/gch2.202300155
9. Cortes C, Vapnik V. Support-vector networks. Machine Learning. 1995; 20(3): 273–297. doi: 10.1007/bf00994018
10. Ul Din S, Mak HWL. Retrieval of Land-Use/Land Cover Change (LUCC) Maps and Urban Expansion Dynamics of Hyderabad, Pakistan via Landsat Datasets and Support Vector Machine Framework. Remote Sensing. 2021; 13(16): 3337. doi: 10.3390/rs13163337
11. Shi D, Yang X. Support Vector Machines for Land Cover Mapping from Remote Sensor Imagery. In: Li J, Yang X. (editors) Monitoring and Modeling of Global Changes: A Geomatics Perspective. Springer Remote Sensing/Photogrammetry. Springer, Dordrecht; 2015.
12. Waske B, Benediktsson JA. Fusion of Support Vector Machines for Classification of Multisensor Data. IEEE Transactions on Geoscience and Remote Sensing. 2007; 45(12): 3858–3866. doi: 10.1109/tgrs.2007.898446
13. Kavzoglu T, Mather PM. The use of backpropagating artificial neural networks in land cover classification. International Journal of Remote Sensing. 2003; 24(23): 4907–4938. doi: 10.1080/0143116031000114851
14. Sisay G, Gessesse B, Fürst C, et al. Modeling of land use/land cover dynamics using artificial neural network and cellular automata Markov chain algorithms in Goang watershed, Ethiopia. Heliyon. 2023; 9(9): e20088. doi: 10.1016/j.heliyon.2023.e20088
15. Pal M, Mather PM. Support vector machines for classification in remote sensing. International Journal of Remote Sensing. 2005; 26(5): 1007–1011. doi: 10.1080/01431160512331314083
16. Shao Y, Lunetta RS. Comparison of support vector machine, neural network, and CART algorithms for the land-cover classification using limited training data points. ISPRS Journal of Photogrammetry and Remote Sensing. 2012; 70: 78–87. doi: 10.1016/j.isprsjprs.2012.04.001
17. Lu D, Weng Q. A survey of image classification methods and techniques for improving classification performance. International Journal of Remote Sensing. 2007; 28(5): 823–870. doi: 10.1080/01431160600746456
18. Muttitanon W, Tripathi NK. Land use/land cover changes in the coastal zone of Ban Don Bay, Thailand using Landsat 5 TM data. International Journal of Remote Sensing. 2008; 26. doi: 10.1080/0143116051233132666
19. Zhou W, Huang G, Troy A, et al. Object-based land cover classification of shaded areas in high spatial resolution imagery of urban areas: A comparison study. Remote Sensing of Environment. 2009; 113(8): 1769–1777. doi: 10.1016/j.rse.2009.04.007
20. Li J, Shao G. Big data in smart forest management. Forest Ecology and Management. 2014; 331: 1–3.7
21. Myint SW, Gober P, Brazel A, et al. Per-pixel vs. object-based classification of urban land cover extraction using high spatial resolution imagery. Remote Sensing of Environment. 2011; 115(5): 1145–1161. doi: 10.1016/j.rse.2010.12.017
22. Akar Ö, Gungor O. Integrating GIS and Support Vector Machines for Land Use and Land Cover Classification. Journal of Applied Remote Sensing. 2012; 6(1): 063512.
23. Maxwell AE, Strager MP, Warner TA, et al. Comparison of NAIP orthophotography and RapidEye satellite imagery for mapping of forest disturbances in the southeastern United States. Forest Ecology and Management. 2016; 378: 222–236.
24. Friedl MA, McIver DK, Hodges JCF, et al. Global land cover mapping from MODIS: Algorithms and early results. Remote Sensing of Environment. 2002; 83(1–2): 287–302.
25. Gong P, Howarth PJ. Frequency-based contextual classification and grey-level vector reduction for land-use identification. Photogrammetric Engineering and Remote Sensing. 1992; 58(4): 423–437.
26. Turner BL, Meyer WB. Land use and land cover in global environmental change: considerations for study. International Social Science Journal. 1991; 43: 669–679.
27. Forest Survey of India. State of Forest Report, ISFR. Ministry of Environment, Forest and Climate Change. 2021.

28. Weng Q. Remote sensing of impervious surfaces in the urban areas: Requirements, methods, and trends. Remote Sensing of Environment. 2012; 117: 34–49. doi: 10.1016/j.rse.2011.02.030
29. Rey SJ, Anselin L. PySAL: A Python library of spatial analytical methods. In: Handbook of Applied Spatial Analysis. Springer Nature; 2010. pp. 175–193.
30. Friedl MA, Sulla-Menashe D, Tan B, et al. MODIS Collection 5 global land cover: Algorithm refinements and characterization of new datasets. Remote Sensing of Environment. 2010; 114(1): 168–182. doi: 10.1016/j.rse.2009.08.016

Journal of Geography and Cartography 2025, 8(1), 10224.
https://doi.org/10.24294/jgc10224

Article

Harnessing artificial intelligence (AI) towards the landscape of big earth data: Methods, challenges, opportunities, future directions

Zarif Bin Akhtar[1,*], Ahmed Tajbiul Rawol[2]

[1] Department of Computing, Institute of Electrical and Electronics Engineers (IEEE), Piscataway, NJ 08854, USA
[2] Department of Computer Science, Faculty of Science and Technology, American International University-Bangladesh (AIUB), Dhaka 1229, Bangladesh
*** Corresponding author:** Zarif Bin Akhtar, zarifbinakhtarg@gmail.com

CITATION

Akhtar ZB, Rawol AT. Harnessing artificial intelligence (AI) towards the landscape of big earth data: Methods, challenges, opportunities, future directions. Journal of Geography and Cartography. 2025; 8(1): 10224. https://doi.org/10.24294/jgc10224

ARTICLE INFO

Received: 30 November 2024
Accepted: 31 December 2024
Available online: 21 January 2025

Abstract: The integration of Big Earth Data and Artificial Intelligence (AI) has revolutionized geological and mineral mapping by delivering enhanced accuracy, efficiency, and scalability in analyzing large-scale remote sensing datasets. This study appraisals the application of advanced AI techniques, including machine learning and deep learning models such as Convolutional Neural Networks (CNNs), to multispectral and hyperspectral data for the identification and classification of geological formations and mineral deposits. The manuscript provides a critical analysis of AI's capabilities, emphasizing its current significance and potential as demonstrated by organizations like NASA in managing complex geospatial datasets. A detailed examination of selected AI methodologies, criteria for case selection, and ethical and social impacts enriches the discussion, addressing gaps in the responsible application of AI in geosciences. The findings highlight notable improvements in detecting complex spatial patterns and subtle spectral signatures, advancing the generation of precise geological maps. Quantitative analyses compare AI-driven approaches with traditional techniques, underscoring their superiority in performance metrics such as accuracy and computational efficiency. The study also proposes solutions to challenges such as data quality, model transparency, and computational demands. By integrating enhanced visual aids and practical case studies, the research underscores its innovations in algorithmic breakthroughs and geospatial data integration. These contributions advance the growing body of knowledge in Big Earth Data and geosciences, setting a foundation for responsible, equitable, and impactful future applications of AI in geological and mineral mapping.

Keywords: artificial intelligence (AI); big earth data; computer vision; data science; deep learning (DL); earth observations; geospatial data; machine learning (ML)

1. Introduction

In an era defined by rapid technological advancements, the convergence of Big Earth Data and Artificial Intelligence (AI) is revolutionizing geological and mineral mapping, offering transformative potential for the geosciences and resource management sectors.

Big Earth Data, characterized by its vast, multi-dimensional, and complex nature, provides unparalleled opportunities for analyzing Earth's surface and subsurface dynamics [1–3]. When coupled with AI and machine learning techniques, this data can be translated into actionable insights, facilitating deeper understanding of geological formations, mineral distributions, and critical Earth processes. Traditional geological mapping approaches, while reliable, have relied on labor-intensive methods such as manual interpretation and extensive fieldwork.

These processes, though effective, are often time-consuming, expensive, and constrained in scope [4–6]. The integration of AI into remote sensing and Big Earth Data analysis marks a paradigm shift, enabling the development of efficient, accurate, and scalable mapping techniques.

AI-powered models, particularly machine learning and deep learning algorithms, can identify subtle patterns and anomalies within massive datasets—details that might otherwise go unnoticed by human analysts [7–9]. This capability significantly enhances the precision and reliability of geological interpretations and fosters innovative solutions for industries such as mining, environmental management, and natural resource exploration.

This study provides a comprehensive analysis of the integration of AI with Big Earth Data in geological and mineral mapping. It delves into the critical criteria for selecting AI methodologies, evaluates their performance in comparison to traditional techniques, and examines the ethical and social implications of their application [10–12]. Notably, it highlights the role of organizations like NASA in advancing the use of AI for geospatial data analysis, demonstrating the current relevance and future potential of these technologies. Additionally, the paper incorporates case studies and quantitative analyses to showcase practical applications and performance metrics, emphasizing innovation in algorithms and integration methods.

By addressing challenges such as data quality, computational demands, and model transparency, this research aims to present actionable insights for responsible and equitable applications of AI in geosciences. Through a balanced discussion of the opportunities, challenges, and ethical considerations, this study seeks to advance the understanding of how AI and Big Earth Data can contribute to more sustainable, efficient, and informed approaches to geological exploration and resource management.

2. Methods and experimental analysis

This study adopts a multi-faceted approach combining Big Earth Data, machine learning algorithms, and remote sensing technologies to advance geological and mineral mapping. The methodology is systematically structured into the following phases: data acquisition, data preprocessing, model development, validation, and application to case studies. To ensure clarity and rigor, the selected AI techniques and case studies are elaborated upon, emphasizing their innovative contributions and quantitative evaluation metrics.

The data acquisition phase involves collecting extensive Big Earth Data from diverse sources, including satellite imagery, airborne sensors, and geospatial databases. These datasets include multispectral and hyperspectral images, digital elevation models (DEMs), geological surveys, and other relevant geospatial data. Publicly available datasets from institutions like the United States Geological Survey (USGS), European Space Agency (ESA), and Copernicus Open Access Hub are prioritized to ensure comprehensive spatial and temporal coverage. The selection criteria for these datasets focus on their relevance to the geological formations and mineral deposits under study, aligning with the research’s specific objectives and case study requirements.

For example, regions with active exploration and significant geological complexity were prioritized to demonstrate the robustness of the methodology. Given the complexity and heterogeneity of Big Earth Data, data preprocessing is a critical component of the methodology. Preprocessing tasks include data cleaning to remove noise and artifacts, normalization to standardize data ranges, and transformation to enhance data interpretability. Techniques such as median filtering and principal component analysis (PCA) are applied to improve data quality and reduce redundancy.

For multispectral and hyperspectral datasets, band selection and dimensionality reduction are conducted, focusing on spectral bands most relevant to mineral detection. Geospatial data undergo re-projection and resampling to ensure uniformity across datasets, and diverse sources are integrated through spatial alignment and temporal synchronization. This unified and high-quality dataset forms the foundation for subsequent AI-driven analysis. The model development phase involves tailoring machine learning algorithms for geological and mineral mapping. Both supervised and unsupervised learning methods are employed to address different analytical needs. Supervised learning algorithms, such as Random Forest (RF) and Support Vector Machines (SVM), are used for classification tasks, while unsupervised methods like k-means clustering and self-organizing maps (SOM) are utilized for pattern detection and anomaly identification. For more complex feature extraction and spatial pattern recognition, deep learning models, particularly Convolutional Neural Networks (CNNs), are deployed. The models are trained using labeled datasets where ground truth data, such as known mineral deposits and geological features, provide validation. The training process includes iterative optimization of model parameters to achieve high accuracy and generalization capabilities.

To address challenges related to model interpretability and performance, the methodology incorporates quantitative analysis of model outputs. Metrics such as accuracy, precision, recall, and F1-score are calculated to evaluate model performance. Additionally, confusion matrices and receiver operating characteristic (ROC) curves are used to assess classification reliability. Comparative analyses with traditional geological mapping methods, such as manual interpretation and field surveys, highlight the advancements achieved through AI integration.

The validation process employs cross-validation techniques, where the dataset is partitioned into training and testing subsets to minimize overfitting and enhance reliability. Independent datasets from different geographical regions are used to further validate the models, demonstrating their robustness across varying geological contexts. Quantitative performance comparisons with traditional methods are conducted to underscore the improvements in efficiency and precision.

Finally, the application to real-world case studies provides practical insights into the methodology's effectiveness. Selected regions with known geological complexities and significant mineral potential, such as areas with diverse lithological compositions or active mining zones, serve as test cases. The AI-driven models analyze these regions to identify mineral-rich zones and geological features, with results compared to existing geological maps and field data. This phase includes detailed quantitative performance metrics and visual representation of results through enhanced charts, graphs, and geospatial visualizations to effectively convey complex findings.

The methodology also integrates a discussion of the ethical and social considerations, addressing issues like data privacy, environmental sustainability, and equitable access to AI technologies in geological exploration. By highlighting these dimensions, the research emphasizes responsible innovation and the need for balanced technological advancements. Through this comprehensive and systematic methodology, the study not only demonstrates the feasibility of integrating Big Earth Data and AI for geological and mineral mapping but also establishes a framework that is replicable and adaptable for future research in geosciences. The focus on quantitative analysis, innovative algorithms, and practical applications ensures a credible and impactful contribution to the field.

3. Background research and investigative exploration towards available knowledge

Earth observation (EO) involves the interconnected systematic collection of data regarding both the physical, chemical, and also the biological systems of the Earth. This process can be further executed through various remote-sensing technologies, including satellites that constantly orbit the Earth, as well as all the associated direct-contact sensors which are located on ground-based or airborne platforms, such as the weather stations and various types of balloons. The overall information gathered through EO is very crucial for monitoring and assessing all the changes in both the natural and the built environments [1–3]. The term "Earth observation" has many types of different connotations depending on the particular region. In the areas of Europe, it often refers specifically to the satellite-based remote sensing, though it can also include in situ and the airborne observations. In the areas of the United States, the term "remote sensing" has been in use since the early 1960s and broadly refers to any observation method that utilizes types of remote sensing technology, whether it be from space, air, or any other type of ground-based platforms [4–6].

Recently, the acronym "Satellite Remote Sensing" (SRS) has begun appearing in literature as a more precise term for satellite-based observations. EO encompasses a wide array of activities, ranging from numerical measurements taken by instruments like thermometers and seismometers to photos and radar images captured by satellites or ground-based sensors. The data collected through these various means can be processed into decision-support tools such as maps and models, which are invaluable in a multitude of applications [7–9]. These include numerous weather forecasting, tracking inclusion for biodiversity and wildlife trends, measuring types of land-use changes like deforestation, and also heavily monitoring natural disasters such as fires, floods, and earthquakes.

The field of Earth observation is rapidly evolving at a high pace, with the continuous advancements in both the quality and quantity of the many types of data collected. The deployment of new remote-sensing satellites, along with their associated increasingly sophisticated in situ instruments located on the ground, in the air, and in water bodies, has resulted in comprehensive, nearly real-time observations. These technological advancements have become increasingly very much important in light of the significant impact modern human civilization has on the planet in terms of digital computing.

EO plays a critical role in mitigating these effects, such as monitoring geohazards, and offers opportunities to enhance social and economic well-being. Earth observation is a broad and multifaceted field that combines various technologies and methods to monitor the Earth's systems. Its applications are diverse and very much essential for understanding and responding to the rapid environmental changes, managing natural resources, and improving overall societal welfare [10–12].

A Digital Elevation Model (DEM) is basically a 3D computer graphics representation of the elevation data used to depict terrain or surface features of planets, moons, or asteroids. DEMs are more extensively used in terms of geographic information systems (GIS) as the foundation for digitally produced relief maps [13–15]. The term "DEM" is also often used many times interchangeably with Digital Surface Models (DSM) and Digital Terrain Models (DTM).

While DSMs include natural and man-made features like tree canopies and buildings, DTMs focus solely on representing the bare ground surface, making them crucial for applications such as flood modeling, geological studies, and land-use analysis. Terminology in the field of digital elevation modeling varies.

DEM is a broad term that can encompass both DSMs and DTMs, depending on the context. DSMs mainly represent the Earth's surface, including objects like buildings and trees, while DTMs represent only the bare ground. The term DEM is often used generically, without specifying whether it refers to DSMs or DTMs. The creation of DTMs typically involves filtering out surface objects from high-resolution DSMs through a process called "bare-earth extraction".

There are a lot of different types of DEMs, which can be very much represented either as a raster grid (often referred to as a heightmap when dealing with elevation) or as a vector-based Triangular Irregular Network (TIN). DEMs can be created using various techniques, including photogrammetry, lidar, and radar. Data for DEMs is commonly gathered through remote sensing methods, although traditional land surveying can also be used, especially in areas where remote sensing is less effective. Rendering of DEM data often involves visual forms like contoured topographic maps or color-coded elevation maps [16–18].

In some cases, oblique views are created to provide a more intuitive visualization of the terrain, with techniques like "vertical exaggeration" used to highlight subtle elevation changes. However, the use of vertical exaggeration is sometimes criticized for potentially misleading viewers about the actual landscape.

Production methods for DEMs have evolved a lot over time. While the early methods mainly relied on interpolating contour maps from land surveys, modern DEMs are mainly primarily generated using remote sensing technologies such as radar and satellite imagery. For instance, interferometric synthetic aperture radar (InSAR) is a very powerful technique that allows for the creation of DEMs over large types of areas with much high resolution.

Satellite missions like SPOT, ERS, SRTM, and ASTER have provided significant contributions to the global availability of DEM data. In planetary mapping, DEMs have become invaluable tools, especially through the use of orbital altimetry. Instruments much like the Mars Orbiter Laser Altimeter (MOLA) and the Lunar Orbital Laser Altimeter (LOLA) have been very much instrumental in terms of mapping the topography of Mars and the Moon, respectively.

Accuracy is a critical aspect of DEMs, influenced by factors such as terrain roughness, sampling density, grid resolution, and the algorithms used for interpolation and terrain analysis [19–21]. DEM quality is typically assessed by comparing DEMs from different sources. High-quality DEMs are essential for accurate modeling of terrain-related phenomena. DEMs have a wide range of applications, including geomorphology, hydrology, infrastructure design, and 3D visualizations. They are used for modeling water flow, creating relief maps, planning flights, and even for precision farming. DEMs are also used in engineering, satellite navigation, and archaeology, among other fields.

Sources of DEM data vary by a great margin globally. Free global DEM datasets like FABDEM and GTOPO30 provide a very wide coverage, although the resolution and quality can vary by a great amount significantly. Higher resolution DEMs are also available from sources like the ASTER instrument and the Shuttle Radar Topography Mission (SRTM). These types of datasets are crucial for a wide range of scientific and practical applications, including both global relief modeling and terrain analysis.

Digital Elevation Models are also the essential tools in terms of various scientific and engineering fields, offering a more detailed representations of the Earth’s surface and other planetary bodies.

The development and application of DEMs still continue to advance with improvements in terms of remote sensing technology and data processing techniques. Environmental data which mainly refers to the information derived from measuring environmental pressures, along with the state of the environment, and the impacts on the interconnected ecosystems [22–24].

These components are integral to the DPSIR (Drivers, Pressures, State, Impact, Response) model, commonly used in environmental science to analyze and manage environmental issues. While environmental data primarily encompasses the “P,” “S,” and “I” elements of this model, it excludes socio-economic data and other statistical information often associated with the “D” and “R” components. However, for a comprehensive environmental assessment, these socio-economic and statistical data are crucial, though they are typically managed by institutions outside the environmental sector, such as National Statistical Offices.

Similarly, geo-basis data, while not classified as environmental data, are essential for effective environmental policy-making and information management. Environmental data is predominantly generated by institutions engaged in executing environmental laws or conducting environmental research [25–27]. This data serves as the backbone for environmental assessments, regulatory compliance, and policy-making. The increasing significance of environmental data in various sectors has also been recognized by the financial industry.

For instance, Bloomberg L. P. has begun providing Environmental, Social, and Governance (ESG) data through its terminals, reflecting the growing demand for this information among investors. ESG data, which includes environmental data, is becoming a critical factor in investment decisions, as investors seek to align their portfolios with sustainable and socially responsible business practices. To manage the complexities of collecting, processing, and reporting environmental data, especially in compliance with legal and regulatory requirements, Environmental Data Management Systems (EDMS) are increasingly being adopted.

These systems are designed to handle the various aspects of environmental data management, such as monitoring programs, data validation, and the generation of compliance reports. The implementation of EDMS is driven by the need to ensure accurate and timely data collection, meet compliance requirements, and reduce the administrative burden associated with environmental data management [28,29].

The growing importance of ESG factors, including environmental data, is further highlighted by predictions that ESG assets under management could reach $53 trillion within the next few years, accounting for one-third of all global assets under management. This trend is driven by factors such as fee pressure, increasing regulatory demands, and the push from asset owners for investments that are not only financially profitable but also aligned with sustainable and socially just practices. As a result, environmental data is truly playing an increasingly critical role in terms of shaping the future of both the environmental policy and global investment strategies [30–32].

An Earth observation satellite, also known as an Earth remote sensing satellite, is mainly a type of satellite which is specifically designed to observe and monitor the Earth's environment from space. These satellites also serve other types of various purposes, including environmental monitoring, meteorology, cartography, and even intelligence gathering, as seen with many spy satellites [33–35]. The most common type of Earth observation satellites are the imaging satellites, which capture images of the Earth's surface, similar to the aerial photographs.

However, some other satellites perform remote sensing without producing images, such as those which are mainly involved in GNSS (Global Navigation Satellite System) radio occultation, which measures atmospheric properties.

The root history of satellite remote sensing began mainly with the launch of Sputnik 1 by the Soviet Union on 4 October 1957. Sputnik 1 sent radio signals back to Earth, which scientists actually used to study the ionosphere, marking the first instance of satellite-based remote sensing. Following this, the United States also launched its first satellite, Explorer 1, on 31 January 1958. The data from Explorer 1's radiation detector led to the root discovery of the Earth's Van Allen radiation belts. Another significant milestone was the launch of TIROS-1 on 1 April 1960, by NASA. TIROS-1 which was the first satellite to send back the television footage of weather patterns from space, laying the root foundation for modern types of weather satellites. By 2008, there were almost over 150 Earth observation satellites in orbit, collecting vast amounts of information data daily. This number grew much significantly, reaching over 950 satellites by 2021, with the majority mainly operated by the US-based company Planet Labs. Most types of Earth observation satellites operate at relatively low altitudes, generally above 500 to 600 km, to fully capture detailed images and data.

However, the lower orbits require frequent reboost of maneuvers due to the atmospheric drag. Many Earths observation satellites, including those which are mainly operated by the European Space Agency (ESA) and the UAE, utilize low Earth orbits (LEO) to provide a much better high-resolution imagery and data [36–38].

To achieve global coverage, many Earth observation satellites are placed within the polar or Sun-synchronous orbits. A polar orbit mainly allows the satellite to scan different parts and sections of the Earth with each orbit due to the Earth's rotation.

Sun-synchronous orbits additionally ensures that the satellite passes over the same spot-on Earth at the same time each day, providing a more consistent lighting conditions for observations.

In contrast with that, geostationary orbits, located at a high altitude of 36,000 kilometers, allow the satellites to remain at fixed over a specific point on the Earth's surface, providing more continuous coverage of that particular area. This type of orbit is primarily used for meteorological satellites. Earth observation satellites have also many numerous applications, including weather monitoring, environmental monitoring, and mapping. Weather satellites, for example, tracks the cloud patterns, monitor volcanic ash clouds, and observing for smoke from wildfires. Environmental satellites detect changes within vegetation, atmospheric gases, sea conditions, and ice fields, aiding within the monitoring of droughts, oil spills, and pollution. Mapping satellites, such as the Radarsat-1 and TerraSAR-X, provide detailed terrain maps using the radar technology.

International regulations that govern the use of Earth observation satellites, particularly regarding the allocation of many radio frequencies for communication between satellites and their associated ground stations. The International Telecommunication Union (ITU) mainly defines Earth exploration-satellite service as a radiocommunication service that mainly collects and distributes data related to the Earth's characteristics and its natural phenomena. These regulations ensure that satellite operations are harmonized globally, with frequency allocations managed by national administrations.

Earth observation satellites play a crucial role in monitoring and understanding the Earth's environment, providing valuable data for various scientific, environmental, and commercial applications. Their importance continues to grow as technology advances and the demand for accurate and timely environmental data increases [39,40]. Geographic data and information, also known as geospatial data, refers to any data that is implicitly or explicitly associated with a specific location on Earth.

This type of data is critical for understanding and analyzing spatial relationships and patterns. It is commonly stored in Geographic Information Systems (GIS), which are specialized systems designed to capture, store, manipulate, analyze, and manage spatial or geographic data. GIS allows for the integration of various types of geographic information, enabling users to visualize, interpret, and understand spatial relationships and trends in the data.

There are several different types of geospatial data, including vector files, raster files, geographic databases, web files, and multi-temporal data. Each type of data has its unique characteristics and uses. For instance, vector files represent geographic features as points, lines, and polygons, making them ideal for mapping boundaries, roads, and other discrete objects.

Raster files, on the other hand, consist of grid cells that store data, such as satellite imagery or elevation models, making them suitable for continuous data representation. Geographic databases are used to store and manage large volumes of geospatial data, while web files allow for the sharing and dissemination of geographic information over the internet. Multi-temporal data refers to geospatial data collected at different times, which is essential for analyzing changes over time, such as in environmental monitoring or urban development studies.

Geospatial data and information are central to the various type areas fields of study, including geocomputation, geographic information science (GIScience), geoinformatics, and also geomatics. These fields also overlap in their focus on the acquisition, analysis, and interpretation of the geographic data [41,42]. For instance, geocomputation involves the use of computational techniques to solve geographic problems, while GIScience focuses on the theoretical and scientific aspects of geographic information systems and technology. Geoinformatics and geomatics encompass a broader range of activities, including the collection, processing, and analysis of geographic data using various technologies. In addition to these core fields, geospatial data and information are also relevant to other related disciplines such as cartography, geodesy, geography, geostatistics, photogrammetry, remote sensing, spatial data analysis, surveying, and topography. Cartography is termed the art and science of map-making, geodesy deals with the measurement and representation of the Earth, and geography studies the overall physical and human features of the Earth's surface [43,44].

Geostatistics involves statistical analysis of spatial data, photogrammetry focuses on obtaining measurements from photographs, and remote sensing refers to the acquisition of information about the Earth's surface using satellite or aerial sensors. Spatial data analysis is concerned with examining spatial patterns and relationships in data, surveying involves the precise measurement of land, and topography studies the Earth's surface features. Geographic data and information are fundamental to a wide range of scientific, engineering, and planning activities. They enable the visualization and analysis of spatial patterns and relationships, which are essential for making informed decisions in areas such as urban planning, environmental management, transportation, and disaster response. The growing availability of geospatial technologies and data has expanded the possibilities for research and application, making geographic information a vital component of modern science and technology.

The Earth Observing System Data and Information System (EOSDIS) is a very vital component of NASA's Earth Science Data Systems Program. Designed and mainly maintained by Raytheon Intelligence & Space, EOSDIS provides a very detailed with a comprehensive platform for managing and disseminating Earth science data [33–44]. This system also supports a wide range of users, from casual individuals to the specialized research scientists selected through NASA's peer-reviewed processes. EOSDIS offers many several key services, including the user support, data archiving, management, distribution, information management, and product generation, all which are overseen by the Earth Science Data and Information System (ESDIS) Project. EOSDIS is integral to the handling of data information from NASA's Earth-observing satellites. The whole system ingests, processes, archives, and distributes vast amounts of data information from these satellites, as well as data information from aircraft, field measurements, and other types of programs. The system also provides end-to-end capabilities for managing this type of data, ensuring that it is also very much accessible to a global user base. EOSDIS's capabilities are divided into many mission operations, managed by the Earth Science Mission Operations (ESMO) Project, and science operations, overseen by the ESDIS Project. These operations also include data capture, initial processing, and higher-level science data product generation, archiving, and distribution.

A key feature of the EOSDIS is its distributed system of processing the facilities and Distributed Active Archive Centers (DAACs), spread all across the United States. These DAACs serve as the custodians of Earth science data, ensuring its associated long-term preservation and accessibility. Each DAAC specializes in a very specific Earth science discipline, providing tailored services and tools to its designated user community.

The DAACs manage a massive and ever-growing database, with EOSDIS reporting around 10 petabytes of data by 2012, with a daily ingestion rate of approximately around 8.5 terabytes. EOSDIS also includes many systems for searching and accessing data, such as the Global Change Master Directory (GCMD) and the Common Metadata Repository (CMR). The GCMD is a directory of over 30,000 Earth science data information sets and services, while the CMR serves as a metadata catalog and complex registry for NASA's EOS data. In 2018, Earthdata Search replaced Reverb as the web-based client for discovering and ordering data across EOSDIS's holdings, allowing many users to search, retrieve, and order data through a much better user-friendly interface. The root level history of EOSDIS dates back to the early 1980s, when NASA began mainly exploring the feasibility of publicly accessible electronic data information systems. By 1990, the EOS mission, which also included the NASA Earth Science Enterprise, had been approved by the Congress. This mission supported the entire development of EOSDIS, designed as a long-term data and information system accessible to both the scientific community and the interconnected broader public. Over the years, EOSDIS has evolved to a great scale in terms to meet the growing demands of Earth science research, providing a more critical support for NASA's Earth-observing missions and serving a diverse global community of users around the globe.

Microsoft AI for Earth is another significant initiative launched within July 2017, focused on leveraging artificial intelligence (AI) to address critical environmental challenges. The project is part of Microsoft's broader commitment to social good, particularly in areas related to agriculture, water, biodiversity, and climate change [40–45]. The AI for Earth program is active in 40 countries, working on various projects aimed at improving the sustainability and management of the planet's resources. The initiative was launched with an initial investment of $2 million, but due to its growing impact and potential, Microsoft later expanded its strategic approach and allocated a $50 million budget to support its goals. AI for Earth has formed 50 partnerships and supported 950 projects globally, demonstrating its expansive reach and commitment to addressing environmental issues through AI-driven solutions.

One of the program's most notable developments is the creation of the "Planetary Computer." This platform also offers a wide range of tools and resources, including APIs, data catalogs through Azure storage, and many open-source tools, all designed to empower researchers and organizations to analyze and act on environmental data. The Planetary Computer represents a momentous advancement in the availability of data and computational resources for environmental science, enabling more operative and scalable solutions to the challenges facing our planet. Key figures involved in the AI for Earth initiative include Lucas Joppa, Bruno Sánchez-Andrade Nuño, Alma Cárdenas, and Harry Shum, who have been instrumental in driving the program's vision and execution.

The initiative aligns with Microsoft's broader mission of using technology for social good, with AI for Earth serving as a prime example of how AI can be harnessed to create a positive impact on both the environment and society.

4. Big earth data: The AI perspectives

Artificial Intelligence (AI) has truly become an integral part of NASA's efforts to enhance the analysis and utilization of the overall vast amounts of Earth observation data. AI, particularly through machine learning (ML), enables machines to simulate the human decision-making processes and identify many complex patterns within large amounts of datasets that would be difficult, if not impossible, for humans to discern manually. This advanced capability is especially valuable in processing and analyzing Big Data collections, such as the overall extensive data generated by NASA's Earth observing missions.

NASA's Earth Science Data Systems (ESDS) Program is also very much deeply committed to incorporating AI and ML into its associated operations to maximize the scientific return of its missions. This commitment is very much evident in the work conducted by NASA's Interagency Implementation and Advanced Concepts Team (IMPACT) at the Marshall Space Flight Center in Huntsville, Alabama. The IMPACT team comprises machine learning (ML) specialists, computer scientists, and Earth science data experts who also collaborate to develop tools and pipelines that apply within ML algorithms to NASA's Earth science datasets.

These tools significantly enhance data discovery and the overall efficiency of all the research processes. In addition to this groundbreaking work of IMPACT, AI and ML are also being utilized at NASA's Distributed Active Archive Centers (DAACs). For instance, the Goddard Earth Sciences Data and Information Services Center (GES DISC) is implementing a machine learning (ML) framework that uses natural language processing (NLP) to streamline the whole search process for data users, making it much easier for them to actually locate all the required relevant datasets.

NASA also fosters AI and ML research through its Advancing Collaborative Connections for Earth System Science (ACCESS) program. This competitive program mainly focuses on developing and implementing new technologies to manage, discover, and utilize NASA's extensive archive of Earth observations. The ACCESS 2019 solicitation specifically targeted technology developments in ML, including the innovative creation of new training datasets for machine learning applications further related to Earth science.

Furthermore, NASA supports AI and ML research through initiatives like the Frontier Development Lab (FDL), which mainly operates as an applied research accelerator at NASA's Ames Research Center in Silicon Valley, California. The FDL, created by NASA's Office of the Chief Technologist, collaborates with many academic institutions and Silicon Valley companies to advance AI research, further extending NASA's AI capabilities.

AI and ML are rapidly playing increasingly critical roles in NASA's Earth science endeavors, driving innovations that improve the utility and accessibility of Earth observation data information. Through collaborative efforts, research programs, and technological advancements, NASA still continues to push the boundaries of what AI and ML can achieve within the realm of Earth science, contributing to a more efficient and effective research and applications that will benefit both the scientific community and society at large.

5. NASA AI, DL, ML perspectives: Case studies analysis

5.1. Case study 1: Radiant earth

Radiant Earth has made significant strides within enhancing access to the Earth observation training data and machine learning (ML) models through the accelerated development of an open-access repository, Radiant MLHub. This initiative, part of the ACCESS-19 project, has focused on three main areas: creating a comprehensive global land cover training dataset, developing an open API for machine learning model registration and retrieval, and improving user accessibility through a Python client. One of the key achievements of this project is the production of the LandCoverNet dataset, a multi-mission global land cover training dataset.

This dataset consists of 8941 image chips, each measuring 256 × 256 pixels, derived from 300 geographically diverse tiles of Sentinel-2 imagery. These images span various many regions, including Africa, Asia, Australia and Oceania, Europe, North America, and also South America. The dataset also includes a yearly time series of matching Sentinel-1, Sentinel-2, and Landsat-8 imagery. Published in 2020, LandCoverNet has become one of Radiant MLHub's most downloaded datasets, underscoring its value to the machine learning and Earth observation communities.

In addition to the dataset, Radiant Earth has expanded the functionality of Radiant MLHub to support the publishing and retrieval of machine learning models. Users can now access a catalog of models through the STAC API, complete with documentation, model weights, and code, all accessible via the web interface. This expansion significantly broadens the utility of Radiant MLHub, making it a more comprehensive resource for researchers and developers working with Earth observation data. To further simplify the process of accessing these resources, Radiant Earth developed a Python client. This client allows users to programmatically search for, access, and download machine learning training datasets and models from Radiant MLHub. The introduction of this tool has reduced the complexity of interacting with the repository, making it more user-friendly and accessible to a broader audience.

Looking ahead, Radiant Earth has begun developing the next generation of Radiant MLHub, known as Source Cooperative. This new platform is designed to support extremely large training datasets and expands the dataset publishing capabilities beyond just machine learning training data. Currently in private beta, Source Cooperative is expected to enter public beta in the third quarter of 2023, marking the next phase in Radiant Earth's mission to democratize access to high-quality Earth observation data and ML resources.

5.2. Case study 2: The ESDS program project

The ESDS program project focuses on the development of an advanced platform that mainly integrates satellite observations, 3D radiative transfer simulations, deep learning (DL) techniques, and cloud computing to further enhance global cloud property retrieval. By utilizing data information from the Visible Infrared Imaging Radiometer Suite (VIIRS) on the Suomi National Polar-orbiting Satellite (Suomi NPP) and the Advanced Baseline Imager (ABI) on the Geostationary Operational Environmental Satellite-16 (GOES-16), the project aims to establish a versatile framework applicable across different satellites for retrieving the cloud properties. This initiative is crucial for refining and benchmarking various algorithms used in satellite-based cloud remote sensing. The primary objectives of the project include generating high-quality cloud physics property retrievals, such as cloud masks and cloud phases, through deep learning models that can handle multi-sensor heterogeneous data.

The project seeks to produce realistic cloud microphysics and optical property retrievals, including Cloud Optical Thickness (COT) and Cloud Effective Radius (CER), using the 3D radiative transfer simulations combined with many types of deep learning (DL) models. Another key goal is to develop scalable cloud computing-based services for enhanced processing and analyzing vast amounts of data, facilitating the implementation of cloud retrieval algorithms on a global scale. Clouds, which cover about two-thirds of Earth's surface, also plays a vital role in regulating the climate and influencing the types of various environmental cycles. Given their significance, satellite-based remote sensing has truly become essential for global cloud observation. This project aligns with the priorities set within NASA's latest Decadal Survey, which also emphasizes the importance of cloud observations in Earth science missions.

Various types of satellite sensors, both active and passive, have been developed to observe and retrieve cloud properties. Active sensors, like those available on the Cloud Aerosol Lidar and Infrared Pathfinder Satellite Observation (CALIPSO) and CloudSat missions, excel within resolving the vertical location of cloud layers, especially during nighttime and mainly over polar regions. In contrast to that, passive sensors, such as MODIS, VIIRS, and ABI, offer the superior spatial sampling rates.

5.3. Case study 3: Machine learning (ML) data workflows

Machine learning (ML) has revolutionized many fields, including satellite remote sensing. In this project, ML and deep learning (DL) techniques are mainly employed to improve cloud property retrieval. High-quality training datasets are very crucial for these models, which is why the project combines data from both active and passive sensors, advances in 3D radiative transfer simulations, and deep learning methods. This approach addresses the biases and uncertainties associated with traditional 1D radiative transfer models and facilitates the development of 3D cloud property retrievals. Additionally, the project leverages cloud computing and Big Data technologies to manage and analyze the vast archive of Earth observations efficiently.

Among the project's major accomplishments are the development of scalable satellite collocation data and toolkits, including CALIPSO-VIIRS and CALIPSO-ABI collocation datasets. These tools have been approved for the New Technology Report (NTR) and Software Release Request (SRS), and are now open-source on GitHub. The project also produced 3D radiative transfer simulation data information for synthetic cloud fields, such as fractal and Large-Eddy-Simulation (LES) clouds.

Furthermore, the collaborative team developed two deep learning (DL) models for cloud property retrieval, which have demonstrated superior performance compared to existing physics-based and deep learning approaches. These models have also received NTR approvals, and their source codes will be made available as open-source software, contributing to the broader scientific community's efforts in atmospheric remote sensing.

5.4. Case study 4: Geoweaver workflow management system

GeoWeaver is an innovative workflow management system designed to enhance the productivity and collaboration of Earth scientists by integrating Python code and Shell scripts into seamless, shareable pipelines. The system addresses the need for a flexible and intuitive tool that enables researchers to efficiently manage and execute complex workflows while ensuring that these workflows are Findable, Accessible, Interoperable, and Reusable (FAIR). By providing an intuitive interface that simplifies the creation, execution, and sharing of AI workflows, GeoWeaver aims to eliminate duplicated efforts, streamline knowledge transfer, and foster collaboration among scientists with varying technical expertise. One of the primary objectives of GeoWeaver is to make AI workflows more tangible and accessible to both beginners and experienced researchers.

The platform's design allows its associated users to quickly understand and contribute to existing projects, thereby accelerating the transition from learners to contributors. GeoWeaver achieves this by decoupling workflows from datasets and computing platforms, making them clean, safe, and portable. It also records the history of code and execution logs, ensuring that every step is permanently documented, which is crucial for maintaining the integrity and reproducibility of scientific research. Key features of GeoWeaver include the ability to execute processes on any chosen host, whether locally or remotely, and to wrap entire workflows into simple, shareable zip files. These files can be easily distributed through various channels, such as Slack, email, or social media. Additionally, GeoWeaver condenses thousands of lines of code into an intuitive graph, allowing users to browse and edit workflows within a single view. This functionality not only simplifies the overall management of complex workflows but also ensures that team members are synchronized, allowing them to collaborate effectively on the same project.

Throughout its development, the GeoWeaver team has actively engaged with the Earth science community to address user feedback and promote the adoption of the platform. The team has developed the pygeoweaver library, which has been well-received by the community, particularly among those using Python. The software is currently being utilized for various AI workflows, including the Community Multiscale Air Quality (CMAQ) AI operation site, severe weather event forecasting, and ocean eddy detection. In addition to its technical achievements, GeoWeaver has made significant strides in outreach and collaboration. The team has sponsored Earth Science Information Partners (ESIP) mini grants and worked closely with domain scientists to address the challenges of implementing FAIR Earth AI workflows. One notable project involved using GeoWeaver to create a snow workflow, which was presented at the American Geophysical Union (AGU).

Moving forward, the team plans to further expand the use of GeoWeaver in operational settings, including collaborations with NASA scientists to integrate the platform into high-performance computing (HPC) and cloud environments.

The GeoWeaver team has also contributed to the broader Earth science community by sharing their experiences with NASA's Earth Science Data System Working Group (ESDSWG) and the ESIP machine learning (ML) cluster. They have drafted a comprehensive paper titled "A Review of Earth Artificial Intelligence," which has become one of the most popular papers in the journal Computers and Geosciences. This paper aims to demystify Earth AI by providing an overview of representative AI research across the types of major spheres of the Earth system. In terms of major accomplishments, the GeoWeaver team has successfully released GeoWeaver 1.0.0-rc10, which is now ready for use, along with pygeoweaver 0.6.6, available for installation via pip. The CMAQ AI operational workflow, developed using GeoWeaver, is currently running daily, showcasing the platform's capability to support continuous, reliable operations in Earth science research.

5.5. Case study 5: Passive microwave measurements from satellites

Passive microwave measurements from satellites provide invaluable data for retrieving various surface and atmospheric parameters, but their complexity has often limited their accessibility to those with specialized satellite knowledge. These measurements, which are available in raw swath formats, are challenging to align with data from other satellites or ancillary data necessary for comprehensive analysis.

To address this issue, a project has been undertaken to resample and organize these microwave data onto fixed Earth grids, significantly lowering the barriers for broader scientific use and enabling easier integration into machine learning (ML) algorithms. The main objectives of the project include resampling microwave measurements from multiple satellites onto fixed latitude/longitude and polar grids, providing a consistent set of ancillary data aligned with these grids, and offering comprehensive documentation to assist users in creating machine learning datasets from this organized data collection. By achieving these objectives, the project mainly aims to democratize the use of passive microwave data information, allowing researchers and developers to work with these data without needing deep expertise in satellite-specific formats.

The project has also successfully resampled microwave radiances measured by the Advanced Microwave Scanning Radiometer 2 (AMSR2) onto two types of Earth grids: a global 0.25-degree latitude/longitude grid and a 25 km EASE2 polar grid for the Northern Hemisphere. The resampling process utilized the Backus-Gilbert method to achieve the high accuracy, combined with 2D interpolation to precisely place the resampled footprints. These grids support two footprint sizes: 30 km and 70 km circular footprints, depending on the frequency and polarization of the measurements. The result is a set of microwave data information that is much easier to work with and more compatible with other Earth observation datasets.

In addition to the resampled microwave data, the project also provides various ancillary datasets on the same grids, resampled to match the footprint sizes and shapes of the microwave measurements.

These ancillary datasets include land/water fraction from MODIS, precipitation data from the Integrated Multi-satellite Retrievals for GPM (IMERG), and several atmospheric parameters from the European Centre for Medium-Range Weather Forecasts Reanalysis v5 (ERA5), such as skin temperature, total column water vapor, total column cloud water, and vector winds.

These ancillary datasets are very much critical for further developing and testing retrieval algorithms, as they can serve as both the input parameters and target outputs for different ML models. The project has made many significant strides in improving the usability of this data information collection for algorithm development. The team has developed a Jupyter notebook that demonstrates how to construct a machine learning dataset using the resampled microwave data and ancillary datasets. This notebook provides simple examples that guide users through the process, making it easier for them to apply these data in their own research and development projects.

The major accomplishments of the project include the resampling of AMSR2 measurements from 2012 to 2021 onto regular grids, the collocation of ancillary data in time and space with the microwave measurements, and the development of user-friendly resources like the Jupyter notebook. These achievements represent a great significant step forward in terms of making passive microwave data more accessible and usable for a wide range of Earth science applications, particularly those involving machine learning (ML) and data integration from multiple sources.

5.6. Case study 6: DL, ML datasets

The collection of high-quality training data information is still a very significant challenge in large-area land cover classification and disturbance mapping, particularly when it comes to ensuring the minimal error and achieving higher spatial resolution than the satellite data being classified or validated. Recent advancements in deep learning (DL) and active learning approaches, combined with the availability of commercial high spatial resolution data (less than 10 meters), offer promising opportunities for generating many types of training datasets that are suitable for application to 30-meter Landsat and 10 to 20-meter Sentinel-2 data.

The primary objectives of this project include developing an active-learning-based solution to efficiently create large-scale training datasets from PlanetScope time series for specific classes such as burned areas and tree cover. The project also aims to generate high-quality 3-meter resolution training datasets for these classes, provide clean and quality-controlled labeled data to the broader research community, and share the developed algorithms and software through peer-reviewed research publications and open-source code repositories.

To achieve all these objectives, the project has developed an active learning framework based on the U-Net architecture, designed to efficiently generate training data information from PlanetScope imagery. This framework follows a systematic approach.

1) Initial Training: The U-Net model is first trained using either coarser resolution burned/unburned validation data from a globally distributed, manually-labeled set of 30-meter Landsat images or by manually annotating PlanetScope images to classify tree/no-tree classes in various forested environments.

2) Initial Classification and Quality Assessment: The trained U-Net model is then applied to classify a small set of unlabeled PlanetScope images. The resulting classifications are quality-assessed and manually corrected as necessary.
3) Validation: The U-Net model is subsequently applied to classify a predetermined set of validation images, which have been independently annotated, to assess the classification accuracy.
4) Iteration or Completion: If the classification accuracy meets the required standards, the process stops. If not, the corrected classified images from the second step are added to the existing training dataset, and the U-Net model is retrained. This iterative process continues until the desired accuracy is achieved.

The project has made significant progress and achieved several major accomplishments. Notably, it has generated burned area training data for all of Africa, utilizing 575 pairs of two-date PlanetScope images. Additionally, the methodology for generating tree cover training data has been refined through the active learning approach.

The results and methodologies have been disseminated through the publication of two peer-reviewed journal papers, contributing valuable resources and knowledge to the field of land cover classification and disturbance mapping.

5.7. Case study 7: The pangeo-ML project

The Pangeo-ML project builds upon on the foundation of the Pangeo Project to further enhance machine learning (ML) workflows for researchers and data scientists working with many types of complex multi-dimensional datasets. Recognizing the unique challenges in geoscientific ML workflows, such as data dimensionality, transformations, and large volumes, the Pangeo-ML team has focused on developing high-level tools that can bridge the gaps between commonly used geoscientific exploratory data analysis software and deep learning (DL) frameworks.

This project aims to simplify data preprocessing, expand software interoperability, and foster an open-source community equipped with the tools and knowledge to work with Earth observation (EO) data in ML applications. A core objective of Pangeo-ML has been to improve the interoperability of the scientific Python ecosystem, making it easier to construct preprocessing pipelines for ML applications. To this end, the team has contributed to the integration of the Holoviz suite of tools (including hvPlot, GeoViews,

Holoviews, Datashader, SpatialPandas) with other key components of the scientific Python ecosystem, such as Zarr, Xarray, and Rioxarray. This integration has greatly simplified the interactive exploration and preprocessing of Earth science and ML datasets. Additionally, the project has enhanced the interoperability between Xarray, Dask, and geospatial libraries like Pytroll Satpy and Pyresample, streamlining common tasks such as geographic resampling in preprocessing pipelines. Another significant achievement of the Pangeo-ML project is the development of new software interfaces between Xarray and machine learning libraries. The Xbatcher library, a notable outcome of this work, simplifies batch data generation from Xarray datasets, supporting direct integration with popular ML frameworks like TensorFlow and PyTorch.

This library facilitates lazy batch generation, parallel loading, caching, and data loaders, making it easier to handle large datasets in deep learning workflows.

Beyond software development, the Pangeo-ML team has actively engaged with the open-source community, providing expanded documentation, tutorials, talks, and workshops to support scalable machine learning workflows. Their efforts have led to the release of new and improved open-source software, such as Xbatcher and Kerchunk, as well as foundational packages like Xarray and Dask. The team has also developed machine learning applications that both motivate and guide tool development, including a biomass mapping workflow using Landsat and ICESat/GLAS data, a hydrometeorological data assimilation project using FluxNet, a climate downscaling application, and ocean surface current estimation from remote sensing observations. The Pangeo-ML project has made significant strides in improving ML workflows for geoscientific research by enhancing software interoperability, developing new tools, and fostering an active open-source community. Their work has simplified the process of working with complex multi-dimensional datasets, enabling more efficient and scalable ML applications in the geosciences.

5.8. Case study 8: The global vegetation structure (GVS) project

The Global Vegetation Structure (GVS) project focuses on developing machine learning models to integrate data from various remote sensing technologies, aiming to study and map global vegetation structure. By leveraging the strengths of different remote sensing instruments, particularly lidar sensors, radar, and optical sensors, the project seeks to overcome the limitations of individual technologies and create comprehensive, high-resolution maps of vegetation structure and its changes over time.

Lidar sensors, whether deployed on satellites or from airborne campaigns, offer direct measurements of the vertical profile of vegetation, but their availability and coverage are limited. In contrast, radar and optical sensors, while providing indirect estimates of vegetation structure, offer excellent global coverage.

The GVS project aims to combine the detailed, yet sparse, data from lidar with the broad coverage of radar and optical sensors using advanced machine learning techniques, enabling the creation of wall-to-wall maps of vegetation structure on a global scale. The project is structured around several key objectives, beginning with the assessment and inter-calibration of lidar data from different instruments, both space-borne and airborne. This involves collecting and validating airborne lidar campaign data and comparing it with space-borne products. Where necessary, inter-calibration techniques are mainly applied to harmonize data from different types of instruments, ensuring that the aggregated dataset is of high quality and suitable for integration with other types of remote sensing data. Preprocessing of dense predictors is another very crucial step in the GVS project.

This involves developing and applying many types of methodologies to preprocess input datasets, such as optical imagery from Landsat and Sentinel-2, and radar data from the Advanced Land Observing Satellite (ALOS) PALSAR, on a global scale.

The preprocessing ensures that these datasets are aggregated to different resolutions and aligned on compatible grids, facilitating their integration with lidar data. Once the data is collected and preprocessed, the project focuses on testing and comparing various machine learning models. By utilizing the diverse input data sources, the team evaluates different models to identify the most effective approach for estimating vegetation structure.

This process involves assessing the drawbacks and limitations of each method, ensuring a comprehensive evaluation that leads to improvements in the models. The goal is to establish a consistent multiscale approach that can be applied globally while also considering the costs associated with each methodology.

A critical aspect of the project is the intercomparison of the derived products with ground truth airborne datasets. By benchmarking the machine learning model outputs against these ground truth datasets, the GVS project can assess the accuracy and reliability of its methods. This benchmarking is essential for validating the models and ensuring that they provide robust and accurate estimates of vegetation structure on a global scale.

Major accomplishments of the GVS project include the development of a methodology to combine data information from two types of different lidar instruments, the Ice, Cloud, and land Elevation Satellite-2 (ICESat-2) and the Global Ecosystem Dynamics Investigation (GEDI) missions. This approach helps to fill out the observation gaps in GEDI data over boreal areas, enhancing the overall coverage and accuracy of vegetation structure mapping. Multiple machine learning (ML) models for estimating vegetation structure from optical and radar imagery have been tested and applied globally, yielding results that are on par with the current state-of-the-art in the field.

The GVS project represents a very comprehensive effort to advance the study of global vegetation structure through the integration of lidar, radar, and optical remote sensing data. By combining all these types of diverse data sources with cutting-edge machine learning (ML) techniques, the project aims to produce accurate, high-resolution maps of vegetation structure, contributing valuable insights for ecological research and environmental management on a global scale.

5.9. Case study 9: Training data for streamflow estimations

The collaborative project between NASA's Goddard Space Flight Center, the Alaska Satellite Facility, the University of Arizona, and the University of Maryland is focused on developing a comprehensive dataset of river width measurements using ESA Sentinel-1 C-Band Synthetic Aperture Radar (SAR) data. This dataset is intended for training machine learning models that estimate river flow rates and for use in related hydrological models. Sentinel-1 SAR data, with its ability to provide high-resolution, all-weather, day-and-night data at a nominal six-day revisit time, is central to this initiative.

The project has combined several key objectives. First, it aims to provide the research community with a more robust dataset of the river width measurements through NASA's Physical Oceanography Distributed Active Archive Center (PO.DAAC).

This dataset will also be very instrumental in enhancing the overall capability of the research community to map surface water at a 10-meter resolution using Sentinel-1 data distributed by the Alaska Satellite Facility. Additionally, the project also seeks to demonstrate the utility of these river width measurements in deriving accurate river flow rate estimates, which are also very much crucial for various hydrological studies and applications.

To achieve all these objectives, the project is developing a workflow for generating effective river width measurements, defined as the surface water area divided by the river reach length. This workflow is being executed on the Alaska Satellite Facility's (ASF) OpenScienceLab System and comprises three primary components: preprocessing using standard ASF Sentinel-1 methods, a surface water extent mapping program, and a river width measurement program that utilizes the surface water maps as input. An essential feature of the system is a module that filters out Sentinel-1 scenes that do not include river reaches of interest, specifically those listed in the NASA Surface Water and Ocean Topography (SWOT) Mission SWOT River Database (SWORD). The project is evaluating several surface water mapping algorithms using Sentinel-1 SAR data.

These include HydroSAR, developed by the Alaska Satellite Facility; the Equal Percent Solution, developed by the project's principal investigator; and a machine learning algorithm from the University of Arizona. Additionally, the team is considering algorithms from the NASA Observational Products for End-Users from Remote Sensing Analysis (OPERA) Project and a hybrid algorithm that combines elements of the Equal Percent Solution and the OPERA algorithm.

The accuracy of these water maps is now being assessed using hand-labeled water maps derived from high-resolution commercial data provided by the Planetscope constellation. The algorithm deemed most effective will be integrated into the ASF processing system and made available to the research community through an interface provided by ASF. The river width measurement program, a modification of the RivWidth Cloud Program developed by the University of North Carolina, will be adapted to use the Sentinel-1 water maps and interface with the SWORD database.

This integration will automate the measurement of effective river width for the nodes and reaches in the database. The accuracy of the river width data will be evaluated using hand measurements based on Planetscope data. The project will also assess the utility of these river width measurements for deriving river flow rates in a machine learning model and within the SWOT Mission GeoBAM model.

The project has achieved a large number of significant milestones, including the development of a new algorithm for mapping surface water using Sentinel-1 data, known as "The Equal Percent Solution." This algorithm adjusts a radar backscatter threshold to balance false positives and false negatives, improving the accuracy of water detection. A high-resolution dataset of hand-labeled water maps based on Planetscope data has been created and made available to the research community for training machine learning models and evaluating water maps.

The project also implemented an end-to-end system for measuring river width using Sentinel-1 SAR data, although an issue with releasing the river width measurement code to the public led to its removal, with replacement code currently in development.

This project represents a very significant effort to advance the use of remote sensing data for hydrological modeling and river flow rate estimation. By developing and providing high-quality datasets and tools to the research community, the project aims to enhance the overall understanding and management of global water resources.

To provide a better retrospect on the matter of perspectives and how they perform in real time dynamics **Figures 1–3** offers visualizations for a better understanding.

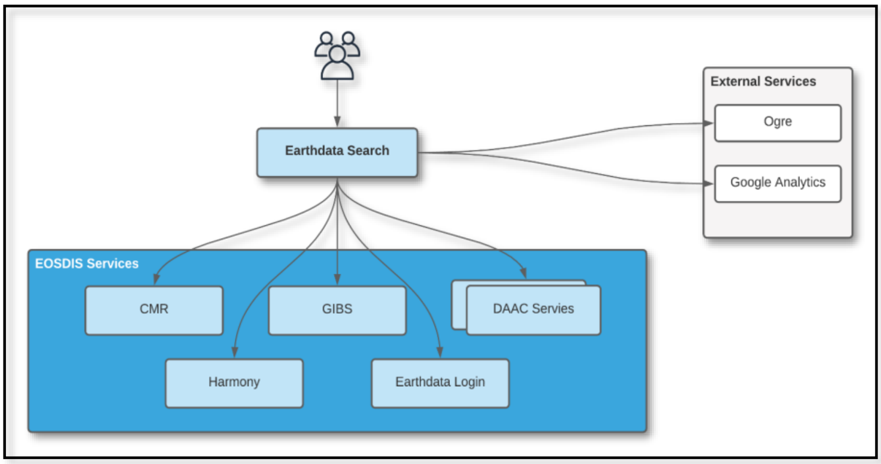

Figure 1. An overview of earth data in action (EOSDIS).

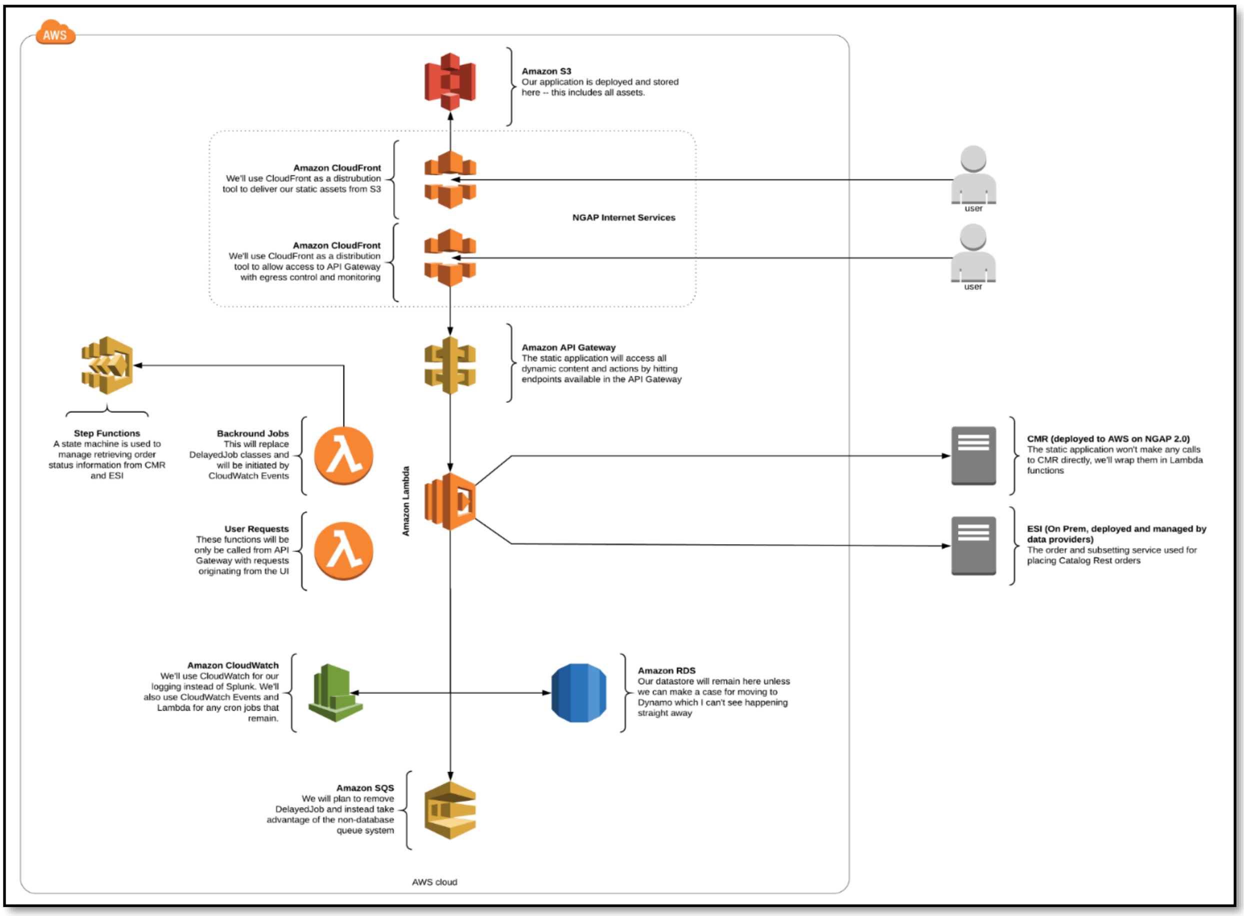

Figure 2. An overview of aws services in action (EOSDIS).

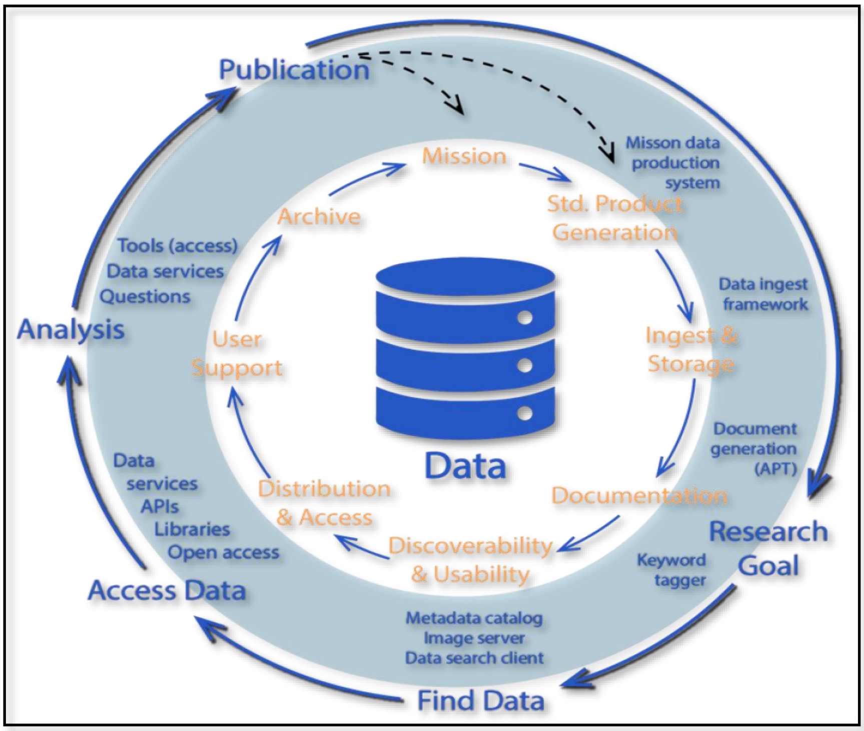

Figure 3. An overview of NASA's AI workflow for earth data.

6. Results and findings

This section presents the detailed results and findings of the research exploration investigations, highlighting the integration of Big Earth Data, machine learning algorithms, and remote sensing technologies for geological and mineral mapping. The outcomes are contextualized to provide a refined clarity on the overall improvements achieved, insights gained, and the various types of associated challenges which were encountered.

6.1. Geological and lithological mapping

The application of machine learning techniques to geological and lithological mapping demonstrated significant advancements in the classification of geological features. For example, using AVIRIS-NG hyperspectral data for mapping gold-bearing granite-greenstone rocks in Hutti, India, support-vector machines (SVM) outperformed other algorithms, achieving an accuracy of 90.3%.

In Brazil's Cinzento Lineament, the combination of spatial constraints with remote sensing data achieved 78.7% accuracy, underscoring the role of integrating spatial data for enhanced results. Similarly, hyperspectral data in Morocco's Central Jebilet region yielded a classification accuracy of 93.05%, slightly higher than the 89.24% achieved with multispectral data. These results validate the robustness of machine learning in processing complex geospatial data.

However, challenges such as vegetation cover significantly impacted the results, necessitating preprocessing techniques like band selection and dimensionality reduction. **Table 1** lists the datasets, models, and performance metrics, providing an overview of the experimental framework and the respective outcomes for each case study.

6.2. Landslide susceptibility and hazard mapping

The integration of topographic and lithological datasets with satellite imagery enabled accurate landslide susceptibility mapping. For instance, in Fruška Gora Mountain, Serbia, the SVM algorithm outperformed Decision Trees and Logistic Regression with an accuracy exceeding 85%, effectively identifying high-risk zones. In Honshu Island, Japan, the combination of ASTER geomorphic data and geological maps with Artificial Neural Networks (ANN) achieved a prediction accuracy of over 90%, showcasing the reliability of machine learning in disaster-prone areas.

These results were validated through the exploration investigations coupled with the associated cross-validation techniques and independent datasets, demonstrating the overall robustness across many types of diverse terrains. The findings emphasize the role of advanced models in urban planning and disaster management.

6.3. Discontinuity analyses

Machine learning, particularly Convolutional Neural Networks (CNNs), excelled in recognizing geological discontinuities like fault planes and bedding planes. For instance, experiments in Korea revealed that CNN-based models achieved a specificity and negative predictive value (NPV) exceeding 0.99, ensuring highly accurate fracture detection even under challenging conditions, such as overlapping geological features or dense vegetation cover. Data augmentation techniques, including flipping and cropping, were instrumental in enhancing model generalization.

6.4. Carbon dioxide leakage detection

Hyperspectral imaging combined with machine learning algorithms identified vegetation stress signals indicative of CO_2 leakage from underground sequestration sites. The ISODATA clustering technique was particularly effective, clustering pixels with similar stress responses to detect leakage zones. In the ZERT site in the US, this method yielded promising results, albeit influenced by seasonal and vegetative variations. These findings highlight the potential for machine learning in environmental monitoring and mitigation efforts.

6.5. Quantification of water inflow in rock tunnels

Using CNNs to classify tunnel face conditions into non-damage, wet, and dripping states achieved an accuracy of 93.01%, significantly improving the automation of water inflow quantification processes. This capability reduces reliance on subjective visual assessments and provides a scalable solution for large-scale infrastructure projects.

6.6. Soil and geological structure classification

Machine learning models demonstrated exceptional performance in classifying soil types and geological structures. For soil classification using Cone Penetration Testing (CPT) logs, ANN models achieved the highest accuracy across various soil types. Similarly, CNNs and Transfer Learning approaches were highly effective in identifying geological structures such as folds, faults, and dikes, achieving classification accuracies of 80%–90%.

7. Earthquake early warning systems and forecasting

Machine learning enhanced earthquake detection and forecasting by effectively distinguishing earthquake signals from noise. Models like Random Forest and GANs accurately recognized P-waves, with laboratory experiments showcasing their ability to predict fault failure time, contributing to improved early warning systems.

The results collectively underscore the transformative role of machine learning in geological and mineral mapping. The AI models demonstrated superior accuracy, efficiency, and adaptability compared to traditional methods. By integrating Big Earth Data, the research addressed challenges such as vegetation cover and data heterogeneity, paving the way for more precise and automated mapping solutions.

The findings revealed that algorithm selection significantly impacts outcomes, with SVMs and CNNs often outperforming other methods for specific applications. However, challenges such as algorithm transparency (e.g., neural networks as “black-box” models) and computational costs require further exploration to optimize their deployment.

Future experimental outlook

To build upon the current findings, future experiments will focus on:

- Enhanced algorithm transparency: Developing interpretable machine learning models to improve stakeholder trust and usability.
- Dynamic data integration: Incorporating temporal changes in Big Earth Data to study evolving geological and environmental processes.
- Scalable solutions: Exploring distributed computing and cloud-based frameworks for real-time data processing and analysis.
- Interdisciplinary approaches: Combining AI with domain-specific knowledge to address complex earth science challenges.

Figures 4–8 visually illustrate key results and findings, while **Table 1** provides a consolidated view of the datasets, methodologies, and performance metrics, facilitating a comprehensive understanding of the research outcomes.

Table 1. The various data sources results and findings in action.

Objective	Input dataset	Location	Machine learning algorithms (MLAs)	Performance
Lithological Mapping of Gold-bearing granite-greenstone rocks [46]	AVIRIS-NG hyperspectral data	Hutti, India	Linear Discriminant Analysis (LDA), Random Forest, Support Vector Machine (SVM)	Support Vector Machine (SVM) outperforms the other Machine Learning Algorithms (MLAs)
Lithological Mapping in the Tropical Rainforest [45]	Magnetic Vector Inversion, Ternary RGB map, Shuttle Radar Topography Mission (SRTM), False color (RGB) of Landsat 8 combining bands 4, 3 and 2	Cinzento Lineament, Brazil	Random Forest	Two predictive maps were generated: (1) Map generated with remote sensing data only has a 52.7% accuracy when compared to the geological map, but several new possible lithological units are identified

Table 1. (*Continued*).

Objective	**Input dataset**	**Location**	**Machine learning algorithms (MLAs)**	**Performance**
				(2) Map generated with remote sensing data and spatial constraints has a 78.7% accuracy but no new possible lithological units are identified
Geological Mapping for mineral exploration [47]	Airborne polarimetric Terrain Observation with Progressive Scans SAR (TopSAR), geophysical data	Western Tasmania	Random Forest	Low reliability of TopSAR for geological mapping, but accurate with geophysical data.
Geological and Mineralogical mapping	Multispectral and hyperspectral satellite data	Central Jebilet, Morocco	Support Vector Machine (SVM)	The accuracy of using hyperspectral data for classifying is slightly higher than that using multispectral data, obtaining 93.05% and 89.24% respectively, showing that machine learning is a reliable tool for mineral exploration.
Integrating Multigeophysical Data into a Cluster Map [48]	Airborne magnetic, frequency electromagnetic, radiometric measurements, ground gravity measurements	Trøndelag, Mid-Norway	Random Forest	The cluster map produced has a satisfactory relationship with the existing geological map but with minor misfits.
High-Resolution Geological Mapping with Unmanned Aerial Vehicle (UAV) [42]	Ultra-resolution RGB images	Taili waterfront, Liaoning Province, China	Simple Linear Iterative Clustering-Convolutional Neural Network (SLIC-CNN)	The result is satisfactory in mapping major geological units but showed poor performance in mapping pegmatites, fine-grained rocks and dykes. UAVs were unable to collect rock information where the rocks were not exposed.
Surficial Geology Mapping [49] Remote Predictive Mapping (RPM)	Aerial Photos, Landsat Reflectance, High-Resolution Digital Elevation Data	South Rae Geological Region, Northwest Territories, Canada	Convolutional Neural Networks (CNN), Random Forest	The resulting accuracy of CNN was 76% in the locally trained area, while 68% for an independent test area. The CNN achieved a slightly higher accuracy of 4% than the Random Forest.
Landslide Susceptibility Assessment [50]	Digital Elevation Model (DEM), Geological Map, 30m Landsat Imagery	Fruška Gora Mountain, Serbia	Support Vector Machine (SVM), Decision Trees, Logistic Regression	Support Vector Machine (SVM) outperforms the others
Landslide Susceptibility Mapping [51]	ASTER satellite-based geomorphic data, geological maps	Honshu Island, Japan	Artificial Neural Network (ANN)	Accuracy greater than 90% for determining the probability of landslide.
Landslide Susceptibility Zonation through ratings [52]	Spatial data layers with slope, aspect, relative relief, lithology, structural features, land use, land cover, drainage density	Parts of Chamoli and Rudraprayag districts of the State of Uttarakhand, India	Artificial Neural Network (ANN)	The AUC of this approach reaches 0.88. This approach generated an accurate assessment of landslide risks.
Regional Landslide Hazard Analysis [53]	Topographic slope, topographic aspect, topographic curvature, distance from drainage, lithology, distance from lineament, land cover from TM satellite images, Vegetation index (NDVI), precipitation data	The eastern part of Selangor state, Malaysia	Artificial Neural Network (ANN)	The approach achieved 82.92% accuracy of prediction.

Table 1. (*Continued*).

Objective	Input dataset	Location	Machine learning algorithms (MLAs)	Performance
Recognition of Rock Fractures [54]	Rock images collected in field survey	Gwanak Mountain and Bukhan Mountain, Seoul, Korea and Jeongseon-gun, Gangwon-do, Korea	Convolutional Neural Network (CNN)	The approach was able to recognize the rock fractures accurately in most cases. The Negative Prediction Value (NPV) and the Specificity are over 0.99.
Detection of CO2 leak from a geologic sequestration site [55]	Aerial hyperspectral imagery	The Zero Emissions Research and Technology (ZERT), US	Iterative Self-Organizing Data Analysis Technique (ISODATA) method	The approach was able to detect areas with CO_2 leaks however other factors like the growing seasons of the vegetation also interfere with the results.
Quantification of water inflow in rock tunnel faces [56]	Images of water inflow		Convolutional Neural Network (CNN)	The approach achieved an average accuracy of 93.01%.
Soil classification [57]	Cone Penetration Test (CPT) logs		Decision Trees, Artificial Neural Network (ANN), Support Vector Machine	The Artificial Neural Network (ANN) outperformed the others in classifying humous clay and peat, while the Decision Trees outperformed the others in classifying clayey peat. Support Vector Machine gave the poorest performance among the three.
Geological structures classification [58]	Images of geological structures		K nearest neighbors (KNN), Artificial Neural Network (ANN), Extreme Gradient Boosting (XGBoost), Three-layer Convolutional Neural Network (CNN), Transfer Learning	Three-layer Convolutional Neural Network (CNN) and Transfer Learning reached accuracies up to about 80% and 90% respectively, while others were relatively low, ranges from about 10% to 30%.
Discriminating earthquake waveforms [59]	Earthquake dataset	Southern California and Japan	Generative Adversarial Network (GAN), Random Forest	The approach can recognise P waves with 99.2% accuracy and avoid false triggers by noise signals with 98.4% accuracy.
Predicting time remaining for next earthquake [60]	Continuous acoustic time series data		Random Forest	The R^2 value of the prediction reached 0.89, which demonstrated excellent performance.
Streamflow Estimate with data missing [61]	Streamgage data from NWIS-Web	Four diverse watersheds in Idaho and Washington, US	Random Forests	The estimates correlated well to the historical data of the discharges. The accuracy ranges from 0.78 to 0.99.

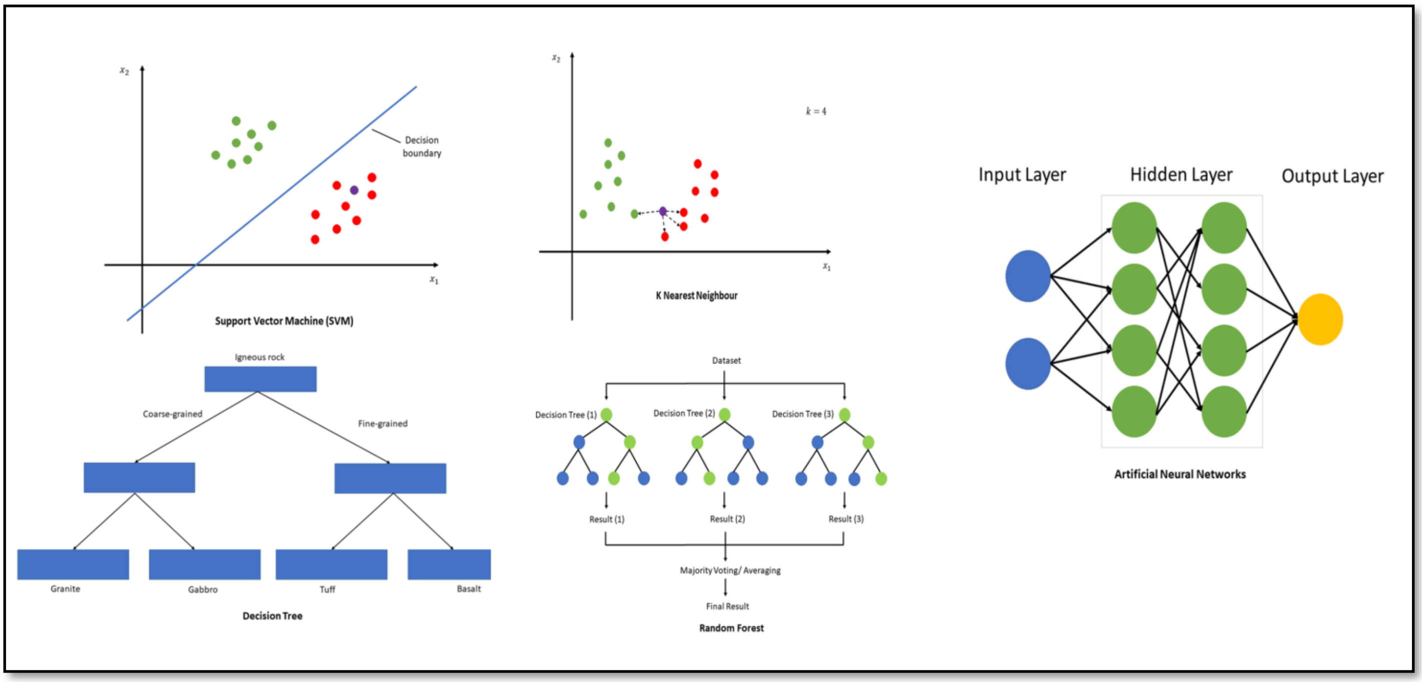

Figure 4. The AI, DL, ML perspectives in action.

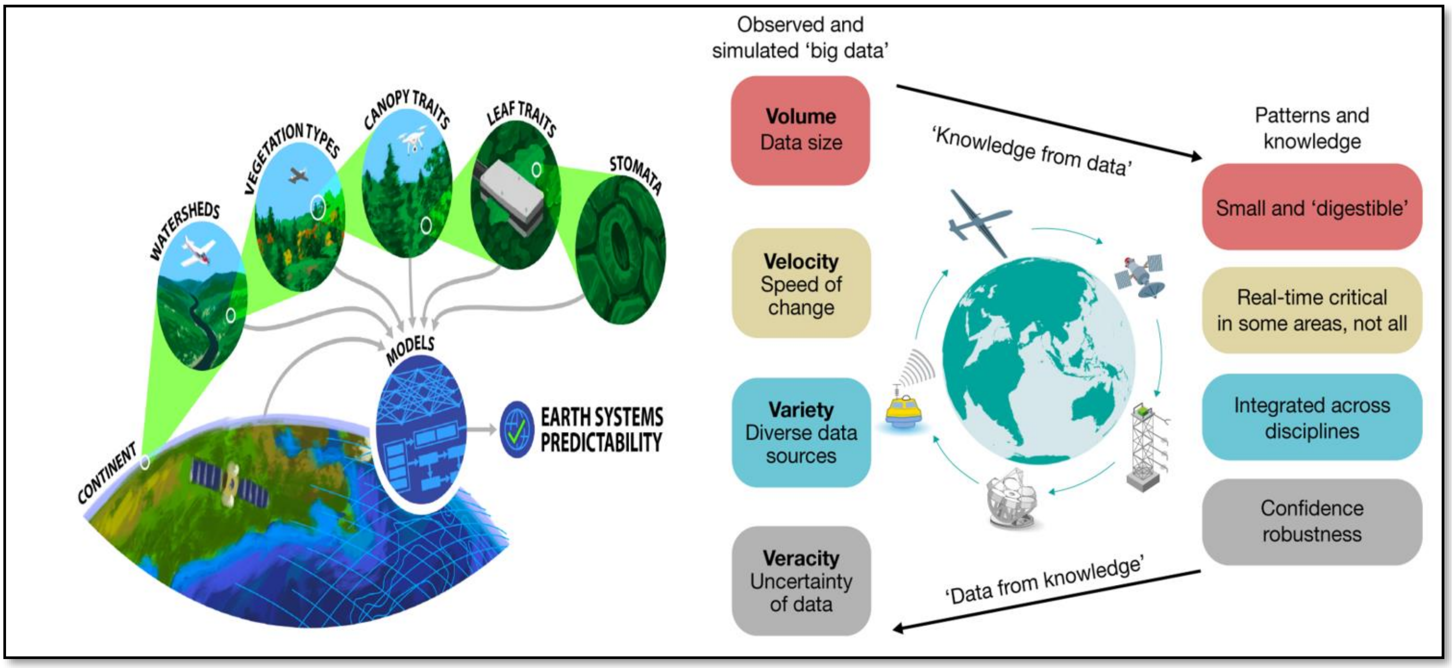

Figure 5. The results and findings from the research explorations 1.

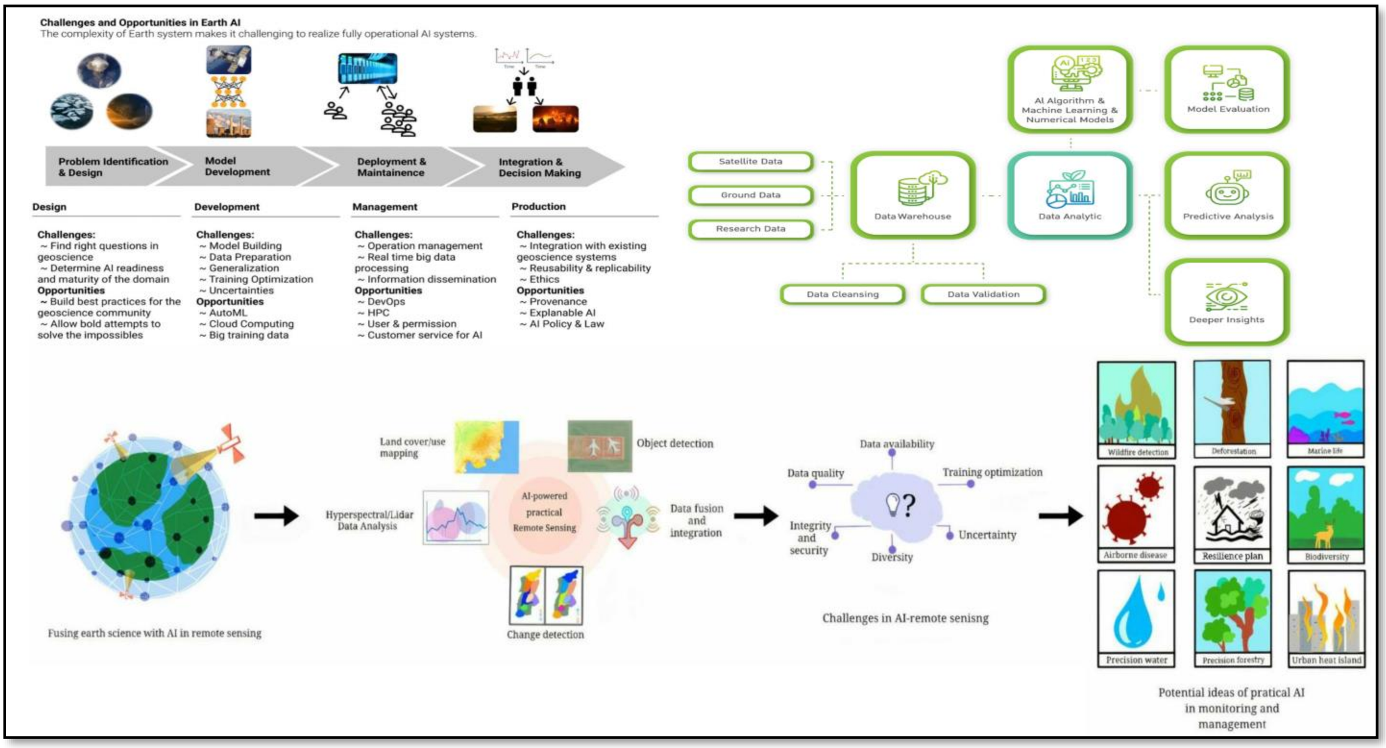

Figure 6. The results and findings from the research explorations 2.

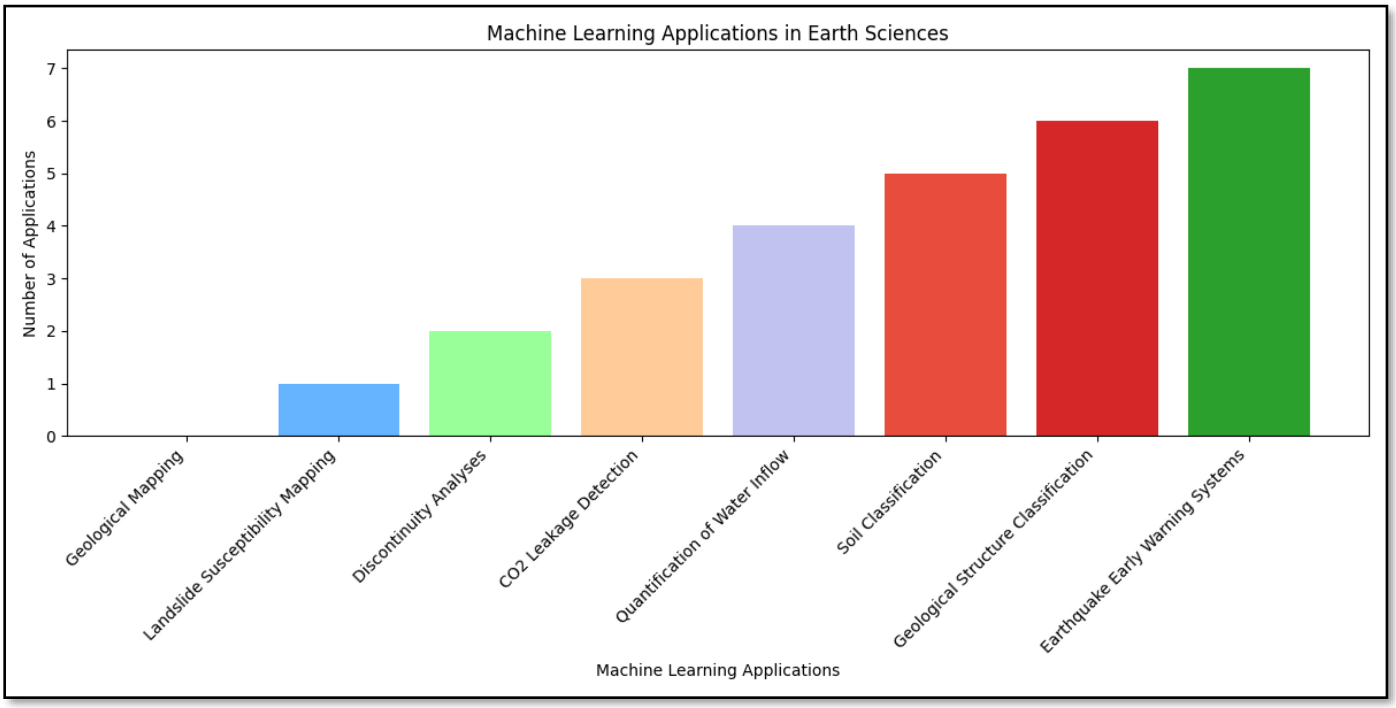

Figure 7. The results and findings from the research explorations 3.

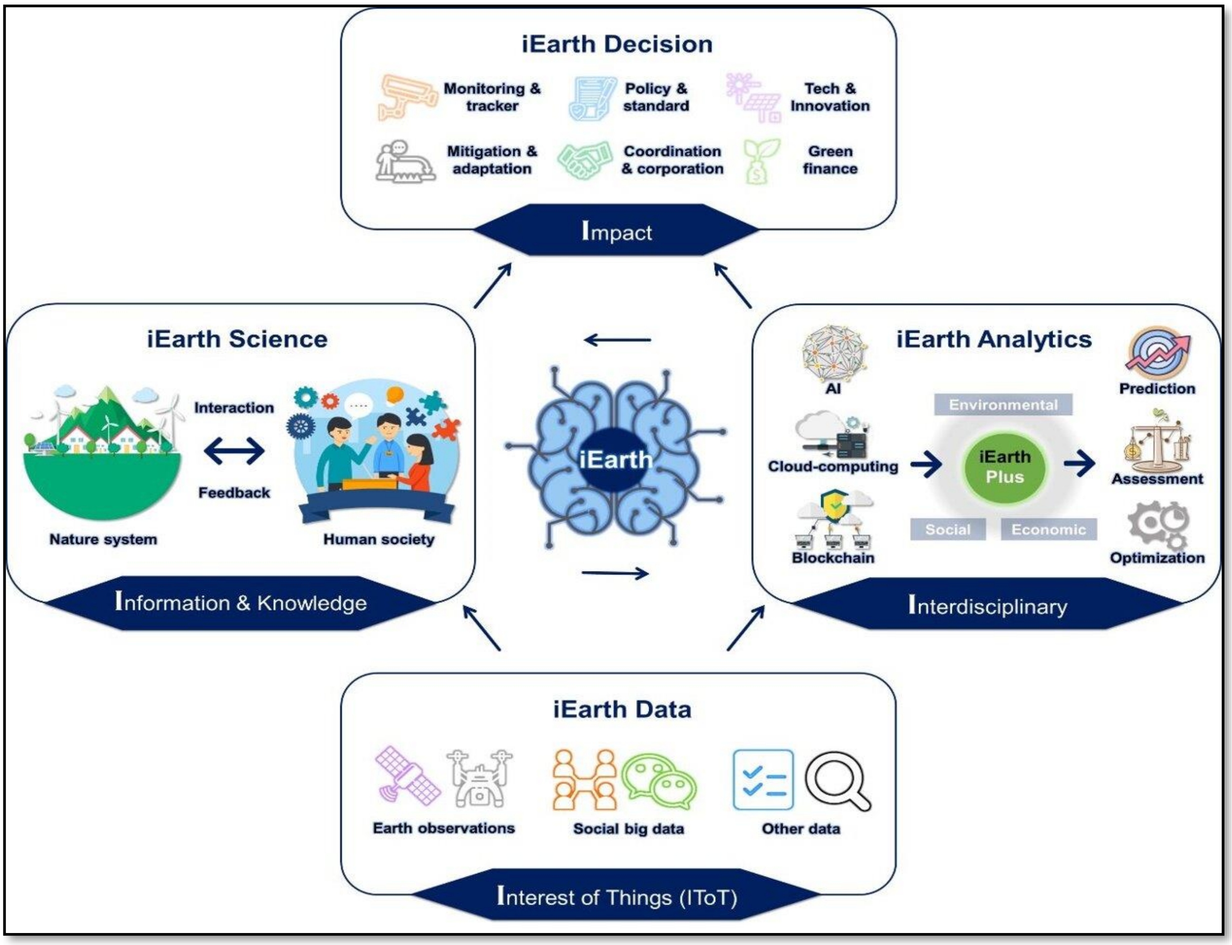

Figure 8. A future outlook for iEarth (experimental).

8. Discussions and future directions

The integration of Big Earth Data and Artificial Intelligence (AI) has revolutionized geological and mineral mapping by addressing the limitations of traditional methodologies, particularly in handling vast and complex datasets. The study highlights the transformative role of machine learning (ML) and deep learning (DL) algorithms in geosciences, offering robust solutions for data-driven analyses.

One of the most notable findings of this research is the demonstrated efficacy of Convolutional Neural Networks (CNNs) in identifying intricate geological formations and mineral deposits. These models excel in capturing subtle spatial patterns, which are often overlooked or misinterpreted during manual analyses. For instance, CNNs successfully analyzed hyperspectral and multispectral datasets [60–66], providing accurate classifications of mineral types and their associated geological features. The fusion of spectral data with AI algorithms has proven particularly effective in regions with dense vegetation cover or complex geological formations, reducing uncertainties and improving prediction reliability. Additionally, the case studies included in this research—spanning diverse geological settings—validate the adaptability of AI-driven approaches. For example, the use of Support Vector Machines (SVM) and Random Forest algorithms demonstrated high accuracy in specific applications, such as lithological mapping and mineral prospectivity.

These findings underline the importance of selecting context-appropriate algorithms to address the unique challenges presented by different geological environments. Despite these advancements, several limitations persist. The variability of Big Earth Data, compounded by noise, artifacts, and limited access to high-quality labeled datasets, poses significant challenges. These issues can lead to overfitting or inaccuracies in AI models. Furthermore, the interpretability of AI algorithms remains a pressing concern. While complex models like neural networks provide superior performance, their "black-box" nature complicates understanding the reasoning behind their classifications, which is critical for decision-making in resource exploration [60–75]. Addressing these challenges necessitates ongoing refinement of both the data inputs and the algorithms themselves. To maximize the potential of Big Earth Data and AI in geological and mineral mapping, the following key areas merit focused exploration and development.

1) Enhanced Data Integration and Fusion

The geosciences field relies on diverse datasets, including seismic surveys, geophysical data, geochemical analyses, and satellite imagery. Future research should prioritize advanced data fusion techniques to integrate these sources seamlessly. By combining multispectral and hyperspectral data with subsurface information, researchers can develop holistic geological models that provide a more accurate representation of subsurface structures and mineral distributions. Techniques such as generative adversarial networks (GANs) and multi-modal learning may offer innovative solutions for handling heterogeneous data sources.

2) Explainable AI (XAI) and Model Interpretability

As AI algorithms grow more sophisticated, there is a critical need for transparency in their decision-making processes. Explainable AI (XAI) tools, such as saliency maps and feature attribution methods, can shed light on the internal workings of AI models. This is especially crucial for applications like mineral prospectivity mapping, where actionable insights are required. Researchers should investigate new frameworks for balancing model complexity with interpretability, ensuring that stakeholders, including geologists and policymakers, can trust and understand the predictions.

3) Scalability and Real-time Processing

The exponential growth of Big Earth Data demands scalable and efficient AI solutions. Future studies should explore distributed computing environments, such as cloud platforms and edge computing, to facilitate real-time data processing. These technologies could enable on-the-fly geological analyses, especially during field surveys or emergency scenarios like landslides. Moreover, developing lightweight AI models optimized for mobile and UAV platforms could revolutionize real-time geological mapping and monitoring.

4) Hybrid AI-Geoscience Approaches

While AI models offer powerful analytical capabilities, geoscientific expertise remains indispensable for contextual interpretation. Future research should focus on hybrid frameworks that combine the strengths of AI with domain-specific knowledge. These approaches could include embedding geoscientific principles into AI algorithms or creating workflows where human expertise complements AI-driven analyses.

Collaborative efforts between AI developers and geoscientists are essential for achieving more reliable and context-aware models.

5) Applications in Sustainable Resource Management

The adoption of AI in geological mapping has significant implications for sustainable resource management. AI can optimize mineral exploration by identifying high-potential areas, thereby minimizing environmental impact and financial costs. Future research should expand on using AI to monitor environmental changes resulting from mining activities, such as soil degradation or water contamination. Additionally, integrating conservation-focused data, such as biodiversity indices, with mineral exploration datasets could promote sustainable practices in natural resource management.

6) Improved Training Data and Validation Methods

The quality of training datasets is paramount for AI model performance. Researchers should focus on generating high-quality labeled datasets through methods such as data augmentation, synthetic data generation, and crowd-sourced labeling. Moreover, robust validation methods, including cross-validation and independent test areas, should be employed to ensure the generalizability of AI models across different geological settings.

7) Ethical Considerations and Policy Integration

As AI technologies become integral to geological mapping, ethical considerations must be addressed. Issues such as data privacy, algorithmic bias, and environmental sustainability should be at the forefront of future research. Policymakers and researchers should work together to establish guidelines for the ethical use of AI in resource exploration and land management.

The integration of Big Earth Data and AI represents a paradigm shift in geological and mineral mapping. While significant challenges remain, ongoing advancements in data integration, model interpretability, and computational efficiency offer a promising trajectory for this interdisciplinary field. By addressing these challenges and exploring future directions, researchers can unlock the full potential of AI-driven geosciences, paving the way for more accurate, efficient, and sustainable resource exploration and management practices.

9. Conclusions

The convergence of Big Earth Data and Artificial Intelligence (AI) has introduced transformative opportunities in geological and mineral mapping, marking a significant milestone in the field of geosciences. This study underscores the pivotal role of AI-driven techniques in addressing the complexities of analyzing large-scale geospatial datasets, enabling enhanced accuracy, efficiency, and depth in geological investigations. The integration of advanced machine learning (ML) and deep learning (DL) methodologies with remote sensing technologies has proven instrumental in uncovering detailed insights into the spatial distribution of geological formations and mineral deposits. A key achievement of this research lies in the successful application of AI models, particularly Convolutional Neural Networks (CNNs), to extract intricate spatial patterns and identify subtle spectral signatures from multispectral and hyperspectral datasets.

These capabilities surpass traditional geological mapping methods, which are often limited by their manual nature and susceptibility to human error. Furthermore, the ability of AI to synthesize diverse data sources and detect relationships within complex geological structures has been a significant advancement, offering precision and reliability in mineral prospectivity analysis.

However, this study also highlights notable challenges that must be addressed to fully realize AI's potential in geosciences. The reliance on high-quality training datasets is critical, as inconsistencies or inadequacies in labeled data can compromise model performance and lead to misclassifications. Additionally, the computational intensity of processing Big Earth Data necessitates scalable solutions, such as distributed computing and cloud-based architectures, to enable efficient analysis. Another pressing concern is the interpretability of AI models, often hindered by their "black-box" nature, which can limit their usability in critical decision-making scenarios.

To overcome these challenges, this research emphasizes the need for continuous innovation in AI techniques and closer collaboration between AI specialists and geoscientists. Enhanced transparency through explainable AI (XAI) frameworks and the integration of domain-specific knowledge into AI workflows are identified as key strategies to improve the interpretability and contextual relevance of AI models. Moreover, advancing data integration and fusion methodologies—incorporating geophysical, geochemical, and remote sensing data—can lead to the development of more comprehensive and holistic geological models.

Looking forward, the potential applications of AI in geosciences are expansive. These include not only refined mineral exploration processes but also contributions to sustainable resource management, real-time geological surveys, and environmental monitoring. The findings of this study highlight the critical importance of balancing technological innovation with ethical considerations and sustainability, ensuring responsible use of AI in resource exploration and management.

By addressing current limitations and harnessing emerging opportunities, researchers and practitioners can unlock the full potential of Big Earth Data and AI in geosciences. This study contributes valuable insights into the academic discourse on AI applications while providing practical recommendations for developing more advanced, reliable, and interpretable geological mapping techniques. These advancements pave the way for a new era of accurate, efficient, and sustainable practices in geological and mineral mapping, reinforcing the transformative role of AI in shaping the future of geosciences.

Author contributions: Conceptualization, ZBA; methodology, ZBA; software, ATR; validation, ZBA; formal analysis, ZBA; investigation, ZBA; resources, ZBA; data curation, ATR; writing—original draft preparation, ZBA; writing—review and editing, ZBA; visualization, ZBA; supervision, ZBA; project administration, ZBA; funding acquisition, ZBA. All authors have read and agreed to the published version of the manuscript.

Acknowledgments: The authors would like to acknowledge and thank the GOOGLE Deep Mind Research with its associated pre-prints access platforms. This research was deployed and utilized under the platform provided by GOOGLE Deep Mind which is under the support of the GOOGLE Research and the GOOGLE Research Publications under GOOGLE Gemini platform. Also, a huge shout out and thanks to the NASA EARTHDATA open-source database along with their massive NASA EARTHDATA datasets, data models, data tools and NASA EARTH SCIENCE DATA repo for providing access to their enormous pool of scientific data sources. Using their provided platform of datasets and database associated files with digital software layouts consisting of free web access to a large collection of recorded models that are found within research access and its related open-source software distributions which is the implementation and simulation of analytics for the proposed research which was undergone and set in motion. There are many data sources some of which are resourced and retrieved from a wide variety of GOOGLE service domains. All the data sources and various domains from which data has been included and retrieved for this research are identified, mentioned and referenced where appropriate. However, the various types of original data sources some of which are not all publicly available, because they contain various types of private information. The available platform provided data sources that support the research results with findings and information of the research investigations are referenced where appropriate.

Availability of data and materials: The various original data sources some of which are not all publicly available, because they contain various types of private information. The available platform provided data sources that support the findings and information of the research investigations are referenced where appropriate.

Conflict of interest: The authors declare no conflict of interest.

References

1. Paravano A, Patrizi M, Razzano E, et al. The impact of the new space economy on sustainability: an overview. Acta Astronautica. 2024; 222: 162-173. doi: 10.1016/j.actaastro.2024.05.046
2. Earth observation. Available online: joint-research-centre.ec.europa.eu (accessed on 6 January 2025).
3. Newcomers Earth Observation Guide | ESA Business Applications. Available online: business.esa.int (accessed on 6 January 2025).
4. GEO at a Glance. Available online: https://earthobservations.org/ (accessed on 6 January 2025).
5. Pennisi E. Meet the Landsat pioneer who fought to revolutionize Earth observation. Science. 2021; 373 (6561): 1292. doi:10.1126/science.acx9080
6. Eklundh L. Remote sensing and Earth observation. Available online: www.nateko.lu.se (accessed on 6 January 2025).
7. Ashley S. Game changer satellite will measure most of the water on the planet. CNN; 2022.
8. Tomás R, Li Z. Earth Observations for Geohazards: Present and Future Challenges. Remote Sensing. 2017; 9(3): 194. doi:10.3390/rs9030194
9. Balenovic I, Marjanovic H, Vuletic D, et al. Quality assessment of high density digital surface model over different land cover classes. Periodicum Biologorum. 2015; 117(4): 459–470. doi: 10.18054/pb.2015.117.4.3452
10. Appendix A—Glossary and Acronyms. Severn Tidal Tributaries Catchment Flood Management Plan—Scoping Stage. UK: Environment Agency; 2009. https://assets.publishing.service.gov.uk/media/5a7c871ae5274a7b7e321087/Severn_Tidal_Tributaries_Catchment_Management_Plan.pdf
11. Ronald T. Terrain models—A tool for natural hazard Mapping. In: Avalanche Formation, Movement and Effects. IAHS Publ; 1987.
12. Making 3D Terrain Maps, Shaded Relief. Available online: https://www.shadedrelief.com/ (accessed on 6 January 2025).

13. Robert S. Elegant Figures What Not To Do: Vertical Exaggeration. NASA Earth Observatory; 2010.
14. Hargitai H, Willner K, Buchroithner M. Methods in Planetary Topographic Mapping: A Review. In: Planetary Cartography and GIS. Springer International Publishing; 2019. pp. 147–174.
15. Banerdt B. Orbital Laser Altimeter. In: The Martian Chronicle. NASA. 2024; 1(3). https://nssdc.gsfc.nasa.gov/nmc/experiment/display.action?id=1996-062A-03
16. NASA, LOLA. Available online: https://science.nasa.gov/mission/lro/lola/ (accessed on 6 January 2025).
17. Cavanaugh JF, Smith JC, Sun X, et al. The Mercury Laser Altimeter Instrument for the MESSENGER Mission. In: Space Science Review. Springer Nature; 2007.
18. Hargitai H, Willner K, Hare T. Fundamental Frameworks in Planetary Mapping: A Review. In: Planetary Cartography and GIS. Springer International Publishing; 2019. pp. 75–101.
19. ALOS World 3D-30m. Available online: www.eorc.jaxa.jp (accessed on 6 January 2025).
20. ALOS World 3D. Available online: www.aw3d.jp (accessed on 6 January 2025).
21. Emisoft. 8 Things To Look For When Selecting Environmental Data Software. Available online: www.emisoft.com (accessed on 6 January 2025).
22. ESG assets may hit $53 trillion by 2025, a third of global AUM. Available online: https://www.bloomberg.com/professional/insights/trading/esg-assets-may-hit-53-trillion-by-2025-a-third-of-global-aum/ (accessed on 6 January 2025).
23. Kuznetsov VD, Sinelnikov VM, Alpert SN. Yakov Alpert: Sputnik-1 and the first satellite ionospheric experiment. Advances in Space Research. 2015; 55(12): 2833–2839. doi: 10.1016/j.asr.2015.02.033
24. How many Earth observation satellites are orbiting the planet in 2021? Available online: https://geospatialworld.net/blogs/how-many-satellites-are-orbiting-the-earth-in-2021/ (accessed on 6 January 2025).
25. Introduction to satellite. Available online: www.sasmac.cn (6 January 2025).
26. NASA. Drought in Iraq: Image of the Day. Available online: https://archive.org/details/ge_08797 (accessed on 6 January 2025).
27. Earth Observing System Data and Information System. Available online: https://www.nasa.gov/stem-content/earth-observing-system-data-and-information-system/ (accessed on 6 January 2025).
28. Earth Science Data and Information System (ESDIS) Project. Available online: https://www.earthdata.nasa.gov/about/esdis (accessed on 6 January 2025).
29. Behnke J, Kittel D. Looking Back at 25 Years With NASA's EOSDIS Distributed Active Archive Centers. AGU Fall Meeting Abstracts (Report). 2017; 2017: IN43A–0060.
30. Topics | Earthdata. Available online: https://www.earthdata.nasa.gov/ (accessed on 6 January 2025).
31. Wanchoo L, James N, Ramapriyan HK. NASA EOSDIS Data Identifiers: Approach and System. Data Science Journal. 2017; 16.
32. Blumenfeld J. The Global Change Master Directory: Data, Services, and Tools Serving the International Science Community. Earthdata (Report); 2017
33. ECHO—Application Program Interfaces (APIs) for Search and Order Global Change Master Directory. Available online: https://www.earthdata.nasa.gov/news/feature-articles/common-metadata-repository-foundation-nasas-earth-observation-data (accessed on 6 January 2025).
34. Bach D. With Azure, the US Army Corps of Engineers gains a 'powerful tool' for storm modeling. Available online: https://news.microsoft.com/source/features/digital-transformation/with-azure-the-us-army-corps-of-engineers-gains-a-powerful-tool-for-storm-modeling/ (accessed on 6 January 2025).
35. Retooling AI for Earth grants with Microsoft Dynamics 365. Available online: https://www.microsoft.com/insidetrack/blog/retooling-ai-for-earth-grants-with-microsoft-dynamics-365/ (accessed on 6 January 2025).
36. Lunden I. Microsoft launches AI for Earth to give $2M in services to environmental projects. TechCrunch; 2017.
37. Microsoft Planetary Computer. Available online: https://planetarycomputer.microsoft.com/ (accessed on 6 January 2025).
38. Microsoft wants to be a major AI player. In: Here's its master plan. Wired UK. https://www.wired.com/story/inside-microsofts-ai-comeback/
39. Smith B. AI for Earth can be a game-changer for our planet. Available online: https://blogs.microsoft.com/on-the-issues/2017/12/11/ai-for-earth-can-be-a-game-changer-for-our-planet/ (accessed on 6 January 2025).

40. AI for Earth - Microsoft AI. Available online: www.microsoft.com (accessed on 6 January 2025).
41. Mueller JP, Massaron L. Machine learning for dummies. John Wiley & Sons; 2021.
42. Sang X, Xue L, Ran X, et al. Intelligent High-Resolution Geological Mapping Based on SLIC-CNN. ISPRS International Journal of Geo-Information. 2020; 9(2): 99. doi: 10.3390/ijgi9020099
43. Si L, Xiong X, Wang Z, et al. A Deep Convolutional Neural Network Model for Intelligent Discrimination between Coal and Rocks in Coal Mining Face. Mathematical Problems in Engineering. 2020; 2020: 1–12. doi: 10.1155/2020/2616510
44. Merembayev T, Yunussov R, Yedilkhan A. Machine Learning Algorithms for Classification Geology Data from Well Logging. 2018 14th International Conference on Electronics Computer and Computation (ICECCO). Published online November 2018: 206–212. doi: 10.1109/icecco.2018.8634775
45. Costa I, Tavares F, Oliveira J. Predictive lithological mapping through machine learning methods: a case study in the Cinzento Lineament, Carajás Province, Brazil. Journal of the Geological Survey of Brazil. 2019; 2(1): 26–36. doi: 10.29396/jgsb.2019.v2.n1.3
46. Kumar C, Chatterjee S, Oommen T, et al. Automated lithological mapping by integrating spectral enhancement techniques and machine learning algorithms using AVIRIS-NG hyperspectral data in Gold-bearing granite-greenstone rocks in Hutti, India. International Journal of Applied Earth Observation and Geoinformation. 2020; 86: 102006. doi: 10.1016/j.jag.2019.102006
47. Radford DDG, Cracknell MJ, Roach MJ, et al. Geological Mapping in Western Tasmania Using Radar and Random Forests. IEEE Journal of Selected Topics in Applied Earth Observations and Remote Sensing. 2018; 11(9): 3075–3087. doi: 10.1109/jstars.2018.2855207
48. Wang Y, Ksienzyk AK, Liu M, et al. Multigeophysical data integration using cluster analysis: assisting geological mapping in Trøndelag, Mid-Norway. Geophysical Journal International. 2020; 225(2): 1142–1157. doi: 10.1093/gji/ggaa571
49. Latifovic R, Pouliot D, Campbell J. Assessment of Convolution Neural Networks for Surficial Geology Mapping in the South Rae Geological Region, Northwest Territories, Canada. Remote Sensing. 2018; 10 (2): 307. doi:10.3390/rs10020307
50. Marjanović M, Kovačević M, Bajat B, et al. Landslide susceptibility assessment using SVM machine learning algorithm. Engineering Geology. 2011; 123(3): 225–234. doi: 10.1016/j.enggeo.2011.09.006
51. Kawabata D, Bandibas J. Landslide susceptibility mapping using geological data, a DEM from ASTER images and an Artificial Neural Network (ANN). Geomorphology. 2009; 113(1–2): 97–109. doi: 10.1016/j.geomorph.2009.06.006
52. Chauhan S, Sharma M, Arora MK, et al. Landslide Susceptibility Zonation through ratings derived from Artificial Neural Network. International Journal of Applied Earth Observation and Geoinformation. 2010; 12(5): 340–350. doi: 10.1016/j.jag.2010.04.006
53. Biswajeet P, Saro L. Utilization of Optical Remote Sensing Data and GIS Tools for Regional Landslide Hazard Analysis Using an Artificial Neural Network Model. Earth Science Frontiers. 2017; 14 (6): 143–151. doi:10.1016/s1872-5791(08)60008-1
54. International society for rock mechanics commission on standardization of laboratory and field tests. International Journal of Rock Mechanics and Mining Sciences & Geomechanics Abstracts. 1978; 15(6): 319–368. doi:10.1016/0148-9062(78)91472-9. https://www.sciencedirect.com/science/article/abs/pii/0148906278914729
55. Bellante GJ, Powell SL, Lawrence RL, et al. Aerial detection of a simulated CO2 leak from a geologic sequestration site using hyperspectral imagery. International Journal of Greenhouse Gas Control. 2013; 13: 124–137. doi: 10.1016/j.ijggc.2012.11.034
56. Chen J, Zhou M, Zhang D, et al. Quantification of water inflow in rock tunnel faces via convolutional neural network approach. Automation in Construction. 2021; 123: 103526. doi: 10.1016/j.autcon.2020.103526
57. Bhattacharya B, Solomatine DP. Machine learning in soil classification. Neural Networks. 2006; 19(2): 186–195. doi: 10.1016/j.neunet.2006.01.005
58. Zhang Y, Wang G, Li M, et al. Automated Classification Analysis of Geological Structures Based on Images Data and Deep Learning Model. Applied Sciences. 2018; 8(12): 2493. doi: 10.3390/app8122493
59. Li Z, Meier M, Hauksson E, et al. Machine Learning Seismic Wave Discrimination: Application to Earthquake Early Warning. Geophysical Research Letters. 2018; 45(10): 4773–4779. doi: 10.1029/2018gl077870

60. Rouet-Leduc B, Hulbert C, Lubbers N, et al. Machine Learning Predicts Laboratory Earthquakes. Geophysical Research Letters. 2017; 44(18): 9276–9282. doi: 10.1002/2017gl074677
61. Petty TR, Dhingra P. Streamflow Hydrology Estimate Using Machine Learning (SHEM). JAWRA Journal of the American Water Resources Association. 2017; 54(1): 55–68. doi: 10.1111/1752-1688.12555
62. Merghadi A, Yunus AP, Dou J, et al. Machine learning methods for landslide susceptibility studies: A comparative overview of algorithm performance. Earth-Science Reviews. 2020; 207: 103225. doi: 10.1016/j.earscirev.2020.103225
63. Akhtar ZB, Tajbiul Rawol A. Unlocking the Future for the New Data Paradigm of DNA Data Storage : An Investigative Analysis of Advancements, Challenges, Future Directions. Journal of Information Sciences. doi: 10.34874/IMIST.PRSM/JIS-V23I1.47102
64. Bin Akhtar Z. Artificial intelligence (AI) within manufacturing: An investigative exploration for opportunities, challenges, future directions. Metaverse. 2024; 5(2): 2731. doi: 10.54517/m.v5i2.2731
65. Bin Akhtar Z. From bard to Gemini: An investigative exploration journey through Google’s evolution in conversational AI and generative AI. Computing and Artificial Intelligence. 2024; 2(1): 1378. doi: 10.59400/cai.v2i1.1378
66. Akhtar ZB. Unveiling the evolution of generative AI (GAI): a comprehensive and investigative analysis toward LLM models (2021–2024) and beyond. Journal of Electrical Systems and Information Technology. 2024; 11(1). doi: 10.1186/s43067-024-00145-1
67. Unraveling the Promise of Computing DNA Data Storage: An Investigative Analysis of Advancements, Challenges, Future Directions. Journal of Advances in Artificial Intelligence. 2024; 2(1). doi: 10.18178/jaai.2024.2.1.122-137
68. Akhtar ZB. The design approach of an artificial intelligent (AI) medical system based on electronical health records (EHR) and priority segmentations. The Journal of Engineering. 2024; 2024(4). doi: 10.1049/tje2.12381
69. Akhtar ZB. Securing Operating Systems (OS): A Comprehensive Approach to Security with Best Practices and Techniques. International Journal of Advanced Network, Monitoring and Controls. 2024; 9(1): 100–111. doi: 10.2478/ijanmc-2024-0010
70. Akhtar ZB. Generative artificial intelligence (GAI): From large language models (LLMs) to multimodal applications towards fine tuning of models, implications, investigations. Computing and Artificial Intelligence. 2024; 3(1): 1498. doi: 10.59400/cai.v3i1.1498
71. Akhtar ZB, Rawol AT. Harnessing artificial intelligence (AI) for cybersecurity: Challenges, opportunities, risks, future directions. Computing and Artificial Intelligence. 2024; 2(2): 1485. doi: 10.59400/cai.v2i2.1485
72. Akhtar ZB, Tajbiul Rawol A. Enhancing Cybersecurity through AI-Powered Security Mechanisms. IT Journal Research and Development. 2024; 9(1): 50–67. doi: 10.25299/itjrd.2024.16852
73. Zarif BA, Ahmed TR. Artificial Intelligence (AI), Extended Reality (XR): A Biomedical Engineering (BME) Perspective Investigation Analysis. RPC Journal of Bio-Med and Clinical Research. RPC Publishers. 2024; 1(1).
74. Akhtar ZB. Artificial Intelligence (AI) within the Realm of Cyber Security. Insight. Electr. Electron. Eng. 2024; 1(1): 1–11.
75. Akhtar Z. Trends Tech Sci Res Computer Vision and Beyond: A Deep Dive Exploration and Investigation. IEEE Region 10 Trends Tech Sci Res. 2024; 7(3). doi: 10.19080/TTSR.2024.07.555711

EnPress Publisher, LLC

Add: 9650 Telstar Avenue, Unit A, Suite 121, El Monte, CA 91731, USA.
Email: editorial@enpress-publisher.com
Web: https://systems.enpress-publisher.com